Precision Measurement in Atom Interferometry Using Bragg Diffraction

by

Brian Vincent Estey

A dissertation submitted in partial satisfaction of the
requirements for the degree of

Doctor of Philosophy

in

Physics

in the

Graduate Division

of the

University of California, Berkeley

Committee in charge:

Associate Professor Holger Müller, Chair
Associate Professor Hartmut Häffner
Professor Eli Yablonovitch

Fall 2016

Precision Measurement in Atom Interferometry Using Bragg Diffraction

Abstract

Precision Measurement in Atom Interferometry Using Bragg Diffraction

by

Brian Vincent Estey

Doctor of Philosophy in Physics

University of California, Berkeley

Associate Professor Holger Müller, Chair

We experimentally and theoretically study Bragg diffraction as a tool for large-momentum transfer beam splitters in atom interferometry. A theoretical framework is developed to quantify the diffraction phase systematic caused by Bragg diffraction and experiments are performed to confirm these predictions using a Ramsey-Bordé atom interferometer. We then develop methods to systematically cancel and reduce the diffraction phase systematic by carefully selecting Bragg diffraction parameters and utilizing Bloch oscillations. These techniques are then applied to an ongoing precision measurement of h/m_{Cs} for cesium, with the end goal of measuring the fine structure constant α. We demonstrate a high contrast simultaneous conjugate Ramsey-Bordé interferometer using 5th order Bragg diffraction and 25 common mode Bloch oscillations which achieves 2.5×10^6 radians of phase. We also demonstrate an interferometer with a statistical uncertainty of $\delta\alpha/\alpha = 0.25$ ppb after 25 hours of integration time that has diffraction phase systematic error of around 1 ppb. Other sources of systematic uncertainty are also thoroughly explored and determined to better than 0.1 ppb. The techniques and theories developed in this thesis will hopefully help enable future precision measurements based on Bragg diffraction.

To my sanity.

Contents

List of Figures

List of Tables

Chapter 1

Introduction

1.1 Interferometry

The basic concept behind any interferometric measurement is relatively straightforward and relies on two important principles: coherent superposition and counting. When a wave-function (whether it be a light field, a quantum particle, or even a classical wave) is coherently split along two paths and brought back together, the resulting interference pattern will be a function of the relative phase difference between the split wave-functions. Since the phase of the wave-function is 2π periodic, the interference (and therefore the relative phase difference) can theoretically be measured to the same precision regardless of the absolute phase difference. The power of interferometry occurs when the signal of interest (whether it be time, distance, etc.) is proportional to the absolute phase difference. Since counting the number of oscillations can be done with negligible probability of error for a well resolved fringe, one can perform a more precise measurement by increasing the absolute phase difference without the need for a better measurement of the interference.

This theoretical scalability of the signal relative to a fixed absolute measurement error in an interferometer makes it very appealing for precision measurement. One of the quintessential uses of precision interferometry was in 1887 when Michelson and Morley [1] set up an optical interferometer which helped disprove the aether theory of electromagnetism. Optical interferometers have continued to increase in sensitivity in large part due to the invention of the laser, which enabled extremely strong coherent sources of light. While laser interferometers have the benefit of high signal-to-noise, their ultimate accuracy is limited by the need to contain the light using macro-scale systems (mirrors, fiber optics) which are subject to thermal variation. As an optical interferometer changes in temperature, the total path length of the light varies and therefore so does the absolute phase shift. These shifts cause errors when converting the interference signal to an absolute signal since the scale factor between the two is less well known. The stability of this scale factor determines the accuracy of the device and therefore is an intense area of research [2].

Atom interferometers work along the same principles as an optical interferometer, except

that atoms play the role of the wave and light is instead used to manipulate the path of the atoms. Since atoms are (usually) non-relativistic, they can easily be contained for limited periods of time in an inertial free-fall frame where coupling to the thermodynamic world is significantly reduced. Consider an atom in free-fall that interacts with a laser field such that two photon momentum quanta are transferred to the atom with 50% probability creating a superposition state. As two atom wave-packets propagate, they will acquire phases proportional to their kinetic and potential energy. After the two superpositions are brought back together and interfered with additional laser pulses, a determination of the energy difference can be made from the resulting interference. By measuring the laser frequency [3] which determines the atom's path, the total phase shift can be determined to very high accuracy, enabling a precision measurement of the energy difference.

Atom interferometry has proven to be an exceptionally powerful tool in precision measurement over the last couple of decades. Applications have ranged from inertial sensing with accelerometers [4] and gyroscopes [5, 6] to measurements of gravitational tides [7] and gravity gradients [8]. Where atom interferometers are especially useful is in fundamental physics research where they have been used to measure the gravitational constant [9], test the equivalence principle [10], put bounds on theories of dark energy [11], and serve as microscopic mass standards [12]. There are even proposals to measure the charge neutrality of atoms [13] and investigate the gravitational AharonovBohm effect [14].

The main focus of our atom interferometer (on which this thesis is based) is to measure the fine structure constant [15]. By utilizing higher order momentum transfer techniques, the phase sensitivity of our atom interferometer can be increased to hopefully pave the way for an improved measurement and enable future tests of fundamental physics.

1.2 Fine Structure Constant

The fine structure constant α is a parameter in the standard model that characterizes the strength of the electromagnetic field and relates the binding energy of an electron-proton system to the rest mass energy of the electron through the relationship

$$hcR_\infty = \frac{1}{2}\alpha^2 m_e c^2, \tag{1.1}$$

where h is the Plank constant, c is the speed of light, R_∞ is the Rydberg constant, and m_e is the mass of an electron. Historically, measurements of the fine structure constant have come from many branches of physics including spectroscopy of muonium [16], h/m_N for neutrons [17], measurements of the proton gyromagnetic ratio [18], and the quantum Hall effect [19]. The most accurate measurements of α by far, however, come exclusively from a measure of h/m for neutral atoms [15, 20] and the anomalous magnetic momentum of the electron $(g-2)$ [21, 22]. A list of α measurements and their relative uncertainty are shown in Fig. 1.1, with the last two measurements being of prime importance. The measurements

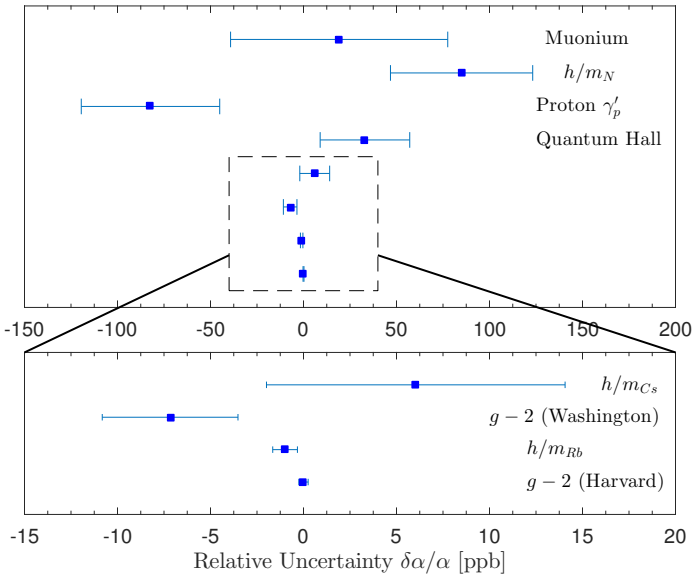

Figure 1.1: The relative uncertainty of various types of fine structure constant measurements.

of h/m and $g-2$ are fortunately very different in nature and provide a means to test the theory of quantum electrodynamics in the laboratory.

To determine α from a measurement of h/m_{x} for some atom with mass m_x, one relies on the relationship (1.1) which can be rewritten as

$$\begin{aligned}\alpha^2 &= 2\frac{R_\infty}{c}\frac{m_e}{h} \\ &= 2\frac{R_\infty}{c}\frac{m_e}{u}\frac{u}{m_x}\frac{m_x}{h},\end{aligned} \tag{1.2}$$

where u is the atomic mass unit. Instead of measuring h/m_e for the electron directly, the fine structure can be determined by the ratio of the electron mass to the atomic mass unit [23,24] and the ratio of the atomic mass unit to some other atom [25,26], in combination with h/m_x for that atom. This chain of different measurements ends up being easier than determining h/m_e due to the inherent difficulty of containing and manipulating free electrons. The uncertainties for these quantities are listed in Table 1.1 for two popular atom species, with the largest of these uncertainties coming from the values of h/m. Since the fine structure constant is related to h/m by a square root, the relationship (1.2) means that the uncertainty in α is half that of h/m and, thus, the best measurement using this method has an uncertainty of 0.66 ppb [15].

The other method of measuring α involves the anomalous magnetic moment of the electron $g-2$, which can be written as a power series in α using corrections from quantum electrodynamics (QED)

Table 1.1: Sources of uncertainty in determining α with a h/m measurement (left) and a $g-2$ measurement (right). The uncertainties are taken from the references listed in this section and from CODATA [27].

	Uncertainty
R_∞	0.005 ppb
m_e/u	0.03 ppb
m_{Rb}/u	0.012 ppb
h/m_{Rb}	1.3 ppb
m_{Cs}/u	0.01 ppb
h/m_{Cs}	15 ppb

	Uncertainty
$g-2$	0.24 ppb
a_4	0.05 ppb
a_5	0.034 ppb
a_{QCD}	0.013 ppb

$$g-2=\sum_{n=1}\left(\frac{\alpha}{\pi}\right)^n a_n+\alpha_{\mathrm{weak}}+\alpha_{\mathrm{QCD}}, \tag{1.3}$$

where the coefficients a_n come from calculating all possible QED corrections of order $2n$ and the factors α_{weak} and α_{QCD} are electroweak and quantum chromodynamics corrections obtained from particle physics data [28]. From a measurement of $g-2$ for an electron, the value of the fine structure constant can be obtained by inverting (1.3). A summary of the QED corrections are shown in Fig. 1.2, with relevant uncertainties listed in Table 1.1, which give a combined uncertainty of 0.25 ppb in α.

A measurement of α using h/m and (1.2) is essentially free from the theory of QED, with only small correction to R_∞ from the Lamb shift [29]. Therefore by comparing α as measured by h/m (1.2) and $g-2$ (1.3), one can test the theory of QED to extremely high accuracy. From the data in Fig. 1.2, one can see that improving the measurement of h/m has the potential to test QED at the level of 10th order corrections.

In addition, there is speculative evidence for new physics in measurements of the anomalous magnetic momentum of the muon [30]. When the experimentally measured value is compared to theoretical calculations derived from particle physics data, the measured value deviates from theory by approximately 3.6 standard deviations. If this deviation is caused by new physics which couples to the muon with a strength Λ_μ, then the new physics will also cause a deviation in the electron anomalous moment

$$\frac{\Delta a_e}{\Delta a_\mu}=\frac{m_e^2}{m_\mu^2}\frac{\Lambda_\mu^2}{\Lambda_e^2},$$

where Λ_e is the coupling between the new physics and the electron [31]. If the couplings are approximately equal, $\Lambda_\mu/\Lambda_e\approx 1$, then this shift could show up in the electron $g-2$ at the

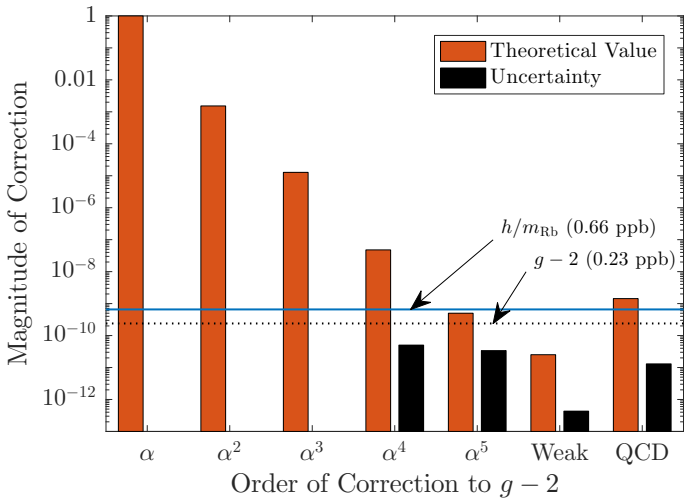

Figure 1.2: The relative magnitude of the different QED corrections that go into calculating the electron anomalous magnetic moment $g-2$. Also listed is the uncertainty in the experimental $g-2$ measurement and the corresponding value using α derived from h/m_{Rb}.

0.06 ppb level. Therefore if α is measured with $g-2$ and h/m independently at the 0.06 ppb level, this new physics could potentially be tested (if the muon measurement is verified).

1.3 h/m Measurement

When an atom of mass m absorbs a photon of known wavenumber k, then the atom will recoil with a velocity $v_r = \hbar k/m$ (where $\hbar = h/2\pi$). From a measurement of the imparted kinetic energy

$$\begin{aligned}\frac{1}{2}mv_r^2 &= \hbar\left(\frac{\hbar k^2}{2m}\right)\\ &= \hbar\omega_r,\end{aligned}$$

a value for $\hbar/m$ can be obtained by taking into account the laser frequency. Since this recoil frequency ω_r shifts the energy of the atom, it can be measured with interferometry techniques.

Consider an atom that absorbs a photon from one laser field and is stimulated to emit a photon in the counter-propagating direction such that the atom is coherent kicked with a momentum of $2\hbar k$. If this is done such that the atom ends up in a momentum superposition, then the moving part of the atom's wave-function will gain energy at a rate $\hbar\omega_r$ faster than the stationary component. The moving part of the superposition is then kicked several more

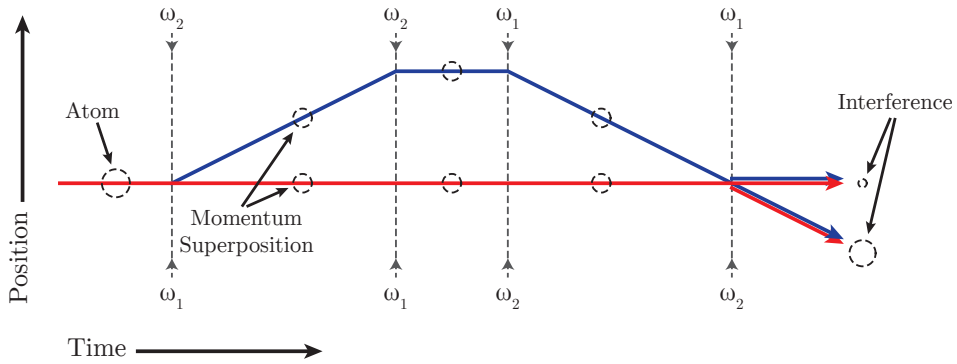

Figure 1.3: A simple interferometer to measure the recoil energy of an atom, also called a Ramsey-Bordé interferometer. The atom is coherently split by atom-light beam splitters (vertical dashed lines) and recombined to produce interference proportional to the kinetic energy.

times to bring the wave-function back together as shown in Fig. 1.3, where the resulting interference will be proportional to the energy difference (and thus to the kinetic energy).

An interferometer with this configuration, also called a Ramsey-Bordé interferometer, typically relies on Raman transitions for the beam splitters to transfer two photon momenta to the atom [32]. In order to scale up the interferometer phase and increase the accuracy, the time between pulses can be increased so that the atom accumulates a larger kinetic energy phase shift during its evolution. A different way to scale up the sensitivity is to increase the number of photons the atom absorbs, so that the kinetic energy changes from

$$\frac{1}{2}m\left(\frac{2\hbar k}{m}\right)^2 \rightarrow \frac{1}{2}m\left(\frac{2n\hbar k}{m}\right)^2,$$

where n is an integer. This has the advantage that the signal is proportional to the square of the photon number, $(2n)^2$, which is a very appealing scaling. The focus of the work in this thesis is on using a multi-photon beam splitter process called Bragg diffraction [33] to increase the Ramsey-Bordé signal and hopefully enable a new measurement of α.

1.4 Overview of this Thesis

In Chapter 2, the total phase of the atom interferometer is calculated, including the phase from atom-light interactions. In addition, the theory of Bragg diffraction beam splitters is discussed in detail. Chapters 3 and 4 will focus on the experimental setup of the various optical systems and techniques needed to implement our atom interferometer. Some experimental results are discussed in Chapter 5, focusing on increasing the interferometer phase through high momentum transfer beam splitters and decreasing the systematic influences of

those beam splitters on our recoil measurement. Finally, Chapter 6 will briefly discuss other possible systematic effects and their influence on h/m.

Chapter 2

Theory

The simplest interferometer that can be constructed in quantum mechanics is one in which an initial state $|\psi_1\rangle$ is placed into a superposition state via a rotation between $|\psi_1\rangle$ and $|\psi_2\rangle$, allowed to evolve in time, and then rotated back:

$$\hat{S}\hat{U}\hat{S}\,|\psi_1\rangle\,, \tag{2.1}$$

where the rotation operator $\hat{S}$ (colloquially called a beam splitter) and evolution operator $\hat{U}$ are in their most basic form:

$$\hat{S} = \frac{1}{\sqrt{2}}\begin{pmatrix} 1 & i \\ i & 1 \end{pmatrix}, \qquad\qquad \hat{U} = \begin{pmatrix} e^{i\phi_1} & 0 \\ 0 & e^{i\phi_2} \end{pmatrix}.$$

The probability that the final measured state ends up in $|\psi_1\rangle$ or $|\psi_2\rangle$ is then the projection of (2.1) onto $|\psi_j\rangle$, which gives

$$\begin{aligned} \left|\langle\psi_1|\,\hat{S}^\dagger\hat{U}\hat{S}\,|\psi_1\rangle\right|^2 &= \left|\frac{1}{2}e^{i\phi_1} - \frac{1}{2}e^{i\phi_2}\right|^2 \\ &= \sin^2\left(\frac{\phi_1-\phi_2}{2}\right), \\ \left|\langle\psi_2|\,\hat{S}^\dagger\hat{U}\hat{S}\,|\psi_1\rangle\right|^2 &= \cos^2\left(\frac{\phi_1-\phi_2}{2}\right). \end{aligned}$$

Therefore the probability to end up in a given state then depends on the phase acquired under the evolution operator $\hat{U}$ and from the beam splitters $\hat{S}$. For interferometry in general, it is therefore important to understand how the wave-function (whether it be particle, atom, etc.) acquires phase during the wave-function's free evolution and from the beam splitter interactions.

2.1 Free Evolution Phase

The free evolution of a particle in atom interferometry is dependent on the Hamiltonian $\hat{H}$ that determines the particle's energy. For generality, consider a Hamiltonian that consists of the particle's kinetic energy along with a potential energy term which encompasses conservative forces such as gravity or magnetic fields.

In quantum mechanics, the dynamics of the system are described by the Schrödinger equation

$$\hat{H}\left|\psi(t)\right\rangle = i\hbar\frac{\partial}{\partial t}\left|\psi(t)\right\rangle.$$

For a time-independent Hamiltonian and a particle initially in the state $|\psi(t_I)\rangle$ at a time t_I, the Schrödinger equation can be directly integrated to find state $|\psi\rangle$ at a later time t.

$$\begin{aligned}\left|\psi(t)\right\rangle &= e^{-iH(t-t_I)/\hbar}\left|\psi(t_I)\right\rangle \\ &= \hat{U}\left|\psi(t_I)\right\rangle.\end{aligned}$$

Consider a particle in one dimension that moves along the x-axis, which is initially located at x_I at a time t_I. The probability amplitude that the initial particle $|\psi(t_I)\rangle$ can be found at a position x_1 after a time δt is then

$$\begin{aligned}\left\langle x_1|\psi(t_I+\delta t)\right\rangle &= \left\langle x_1\right| e^{-iH\delta t/\hbar}\left|\psi(t_I+\delta t)\right\rangle \\ &= \left\langle x_1\right| e^{-iH\delta t/\hbar}\left|x_I\right\rangle.\end{aligned}$$

This process can be repeated for the next time step δt to find the probability amplitude of a state which starts at $|x_1\rangle$ to end up at $|x_2\rangle$ and so on. To find the amplitude of a particular path $(x_1, x_2, \cdots, x_{N-1})$ between x_I and x_F, it is just a matter of multiplying the amplitudes of each intermediate path $x_j \to x_{j+1}$:

$$\left\langle x_F\right| e^{-iH\delta t}\left|x_{N-1}\right\rangle\left\langle x_{N-1}\right| e^{-iH\delta t}\left|x_{N-2}\right\rangle\ldots\left\langle x_1\right| e^{-iH\delta t}\left|x_I\right\rangle,$$

where $\hbar$ has been set to 1 for simplicity. The path integral formulation of quantum mechanics then states that the amplitude for a state starting at x_I to end up at x_F, is the integral over all possible paths from $x_I(t_I)$ to $x_F(t_F)$ [34].

$$\left\langle x_F\right| e^{-iH(t_F-t_I)}\left|x_I\right\rangle = \prod_{j=1}^{N-1}\int dx_j\left\langle x_F\right| e^{-iH\delta t}\left|x_{N-1}\right\rangle\left\langle x_{N-1}\right| e^{-iH\delta t}\left|x_{N-2}\right\rangle\ldots, \tag{2.2}$$

where $\delta t = (t_F - t_I)/N$. To simplify the integral, a small piece of the path between x_j and x_{j+1},

$$\langle x_{j+1}| e^{-iH\delta t} |x_j\rangle , \tag{2.3}$$

is evaluated during a time-step δt. Since the Hamiltonian is of the form $H = \hat{p}^2/2m + V(\hat{x})$, inserting a complete set of momentum states

$$\int \frac{dp}{2\pi} |p\rangle \langle p| = 1$$

into (2.3) allows us to rewrite it as:

$$\begin{aligned} \langle x_{j+1}| e^{-i\delta t\left(\hat{p}^2/2m+V(\hat{x})\right)} |x_j\rangle &= \int \frac{dp}{2\pi} \langle x_{j+1}| e^{-i\delta t\left(\hat{p}^2/2m+V(\hat{x})\right)} |p\rangle \langle p|x_j\rangle \\ &= e^{-i\delta t V(x_j)} \int \frac{dp}{2\pi} e^{-i\delta t\left(p^2/2m\right)} \langle x_{j+1}|p\rangle \langle p|x_j\rangle \\ &= e^{-i\delta t V(x_j)} \int \frac{dp}{2\pi} e^{-i\delta t\left(p^2/2m\right)} e^{ip(x_{j+1}-x_j)}, \end{aligned} \tag{2.4}$$

where the position and momentum operators have been applied to the states $|p\rangle$ and $|x_j\rangle$ to yield their eigenvalues and we have made use of the relation $\langle x_j|p\rangle = e^{ipx_j}$. Since the potential does not depend on the momentum, we may perform the Gaussian integral[1] over dp in (2.4), which can then be written as

$$\langle x_{j+1}| e^{-i\delta t\left(\hat{p}^2/2m+V(\hat{x})\right)} |x_j\rangle = \left(\frac{-im}{2\pi\delta t}\right)^{\frac{1}{2}} e^{i\delta t\left[\frac{m}{2}[(x_{j+1}-x_j)/\delta t]^2 - V(x_j)\right]}. \tag{2.5}$$

To evaluate the remaining path segments, simply apply the results from (2.5) to each discrete step of Eq. (2.2) to obtain

$$\langle x_F| e^{-iH(t_F-t_I)} |x_I\rangle = \left(\frac{-im}{2\pi\delta t}\right)^{\frac{N}{2}} \left(\prod_{j=1}^{N-1} \int dx_j\right) e^{i\delta t \sum_{j=0}^{N-1}\left[\frac{m}{2}[(x_{j+1}-x_j)/\delta t]^2 - V(x_j)\right]}. \tag{2.6}$$

Since the $(x_{j+1} - x_j)/\delta t$ factor in the exponential is approximately a discrete time derivative of x_j, the terms in the exponential can be written as

$$\begin{aligned} \delta t \sum_{j=0}^{N-1} \frac{m}{2} \left(\frac{x_{j+1} - x_j}{\delta t}\right)^2 &\to \int_{t_I}^{t_F} \frac{m}{2} \dot{q}^2 dt, \\ \delta t \sum_{j=0}^{N-1} V(x_j) &\to \int_{t_I}^{t_F} V(q) dt, \end{aligned}$$

[1] A Gaussian integral with complex argument is evaluated as $\int \exp[\frac{1}{2}iax^2 + ibx]dx = \sqrt{2\pi i/a}\exp[-i\frac{b^2}{2a}]$.

where the parameterized function $q(t)$ is the continuum limit of the path $(x_I, x_1, \ldots, x_{N-1}, x_F)$ as $\delta t \to 0$ with $q(t_I) = x_I$ and $q(t_F) = x_F$. The full path integral (2.6) is then

$$\begin{aligned} \langle x_F | \, e^{-iH(t_F - t_I)} \, | x_I \rangle &= \lim_{N\to\infty} \left(\frac{-im}{2\pi\delta t} \right)^{\frac{N}{2}} \left(\prod_{j=1}^{N-1} \int dx_j \, e^{i \int_{t_I}^{t_F} [m\dot{q}^2/2 - V(q)] dt} \right) \\ &= \int \mathcal{D}x \, e^{i \int_{t_I}^{t_F} [m\dot{q}^2/2 - V(q)] dt}. \end{aligned} \tag{2.7}$$

While this formalism of integrating over all paths is very useful in field theory, it is somewhat impractical for atom interferometry and therefore beneficial to make some approximations.

Recognizing that the bracketed term in the exponent of (2.7) is the Lagrangian $L(q, \dot{q}) = m\dot{q}^2/2 - V(q)$, the integral $\int_{t_I}^{t_F} L(q, \dot{q}) dt$ is simply the action S of a given path $q(t)$. The phase and amplitude of a state starting at x_I and ending at x_F is therefore determined by the interference between all possible paths $e^{i \int dt \, L(q,\dot{q})}$ between $|x_I\rangle$ and $|x_F\rangle$. If the units of $\hbar$ are restored,

$$\langle x_F | \, e^{-iH(t_F - t_I)} \, | x_I \rangle = \lim_{N\to\infty} \left(\frac{-im}{2\pi\hbar\delta t} \right)^{\frac{N}{2}} \left(\prod_{j=1}^{N-1} \int dx_j \, e^{iS(q)/\hbar} \right), \tag{2.8}$$

it becomes clear that the exponential $e^{iS/\hbar}$ will oscillate rapidly when the action is large compared to $\hbar$, tending to destructively interfere with neighboring paths. The path integral will instead be dominated by constructive interference from the slower varying terms, which occur around the minimum of $S/\hbar$. Minimizing the action $S = \int_{t_I}^{t_F} L(q, \dot{q}) dt$ yields the familiar Euler-Lagrange equations:

$$\frac{d}{dt} \left(\frac{\partial L}{\partial \dot{q}} \right) - \frac{\partial L}{\partial q} = 0,$$

which implies that the path integral will be dominated by the classical trajectories of the particle.

Since only paths near the classical trajectory will contribute to the integral, we can Taylor expand the action about the classical path q_c. Recalling that the parameterized function $q(t)$ is the continuum of the path $(x_I, x_1, \ldots, x_{N-1}, x_F)$, we can rewrite $q(t)$ as a perturbation of the classical path $q_c(t) \approx \vec{q}_c = \{x_I, x_c(t_I + \delta t), \ldots, x_c(t_I + (N-1)\delta t), x_F\}$ by an amount $\delta q(t) \approx \vec{\epsilon} = \{0, \epsilon_1, \ldots, \epsilon_{N-1}, 0\}$:

$$q(t) = q_c(t) + \delta q(t).$$

By making a change of variables $x_j \to x_c(t_j) + \epsilon_j$ and $dx_j \to d\epsilon_j$, the path integral (2.8) becomes

$$\lim_{N\to\infty} \left(\frac{-im}{2\pi\hbar\delta t} \right)^{\frac{N}{2}} \left(\prod_{j=1}^{N-1} \int d\epsilon_j \, e^{iS[q_c(t) + \delta q(t)]/\hbar} \right). \tag{2.9}$$

The action can now be power series expanded about $q_c(t)$ for small deviations $\delta q(t)$ about the classical path. Since $\delta q(t)$ is actually a function of multiple variables $(\epsilon_1, \ldots, \epsilon_{N-1})$, the familiar power series needs to be generalized to

$$\begin{aligned} S(\vec{q}_c + \vec{\epsilon}) &= \sum_{n=0}^{\infty} \frac{1}{n!} (\vec{\epsilon} \cdot \nabla)^n S(\vec{q}) \Big|_{q=q_c} \\ &\approx S(q_c) + \left(\sum_{j=1}^{N-1} \frac{\partial S}{\partial x_j} \epsilon_j \right) \Big|_{q=q_c} + \frac{1}{2} \left(\sum_{i=1}^{N-1} \sum_{j=1}^{N-1} \frac{\partial^2 S}{\partial x_i \partial x_j} \epsilon_i \epsilon_j \right) \Big|_{q_c} + \mathcal{O}(\epsilon^3), \end{aligned}$$

where the first order term in the power series should be zero since the expansion is about the minimum of S. Using the discrete definition of the action from (2.6)

$$S = \delta t \sum_{j=0}^{N-1} \frac{m}{2} \frac{(x_{j+1} - x_j)^2}{\delta t^2} - V(x_j)$$

where the first order term of the power series can be calculated as

$$\begin{aligned} \sum_{j=1}^{N-1} \frac{\partial S}{\partial x_j} \Big|_{q=q_c} &= \left(\delta t \sum_{j=1}^{N-1} -m \frac{(x_{i+1} - 2x_i + x_{i-1})}{\delta t^2} - \frac{\partial V(x_j)}{\partial x_j} \right) \Big|_{q=q_c} \\ &\cong \int_{t_I}^{t_F} \left(-m \frac{\partial q}{\partial t^2} - \frac{\partial V(q)}{\partial q} \right) dt \Big|_{q=q_c} = 0, \end{aligned}$$

where the finite second derivative is replaced by a continuous second derivative as $\delta t \to 0$. The integrand is equal to the Euler-Lagrange equations, which is zero along the classical path by definition. The total path integral (2.8) can then be approximated as

$$\begin{aligned} &\langle x_F | \, e^{iH(t_F - t_I)/\hbar} \, | x_I \rangle \approx \\ &\lim_{N \to \infty} \left(\frac{-im}{2\pi\hbar\delta t} \right)^{\frac{N}{2}} e^{iS(q_c)/\hbar} \left(\prod_{j=1}^{N-1} \int d\epsilon_j \, \exp \left[\frac{i}{2\hbar} \left(\sum_{i=1}^{N-1} \sum_{j=1}^{N-1} \frac{\partial^2 S}{\partial x_i \partial x_j} \epsilon_i \epsilon_j \right) \Big|_{q_c} + \mathcal{O}(\epsilon^3) \right] \right), \end{aligned} \tag{2.10}$$

where terms of $\mathcal{O}(\epsilon^3)$ are dropped. In the case of a quadratic potential where $\partial^3 S / \partial x^3 = 0$, then these higher order terms are identically zero and (2.10) is therefore exact. To compute the second order term for this approximation, first construct the matrix

$$\mathcal{A}_{ij} = \frac{\partial^2 S}{\partial x_i \partial x_j} \Big|_{q=q_c}.$$

Since $\mathcal{A}$ is real and symmetric, the eigenvectors-eigenvalues pairs $[\vec{v}_n, \lambda_n]$ for $\mathcal{A}$ (of which there are $N-1$) may be found by solving the eigenvalue problem,

$$\mathcal{A}\vec{v}_n = \lambda_n \vec{v}_n, \tag{2.11}$$

where the eigenvectors are chosen such that they are orthogonal and normalized:

$$\vec{v}_m^T \vec{v}_n = \delta_{mn}. \tag{2.12}$$

Since the eigenvectors $\vec{v}_n$ make up a complete basis, the perturbation $\vec{\epsilon}$ can be written as a superposition of the basis α_n which results from diagonalizing $\mathcal{A}$,[2]

$$\epsilon_j = \sum_n \alpha_n v_n^j, \tag{2.13}$$

where v_n^j is the jth component of the nth eigenvector. This change of basis allows the expansion of the double sum in (2.10),

$$\begin{aligned}
\sum_{i,j} \epsilon_i \frac{\partial^2 S}{\partial x_i \partial x_j} \epsilon_j &\to \sum_{i,j}\sum_{n,m} \alpha_n v_n^i \mathcal{A}_{ij} \alpha_m v_m^j \\
&= \sum_{n,m} \alpha_n \alpha_m \vec{v}_n^T \mathcal{A} \vec{v}_m \\
&= \sum_{n,m} \alpha_n \alpha_m \left(\lambda_m \delta_{mn}\right) \\
&= \sum_n \alpha_n^2 \lambda_n,
\end{aligned}$$

where we have made use of the identities (2.11) and (2.12). The differential elements $d\epsilon_j$ can also be written in the basis of α_n by doing a multi-variable coordinate transform

$$\prod_{j=1}^{N-1} \int d\epsilon_j = |\det(\mathcal{V})| \prod_{n=1}^{N-1} \int d\alpha_n,$$

where $\mathcal{V}$ is the matrix of all eigenvectors $\vec{v}_n$. Since all the eigenvectors are normalized and orthogonal from (2.12), $|\det(\mathcal{V})| = 1$. Each integral $d\alpha_n$ in (2.10) can then be sequentially performed independently from the other variables $d\alpha_m$ using Gaussian integrals to give

$$\prod_{n=1}^{N-1} \int d\alpha_n \, \exp\left[\frac{i}{2\hbar} \sum_{m=1}^{N-1} \lambda_m \alpha_m^2\right] = \prod_{n=1}^{N-1} \left(\frac{2\pi i \hbar}{\lambda_n}\right)^{\frac{1}{2}},$$

[2]The set of eigenvectors $\vec{v}_n$ diagonalize $\mathcal{A} = \mathcal{V}^T \Lambda \mathcal{V}$. Therefore $\mathcal{V}_{jn} = v_n^j$ maps the usual position basis $\vec{\epsilon} = (\epsilon_1, \epsilon_2, \ldots, \epsilon_{N-1})$ into a new basis $\vec{\alpha} = (\alpha_1, \alpha_2, \ldots, \alpha_{N-1}) = \mathcal{V}\vec{\epsilon}$ in which there is no coupling between basis variables through $\mathcal{A}$. This mapping can be inverted to instead write ϵ_j in terms of α_n.

resulting in the complete path integral:

$$\begin{aligned}\langle x_F|\, e^{iH(t_F-t_I)/\hbar}\,|x_I\rangle &\approx \lim_{N\to\infty}\left(\frac{-im}{2\pi\hbar\delta t}\right)^{\frac{N}{2}} e^{iS(q_c)/\hbar}\prod_{n=1}^{N-1}\left(\frac{2\pi i\hbar}{\lambda_n}\right)^{\frac{1}{2}}\\ &= \lim_{N\to\infty}\sqrt{\frac{1}{2\pi i\hbar}}\left(\frac{m}{\delta t}\right)^{\frac{N}{2}}\left(\prod_n \lambda_n\right)^{-\frac{1}{2}} e^{iS(q_c)/\hbar} \qquad (2.14)\\ &= \lim_{N\to\infty}\sqrt{\frac{1}{2\pi i\hbar}}\left(\frac{m}{\delta t}\right)^{\frac{N}{2}}\frac{1}{\sqrt{\det(\mathcal{A})}}e^{iS(q_c)/\hbar}.\end{aligned}$$

The only remaining step is to calculate that value of $\det(\mathcal{A})$ if desired. One might be concerned about the behavior of (2.14) as $\delta t \to 0$, but it turns out that the path integral is well behaved for particular choices of the Lagrangian.[3] In the case of a quadratic potential, $\mathcal{A}(q_c)_{ij} = \partial^2 S/\partial q_i \partial q_j|_{q=q_c}$ is independent of the particular choice of classical path $q_c(t)$ and, therefore, $\det(\mathcal{A})$ is just a normalization constant [35]. As a caveat, the normalization "constant" does depend on the time $(t_F - t_I)$ a trajectory takes [36], but as long as two paths are compared at the same time, this normalization cancels.

2.1.1 Interference of Paths

Consider an interferometer in which a particle initially in the state $|x_I, p_1\rangle$ is coherently split into two different states $|x_I, p_1\rangle$ and $|x_I, p_2\rangle$ with momentums p_i. If these states follow the two classical trajectories $[q_{c_1}, q_{c_2}]$ such that they both end up at x_F after a time T, then a final beam splitter can recombine the states to give the probability amplitude of finding the particle in $|x_F, p_1'\rangle$ as

$$\begin{aligned}|\Psi_F\rangle &\equiv \frac{1}{2}\,|x_F, p_1'\rangle\left(\langle x_F, p_1'|\, e^{iHT/\hbar}\,|x_I, p_1\rangle\,\big|_{q_{c_1}} + \langle x_F, p_2'|\, e^{iHT/\hbar}\,|x_I, p_2\rangle\,\big|_{q_{c_2}}\right)\\ &= \frac{1}{2}\,|x_F, p_1'\rangle\left(e^{iS(q_{c_1})/\hbar} + e^{iS(q_{c_2})/\hbar}\right)\end{aligned}$$

and, therefore,

$$\begin{aligned}|\langle\Psi_F|\,\Psi_F\rangle|^2 &\propto \frac{1}{2} + \frac{1}{4}\left(e^{i[S(q_{c_1})-S(q_{c_2})]/\hbar} + e^{-i[S(q_{c_1})-S(q_{c_2})]/\hbar}\right)\\ &= \cos^2\left(\frac{S(q_{c_1}) - S(q_{c_2})}{2\hbar}\right)\\ &= \cos^2\left(\frac{\phi_1 - \phi_2}{2}\right).\end{aligned}$$

[3] In the special case that the Lagrangian $L = m\dot{q}^2/2 - mgq + m\gamma q^2/2$, the normalization factor turns out to be $\det(\mathcal{A}) = (m/\delta t)^N \cdot (t_F - t_I)/m \cdot \sinh(\sqrt{\gamma}(t_F - t_I))/\sqrt{\gamma}$. In the limit of $\gamma \to 0$ the normalization becomes that of a free particle and $\sqrt{\gamma} \to i\omega$ for a harmonic oscillator.

Thus, the resulting interference is equivalent to the particle acquiring a free evolution phase

$$\phi_j = \frac{1}{\hbar} S(q_{c_j}) \tag{2.15}$$

along the trajectory q_{c_j}. Corrections to this phase are potentially required if the Lagrangian is not quadratic, but we will not concern ourselves with those as quadratic potentials are enough to approximately describe gravity and gravity-gradients near Earth's surface. Therefore the phase of the evolution operator in (2.1) is simply

$$\hat{U} \left|\psi\right\rangle\Big|_{q_c} \propto e^{iS(q_c)/\hbar} \left|\psi\right\rangle .$$

2.1.2 Separation Phase

While the derivation in the previous section assumes that the two wave-packets end up with the same position and momentum when they interfere, this may not always be the case due to perturbations in the potential and atom-light interactions. If the two wave-packets are separated by an amount δx at the moment of the last beam splitter, then there will be an addition phase shift

$$\left|\Psi_F\right\rangle = \frac{1}{2} \left|x_F, p_1'\right\rangle \left(e^{iS(q_{c_1})/\hbar} + e^{i\bar{p}\,\delta x/\hbar} e^{iS(q_{c_2})/\hbar}\right)$$

due to the displaced overlap of the two wave packets, where $\bar{p}$ is the average momentum of the two interfering states at the moment of the last beam splitter [37, 38]. This extra phase shift $\delta\phi = \bar{p}\,\delta x/\hbar$ will end up contributing to the gravity gradient phase in Section 5.3 and the wave-vector systematic in Section 6.7.

2.2 Atom-Laser Interaction Phase

The beam splitters in an atom interferometer typically rely of the absorption and emission of photons of well defined momentum to coherently separate the atomic wave-packets. This atom-photon interaction will apply a phase shift to the atoms and therefore must be understood. Although the laser fields in the experiment are macroscopic in nature, the derivation presented here uses electromagnetic field operators to more closely follow the photon interaction picture.

The Hamiltonian that describes the interactions of a system with electromagnetic fields is given by

$$\begin{aligned}\hat{H} &= \frac{1}{2m}\left(\hat{p} - q_e \hat{A}(\vec{r}, t)\right)^2 + q_e V(\vec{r}) \\ &= \frac{\hat{p}^2}{2m} - \frac{q_e}{2m}\left(\hat{p}\cdot\hat{A}(\vec{r}, t) + \hat{A}(\vec{r}, t)\cdot\hat{p}\right) + \frac{q_e^2}{2m}\left|\hat{A}(\vec{r}, t)\right|^2 + q_e V(\vec{r}),\end{aligned}$$

where $V(\vec{r})$ is the electric potential and $\hat{A}(\vec{r},t)$ is the magnetic vector potential. If we choose to work in the Coulomb gauge where $\nabla \cdot \hat{A}(\vec{r},t) = 0$, then the commutation relation

$$\begin{aligned}[\hat{p},\hat{A}]\psi &= -i\hbar\nabla\cdot(\hat{A}\psi) + i\hbar\hat{A}\cdot(\nabla\psi) \\ &= -i\hbar\psi\cancelto{0}{(\nabla\cdot\hat{A})} - i\hbar\hat{A}\cdot(\nabla\psi) + i\hbar\hat{A}\cdot(\nabla\psi) = 0\end{aligned}$$

and therefore $\hat{p}\cdot\hat{A} = \hat{A}\cdot\hat{p}$. In the case of an atom where the free electrons are bound to a heavy nucleus, the electron wave-function is bound to a length scale of the Bohr radius a_0, with a momentum of order $\hbar/a_0$. The relative size of the $q_e^2|\hat{A}|^2$ and $q_e\hat{A}\cdot\hat{p}$ terms are then $\sim q_e E_0 a_0/\hbar\omega$, where E_0 is the electric field strength of the laser. For typical conditions, the $\hat{A}^2$ term is negligible and can be dropped[4] resulting in the simplified Hamiltonian

$$\hat{H} \simeq \frac{\hat{p}^2}{2m} - \frac{q_e}{m}\hat{A}(\vec{r},t)\cdot\hat{p} + q_e V(\vec{r}). \tag{2.16}$$

Without loss of generality, consider a monochromatic transverse electromagnetic wave with linear polarization along the x-axis. The quantized field operator in the Coulomb gauge can be expressed as

$$\hat{A}(z,t) = \frac{\mathcal{E}_0}{\omega}\left(\hat{a}e^{ik(z'-z)-i\omega t} + \hat{a}^\dagger e^{-ik(z'-z)+i\omega t}\right)\hat{x},$$

where $\hat{a}^\dagger$ and $\hat{a}$ are creation and annihilation operators for a photon with wave-vector k and $\mathcal{E}_0 \equiv \sqrt{\hbar\omega/2\epsilon_0 V}$ is a normalization factor. Additionally, since the relative phase of $\hat{A}$ will turn out to be important, the system's center of mass coordinate z is chosen relative to a reference coordinate z'. By applying the gauge transformation

$$\begin{aligned}\hat{A}'(z,t) &= \hat{A}(z,t) - \nabla\left(\vec{r}\cdot\hat{A}(0,t)\right) \\ &= \hat{A}(z,t) - \hat{A}(0,t)\end{aligned}$$

and power series expanding the field operator $\hat{A}(z,t)$ about $z = z'$, the field becomes

$$\begin{aligned}\hat{A}'(z,t) &= \frac{\mathcal{E}_0}{\omega}\left[\hat{a}e^{ikz'-i\omega t}\left(1 - ikz + \ldots\right) + h.c.\right]\hat{x} - \frac{\mathcal{E}_0}{\omega}\left[\hat{a}e^{ikz'-i\omega t} + h.c.\right]\hat{x} \\ &\approx -ikz\frac{\mathcal{E}_0}{\omega}\left[\hat{a}e^{ikz'-i\omega t} - \hat{a}^\dagger e^{-ikz'+i\omega t}\right]\hat{x}.\end{aligned}$$

The new $\hat{A}\cdot\hat{p} \to \hat{A}'\cdot\hat{p}$ term in (2.16) is of order $kz \sim a_0/\lambda$ and can be ignored for visible/UV wavelengths (i.e. the so-called electric-dipole approximation). Since we applied a gauge transformation on the vector potential, we must also transform the scalar potential

[4]For laser frequencies in the visible, the $\hat{A}^2$ term is no longer negligible at laser intensities $I = c\epsilon_0|E_0|^2/2$ of order 1 GW/cm^2.

$$\begin{aligned} V'(\vec{r}) &= V(\vec{r}) + \vec{r}\cdot\frac{\partial \hat{A}(0,t)}{\partial t} \\ &= V(\vec{r}) - ix\mathcal{E}_0\left[\hat{a}e^{ikz'-i\omega t} - \hat{a}^\dagger e^{-ikz'+i\omega t}\right], \end{aligned}$$

where $V(\vec{r})$ is the usual Coulomb potential of the nucleus and the second term is the dipole-electric field interaction term. It should be noted that performing the gauge transformation $\hat{A}' = \hat{A} + \nabla\Lambda$ is equivalent to applying the unitary transformation $\psi'(\vec{r},t) = e^{iq_e\Lambda/\hbar}\psi(\vec{r},t)$, which for $\Lambda = -\vec{r}\cdot\hat{A}(0,t)$ is just a translation in momentum space [39]. The transformed Hamiltonian (2.16) is then

$$\begin{aligned} \hat{H} &\approx \frac{\hat{p}^2}{2m} + q_e V(\vec{r}) \; -iq_e x\mathcal{E}_0\left[ae^{ikz'-i\omega t} - a^\dagger e^{-ikz'+i\omega t}\right] \\ &= \qquad \hat{H}_0 \qquad -iq_e x\mathcal{E}_0\left[\hat{a}e^{ikz'-i\omega t} - \hat{a}^\dagger e^{-ikz'+i\omega t}\right], \end{aligned} \tag{2.17}$$

where $\hat{H}_0$ is the usual Hamiltonian for an atom in the absence of external electromagnetic fields. The relative strength of the dipole interaction term to the atomic Hamiltonian H_0 is approximately $q_e E_0 a_0/\hbar\omega_0$, where $\hbar\omega_0$ is the characteristic binding energy of an atom, allowing the interaction term to be treated as a perturbation $\hat{H}_1$.

One term that has been neglected in (2.17) is the energy of the bare electromagnetic field, which can be written as

$$\begin{aligned} \hat{H}_{\mathrm{EM}} &= \frac{\epsilon_0}{2}\int\left(|E|^2 + c^2|B|^2\right)dV \\ &= \frac{\epsilon_0}{2}\int\left(\left|\frac{\partial\hat{A}}{\partial t}\right|^2 + c^2\left|\nabla\times\hat{A}\right|^2\right)dV = \hbar\omega\left(\hat{a}^\dagger\hat{a} + \frac{1}{2}\right). \end{aligned}$$

This Hamiltonian has the same form as a simple harmonic oscillator, with number eigenstates $|n\rangle$ such that $\hat{a}\,|n\rangle = \sqrt{n}\,|n-1\rangle$ and $\hat{a}^\dagger\,|n\rangle = \sqrt{n+1}\,|n+1\rangle$. Therefore, the expectation value for the energy of the electromagnetic field is $\langle n|\,\hat{H}_{\mathrm{EM}}\,|n\rangle = \hbar\omega(n+1/2)$, approximately the energy of n photons. The relative energy scale of $\hat{H}_{\mathrm{EM}}$ and the atom-field interaction Hamiltonian $\hat{H}_1$ is $q_e E_0 a_0/\hbar\omega \ll 1$, which means that $\hat{H}_1$ can also be treated as a perturbation to $\hat{H}_{\mathrm{EM}}$. This allows the use of number eigenstates $|n\rangle$ as the basis for the electromagnetic field when calculating the interaction term.

For a standard laser that follows Poisson statistics (shot-noise limited), the laser wavefunction can be described by a coherent state $|\alpha\rangle$,

$$|\alpha\rangle = e^{\frac{1}{2}\alpha^2}\sum_{n=0}^{\infty}\frac{\alpha^n}{\sqrt{n!}}\,|n\rangle\,,$$

where $\alpha^2 = \bar{n}$ is the mean number of photons in the field. A coherent state has properties such that $\hat{a}\,|\alpha\rangle = \alpha\,|\alpha\rangle$ and $\langle\alpha|\,\hat{a}^\dagger = (\hat{a}\,|\alpha\rangle)^\dagger = \langle\alpha|\,\alpha^*$, with an energy expectation value $\langle\alpha|\,\hat{H}_{\mathrm{EM}}\,|\alpha\rangle = \hbar\omega(\alpha^2 + 1/2)$.

Consider an atom in the ground state ψ_g, interacting with a laser field with $\bar{n}$ photons. The combined wave-function of the atom-laser system is

$$\Psi_g(\vec{r}, t) = |\alpha\rangle\,\psi_g(\vec{r}, t).$$

The coupling of the ground state Ψ_g to the excited atomic state, $\Psi_e = |\alpha\rangle\,\psi_e(\vec{r}, t)$, is equal to

$$\langle\Psi_e|\,\hat{H}_1\,|\Psi_g\rangle = -iq_e\mathcal{E}_0 \int dV\ \psi_e^*(\vec{r}, t)\,\langle\alpha|\,x\left[\hat{a}e^{ikz'-i\omega t} - \hat{a}^\dagger e^{-ikz'+i\omega t}\right]|\alpha\rangle\,\psi_g(\vec{r}, t). \tag{2.18}$$

Since z' is a constant referencing the atom's center of mass to some external coordinate system, we can move the photon interaction term outside of the integral and evaluate it separately as

$$\begin{aligned}\langle\alpha|\,\hat{a}e^{ikz'-i\omega t} - \hat{a}^\dagger e^{-ikz'+i\omega t}\,|\alpha\rangle &= \alpha e^{ikz'-i\omega t}\,\langle\alpha|\alpha\rangle - \alpha^* e^{-ikz'+i\omega t}\,\langle\alpha|\alpha\rangle \\ &= \alpha\left(e^{ikz'-i\omega t} - e^{-ikz'+i\omega t}\right).\end{aligned} \tag{2.19}$$

For the integral in (2.18), the atomic wave-functions consist of two parts: the spatial part $\psi(\vec{r})$, which comes from solving the time-independent Schrödinger equation $\hat{H}_0\psi = E\psi$ and an energy phase term $e^{iEt/\hbar}$, which is a result of time-dependent part of the Schrödinger equation $i\hbar\partial_t\psi = E\psi$. Therefore the total atom wave-function is

$$\psi_j(\vec{r}, t) = e^{-iE_j t/\hbar}\psi_j(\vec{r})$$

and the integral

$$\begin{aligned}q_e\int \psi_e^*(\vec{r}, t)x\psi_g(\vec{r}, t) &= e^{i(E_e-E_g)t/\hbar}q_e\int \psi_e^*(\vec{r})x\psi_g(\vec{r})dV \\ &= e^{i(E_e-E_g)t/\hbar}\cdot d_{ge},\end{aligned}$$

where d_{ge} is the dipole transition matrix element to go from ψ_g to ψ_e (which depends on the specifics of the two atomic states and the polarization of the electro-magnetic field). All together (2.18) simplifies to

$$\langle\Psi_e|\,\hat{H}_1\,|\Psi_g\rangle = -id_{ge}\mathcal{E}_0\alpha\Big(e^{ikz'}e^{-i[\omega-(E_e-Eg)/\hbar]t} - e^{-ikz'}e^{i[\omega+(E_e-Eg)/\hbar]t}\Big).$$

For laser frequencies ω close to the transition energy $(E_e - E_g)/\hbar$, the second term will oscillate very fast compared to the first term and therefore average out to zero. This is the

rotating wave approximation and makes physical sense as a photon should not be emitted when an atom is excited due to conservation of energy. A similar calculation can be done for transitioning from the excited state to the ground state where a photon is emitted instead. All together, the two expectation values are:

$$\begin{aligned}\langle\Psi_e|\,\hat{H}_1\,|\Psi_g\rangle &= -id_{ge}\alpha\mathcal{E}_0\cdot e^{ikz'-i\omega t}e^{i(E_e-E_g)t/\hbar}\\ \langle\Psi_g|\,\hat{H}_1\,|\Psi_e\rangle &= id^*_{ge}\alpha\mathcal{E}_0\cdot e^{-ikz'+i\omega t}e^{-i(E_e-E_g)t/\hbar},\end{aligned} \tag{2.20}$$

where $|E_0| = 2\alpha\mathcal{E}_0$ is the effective electric field. These expectation values imply that whenever a photon is absorbed, a phase $e^{ikz'-i\omega t}$ is imparted on the atom wave-function, and when emitted, the opposite sign phase is transferred. If we drive the system with two laser fields k_1 and k_2 such that nk_1 photons are absorbed and nk_2 photons are emitted, then it follows that the phase transferred to the atoms due to the laser phase is

$$\begin{aligned}\varphi_{\text{laser}} &= \arg\left[\langle\Psi_e|\,\hat{H}_1(k_1)\,|\Psi_g\rangle^n\,\langle\Psi_g|\,\hat{H}_1(k_2,\phi_0)\,|\Psi_e\rangle^n\right]\\ &= \arg\left[e^{in(k_1z'-\omega_1t)}e^{in(E_e-E_g)t/\hbar}e^{-in(k_2z'-\omega_2t+\phi_0)}e^{-in(E_e-E_g)t/\hbar}\right]\\ &= n(k_1z'-\omega_1t)-n(k_2z'-\omega_2t+\phi_0),\end{aligned} \tag{2.21}$$

where ϕ_0 is a phase offset.[5]

2.2.1 Classical Approximation

As a side note, the photon field interaction (2.19) can be re-written as

$$\begin{aligned}i\mathcal{E}_0\,\langle\alpha|\,\hat{a}e^{ikz'-i\omega t}-\hat{a}^\dagger e^{-ikz'+i\omega t}\,|\alpha\rangle &= i\alpha\mathcal{E}_0\left(e^{ikz'-i\omega t}-e^{-ikz'+i\omega t}\right)\\ &= 2\alpha\mathcal{E}_0\sin(kz'-\omega t)\\ &= |E_0|\sin(kz'-\omega t),\end{aligned}$$

which is just a classical electromagnetic wave. In general, the dipole interaction part of (2.17) for a classical electromagnetic field is simply

$$\hat{H}_1 = -\vec{d}_{ge}\cdot\vec{E}(\vec{r}',t)(|\Psi_e\rangle\,\langle\Psi_g|+h.c.).$$

2.3 Atom Interferometer Phase

With the tools to calculate the free evolution phase of the atom's trajectory and the atom-laser phase for the beam splitters, it is then straightforward to calculate the total phase for

[5] A real multi-photon process is more complicated since the excited state is only virtually populated, but the phase shift is the same.

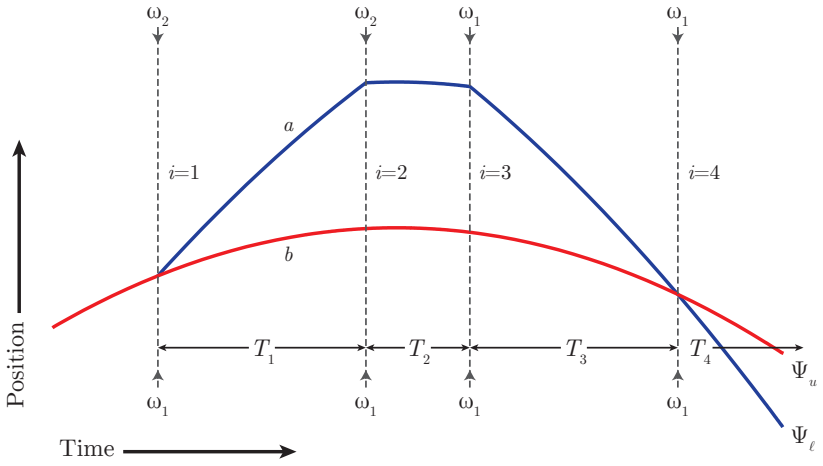

Figure 2.1: A sample space-time diagram for an interferometer (in this case a Ramsey-Bordé interferometer). The two paths a (blue) and b (red) are recombined into one of two outputs Ψ_u and Ψ_ℓ. Vertical dashed lines indicate the ith beam splitter.

a complete interferometer. Consider an interferometer in a single spatial dimension such as the one in Fig. 2.1 consisting of N beam splitters (which impart a momentum $2n\hbar k$ onto the atom), followed by periods of free evolution. The total phase of an atom following either of the four interferometer paths (traveling along trajectory a or b and leaving along the upper or lower beam splitter port) is

$$\Phi_{a/b,u/\ell} = \sum_i^N \left(\frac{1}{\hbar} S[z_i, p_i, T_i] + \phi_\gamma[z_i] \right) \Big|_{a/b,u/\ell}, \tag{2.22}$$

where $\phi_\gamma[z_i]$ is the laser phase acquired during the ith beam splitter for an atom located at position z_i and $S[z_i, p_i, T_i]$ is the action of a particle starting at z_i with momentum p_i, which travels along the classical trajectory for a time T_i. Recall that the action is calculated as the integral of the Lagrangian

$$S[z_0, p_0, T] = \int_0^T L[z(t), p(t)]dt \tag{2.23}$$

such that $z(t)$ and $p(t)$ follow the classical trajectories obtained by solving the Euler-Lagrange equation

$$m\frac{d}{dt}\left(\frac{\partial L}{\partial p}\right) = \frac{\partial L}{\partial z}$$

with initial conditions $z(0) = z_0$ and $p(0) = p_0$ and a Lagrangian given by $L = p^2/2m + V(z)$.

Consider the potential created by the gravitational field of Earth, $V(r) = -GMm/r$ and restrict the motion of atoms to the $z-$axis along the direction of gravity (other potentials

such as those from electromagnetic fields are negligible in this experiment and can be treated as perturbations). Near the Earth's surface, the gravitational potential can be power series expanded about the Earth's radius R_e such that

$$V(R_e + z) \approx mgz - \frac{1}{2}m\gamma z^2 + \mathcal{O}\left(\frac{z^3}{R_e^3}\right),$$

where $g = GM_e/R_e^2$ is the usual gravitational acceleration and $\gamma = 2GM_e/R_e^3$ is the gravity gradient. For simplicity, terms higher order than $(z/R_e)^2$ are dropped as they are too small to have any impact on laboratory distance scales. The simplified Lagrangian

$$L = \frac{1}{2m}p^2 - mgz + \frac{1}{2}m\gamma z^2 \tag{2.24}$$

can then be used to exactly solve the Euler-Lagrangian equations for the position $z(t)$. For a particle starting at z_0 and $p_0 = mv_0$ at $t = 0$, the particle moves along the trajectory

$$\begin{aligned} z(t, x_0, v_0) &= \frac{g}{\gamma} + \left(x_0 - \frac{g}{\gamma}\right)\cosh(t\sqrt{\gamma}) + \frac{v_0}{\sqrt{\gamma}}\sinh(t\sqrt{\gamma}) \\ &\approx \left(x_0 + v_0 t - \frac{gt^2}{2}\right) + \gamma t^2\left(\frac{x_0}{2} + \frac{v_0 t}{6} - \frac{g}{24}\right), \end{aligned}$$

where the approximation assumes that the interferometer timescale T is much smaller than $1/\sqrt{\gamma}$.[6] With the solutions for $z(t)$, the free evolution phase (2.15) for each segment can then be explicitly integrated

$$\begin{aligned} \phi_{\text{free}} &= \frac{1}{\hbar}\int_0^T L[x(t), v(t)]\, dt \\ &= \frac{1}{\hbar}\int_0^T \left[\frac{m}{2}\left(\frac{\partial z(t)}{\partial t}\right)^2 - mgz(t) + \frac{m}{2}\gamma z(t)^2\right] dt \\ &= \frac{m}{\hbar}\Bigg(\frac{1}{3}g^2T^3 - gv_0T^2 + \frac{1}{2}v_0^2T - gx_0T \\ &\qquad + \frac{\gamma}{30}\left[2g^2T^5 - 10gv_0T^4 + 10v_0^2T^3 - 20gx_0T^3 + 15x_0T\right]\Bigg) + \mathcal{O}(\gamma^2). \end{aligned}$$

To compute the total free evolution phase of the entire path, the final position $z_i(T_i)$ is used as the initial position of the next segment $z_{i+1}(0)$ and the final velocity $v_i(T_i)$ is modified to take into account the momentum transfer of the beam splitter.

Similarly, for lasers with frequencies $\{\omega_1, \omega_2\}$, the laser phase for each beam splitter (2.21) can be evaluated at the atom's position $z_i(0) = z_i$ as

[6] The gravity gradient on Earth's surface is approximately 3×10^{-6} s^{-2}.

$$\phi_\gamma[z_i] = \pm\Big[n\left(k_1 z_i - \omega_1 t_i\right) - n\left(-k_2 z_i - \omega_2 t_i + \phi_0\right)\Big],$$

where t_i is the absolute time of the beam splitter

$$t_i = t_0 + \sum_{j=1}^{i-1} T_j$$

and the sign difference between k_1 and k_2 comes from the fact that the lasers are counter-propagating. The overall sign of the laser phase is positive when absorbing photons from the laser field ω_1 and is negative when emitting into the field.

After computing the total phase (2.22) for each of the two trajectories for a given output port, then the amplitude of the interference is given by the phase difference

$$\left|\langle\Psi_u|\Psi_u\rangle\right|^2 = \cos^2\left(\frac{\Phi_{a,u} - \Phi_{b,u}}{2}\right)$$
$$\left|\langle\Psi_\ell|\Psi_\ell\rangle\right|^2 = \sin^2\left(\frac{\Phi_{a,\ell} - \Phi_{b,\ell}}{2}\right).$$

2.3.1 Symbolic Computation of Phase

The actual process of turning the crank and calculating these phases for different types of interferometers is tedious. Additionally, if any perturbations are needed then the computation can get very messy without intuition as to which assumptions can be made. Instead, this section will briefly discuss how these calculations can be done using symbolic computation software such as Mathematica, with a complete code listing in Appendix A. While symbolic computation of the interferometer phase is far from a new idea, the advantage of this code is that it provides a very robust framework to handle arbitrary interferometer geometries and perturbations without significant user involvement. The code is used to generate phase corrections for gravity gradients (Section 5.3) and wave-vector perturbations (Sections 6.1.4 and 6.7), along with the main interferometer phases.

First, start with an initial state vector $[z_0, v_0, A, n_0]$ that has an initial position z_0, velocity v_0, and probability amplitude $A = 1$. The variable n_0 is used to keep track of the diffraction momentum state of the atom. For each beam splitter that transfers atoms from $n_1 \to n_2$, the state vector is checked to see if any state is resonant with the pulse ($n_0 = n_1$ or $n_0 = n_2$). If a state is resonant, its amplitude is changed from $A \to A\cos(\theta/2)$ and another state is added to the vector with amplitude $i\sin(\theta/2)Ae^{i\phi_\gamma[z]}$ to represent the diffracted atom state. The new vector has the same position z_0, a velocity modified by the transferred photon momenta $v_0 \pm 2(n_2 - n_1)\hbar k$, and an updated momentum index (n_1 or n_2).

For the free evolution steps, simply go through each state and calculate the free evolution phase ϕ_{free} along the path (given the state's position and velocity) and change the state's

amplitude from $A \rightarrow Ae^{i\phi_{\text{free}}}$. The state's position and velocity are then updated to reflect the final state of the atom after a free-fall time T.

The somewhat subtle step occurs when checking to see whether the states interfere with each other, as perturbations can cause the interferometer to not completely close. The easiest method is to check if two states have the same position and momentum with the perturbation set to zero. If the two are overlapped, then combine the states together and add their probability amplitudes as $A_1 + A_2 e^{im\bar{v}\,\delta z/\hbar}$, where the extra phase term is the separation phase, the quantity δz is the position difference of the two states with perturbations, and $\bar{v}$ is the average velocity of the states before the beam splitter. All that is left to do is calculate the absolute square of the probability amplitude to get the interference (and therefore the phase difference).

Once the correct signs and factors are figured out, calculations for new interferometer configurations can be done with speed and reliability. In addition, perturbations are easy to incorporate by modifying the potentials, wave-vectors, etc. The only component of the calculation that is not explicitly done in the code in Appendix A is the time-dependent laser phase due to the laser frequency ω. While this could be included, it is easy enough to calculate it by hand (and is done in Section 2.3.3 for a Ramsey-Bordé interferometer).

2.3.2 Ramsey-Bordé

The primary interferometer configuration used in the experiment is the Ramsey-Bordé interferometer [40] shown in Fig. 2.2. An atom initially in momentum state $|0\rangle$ is split with a Bragg beam splitter transferring $2n\hbar k$ momentum with 50% probability to the atom wavefunction (discussed in more detail in Section 2.5). After free-falling for a time T, the states are split with another $\pi/2$-pulse to produce four total trajectories. The resulting $|0\rangle$ states (which will be referred to as the lower interferometer) evolve for a time T' and are followed by a beam splitter in the other direction, kicking the atoms down by $-2n\hbar k$. The $|0\rangle$ and $|-n\rangle$ states then evolve for another period T before being recombined with a fourth and final beam splitter to interfere the states.

Intuitively, one would expect the phase of interferometer to depend on gravity since the two trajectories spend time at different gravitational potentials. Similarly, the upper trajectory has a non-zero relative velocity compared to the lower initial trajectory and will therefore contribute a kinetic energy phase. Since we are only interested in the recoil frequency (and therefore the kinetic energy), a separate conjugate interferometer is used to cancel gravity using the $|n\rangle$ atoms produced by the second beam splitter. The $|n\rangle$ state atoms are deflected up with the last two pulses instead of down to produce an upside-down version of the lower interferometer. Since the gravitation potential mgz is odd in the z coordinate and the kinetic energy $m\dot{z}^2/2$ is even, the relative sign of the two phases reverses. By subtracting the upper interferometer phase from the lower interferometer phase, the acceleration contribution is canceled.

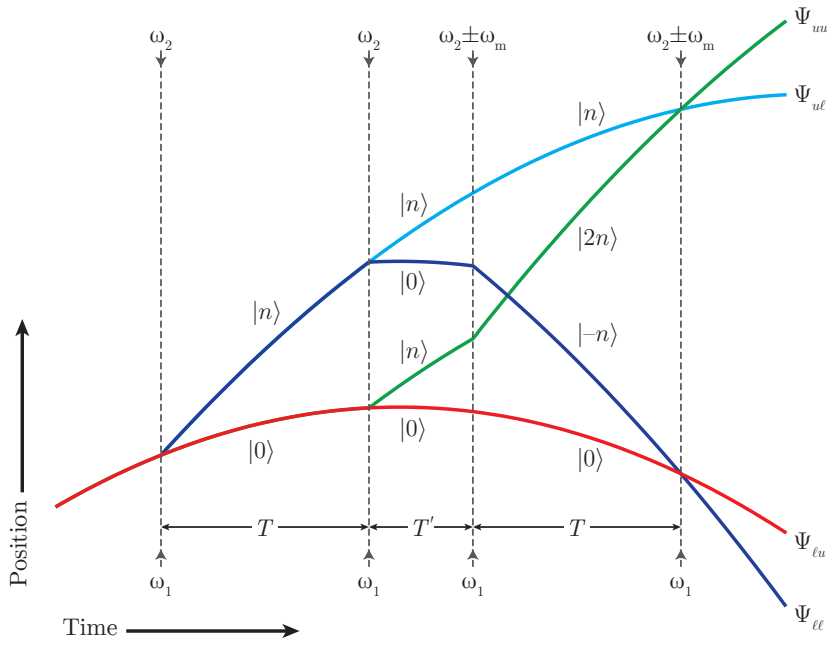

Figure 2.2: Space-time diagram for a conjugate Ramsey-Bordé interferometer when gravity is along the atom trajectory. The relative inertial frame momentum $2n\hbar k$ of each state is labeled as $|n\rangle$ and the four $\pi/2$ Bragg beam splitters are show as vertical dashed lines (the extra atom trajectories from the third and fourth beam splitters are not shown). The subscripts the final states correspond to the upper (u) or lower (ℓ) path followed by the upper or lower output port.

2.3.3 Simultaneous Conjugate Ramsey-Bordé

In theory, the gravitational potential could instead be measured using a Mach-Zehnder interferometer and then subtracted from the Ramsey-Bordé phase. However, since the atoms are in free-fall and are measured with respect to the lab frame, any relative phase fluctuations between the two lasers due to technical noise or vibrations will cause phase shifts that look like a fluctuating gravitational acceleration (due to the equivalence principle). Since these vibrations can cause phase shifts of many radians, extremely well-engineered vibration isolation would be required to have a stable measurement of gravity [41] for both the Mach-Zehnder and Ramsey-Bordé interferometers. For this reason it is also difficult to perform both upper and lower variations of the conjugate Ramsey-Bordé interferometers as separate sequences [42] as the requirements on vibrations are similar.

Instead, both conjugate interferometers are done simultaneously so that phase shifts due to vibrations and gravity are exactly the same. This requires that the last two beam splitters drive both Bragg diffraction orders simultaneously, which can be accomplished by driving the atoms with three laser frequencies (ω_1 and $\omega_2 \pm \omega_m$) instead of two. The vibration phases are then correlated, which allows for extraction of the recoil phase without ever measuring

the gravitational phase.

Since all output trajectories of the interferometer have the same internal state, the states must be sufficiently spatially separated so that the amplitudes can be measured independently of each other. For Ramsey-Bordé interferometers that use Raman transitions to apply $2\hbar k$ momentum splittings, resolving the individual clouds becomes challenging as the separation velocity is usually comparable to the cloud expansion rate. Since Raman transitions transfer the atom between one of two available ground states (for alkali atoms), the two conjugate interferometers are almost required to be done as separate measurements so that state selective detection can be used. For interferometers using Bragg diffraction, the momentum transfer can be much higher so that the atom states separate completely, allowing them to be measured without any state labeling.

Phase

Inputting the conjugate Ramsey Bordé pulse and evolution sequence into the symbolic phase computation results in a net phase of

$$\Delta\Phi_{\ell/u} = \pm 8n^2\omega_r T + nk_{\text{eff}}gT(T+T') + \mathcal{O}\left(\gamma, \delta k\right), \tag{2.25}$$

where the effective wave-vector $k_{\text{eff}} = (\omega_1 + \omega_2)/c$, the recoil frequency $\omega_r = \hbar k_{\text{eff}}^2/8m$, and the plus/minus corresponds to the lower and upper interferometers respectively (the same result is obtained by hand in [43]). The additional terms due to gravity gradients and the difference in wave-vectors δk due to ω_m are described in greater detail in Sections 5.3 and 6.7. Also not included are the time-dependent frequency phases which can easily be calculated by considering the phase accumulation of the laser fields $\{\omega_1, \omega_2\}$ and the difference frequency $2\omega_m$. For the lower interferometer: atoms that follow the upper trajectory and exit the upper output port acquire a time-dependent laser phase of

$$\phi^{\omega}_{\ell uu} = \phi_1(t_0) - \phi_1(t_0+T) - \phi_2(t_0+T+T') + \phi_2(t_0+2T+T'),$$

where the phases $\phi_1(t) = n(\omega_1 - \omega_2)t$ and $\phi_2(t) = n(\omega_1 - (\omega_2 + \omega_m))t$. Atoms that follow the lower trajectory and exit the upper output port receive zero momentum kicks and therefore acquire zero laser phase ($\phi^{\omega}_{\ell\ell u} = 0$). The difference in the time-dependent laser phase is therefore

$$\phi_{\ell uu} - \phi_{\ell\ell u} = -n\omega_m T,$$

which only depends on the frequency ω_m. Doing the same steps for the upper interferometer yields a phase difference $\phi_{uuu} - \phi_{u\ell u} = n\omega_m T$ and, therefore, the total phase for both interferometers is

$$\Delta\Phi_{\ell/u} = \pm 8n^2\omega_r T + nk_{\text{eff}}gT(T + T_1' + T_2') \mp n\omega_m T.$$

The differential phase is then

$$\Delta\Phi_\ell - \Delta\Phi_u = 16n^2\omega_r T - 2n\omega_m T,$$

which is independent of both gravity/accelerations and the pulse separation time T'. Additionally, since the frequency shift required to change the Bragg diffraction order from $+n$ to $-n$ is equal to $8n\omega_r$, setting the frequency modulation frequency $\omega_m = 8n\omega_r$ results in a null differential phase measurement $\Delta\Phi_\ell - \Delta\Phi_u = 0$. This is important because it enables a direct measurement of ω_r by adjusting a frequency synthesizer (ω_m) until the phase is zero.

Ramping Laser Phase: If the laser frequency is ramped common mode to both interferometers (for example to compensate for gravity), then there will be an additional phase shift proportional to $\Lambda_{\text{ramp}}T(T+T')$, where Λ_{ramp} is the frequency ramp rate. This term will have the same sign as gravity and will therefore cancel when measuring the differential phase.

2.3.4 With Bloch Oscillations

For a fixed phase uncertainty $\delta\phi$ (limited ideally by measurement shot-noise), the uncertainty $\delta\omega_m$ in the modulation frequency $\omega_m = 8n\omega_r$ can be improved by increasing the momentum transfer n or the evolution time T since the uncertainty scales as

$$\begin{aligned}\delta\phi &= 16n^2\omega_r T - 2n(\omega_m + \delta\omega_m)T \\ &= -2n\delta\omega_m T.\end{aligned}$$

Additionally, the recoil frequency uncertainty scales as $\delta\omega_r = \omega_m/8n$ and therefore the overall sensitivity to the recoil frequency is

$$\delta\omega_r = \frac{\delta\phi}{16n^2T}.$$

It is therefore very desirable to increase the momentum splitting n due to the quadratic scaling, as long as the phase sensitivity is not degraded by a comparable amount (which can be the case for large n due to decoherence).

Alternatively, if both paths (for a given interferometer) are accelerated by an additional $\pm 2N\hbar k$ during the middle T' pulse separation, as shown in Fig. 2.3, then the modulation frequency required to address the atoms for the third and fourth beam splitters will need to be increased to $8(n+N)\omega_r$. Even though the differential momentum between the two paths of a given interferometer has not changed, the frequency uncertainty $\delta\omega_m$ is the same despite the increase of the absolute value of ω_m. Therefore by changing the common mode velocity of the two paths by $2N\hbar k$, one can increase the measurement sensitivity to ω_r by $(n+N)/n$.

One way to accomplish this additional momentum transfer is to load both arms of the interferometer into the same optical lattice (which is possible since both paths have the same velocity during T') and accelerate the atoms using Bloch oscillations. The atoms bound in

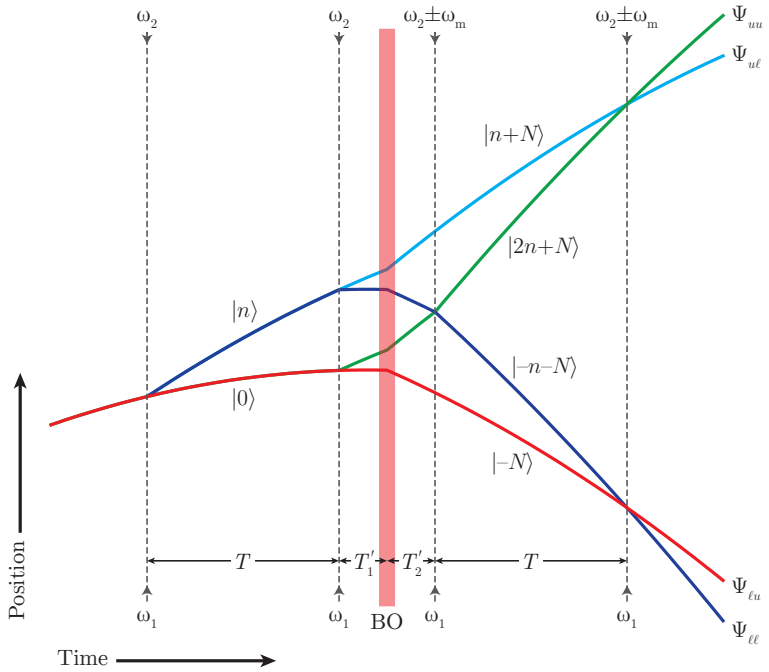

Figure 2.3: Space-time diagram for a conjugate Ramsey-Bordé interferometer with Bloch oscillations (region shaded in red). The relative momentum states reflect the addition momenta transferred by the Bloch oscillations, which accelerates the lower interferometer down to $-2N\hbar k$ and the upper interferometer up to $+2N\hbar k$.

the lattice will undergo oscillations of their momentum as the lattice potential is accelerated, adiabatically changing the atom's momentum in quantized steps of $2\hbar k$. This method has been used in a Raman-based Ramsey-Bordé interferometer to transfer an additional $1600\hbar k$ photon momenta to the common mode velocity as was done in [42]. For a simultaneous Ramsey-Bordé interferometer configuration, the Bloch oscillations must accelerate the upper and lower interferometers at the same time and is described Section 4.5. Since the dynamics of the Bloch oscillations are common mode to both arms of the interferometer, the details are ignored and the process is treated as a single beam splitter which takes the states from $|n\rangle \rightarrow |n+N\rangle$ and $|0\rangle \rightarrow |-N\rangle$. For the sake of computation, the oscillations are treated as starting at a time T_1' after the second beam splitter with a neglectable duration ($t_{\text{bloch}} \ll T_1' + T_2'$).

In total, combining Bloch oscillations with the simultaneous conjugate Ramsey-Bordé interferometer [44] results in a differential phase of

$$\Delta\Phi_\ell - \Delta\Phi_u = 16n(n+N)\omega_r T - 2n\omega_m T + \mathcal{O}(\gamma, \delta k), \tag{2.26}$$

and a common mode phase equal to

$$\Delta\Phi_\ell + \Delta\Phi_u = 2nk_{\text{eff}} gT(T + T_1' + T_2') + \mathcal{O}(\gamma, \delta k).$$

2.4 Ellipse Fitting

While the previous section was focused on calculating the theoretical phase shifts in an atom interferometer, the experimental apparatus is in practice used to solve the inverse problem of measuring the phase shifts given an interference pattern. For an initial atom amplitude of A_0, the upper output ports of each Ramsey-Bordé interferometer shown in Fig. 2.3 have theoretical amplitudes of

$$|\Psi_{\ell u}|^2 = \frac{A_0}{8}\cos^2\left(\frac{1}{2}\left(\phi_c + \phi_d\right)\right)$$
$$|\Psi_{uu}|^2 = \frac{A_0}{8}\cos^2\left(\frac{1}{2}\left(\phi_c - \phi_d\right)\right),$$

where the factor of $1/8$ comes from the four $\pi/2$ beam splitters, the last of which interferes two trajectories. The differential phase ϕ_d and common mode phase ϕ_c were previously calculated as

$$\begin{aligned}\phi_d &= 8n(n+N)\omega_r T - n\omega_m T \\ \phi_c &= nk_{\text{eff}} gT(T + T_1' + T_2')\end{aligned} \tag{2.27}$$

for a Ramsey-Bordé interferometer with Bloch oscillations. If ϕ_c were constant, then one could scan ϕ_d by shifting the modulation frequency ω_m by a small amount $\delta\omega_m$ to trace out two oscillating fringes. By fitting the fringes to a cosine squared function, the phase at $\delta\omega_m = 0$ could be extracted for the two outputs, which would allow for explicit calculation of the phase difference between $\Psi_{\ell u}$ and Ψ_{uu}. This is not possible in practice because ϕ_c fluctuates by more than π radians per shot due to vibrations, washing out the fringes. However, because the common mode phase ϕ_c is correlated between the two output ports, the two amplitudes trace out an ellipse when the lower interferometer output is plotted against the upper interferometer, as shown in Fig. 2.4. In order to extract the differential phase ϕ_d, one must then fit an ellipse to the resulting data points and calculate the phase from the fitted ellipse parameters.[7]

In a real world interferometer, the four output ports might have non-ideal interference contrast and can therefore be generalized to

$$|\Psi_{\ell\ell}|^2 = A_\ell \sin\left(\frac{1}{2}(\phi_c + \phi_d)\right)^2 + b_1, \qquad |\Psi_{\ell u}|^2 = A_\ell \cos\left(\frac{1}{2}(\phi_c + \phi_d)\right)^2 + b_2$$
$$|\Psi_{u\ell}|^2 = A_u \sin\left(\frac{1}{2}(\phi_c - \phi_d)\right)^2 + b_3, \qquad |\Psi_{uu}|^2 = A_u \cos\left(\frac{1}{2}(\phi_c - \phi_d)\right)^2 + b_4,$$

[7]Since the fitting works best when the points are evenly distributed around the ellipse, it is actually beneficial to have a largely varying common mode phase ϕ_c. For this reason, no vibration isolation is used in the experiment.

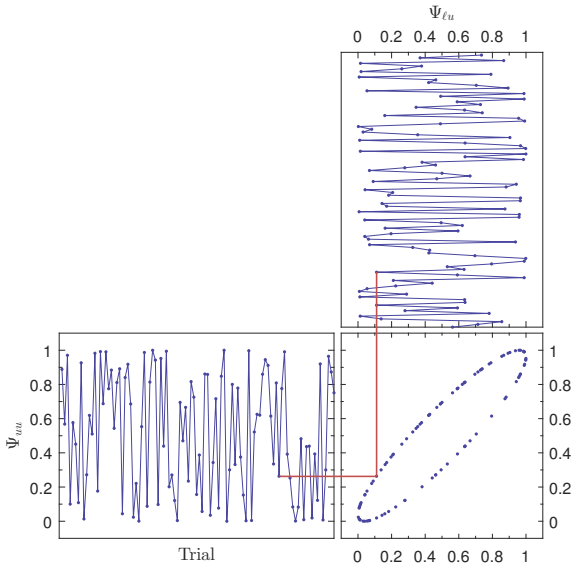

Figure 2.4: Two simulated Ramsey-Bordé interferometer outputs plotted against each other. Despite the seemingly random fluctuations from shot to shot caused by vibrations, the amplitudes are still correlated and form an ellipse.

where $\{A_\ell, A_u\}$ are the interference amplitudes and $\{b_1, b_2, b_3, b_4\}$ are the amplitude offsets due to backgrounds. Since the total atom number for each pair of outputs $|\Psi_{\ell\ell}|^2 + |\Psi_{\ell u}|^2$ and $|\Psi_{u\ell}|^2 + |\Psi_{uu}|^2$ can fluctuate and drift due to imperfections in the atom source, it is useful to first normalize the signal

$$x = \frac{|\Psi_{\ell u}|^2 - |\Psi_{\ell\ell}|^2}{|\Psi_{\ell u}|^2 + |\Psi_{\ell\ell}|^2}, \qquad y = \frac{|\Psi_{uu}|^2 - |\Psi_{u\ell}|^2}{|\Psi_{uu}|^2 + |\Psi_{u\ell}|^2}$$

such that

$$\begin{aligned} x &= A_x \cos(\phi_c + \phi_d) + b_x \\ y &= A_y \cos(\phi_c - \phi_d) + b_y, \end{aligned} \tag{2.28}$$

where A_x, A_y are the normalized fringe contrasts and b_x, b_y are offsets. In order to fit data of this form to an ellipse, we first need to rewrite $\{x, y\}$ in the form of a generalized conic section

$$a_1 x^2 + a_2 xy + a_3 y^2 + a_4 x + a_5 y + a_6 = 0 \tag{2.29}$$

which describes an ellipse when $a_2^2 - 4a_1 a_3 < 0$. To convert the equations for $\{x, y\}$ into this form, first subtract the offsets and normalize to obtain a set of rescaled points

$$\begin{aligned} x' &= (x - b_x)/c_x = \cos\phi_c \cos\phi_d + \sin\phi_c \sin\phi_d \\ y' &= (y - b_y)/c_y = \cos\phi_c \cos\phi_d - \sin\phi_c \sin\phi_d. \end{aligned} \tag{2.30}$$

With these rescaled coordinates, it becomes apparent that the relation

$$\left(\frac{x' - y'}{2\sin\phi_c}\right)^2 + \left(\frac{x' + y'}{2\cos\phi_c}\right)^2 - 1 = 0$$

cancels the common mode phase ϕ_c and has the form of (2.29). Expanding this equation using our definitions for x' and y' from (2.30) yields

$$\begin{aligned} &\frac{1}{c_x^2}x^2 - \frac{2\cos 2\phi_d}{c_x c_y}xy + \frac{1}{c_y^2}y^2 + \left(\frac{2b_y \cos 2\phi_d}{c_x c_y} - \frac{2b_x}{c_x^2}\right)x + \left(\frac{2b_x \cos 2\phi_d}{c_x c_y} - \frac{2b_y}{c_y^2}\right)y \\ &+ \left(\frac{b_x^2}{c_x^2} + \frac{b_y^2}{c_y^2} - \frac{2b_x b_y \cos 2\phi_d}{c_x c_y} - 4\cos^2\phi_d \sin^2\phi_d\right) = 0, \end{aligned} \tag{2.31}$$

which can be matched up term for term with the coefficients a_i from (2.29). A simple substitution will then verify that

$$\phi_d = \frac{1}{2}\cos^{-1}\left(\frac{-a_3}{2\sqrt{a_1 a_2}}\right).$$

By fitting an ellipse to the data and extracting the parameters a_1, a_2, and a_3, the differential phase and therefore the desired recoil frequency phase can be measured.

One might be tempted to assume that the amplitudes of the individual cosines in (2.28) are simply $\sqrt{a_1}$ and $\sqrt{a_3}$ from Eq. (2.31). However, since (2.31) can be scaled by an arbitrary constant, one cannot guarantee that the ellipse is normalized as such. Instead the cosine amplitudes are given by the much more complicated formulas

$$\begin{aligned} c_x^2 &= \frac{4a_3(a_6(a_2^2 - 4a_1a_3) + a_3a_4^2 + a_1a_5^2 - a_2a_4a_5)}{(a_3^2 - 4a_1a_3)^2} \\ c_y^2 &= \frac{4a_1(a_6(a_2^2 - 4a_1a_3) + a_3a_4^2 + a_1a_5^2 - a_2a_4a_5)}{(a_3^2 - 4a_1a_3)^2}, \end{aligned}$$

which are used to compute the contrast of the interferometers.

2.4.1 Least Squares Ellipse Fitting

The normalized data points x and y measured by the experiment will in general tend to have noise. This means the entire data set will not fall perfectly on an ellipse described by (2.29) and instead the ellipse must be chosen as a best fit. There are several methods for determining the best fit for an ellipse, such as minimizing the geometric distance of every

point to the ellipse [45, 46] or by using a probabilistic Bayesian estimation [47].[8] While these methods are powerful in their own right, a simpler least squares fitting is used for the majority of data fitting. Since least squares methods are based in linear algebra, they can be calculated extremely fast which makes it possible to rigorously check for systematic errors due to fitting through simulation.[9]

The least squares fitting method used is based on the paper [49] and seeks to minimizes the conic section equation $a_1x^2 + a_2xy + a_3y^2 + a_4x + a_5y + a_6 = a^T\vec{x}$ for an ellipse where

$$\begin{aligned} a &= [a_1 \quad a_2 \quad a_3 \quad a_4 \quad a_5 \quad a_6]^T, \\ \vec{x}_i &= [x_i^2 \quad x_iy_i \quad y_i^2 \quad x_i \quad y_i \quad 1]^T, \end{aligned}$$

and $\{x_i, y_i\}$ are the normalized data points (2.28) of the interferometer. If the data were to form a perfect ellipse, then a^Tx_i would be zero for every data point and therefore the algebraic distance $(a^Tx_i)^2$ can be treated as a metric to be minimized. The goal of the least squares fit is then to find values for a_i which minimize

$$\epsilon = \sum_i^n (a^Tx_i)^2$$

with the restriction that a describes an ellipse with $a_2^2 - 4a_1a_3 < 0$. For simplicity, assume a is normalized such that $a_2^2 - 4a_1a_3 = -1$, then the ellipse restriction can be written in matrix form as $a^TCa = -1$, where

$$C = \begin{bmatrix} 0 & 0 & -2 & 0 & \\ 0 & 1 & 0 & 0 & \cdots \\ -2 & 0 & 0 & 0 & \\ 0 & 0 & 0 & 0 & \\ & \vdots & & & \ddots \end{bmatrix}.$$

Similarly, the metric ϵ can be written as $\sum_i^n (a^T\vec{x}_i) = (a^TD^T)Da$ with

$$D = [\vec{x}_1 \quad \vec{x}_2 \quad \cdots \quad \vec{x}_n]^T.$$

Then using a Lagrange multiplier λ, the least squares minimization can be written as a system of equations,

[8] There are methods for extracting the phase that do not rely on ellipse fitting, such as analyzing the noise distribution [48], but the systematics phase shifts of these methods have not been thoroughly explored.

[9] This is not true for other fitting methods. For example, Bayesian estimation can take several seconds to compute a single fit, which makes it difficult to run the millions of simulations needed to determine part per billion systematics.

$$\begin{aligned} D^T Da - \lambda Ca &= 0 \\ a^T Ca &= -1 \end{aligned} \tag{2.32}$$

with six eigenvector solutions $a = \vec{u}_j$ and corresponding eigenvalues λ_j. To impose the condition $a^T Ca = -1$ on the eigenvectors, multiply the first equation in (2.32) by a^T and rearrange to obtain

$$a^T D^T Da = \lambda_j a^T Ca.$$

Since the left-hand side $a^T D^T Da = \sum_i^n (a^T \vec{x}_i)$ is positive and $a^T Ca$ is negative from our ellipse constraint, then only negative eigenvalues are valid solutions. Therefore the only unique ellipse solution[10], $a = \vec{u}_k$, occurs when the corresponding eigenvalue $\lambda_k < 0$.

2.4.2 Ellipse Noise

As the least squares ellipse fitting method is the primary way to measure the phase of the interferometer, it is important to understand the limitations and errors caused by the distribution of real data. The interferometer phase for a Ramsey-Bordé interferometer (2.26) with typical experimental parameters of $n = 5$, $N = 25$, and $T = 80$ ms is around 2.5×10^6 radians, which means that for a 0.5 ppb measurement, the phase uncertainty must be less than 1 mrad. Therefore any systematics caused by the ellipse fitting algorithm must be understood at a level below 1 mrad, otherwise the fitting would contribute significantly to the error budget of the measurement.

Consider a simple noise model where the two normalized interferometer outputs (2.28) have an offset noise $\epsilon_{x,y}$ that has a Gaussian distribution with a variance $\sigma_{x,y}^2$:

$$\begin{aligned} x &= c_x \cos(\phi_c + \phi_d) + b_x + \epsilon_x \\ y &= c_y \cos(\phi_c - \phi_d) + b_y + \epsilon_y. \end{aligned}$$

One of the first things to examine is the accuracy of the least squares ellipse fit in the presence of this offset noise. An example of such an analysis is shown in Fig. 2.5, where ellipses with different phases ϕ_d were simulated with offset noise equal to $\sigma_{x,y} = 0.07$. The measured phase is most accurate near $\pm\pi/4$ where the ellipse is a circle and least accurate around $\{0, \pm\pi/2\}$ where the ellipse forms a line (the deviation increases with noise). Therefore it is best to operate the interferometer at a net phase of $\pm\pi/4$ for optimal least squares fitting.

Modulation

Since the differential phase (2.27) is nominally null when the external modulation frequency ω_m matches the recoil frequency $8(n + N)\omega_r$, an extra frequency shift $\delta\omega_r$ is required to

[10]This is proven in reference [49]. Note that in the reference, the constraint $4a_1a_3 - a_2^2 = 1$ is used instead, which leads to a positive eigenvalue solution.

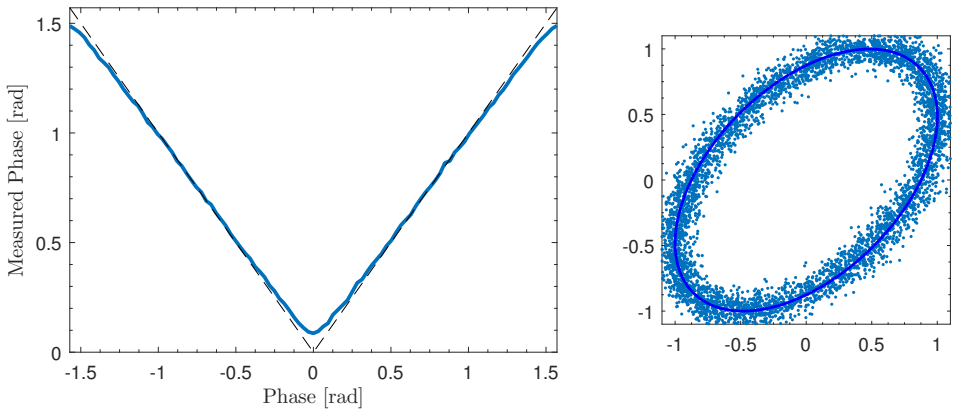

Figure 2.5: Left: The phase measured by the least squares fitting as a function of differential phase ϕ_d in the presence of offset noise $\sigma_{x,y} = 0.07$ using simulated data (note that the ellipse fitting cannot determine the sign of the phase). Right: An example of a simulated ellipse fit with a differential phase $\phi_d = \pi/6$ and the same offset noise.

rotate the ellipse to $\pi/4$. For a given interferometer with Bragg order n and pulse separation time T, the frequency shift is chosen such that

$$\pm\frac{\pi}{4} = 8n(n+N)\omega_r T - n(\omega_m + \delta\omega_m)T,$$

which for $\omega_m = 8(n+N)\omega_r$ gives

$$\pm\frac{\pi}{4} = -n\delta\omega_m T$$

or $\delta f_m = \delta\omega_m/2\pi = \pm 1/(8nT)$. To determine the correct center frequency ω_m and therefore the recoil frequency, two ellipses are taken at $+\delta\omega_m$ and $-\delta\omega_m$ and the measured phases are subtracted to give the phase error $\delta\phi = \varphi(+\delta\omega_m) - \varphi(-\delta\omega_m)$ from null. The modulation frequency ω_m can then be corrected to be on resonance by applying the shift $\omega_m + \delta\phi/2nT$ to obtain a measurement of the recoil frequency

$$\omega_r = \frac{1}{8(n+N)}\left(\omega_m + \frac{\varphi(+\delta\omega_m) - \varphi(-\delta\omega_m)}{2nT}\right).$$

An example of the fitting error in the differential phase as a function of the center phase $\varphi(+\delta\omega_m) - \varphi(-\delta\omega_m)$ using this ellipse modulation procedure is shown in Fig. 2.6. As is apparent from the plots, a modulation of $\pm\pi/4$ gives the lowest error, as does having the two ellipses symmetric about zero phase. For Gaussian offset noise equal to $\sigma = 0.03$, the ellipse must be kept within 200 mrad of symmetric to have a fitting error of less than 1 mrad.

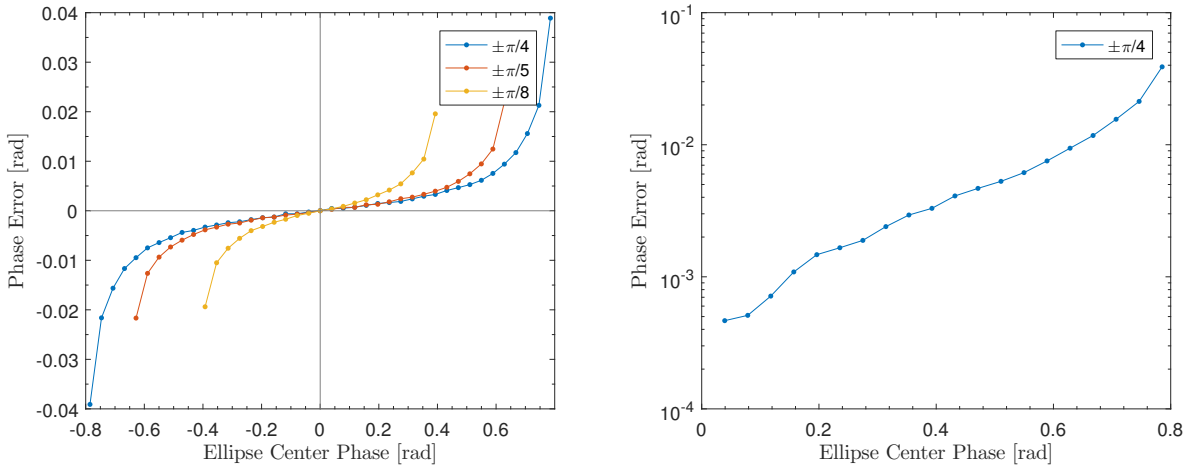

Figure 2.6: Left: A plot of the fitting error as a function of the ellipse center phase (difference between the plus and minus modulation) for ellipses with $\sigma = 0.03$ offset noise. Several other phase modulations are shown to emphasize the benefit of using $\pm\pi/4$ radians. Right: A log scale plot of the $\pm\pi/4$ modulation error to better show the magnitude of the error.

Shot-Noise

Another noise model that could be considered similar to the Gaussian offset noise is the shot-noise caused by quantum projection of the atom state during detection [50, 51]. For an ensemble of N atoms with a probability p_a to be in state a ($\Psi_{\ell\ell}$ for example), then the likelihood of measuring N_a atoms in that state is given by the binomial distribution

$$\mathcal{P}(N_a, N, p_a) = \frac{N}{N_a!(N - N_a)!} p_a^{N_a} (1 - p_a)^{N - N_a}$$

with a variance of

$$\sigma^2 = N p_a (1 - p_a).$$

For an interferometer where the probability of ending up in state $a = \Psi_{\ell\ell}$ is $p_a = \sin^2(\phi_c + \phi_d)^2$, the noise ϵ_a on the amplitude $|\Psi_{\ell\ell}|^2$ is then given by the Gaussian variance

$$\sigma^2 = \frac{\sin^2(\phi_c + \phi_d)\cos^2(\phi_c + \phi_d)}{N}$$

which is anti-correlated with the noise on $|\Psi_{\ell u}|^2$. Similarly, the variance of the upper interferometer port amplitudes can be calculated as $\sigma^2 = \sin^2(\phi_c - \phi_d)\cos^2(\phi_c - \phi_d)/N$. A simulated ellipse with the shot-noise of $N = 500$ atoms is shown in Fig. 2.7. Also plotted is the per-shot ellipse fitting phase uncertainty as a function of the atom number N, which matches to a $1/\sqrt{N}$ line for $N > 10$. This implies that when using ellipse fitting, a shot-noise limited interferometer should obtain a phase resolution of $1/\sqrt{N}$ for a single trial and a per ellipse resolution of $(N_{\text{atom}} N_{\text{bin}})^{-1/2}$, where N_{bin} is the number of points per ellipse.

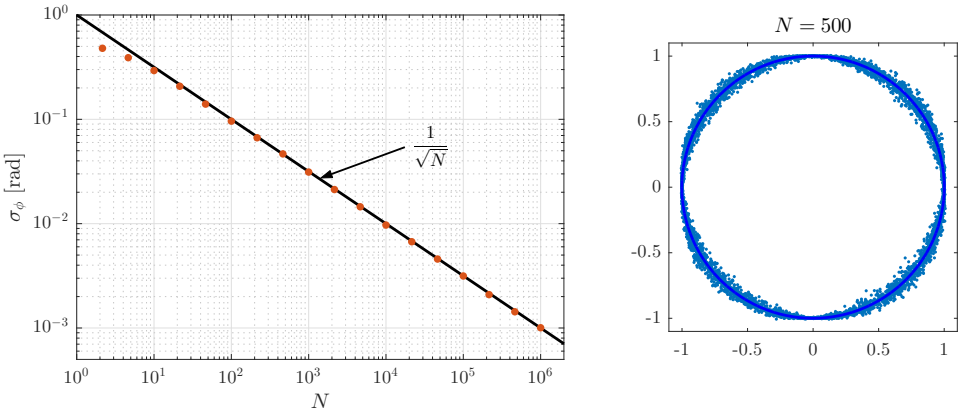

Figure 2.7: Left: The simulated per-shot phase uncertainty σ_ϕ for ellipses that are dominated by shot-noise. Right: A simulated ellipse with $N = 500$ at an angle of $\phi_d = \pi/4$.

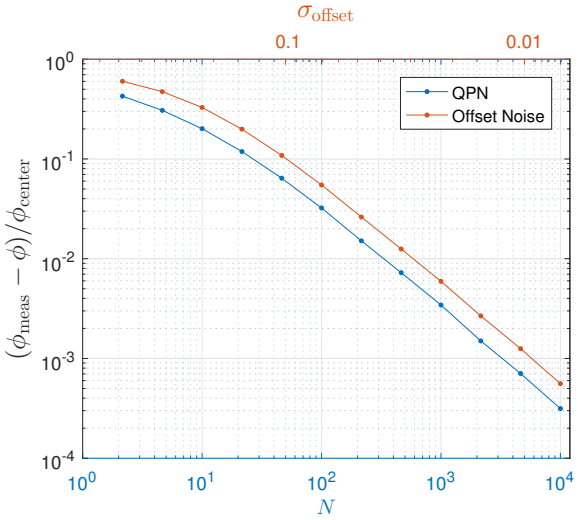

Figure 2.8: A plot of the sensitivity of the phase error $(\phi_{\text{meas}} - \phi)$ to the modulated center phase ϕ_{center}, as a function of noise strengths. The lines show the sensitivity as a function of offset noise σ_{offset} (red) and atom number N quantum projection noise (blue).

To compare the two noise models, a curve similar to that of Fig. 2.6 is calculated for both offset noise σ_{offset} and atom shot-noise N, using the $\pm\pi/4$ modulation scheme. The slope of the resulting phase error versus center phase curve is computed for a variety of noise strengths and plotted in Fig. 2.8. For both noise models, as the noise decreases so does the restriction on the ellipse center phase.

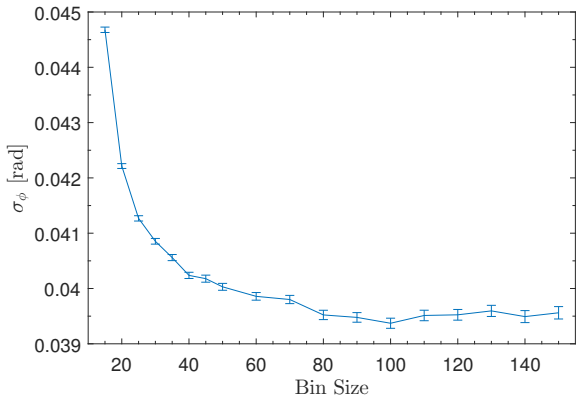

Figure 2.9: A plot of the per-shot standard deviation σ_ϕ for 10,000 simulated points that are grouped into ellipses of bin size N_{bin}. The per-point standard deviation was calculated by taking the standard deviation of the simulated ellipse's phases and multiplying by $\sqrt{N_{\text{bin}}}$. Below a bin size of 15 the standard deviation tends to blows up (not shown).

Binning

One last thing to consider is the choice of bin size for the ellipse fitting. Even though only 6 points are enough to produce ellipse solutions with least squares fitting, a bin size larger than 15 gives much more accurate results as shown in Fig. 2.9. Since making the bin size larger has only a small effect on reducing the per point standard deviation, a modest bin size of 20-30 is typically used to reduce the impact of long timescale drifts.

2.5 Bragg Diffraction

In Section 2.2, a simplified calculation of the atom-light interaction was done to figure out the phase acquired by the atoms during absorption and emission of photons in the beam splitters due to the laser phase. This calculation was generalized to many types of beam splitters and neglected to account for any phase shifts caused by the dynamics of the Bragg beam splitters used in the experiment.

The Hamiltonian describing the interaction between an atomic two-level system and an electromagnetic field, shown in Fig. 2.10, can be written as

$$\hat{H} = \frac{\hat{p}^2}{2m} + \hbar\omega_0 \left|e\right\rangle \left\langle e\right| - \left(\vec{d}_{ge} \cdot \vec{E} \left|e\right\rangle \left\langle g\right| + h.c.\right), \tag{2.33}$$

where $|g\rangle$ is the ground state, ω_0 is the transition frequency of the excited state $|e\rangle$, and $\vec{d_{ge}} \cdot \vec{E} \left|e\right\rangle \left\langle g\right|$ is the interaction matrix element between the atomic dipole moment and the electric field as described in Section 2.3. Here, the momentum p in (2.33) is the center of mass motion of the atom and not the relative motion of the electron-proton system as was used in (2.16). If we consider the electric field of a plane wave with the form

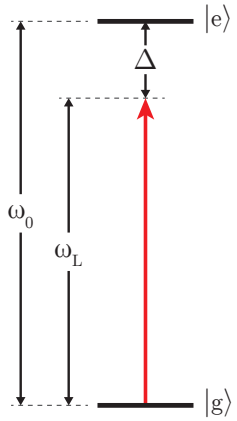

Figure 2.10: A two-level system with ground state $|g\rangle$ and excited state $|e\rangle$ with energy $\omega_0 = \Delta + \omega_L$, driven with an electric field of frequency ω_L.

$$\begin{aligned}\vec{E} &= \vec{E}_0 \cos(kz - \omega_L t) \\ &= \frac{1}{2}\left(e^{ikz - i\omega_L t} + e^{-ikz + i\omega_L t}\right),\end{aligned}$$

then the interaction part of the Hamiltonian can then be written as

$$\begin{aligned}\hat{H}_{\text{int}} &= -\vec{d_{ge}} \cdot \vec{E}\,|e\rangle\langle g| + h.c. \\ &= -\frac{\hbar\Omega}{2}\left(e^{ikz - i\omega_L t} + e^{-ikz + i\omega_L t}\right)|e\rangle\langle g| + h.c.,\end{aligned}$$

where we define the Rabi frequency as $\Omega \equiv \vec{d_{ge}} \cdot \vec{E}_0/\hbar$. If the eigenvector is transformed by applying the unitary transformation $U = e^{i\omega_0 t|e\rangle\langle e|}$, then the interaction part of the Hamiltonian is transformed as

$$\begin{aligned}\hat{H}'_{int} &= \hat{U}\hat{H}_{\text{int}}\hat{U}^\dagger - i\hbar\hat{U}\frac{\partial\hat{U}^\dagger}{\partial t} \\ &= -\frac{\hbar\Omega}{2}\left(e^{ikz - i(\omega_L - \omega_0)t} + e^{-ikz + i(\omega_L + \omega_0)t}\right)|e\rangle\langle g| + h.c.\end{aligned}$$

In the limit where the laser detuning $\Delta \equiv \omega_L - \omega_0$ is much smaller than the excited state energy ω_0, then the rotating wave approximation can be applied to neglect the fast rotating $e^{i(\omega_L + \omega_0)t}$ terms (compared to the slowly rotating $e^{-i(\omega_L - \omega_0)t}$ terms). The inverse unitary transformation $U^\dagger H'_{\text{int}} U$ brings the eigenvectors back into the non-rotating frame

$$\hat{H} \approx \frac{\hat{p}^2}{2m} + \hbar\omega_0\,|e\rangle\langle e| - \left(\frac{\hbar\Omega}{2}e^{ikz - i\omega_L t}\,|e\rangle\langle g| + h.c.\right),$$

which is exactly the same result found in (2.20), only starting from the classical electric field instead of the quantized field. The rotating wave approximation can be generalized for a superposition of plane waves such that for the generalized electric field

$$\vec{E} = \sum_j \vec{E}_j \cos(k_j z - (\omega_L - \delta_j)t),$$

the Hamiltonian after the rotating wave approximation can be written as

$$\hat{H} \approx \frac{\hat{p}^2}{2m} + \hbar\omega_0 \left|e\right\rangle \left\langle e\right| - \hbar\left(\sum_j \frac{\Omega_j}{2} e^{ik_j z - i(\omega_L - \delta_j)t} \left|e\right\rangle \left\langle g\right| + h.c. \right)$$

assuming $|\delta_j| \ll \omega_L$ and where $\Omega_j \equiv \vec{d_{ge}} \cdot \vec{E}_j/\hbar$. As a final step, the eigenvectors are transformed by the unitary operator $U = e^{i\omega_L t|e\rangle\langle e|}$, where the full Hamiltonian is transformed as

$$\begin{aligned} \hat{H}' &= \hat{U}\hat{H}\hat{U}^\dagger - i\hbar\hat{U}\frac{\partial \hat{U}^\dagger}{\partial t} \\ &= \frac{\hat{p}^2}{2m} + \hbar(\omega_0 - \omega_L)\left|e\right\rangle \left\langle e\right| - \hbar\left(\sum_j \frac{\Omega_j}{2} e^{ik_j z + i\delta_j t} \left|e\right\rangle \left\langle g\right| + h.c. \right). \end{aligned} \tag{2.34}$$

So far, the Hamiltonian above is generalized for any two-level system driven by an arbitrary electric field. For the special case of Bragg diffraction, a nearly-standing electric field is used to coherently scatter the atomic wave-function from one momentum state to another through a multi-photon process. The electric field of the standing light wave after the rotating wave approximation is

$$\vec{E} \to \frac{\vec{E}_0}{2} u(z,t) = \frac{\vec{E}_0}{2}\left[e^{-ikz + i\delta t} + e^{ikz - i\delta t}\right], \tag{2.35}$$

where k is the laser wave-vector, 2δ is the detuning between the counter-propagating laser beams (corrections to the wave-vector due to δ are negligible), and

$$\hat{H}' = \frac{\hat{p}^2}{2m} - \hbar\Delta \left|e\right\rangle \left\langle e\right| - \left(\frac{\Omega u(z,t)}{2} \left|e\right\rangle \left\langle g\right| + h.c. \right). \tag{2.36}$$

In general, solutions to this Hamiltonian can be written as the superposition

$$\left|\Psi\right\rangle = e(z,t)\left|e\right\rangle + g(z,t)\left|g\right\rangle,$$

which can be used as an ansatz to the Schrödinger equation, $i\hbar\partial_t \left|\Psi\right\rangle = \hat{H}'\left|\Psi\right\rangle$, with the Hamiltonian from (2.36) to give

$$i\hbar\dot{e}(z,t) = \frac{\hat{p}^2}{2m}e(z,t) - \hbar\Delta e(z,t) - \frac{\hbar\Omega}{2}ug(z,t) \tag{2.37}$$

$$i\hbar\dot{g}(z,t) = \frac{\hat{p}^2}{2m}g(z,t) - \frac{\hbar\Omega^*}{2}u^*e(z,t). \tag{2.38}$$

Since the laser detuning Δ is large compared to the Rabi frequency Ω, we can adiabatically eliminate the excited state by setting $\dot{e}(z,t)$ equal to zero. In addition, the detuning $\Delta \gg \omega_r$ and therefore the kinetic energy term is negligible compared to $\hbar\Delta$ in Eq. (2.37). Solving for $e(z,t)$ and substituting it into Eq. (2.38) yields

$$i\dot{g}(z,t) = -\frac{\hbar}{2m}\frac{\partial^2}{\partial z^2}g(z,t) + \frac{|\Omega|^2}{4\Delta}uu^*g(z,t). \tag{2.39}$$

Due to the periodicity of the electric field, a reasonable ansatz for $g(z,t)$ would be a superposition of plane waves, such as

$$g(z,t) = \sum_{n=-\infty}^{\infty} g_n(t)e^{i2nkz}e^{-i(2n)^2\omega_r t}. \tag{2.40}$$

The second factor is a kinetic energy phase factor[11] for a massive particle with velocity $2n\hbar k/m$ (where $\omega_r \equiv \hbar k^2/2m$). This ansatz, along with the relative field strength u from (2.35),

$$\begin{aligned} u &= e^{-ikz+i\delta t} + e^{ikz-i\delta t} \\ uu^* &= 2 + \left[e^{-i2kz+i2\delta t} + e^{i2kz-i2\delta t}\right], \end{aligned}$$

can be inserted into (2.39), which after some rearranging reduces to

$$\begin{aligned} \sum_{n=-\infty}^{\infty} i\dot{g}_n e^{i2nkz}e^{-i4n^2\omega_r t} = \bar{\Omega}\sum_{n=-\infty}^{\infty} g_n e^{i2nkz}e^{-i4n^2\omega_r t} + \\ \frac{\bar{\Omega}}{2}\left[\sum_{n=-\infty}^{\infty} g_n e^{i2(n-1)kz}e^{i2\delta t}e^{-i4n^2\omega_r t} + \sum_{n=-\infty}^{\infty} g_n e^{i2(n+1)kz}e^{-i2\delta t}e^{-i4n^2\omega_r t}\right], \end{aligned}$$

where $\bar{\Omega} \equiv |\Omega|^2/2\Delta$ is the two-photon Rabi frequency. Note that one of the terms in $i\partial g(z,t)/\partial t$ exactly canceled the momentum term $-(\hbar/2m)\partial^2 g(z,t)/\partial x^2$ in (2.39) as the recoil frequency is defined as $\omega_r \equiv \hbar k^2/2m$.

The first term on the right-hand side can be eliminated by going to a rotating frame $g_n \to g_n e^{-i\bar{\Omega}t}$, which simplifies the system of equations to

$$\sum_{n=-\infty}^{\infty} i\dot{g}_n e^{i2nkz}e^{-i4n^2\omega_r t} = \frac{\bar{\Omega}}{2}\left[\sum_{n=-\infty}^{\infty} g_n e^{i2(n-1)kz}e^{i2\delta t}e^{-i4n^2\omega_r t} + \sum_{n=-\infty}^{\infty} g_n e^{i2(n+1)kz}e^{-i2\delta t}e^{-i4n^2\omega_r t}\right].$$

[11] While not needed, the kinetic energy phase term is also included in the ansatz to reduce the numerical complexity of the final solution.

In general, terms in uu^* that are not a function of z do not couple the momentum states g_n and can be ignored. Instead these terms contribute to common mode ac-Stark shifts, which phase shift all the coefficients g_n and, therefore, all momentum states, by the same amount.

Additional simplifications are made by performing the transformations $(n-1) \rightarrow n$ and $(n+1) \rightarrow n$ on the left and right summation in brackets to obtain:

$$\sum_{n=-\infty}^{\infty} i\dot{g}_n e^{i2nkz} e^{-i4n^2\omega_r t} = \frac{\bar{\Omega}}{2}\left[\sum_{n=-\infty}^{\infty} g_{n+1} e^{i2nkz} e^{i2\delta t} e^{-i4(n+1)^2\omega_r t} + \sum_{n=-\infty}^{\infty} g_{n-1} e^{i2nkz} e^{-i2\delta t} e^{-i4(n-1)^2\omega_r t}\right].$$

Since the solution to g_n must be satisfied for all z, each terms of order e^{i2nkz} must be equal individually, therefore

$$i\dot{g}_n = \frac{\bar{\Omega}}{2}\left[g_{n+1} e^{i2\delta t} e^{-i4(2n+1)\omega_r t} + g_{n-1} e^{-i2\delta t} e^{i4(2n-1)\omega_r t}\right]. \tag{2.41}$$

This result is an infinite set of coupled differential equations, where the two-photon Rabi frequency $\bar{\Omega}$ is in general a function of t. We can immediately see that the plane wave momentum states of the atom are coupled only by integer multiples of the photon wave-vector k. An atom starting in state g_{n_I}, with momentum $2n_I\hbar k$, can only be transferred to other states g_{n_F} with momentum $2n_F\hbar k$.

In the special case where the detuning δ between the counter-propagating fields is zero and the interaction time is long (Bragg regime), atoms in state g_n preferentially end up in g_{-n} (and visa-versa). In general, the Bragg resonance condition to transfer atoms in state g_{n_I} to g_{n_F} occurs when $\delta = 2(n_F + n_I)\omega_r$.

Unfortunately, no closed solution exists for the system of equations (2.41), save for a few special cases. In the Raman-Nath regime, where the interaction time $t \rightarrow 0$, (2.41) simplifies to

$$i\dot{g}_n = \frac{\bar{\Omega}}{2}\left[g_{n+1} + g_{n-1}\right]$$

with solutions $g_n = (-i)^n J_n(4\Omega t)$, where J_n are Bessel functions. While beam splitters in the Raman-Nath regime can be used for interferometry [52], the resulting populations tend to be spread out amongst many momentum states (not just the two of interest). In order to have efficient beam splitters, we would instead like to be in the Bragg regime where population is only transferred between two momentum states. For long interaction times and zero detuning ($\delta = 0$), we can adiabatically eliminate[12] the intermediate states g_{-n+1} through g_{n-1} to obtain a two-level system between g_{-n} and g_n with an effective Rabi frequency [53]

$$\Omega_{\text{eff}} \approx \frac{\bar{\Omega}^n}{(8\omega_r)^{n-1}} \frac{1}{(n-1)!^2} \tag{2.42}$$

[12]One has to be careful when adiabatically eliminating the $\dot{g}_k$ terms for $|k| < n$ since we have rotated all the states g_k by $e^{i4k^2\omega_r t}$ in our ansatz for g(z,t).

for $\bar{\Omega} \ll 4(n-1)\omega_r$. With typical experimental parameters of $n = 5$, the characteristic interaction time Ω_{eff}^{-1} would need to be approximately ω_r^{-1}. This is longer than what is achievable in our experiment,[13] and therefore the strict Bragg regime is an unsuitable approximation for our purposes. Instead, a quasi-Bragg solution is needed which can be accomplished by numerically integrating (2.41) with appropriate boundary conditions.

Consider a resonant system where an atom, initially in a pure momentum state ($g_{-n} = 1$), is transferred to a state g_n for a symmetric detuning $\delta = 0$. For sufficiently long interaction times, any term containing factors proportional to $e^{i4(\pm 2k \pm 1)}$ for $|k| \gg n$ will tend to oscillate rapidly and cancel to zero. This allows the truncation of (2.41) by setting $g_{-k-1}e^{i4(-2k-1)} = 0$ and $g_{k+1}e^{-i4(2k+1)} = 0$ for a sufficiently large momentum cutoff k. Generalizing to a detuning

$$\delta = 2(n_F + n_I)\omega_r$$

which resonantly couples g_{n_I} and g_{n_F}, we can introduce an upper cutoff $n_1 > \max(n_I, n_F)$ and a lower cutoff $-n_2 < \min(n_I, n_F)$ such that (2.41) reduces to the finite system of equations:

$$\begin{aligned}
i\dot{g}_{n_1+1} &= 0 \\
i\dot{g}_{n_1} &= \frac{\bar{\Omega}}{2}\left[g_{n_1-1}e^{-i2\delta t}e^{i4(2n_1-1)\omega_r t}\right] \\
i\dot{g}_{n_1-1} &= \frac{\bar{\Omega}}{2}\left[g_{n_1}e^{i2\delta t}e^{-i4(2n_1-1)\omega_r t} + g_{n_1-2}e^{-i2\delta t}e^{i4(2n_1-3)\omega_r t}\right] \\
&\vdots \\
i\dot{g}_{n} &= \frac{\bar{\Omega}}{2}\left[g_{n+1}e^{i2\delta t}e^{-i4(2n+1)\omega_r t} + g_{n-1}e^{-i2\delta t}e^{i4(2n-1)\omega_r t}\right] \\
&\vdots \\
i\dot{g}_{-n_2+1} &= \frac{\bar{\Omega}}{2}\left[g_{-n_2+2}e^{i2\delta t}e^{-i4(-2n_2+3)\omega_r t} + g_{-n_2}e^{-i2\delta t}e^{i4(-2n_2+1)\omega_r t}\right] \\
i\dot{g}_{-n_2} &= \frac{\bar{\Omega}}{2}\left[g_{-n_2+1}e^{i2\delta t}e^{-i4(-2n_2+1)\omega_r t}\right] \\
i\dot{g}_{-n_2-1} &= 0.
\end{aligned} \tag{2.43}$$

These equations are readily solvable by numerical computing software with reasonable choices for the cutoffs. For typical experimental parameters, choosing cutoffs $\Delta n = 5$ on either side of $\{n_I, n_F\}$ give results with fractional error below 10^{-7} and $\Delta n = 15$ yields results that are limited by numerical machine precision at below the 10^{-17} level. Typical choices for the cutoff are therefore $n_1 = \max(n_I, n_F) + 15$ and $-n_2 = \min(n_I, n_F) - 15$.

Before solving (2.43), it is beneficial to take a closer look at the time-dependent shape of the Rabi frequency $\bar{\Omega}(t)$. Consider Fig. 2.11, where the detuning of the undesired $2m$-photon process $g_0 = |g, 0\hbar k\rangle \rightarrow g_m = |g, 2m\hbar k\rangle$ is $\delta_m = 2m\delta - 4m^2\omega_r$. In order for

[13] The experimental pulses can have a width of at most $0.5\omega_r^{-1}$ before a significant decrease in signal-to-noise is observed (due to loss of coherence).

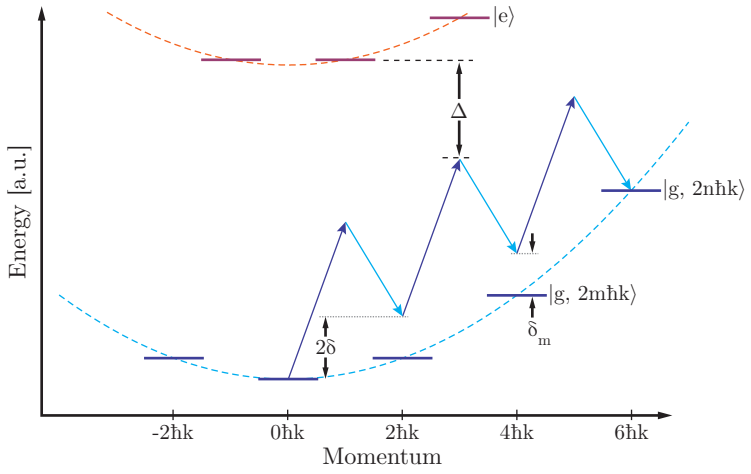

Figure 2.11: A diagram of the relevant momentum states of an atom and the laser fields for Bragg diffraction. The detuning between the laser fields is 2δ and the single photon detuning of the lasers from the excited state $|e\rangle$ is Δ. The multi-photon detuning to an arbitrary intermediate ground state $|g, m\hbar k\rangle$ is δ_m.

intermediate states to remain unpopulated, the detuning δ_m for every state other than the final state $m = n$ should be much greater than the Rabi frequency $\bar{\Omega}$. The obvious way to satisfy this adiabatic requirement is to use very long, low Rabi frequency pulses such that $\bar{\Omega} \ll |2m\delta - 4m^2\omega_r|$ for all intermediate states m (which is the same condition used in the Bragg regime approximation (2.42)). A Rabi frequency this low requires that the atom ensemble have a very small momentum spread, which is outside the capabilities of our experimental apparatus.

The other option is to use shorter, quasi-adiabatic pulses that efficiently transfer the atom through the undesired momentum states in such a way that the intermediate states remain unpopulated at the end of the π or $\pi/2$ pulse.[14] This requirement is essential since the parasitic phase imparted onto the atoms by the beam splitter is proportional to the losses into these intermediate states [53]. There also exist adiabatic rapid-passage techniques for Bragg diffraction, such as those described in [54], but these methods tend to have worse beam splitter phase systematics in the end.

Pulse Shape

While a square pulse is very simple to create and works well in Raman type beam splitters, the high intensities at the edges of the pulse cause large oscillating populations in the intermediate states that are unsuitable for high-order Bragg diffraction (though are manageable

[14]The conditions for efficient π pulses are usually not the same as $\pi/2$ pulses as the intermediate states can oscillate in a manner that is difficult to predict.

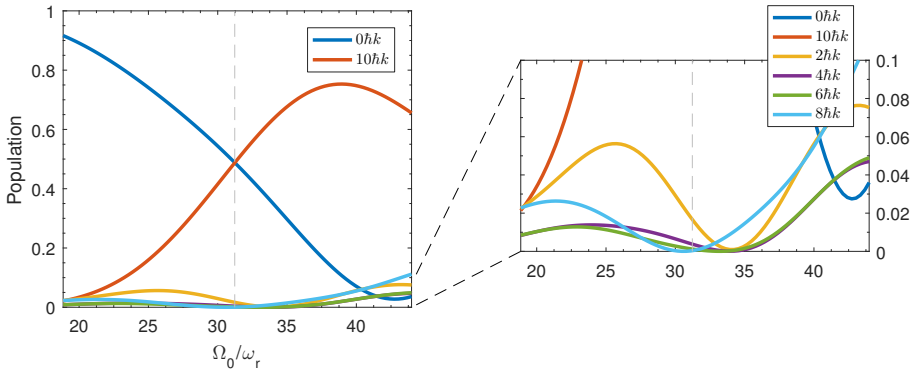

Figure 2.12: Bragg diffraction population transfer versus Rabi frequency Ω_0 for an atom initially in $g_0 = 1$ with detuning for 5th order Bragg diffraction ($\delta = 10\omega_r$) and a zoomed view to emphasize the losses into other orders. The gray dashed line indicates the optimal $\pi/2$ pulse intensity at $\Omega_0 = 31.23\omega_r$. ($\sigma = 0.188\omega_r^{-1}$, $\tau = 3.272\sigma$)

for $2\hbar k$ or $4\hbar k$ Bragg diffraction). Continuous and slowly varying functions such as truncated Gaussian pulses:

$$\bar{\Omega}(t) = \begin{cases} \Omega_0 e^{-t^2/2\sigma^2} & \text{if } -\tau \leq t \leq \tau \\ 0 & \text{otherwise} \end{cases} \tag{2.44}$$

or Blackman pulses:

$$\bar{\Omega}(t) = \Omega_0 \left[\frac{1-\alpha}{2} - \frac{1}{2}\cos\left(\frac{\pi(t-\tau)}{\tau}\right) + \frac{\alpha}{2}\cos\left(\frac{2\pi(t-\tau)}{\tau}\right) \right], \quad \alpha = 0.16$$

tend to minimize these oscillation by quasi-adiabatically transferring the atom through the intermediate states. Since the Rabi frequency is small for these kinds of functions at the start and end of the pulse, coupling to the near detuned states g_{n_I+1} and g_{n_F-1} are minimized during the transfer (see for example Fig. 2.13).

Although Blackman pulses (among other similar functions) have desirable properties, such as being functionally zero at $\pm\tau$, Gaussian pulses have been studied in more detail [44, 53, 54] and have been the focus of our group and this thesis. Solving (2.43) with a Gaussian intensity (2.44) is then straightforward in numerical computation software such as Matlab or Mathematica. The parameters typically used in the experiment are $\sigma = 0.188\omega_r^{-1}$ and $\tau = 3.272\sigma$ and therefore these parameters are used in the remainder of this section unless otherwise noted. In order to determine the appropriate intensity for a π or $\pi/2$ pulse, Ω_0 is varied until $|g_{n_I}|^2 = |g_{n_F}|^2$, such as in Fig. 2.12. This condition does not usually correspond to where the diffraction efficiency is 50 percent, but instead gives the maximum contrast for a Ramsey-Bordé interferometer which is easier to measure experimentally.

The quasi-adiabatic nature of a $\pi/2$ pulse can be seen by looking at the time-dependent dynamics, such as the $10\hbar k$ Bragg diffraction process shown in Fig. 2.13. During the pulse,

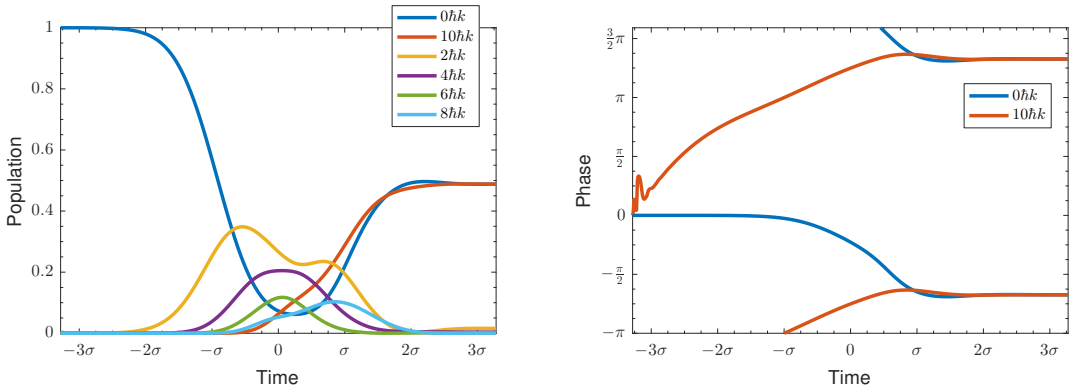

Figure 2.13: Left: The population of different momentum states as a function of time for an optimal Gaussian $\pi/2$ pulse with $\Omega_0 = 31.23\omega_r$, $\sigma = 0.188\omega_r^{-1}$, and $\tau = 3.272\sigma$. Right: Phase of the undeflected $0\hbar k$ order and the desired $10\hbar k$ order (phases shown are 2π periodic). The fast oscillations at the beginning are most likely due to numerical precision errors in calculating the phase (since the amplitude is very small).

atoms are initially transfer to low order states, but are then slowly transferred to higher order states, finally arriving at the final output state. The $-2\hbar k$ and $12\hbar k$ momentum states are also populated, but are not plotted for simplicity. The phase as a function of time is also plotted in Fig. 2.13 for the states g_5 and g_0 with the normal $\pi/2$ beam splitter phase subtracted from the diffracted order g_5 to emphasis the problematic diffraction phase. Even though the final phase difference is small for the simulated parameters ($\Delta\phi = -2.6$ mrad), both the diffracted and un-diffracted states undergo very large phase shifts during the course of the interferometer due to population transfer between neighboring states. The huge asymmetry of the phase shift makes multiple Bragg diffraction pulses [55] a particularly poor choice for large momentum transfer (from a systematics point of view) since a large portion of the diffraction phase remains uncanceled.

Varying the two-photon detuning δ also has a significant effect on the beam splitter as shown in Fig. 2.14. As the detuning is reduced towards lower-order Bragg diffraction ($\delta < 2n\omega_r$), the intermediate states are more resonant and therefore end up with larger populations. The behavior is not symmetric, as increasing the detuning predominately reduces the beam splitter efficiency, with an increase in population transfer to g_{n-1}. One might expect significant losses into g_{n+1} (not shown in the figure); however for a fixed Bragg diffraction order n, the effective Rabi frequency for an $n+1$ transition is reduced by an order of magnitude according to (2.42). The detuning δ also causes a large asymmetry in the diffraction phase for a single beam splitter, though some symmetry will be restored when considering a full conjugate interferometer, as shown in Section 2.5.2.

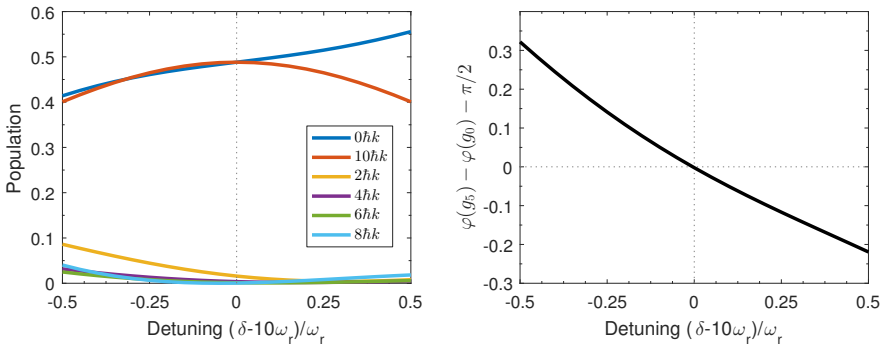

Figure 2.14: Left: Bragg diffraction population transfer versus detuning from resonance $\delta - 10\omega_r$. Right: Phase difference between the desired $10\hbar k$ order and the undeflected $0\hbar k$ order. ($\sigma = 0.188\omega_r^{-1}$, $\tau = 3.272\sigma$, $\Omega_0 = 31.23\omega_r$)

Moving Atoms

The last remaining points to consider are the effects caused by a moving atom. The state $g_0(t)$ has been defined to be at rest with respect to the standing wave formed by the counter-propagating fields when $\delta = 0$. If in our ansatz for $g(z,t)$ we instead chose $g_0(t)$ to have a velocity Δv, then (2.40) becomes

$$g(z,t) = \sum_{n=-\infty}^{\infty} g_n(t) e^{i(2n+\Delta v/v_r)kz} e^{-i(2n+\Delta v/v_r)^2\omega_r t},$$

where $v_r = \hbar k/m$. Following the same steps used to obtain (2.41), the modified system of equations is

$$i\dot{g_n} = \frac{\bar{\Omega}}{2}\left[g_{n+1}e^{i2\delta t}e^{-i4(2n+\Delta v/v_r+1)\omega_r t} + g_{n-1}e^{-i2\delta t}e^{i4(2n+\Delta v/v_r-1)\omega_r t}\right]$$

or, equivalently,

$$i\dot{g_n} = \frac{\bar{\Omega}}{2}\left[g_{n+1}e^{i2(\delta-2\omega_r\Delta v/vr)t}e^{-i4(2n+1)\omega_r t} + g_{n-1}e^{-i2(\delta-2\omega_r\Delta v/vr)t}e^{i4(2n-1)\omega_r t}\right]. \tag{2.45}$$

Therefore atoms with net velocity Δv are out of resonance with the Bragg condition $\delta = 2(n_F + n_I)\omega_r$ by an amount $2\omega_r\Delta v/v_r$, but still only couple to higher or lower momentum states by the same integer multiple of $2\hbar k$. This is an important feature of any beam splitter, since the atom source for an interferometer has a finite velocity distribution. The effects of a velocity distribution on the diffraction phase is more complicated and will be discussed in Section 5.4.

2.5.1 Multi-Frequency Beam Splitters

The third and fourth pulses in a conjugate Ramsey-Bordé interferometer drive the atoms with two different frequency pairs to address the upper and lower interferometers simultaneously. Although it is possible to have four separate frequencies to drive both pairs of interferometers, technical reasons make it easier to use three frequencies, with a common frequency shared between the pairs. The electric field for these pulses has a relative field strength of

$$\begin{aligned} u_{3,4} &= e^{-ikz+i\delta t} + e^{ikz-i\delta t+i\omega_m t} + e^{ikz-i\delta t-i\omega_m t} \\ u_{3,4}u_{3,4}^* &= 3 + 2\cos(2\omega_m t) + 2\cos(\omega_m t)\left[e^{-i2kz+i2\delta t} + e^{i2kz-i2\delta t}\right]. \end{aligned}$$

As before, the terms in $u_{3,4}u_{3,4}^*$ which do not depend on z can be dropped as they only contribute common mode ac-Stark shifts. We can then follow the same procedure outlined above for a single-frequency pair to show that the optical Bloch equation for two-frequency pairs has the solution

$$i\dot{g}_n = \cos(\omega_m t)\bar{\Omega}\left[g_{n+1}e^{i2\delta t}e^{-i4(2n+1)\omega_r t} + g_{n-1}e^{-i2\delta t}e^{i4(2n-1)\omega_r t}\right], \tag{2.46}$$

where $2\omega_m$ is the frequency difference between the two co-propagating fields and 2δ is the frequency difference between the counter-propagating field and the average of the co-propagating fields. Whereas the two-frequency system (2.41) couples g_{n_0} to g_{n_0+n} with a detuning $\delta = 2(2n_0+n)\omega_r$, the multi-frequency system (2.46) instead couples g_{n_0+n+N} to g_{n_0+2n+N} and g_{n_0-N} to g_{n_0-n-N} using a modulation frequency $\omega_m = 8(n+N)\omega_r$ for the same detuning δ. The dual resonance of the multi-frequency system is important as it is needed to drive both interferometers at the same time during a single pulse.

The diffraction efficiency of the multi-frequency system is similar to the two-frequency system (2.41), except that the optimal $\pi/2$ Rabi frequency for g_{n_0+n+N} to g_{n_0+2n+N} is now a function N as seen in Fig. 2.15. The optimal Rabi frequency approaches that of the two-frequency system as N goes to infinity, which is intuitive since the other off-resonant frequency pair has a larger detuning and therefore has a smaller influence. This is further emphasized by comparing the time-dependent dynamics (Fig. 2.16) to the two-frequency system (Fig. 2.13). As the modulation $\omega_m = 8(n+N)\omega_r$ increases, the fast time-dependent oscillations decrease and approach the dynamics of a single Bragg diffraction pulse.

2.5.2 Full Interferometer

Combining the results for single and multi-frequency Bragg diffraction, we can now calculate the total phase shift in the interferometer due to the beam splitter diffraction phase. At each beam splitter along a particular path, the atom acquires a diffraction phase given by solving (2.41) or (2.46). There are eight relevant paths to consider as each of the two interferometers (upper and lower) have two trajectories (upper and lower) and two output ports for each of those trajectories (upper and lower), as shown in Fig. 2.17.

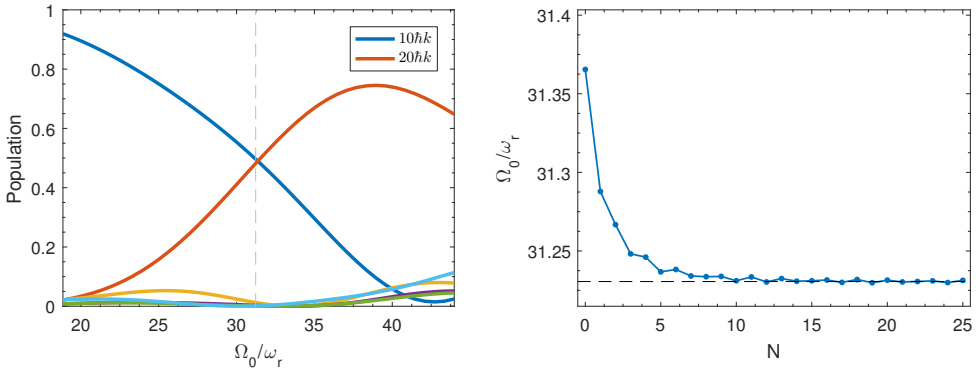

Figure 2.15: Left: Bragg diffraction population transfer versus Rabi frequency Ω_0 for an atom initially in $g_5 = 1$ with detuning $\delta = 10\omega_r$ and $\omega_m = 40\omega_r$. Right: The optimal $\pi/2$ Rabi frequencies that give equal populations in g_{5+N} and g_{10+N} for $\delta = 10\omega_r$ and $\omega_m = 8(5+N)\omega_r$. The dashed line in both plots indicates the $\pi/2$ Rabi frequency for two-frequency Bragg diffraction between g_0 and g_5 with the same detuning. ($\sigma = 0.188\omega_r^{-1}$, $\tau = 3.272\sigma$)

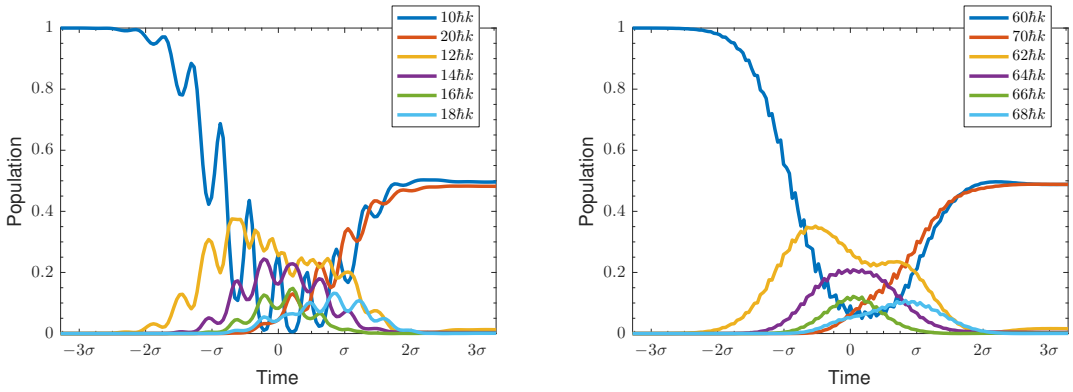

Figure 2.16: Left: The population of different momentum states as a function of time for an optimal multi-frequency Gaussian $\pi/2$ pulse with $\Omega_0 = 31.23\omega_r$, $\sigma = 0.188\omega_r^{-1}$, and $\tau = 3.272\sigma$. Left: Multi-frequency Bragg diffraction from g_5 to g_{10} for $N = 0$. Right: Multi-frequency Bragg diffraction from g_{30} to g_{35} for $N = 25$.

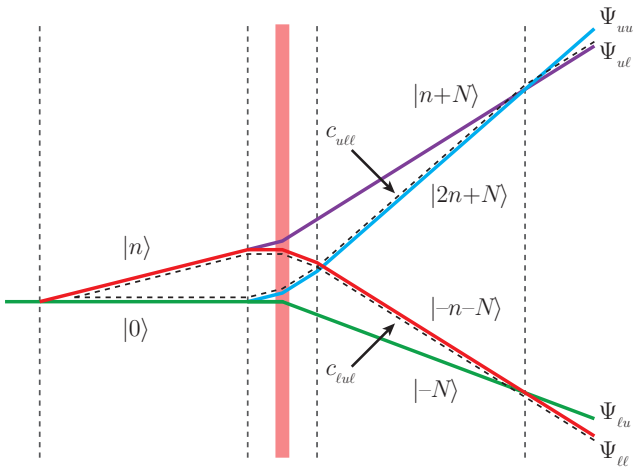

Figure 2.17: The full conjugate Ramsey-Bordé consisting of the lower interferometer (red and green) and the upper interferometer (purple and blue). Each interferometer has a lower (green or blue) and an upper (red or purple) path, each with an upper/lower output. The labeled trajectories $c_{u\ell\ell}$ and $c_{u\ell\ell}$ (dashed) are two of the eight trajectories that make up the interferometer outputs.

Numerically solving the two-frequency optical Bloch equation for the output state g_b given the input state $g_a = 1$ for a detuning $\delta = 4n\omega_r$ yields the matrix elements $\langle b|\,\hat{H}_n\,|a\rangle$. Similarly, the matrix elements $\langle b|\,\hat{H}_{n,N}\,|a\rangle$ can be found by integrating the multi-frequency optical Bloch equation for $\delta = 4n\omega_r$ and $\omega_m = 8(n+N)\omega_r$.

The matrix elements for $\hat{H}_n$ and $\hat{H}_{n,N}$ are symmetric, as well as invariant under a momentum transformation:

$$\begin{aligned}\langle b|\,\hat{H}_{n(,N)}\,|a\rangle &= \langle a|\,\hat{H}_{n(,N)}\,|b\rangle \\ &= \langle b+c|\,\hat{H}_{n+c(,N)}\,|a+c\rangle\,,\end{aligned} \tag{2.47}$$

which follows from Eq. (2.45) after some rearranging. For the two-frequency Hamilton H_n, there is also symmetry about the Bragg resonance condition. For any value $\{a,b,c\} \in \mathbb{R}$, then

$$\langle n+b|\,\hat{H}_{2n+c}\,|n+a\rangle = \langle n-b|\,\hat{H}_{2n-c}\,|n-a\rangle\,.$$

Additionally, for large modulation frequencies ω_m, the multi-frequency Hamiltonian $\hat{H}_{n,N}$ looks like a momentum shifted two-frequency Hamiltonian $\hat{H}_n$.

$$\begin{aligned}\langle b|\,\hat{H}_n\,|a\rangle &= \lim_{N\to\infty}\langle b+n+N|\,\hat{H}_{n,N}\,|a+n+N\rangle \\ &= \lim_{N\to\infty}\langle b-n-N|\,\hat{H}_{n,N}\,|a-n-N\rangle\,.\end{aligned} \tag{2.48}$$

The complex amplitude along a particular interferometer path is labeled as c_{ijk}, where the index i determines the interferometer, j determines the path within that interferometer,

and k determines the output port. Each index can take two values, u or ℓ, signifying "upper" and "lower" respectively. All eight paths can then be described as

$$\begin{aligned}
c_{\ell u\ell} &= \langle -n-N|\,\hat{H}_{n,N}\,|-n-N\rangle\,\langle -N|\,\hat{H}_{n,N}\,|-n-N\rangle\,\langle n|\,\hat{H}_n\,|0\rangle^2\\
c_{\ell\ell\ell} &= \langle -n-N|\,\hat{H}_{n,N}\,|-N\rangle\,\langle -N|\,\hat{H}_{n,N}\,|-N\rangle\,\langle 0|\,\hat{H}_n\,|0\rangle^2\\
c_{\ell uu} &= \langle -N|\,\hat{H}_{n,N}\,|-n-N\rangle^2\,\langle n|\,\hat{H}_n\,|0\rangle^2\\
c_{\ell\ell u} &= \langle -N|\,\hat{H}_{n,N}\,|-N\rangle^2\,\langle 0|\,\hat{H}_n\,|0\rangle^2\\
c_{uu\ell} &= \langle n+N|\,\hat{H}_{n,N}\,|n+N\rangle^2\,\langle n|\,\hat{H}_n\,|n\rangle\,\langle n|\,\hat{H}_n\,|0\rangle\\
c_{u\ell\ell} &= \langle n+N|\,\hat{H}_{n,N}\,|2n+N\rangle^2\,\langle n|\,\hat{H}_n\,|0\rangle\,\langle 0|\,\hat{H}_n\,|0\rangle\\
c_{uuu} &= \langle 2n+N|\,\hat{H}_{n,N}\,|n+N\rangle\,\langle n+N|\,\hat{H}_{n,N}\,|n+N\rangle\,\langle n|\,\hat{H}_n\,|n\rangle\,\langle n|\,\hat{H}_n\,|0\rangle\\
c_{u\ell u} &= \langle 2n+N|\,\hat{H}_{n,N}\,|2n+N\rangle\,\langle n+N|\,\hat{H}_{n,N}\,|2n+N\rangle\,\langle n|\,\hat{H}_n\,|0\rangle\,\langle 0|\,\hat{H}_n\,|0\rangle\,,
\end{aligned}$$

where the individual beam splitter diffraction phases $\phi_{ijk} = \{\phi_{\ell\ell\ell}, \phi_{\ell\ell u}, \ldots\}$ are given by $c_{ijk} = |c_{ijk}|\, e^{i\phi_{ijk}}$.

The free evolution and laser phases along the lower and upper trajectories are then defined to be $\phi_\ell = \phi_c + \phi_d$ and $\phi_u = \phi_c - \phi_d$, taken from the results of (2.26). As before, the differential phase contains the quantity to be measured and the common mode phase fluctuates between zero and 2π due to vibrations. The probability amplitudes of the interferometer output ports are then

$$\begin{aligned}
\Psi_{\ell\ell} &= |-n-N\rangle\left[c_{\ell u\ell} + e^{i\phi_\ell} c_{\ell\ell\ell}\right]\\
\Psi_{\ell u} &= |-N\rangle\left[c_{\ell uu} + e^{i\phi_\ell} c_{\ell\ell u}\right]\\
\Psi_{u\ell} &= |n+N\rangle\left[c_{uu\ell} + e^{i\phi_u} c_{u\ell\ell}\right]\\
\Psi_{uu} &= |2n+N\rangle\left[c_{uuu} + e^{i\phi_u} c_{u\ell u}\right].
\end{aligned}$$

Assuming the amplitudes of all the paths are equal $|c_i| = |c_j|$, the measured populations of the lower interferometer output ports are

$$\begin{aligned}
|\Psi_{\ell\ell}|^2 &= \cos^2\left(\frac{1}{2}\left(\phi_\ell + \phi_{\ell\ell\ell} - \phi_{\ell u\ell}\right)\right)\\
|\Psi_{\ell u}|^2 &= \sin^2\left(\frac{1}{2}\left(\phi_\ell + \phi_{\ell\ell u} - \phi_{\ell uu} - \pi\right)\right),
\end{aligned}$$

where we have inserted a $-\pi$ phase shift by hand to produce the usual sine squared interference result. By applying the substitution $\Phi_\ell = \phi_\ell + \phi_{\ell\ell\ell} - \phi_{\ell u\ell}$, the amplitude of the upper output port simplifies to

$$\begin{aligned}
|\Psi_{\ell u}|^2 &= \sin^2\left(\frac{1}{2}\left(\Phi_\ell + (\phi_{\ell\ell u} - \phi_{\ell uu}) - (\phi_{\ell\ell\ell} - \phi_{\ell u\ell}) - \pi\right)\right)\\
&= \sin^2\left(\frac{1}{2}\left(\Phi_\ell + \Delta\phi_\ell\right)\right),
\end{aligned}$$

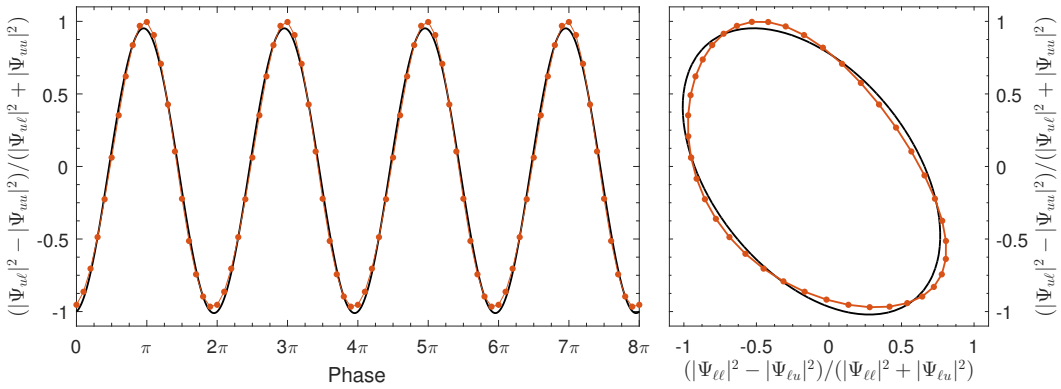

Figure 2.18: A non-ideal ellipse resulting from a simulated interferometer with parameters $n = 5$, $N = 25$, $\Omega_0 = 32.23\omega_r$, and a detuning from Bragg resonance of $\delta = 0.6\omega_r$. The red points indicate the simulated interferometer measurements, while the black curve is a best fit ellipse.

where we have introduced $\Delta\phi_\ell = (\phi_{\ell\ell u} - \phi_{\ell uu}) - (\phi_{\ell\ell\ell} - \phi_{\ell u\ell}) - \pi$ as the difference in diffraction phase between the two output ports of the lower interferometer. Since the beam splitter phases also encode the usual $\pi/2$ phase shifts intrinsic to beam splitters, the aforementioned $-\pi$ phase shift is included to make $\Delta\phi_\ell$ small.

Although it is possible to calculate the phase difference between the upper and lower interferometer by fitting the ellipse $|\Psi_{\ell\ell}|^2$ vs. $|\Psi_{u\ell}|^2$, this method is sensitive to fluctuations in absolute atom number. A more robust technique is to use the normalized difference between the interferometer outputs $(|\Psi_{\ell\ell}|^2 - |\Psi_{\ell u}|^2)/(|\Psi_{\ell\ell}|^2 + |\Psi_{\ell u}|^2)$ and $(|\Psi_{u\ell}|^2 - |\Psi_{uu}|^2)/(|\Psi_{u\ell}|^2 + |\Psi_{uu}|^2)$. For an ideal interferometer with output populations $|\Psi_\ell|^2 = A\cos(\phi/2)^2$ and $|\Psi_u|^2 = A\sin(\phi/2)^2$, the normalized difference reduces to $(|\Psi_\ell|^2 - |\Psi_u|^2)/(|\Psi_\ell|^2 + |\Psi_u|^2) = \cos(\phi)$, independent of the signal amplitude A.

However in the case of Bragg diffraction, the sum of the interfering populations is not unity, $|\Psi_{\ell\ell}|^2 + |\Psi_{\ell u}|^2 \neq 1$, due to beam splitter losses. This non-conservation of probability poses conceptual problems when extracting the phase via ellipse fitting since there does not appear to be a well-defined differential phase. This effect can be seen in Fig. 2.18, where the Bragg diffraction detuning is chosen to be off-resonant for each beam splitter. When parameters are chosen to be far from the ideal, the normalized outputs of the two conjugate interferometers tend not to form an ideal ellipse.

If the difference between the diffraction phase of the two output ports $\Delta\phi_\ell$ is small, then we can approximate the normalized population as

$$\frac{|\Psi_{\ell\ell}|^2 - |\Psi_{\ell u}|^2}{|\Psi_{\ell\ell}|^2 + |\Psi_{\ell u}|^2} \approx \cos(\Phi_\ell) - \frac{1}{2}\Delta\phi_\ell \sin(\Phi_\ell) + \frac{1}{4}\Delta\phi_\ell \sin(2\Phi_\ell) + \mathcal{O}(\Delta\phi_\ell^2). \tag{2.49}$$

Recall that the phase ϕ_ℓ (and therefore Φ_ℓ) contains a common mode term ϕ_c which fluctuates between zero and 2π due to vibrations. Interpreting ϕ_c as a parametric variable, we can

further approximate (2.49) by ignoring the second perturbative term that has twice the frequency in Φ_ℓ (and therefore in ϕ_c) as it will tend to average out when fitting (2.49) to the $\{x, y\}$ components of an ellipse with the functional form $A\cos(\phi_c + \phi) + B$. Utilizing a Taylor series approximation, the normalized population for the lower interferometer can be simplified to

$$\begin{aligned} x = \frac{|\Psi_{\ell\ell}|^2 - |\Psi_{\ell u}|^2}{|\Psi_{\ell\ell}|^2 + |\Psi_{\ell u}|^2} &\approx \cos(\Phi_\ell) - \frac{1}{2}\Delta\phi_\ell \sin(\Phi_\ell) \\ &\approx \cos\left(\Phi_\ell + \frac{\Delta\phi_\ell}{2}\right) \end{aligned}$$

and similarly for the upper interferometer,

$$y = \frac{|\Psi_{u\ell}|^2 - |\Psi_{uu}|^2}{|\Psi_{u\ell}|^2 + |\Psi_{uu}|^2} \approx \cos\left(\Phi_u + \frac{\Delta\phi_u}{2}\right),$$

where $\Phi_u = \phi_u + \phi_{u\ell\ell} - \phi_{uu\ell}$ and $\Delta\phi_u = (\phi_{udu} - \phi_{uuu}) - (\phi_{udd} - \phi_{uud}) - \pi$. The extracted differential phase after ellipse fitting $\{x, y\}$ is then

$$\begin{aligned} \Delta\varphi &= (\Phi_\ell + \frac{\Delta\phi_\ell}{2}) - (\Phi_u + \frac{\Delta\phi_u}{2}) \\ &= 2\phi_d + \frac{1}{2}\left[(\phi_{\ell\ell\ell} - \phi_{u\ell\ell}) - (\phi_{\ell u\ell} - \phi_{uu\ell})\right] + \frac{1}{2}\left[(\phi_{\ell\ell u} - \phi_{u\ell u}) - (\phi_{\ell uu} - \phi_{uuu})\right] \\ &= 2\phi_d + \frac{1}{2}\left[(\phi_{\ell\ell\ell} - \phi_{\ell u\ell}) - (\phi_{u\ell\ell} - \phi_{uu\ell})\right] + \frac{1}{2}\left[(\phi_{\ell\ell u} - \phi_{\ell uu}) - (\phi_{u\ell u} - \phi_{uuu})\right] \\ &= 2\phi_d + \phi_0, \end{aligned} \tag{2.50}$$

where ϕ_0 is the measured diffraction phase systematic due to beam splitter losses. Therefore to leading order, the non-conservation of probability due to beam splitter losses does not produce a systematic shift in the fitted ellipse phase and only the average diffraction phase ϕ_0 is measured (assuming the differential diffraction phases $\Delta\phi_{u,\ell}$ are small).

Interferometer Symmetries

We can also take advantage of certain cancellations to determine which pulses contribute the most to the measured diffraction phase. Expanding out each diffraction phase pair in (2.50) in terms of the Hamiltonian matrix elements:

$$\phi_{\ell\ell\ell} - \phi_{u\ell\ell} = \arg\left(\frac{\langle -n-N|\,\hat{H}_{n,N}\,|-N\rangle\,\langle -N|\,\hat{H}_{n,N}\,|-N\rangle\,\langle 0|\,\hat{H}_n\,|0\rangle^2}{\langle n+N|\,\hat{H}_{n,N}\,|2n+N\rangle^2\,\langle n|\,\hat{H}_n\,|0\rangle\,\langle 0|\,\hat{H}_n\,|0\rangle}\right),$$

$$\phi_{\ell u\ell} - \phi_{uu\ell} = \arg\left(\frac{\langle -n-N|\,\hat{H}_{n,N}\,|-n-N\rangle\,\langle -N|\,\hat{H}_{n,N}\,|-n-N\rangle\,\langle n|\,\hat{H}_n\,|0\rangle^2}{\langle n+N|\,\hat{H}_{n,N}\,|n+N\rangle^2\,\langle n|\,\hat{H}_n\,|n\rangle\,\langle n|\,\hat{H}_n\,|0\rangle}\right),$$

$$\phi_{\ell\ell u} - \phi_{u\ell u} = \arg\left(\frac{\langle -N|\,\hat{H}_{n,N}\,|-N\rangle^2\,\langle 0|\,\hat{H}_n\,|0\rangle^2}{\langle 2n+N|\,\hat{H}_{n,N}\,|2n+N\rangle\,\langle n+N|\,\hat{H}_{n,N}\,|2n+N\rangle\,\langle n|\,\hat{H}_n\,|0\rangle\,\langle 0|\,\hat{H}_n\,|0\rangle}\right),$$

$$\phi_{\ell uu} - \phi_{uuu} = \arg\left(\frac{\langle -N|\,\hat{H}_{n,N}\,|-n-N\rangle^2\,\langle n|\,\hat{H}_n\,|0\rangle^2}{\langle 2n+N|\,\hat{H}_{n,N}\,|n+N\rangle\,\langle n+N|\,\hat{H}_{n,N}\,|n+N\rangle\,\langle n|\,\hat{H}_n\,|n\rangle\,\langle n|\,\hat{H}_n\,|0\rangle}\right),$$

we immediately see that the right-most matrix elements describing the first beam splitter ($\langle 0|\hat{H}_n|0\rangle$ for the lower interferometer and $\langle n|\hat{H}_n|0\rangle$ for the upper interferometer) cancel out in each pair. Therefore the first beam splitter has no effect on the measured diffraction phase in the case of a conjugate Ramsey-Bordé interferometer, even if the Bragg detuning δ is not on resonance.

A slightly less ideal symmetry can be seen by looking at the left-most matrix elements in each pair, which corresponds to the last beam splitter. The contribution to the diffraction phase due to the last beam splitter is

$$\phi_{\text{last}} = \arg\left(\frac{\langle -n-N|\,\hat{H}_{n,N}\,|-N\rangle}{\langle n+N|\,\hat{H}_{n,N}\,|2n+N\rangle} \times \frac{\langle n+N|\,\hat{H}_{n,N}\,|n+N\rangle}{\langle -n-N|\,\hat{H}_{n,N}\,|-n-N\rangle} \times \frac{\langle -N|\,\hat{H}_{n,N}\,|-N\rangle}{\langle 2n+N|\,\hat{H}_{n,N}\,|2n+N\rangle} \times \frac{\langle 2n+N|\,\hat{H}_{n,N}\,|n+N\rangle}{\langle -N|\,\hat{H}_{n,N}\,|-n-N\rangle}\right).$$

The matrix elements that change the atom momentum (e.g. $\langle -n-N|\,\hat{H}_{n,N}\,|-N\rangle$) cancel because of the symmetry (2.47). Additionally, in the limit of large N, the matrix elements that do not change momentum (e.g. $\langle n+N|\,\hat{H}_{n,N}\,|n+N\rangle$) also cancel due to (2.48). This shows that the last beam splitter also does not contribute to the diffraction phase of the interferometer assuming N is large.[15] Therefore, if the interferometer is run with enough Bloch oscillations N, only the second and third Bragg pulses contribute to the total diffraction phase.

The dependence of the diffraction phase on the intensity of the second, third, and last beam splitter is shown in Fig. 2.19 with and without Bloch oscillations. With no Bloch oscillations, $N = 0$, the last pulse intensity has a slightly reduced impact on the diffraction

[15] Although the diffraction phase cancels for the first and last beam splitter in the case of a single atom, transverse motion causes second-order effects when considering the atomic ensemble; see Section 5.4.

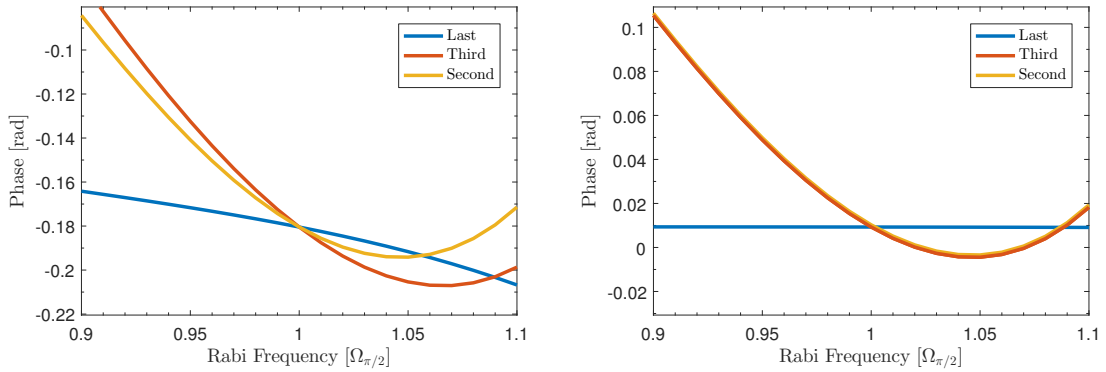

Figure 2.19: The Ramsey-Bordé interferometer diffraction phase as a function of the second, third, or last beam splitter intensity in units of the $\pi/2$ Rabi frequency. Left: An interferometer with $n = 5$ and $N = 0$, Right: The same interferometer with $n = 5$ and $N = 25$ Bloch oscillations. ($\Omega_{\pi/2} = 31.23\omega_r$, $\delta = 10\omega_r$, $\sigma = 0.188\omega_r^{-1}$, $\tau = 3.272\sigma$)

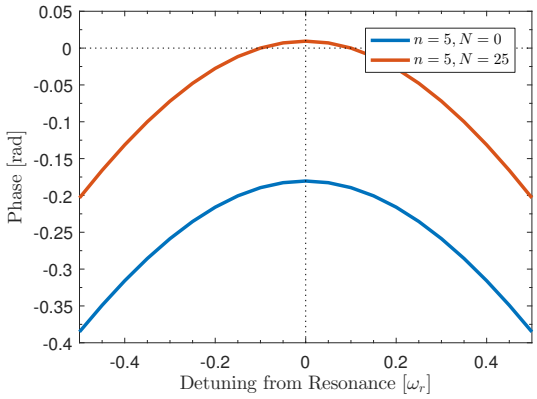

Figure 2.20: The Ramsey-Bordé diffraction phase as a function of the detuning from $n = 5$ Bragg resonance $\delta - 10\omega_r$ (in units of ω_r), with and without $N = 25$ Bloch oscillations. ($\Omega_{\pi/2} = 31.23\omega_r$, $\sigma = 0.188\omega_r^{-1}$, $\tau = 3.272\sigma$)

phase compared to the middle two pulses, but is still significant (2 mrad per percent change in Rabi frequency). When the number of Bloch oscillations is increased to $N = 25$, the intensity dependence of the last pulse all but disappears, with a slope of 10 μrad per percent change in Rabi frequency. Due to the strong dependence on the second and third pulses intensities, it is critical that the two pulses have the same intensity for all experimental configurations (different pulse separation times, etc.) to obtain consistent phase measurements.

The dependence of the diffraction phase on the detuning of the Bragg transition is shown in Fig. 2.20 with and without Bloch oscillations. The change in diffraction phase as a function of the Bragg detuning is similar for Bloch oscillations, with an overall smaller absolute diffraction phase for a given detuning (with the choice of parameters here). The symmetry of the diffraction phase about the Bragg resonance condition $\delta = 2n\omega_r$ turns out

to be incredibly useful. Since the atom velocity is not known to very high accuracy, the exact frequencies needed for resonance are also not well known. By varying the laser detunings and measuring the phase, the resonant frequency can be determined by looking for a phase extremum.

2.5.3 Diffraction Phase

The diffraction phase (2.50) calculated in Section 2.5.2 ends up being a large problem when attempting to measure the recoil frequency ω_r. The parasitic diffraction phases produced by the Bragg interaction adds to the atom's free evolution and laser phase (2.26) to produce a total differential phase of

$$\Delta\Phi = 16n(n+N)\omega_r T - 2n\omega_m T + \phi_0,$$

where ϕ_0 is the diffraction phase. When the modulation frequency ω_m is adjusted to null the interferometer phase $\Delta\Phi = 0$, then the measured frequency is no longer a multiple of the recoil frequency $8(n+N)\omega_r$, but is instead

$$\omega_m = 8(n+N)\omega_r + \frac{\phi_0}{2nT}.$$

Therefore the diffraction phase will shift the measured recoil frequency inversely proportional to the pulse separation time. This is intuitive as the beam splitters are independent of T and increasing the total interferometer phase will decrease the relative size of the fixed diffraction phase ϕ_0.

Since the exact diffraction phase is very sensitive to intensity and detuning, it would be almost impossible to predict ϕ_0 to a high enough accuracy to subtract it from the interferometer phase. Ideally one would just go to a very long pulse separation time T or reduce the diffraction phase such that the error from $\phi_0/2nT$ is below the desired accuracy. For typical parameters of $n = 5$, $N = 25$, and assuming the diffraction phase is zero within an 1σ uncertainty of 5 mrad, then the pulse separation time would need to be larger than 300 ms for a 0.5 ppb measurement of the recoil frequency (which is beyond our capabilities). Instead, the phase is measured at multiple pulse separation times and the value of ω_r is extrapolated by fitting the data and taking the limit as T goes to infinity, which is discussed in more detail in Section 5.2.

Chapter 3

Atomic Source

3.1 Vacuum Chamber

Since the coherence in an atom interferometer depends on it being free from background interactions, the experiment is performed in an ultra-high vacuum (UHV) environment. In order to obtain the vacuum pressures required, the chamber is constructed out of stainless steel and glass, using ConFlat (CF) flanges which are sealed with copper gaskets. The body of the chamber is made of 304 stainless steel components and the optical access is provided by uncoated fused silica view-ports. Besides one custom glass cell, all other components are commercially available to increase the reliability of assembly.

The chamber is evacuated with the aid of a vacuum roughing pump and a turbo-molecular pump to bring the pressure down to 10^{-7} torr, at which point the pressure is limited by the outgassing of volatile materials trapped in the metal surfaces. Since this outgassing rate is proportional to the temperature, the chamber is heated to approximately 200 degrees C. This is accomplished by wrapping the entire vacuum assembly with a resistive heating tape and covering it with layers of aluminum foil, which prevents the heat from escaping and keeps the temperature of the chamber more uniform. The chamber is baked at 200 degrees C for approximately two weeks while the accelerated outgassing is continuously removed with the vacuum pumps. When the chamber is cooled back down to room temperature, the amount of volatile material is significantly reduced and the pressure can now be pumped to below 10^{-10} torr.

Due to significant contaminates from the epoxy used to glue mirrors to the inside of the chamber, our pressure is limited to around 10^{-9} torr. After the baking is finished, the turbo pump is removed to reduce vibrations during the experiment and a Varian 55 l/s ion pump and a titanium sublimation pump are used to maintain the vacuum pressure.

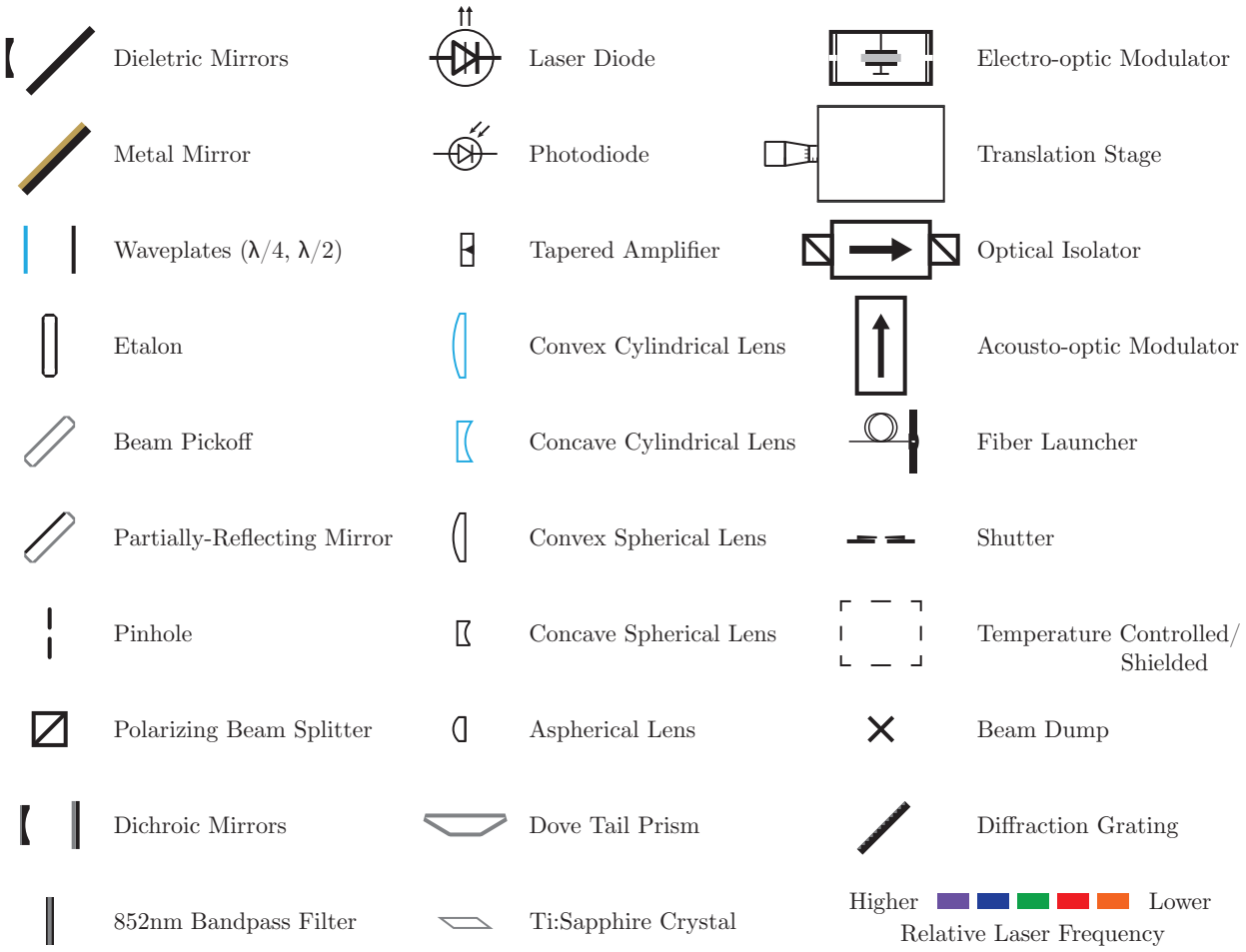

Figure 3.1: Symbols used in the figures detailing the optical setup. Laser colors are shaded based on their relative frequency difference within each figure.

3.2 Spectroscopy

At the heart of an atom-optics experiment is a stable optical frequency that is used for laser cooling and atomic manipulations. One of the more reliable ways to obtain a stable frequency is to perform spectroscopy on an atomic transition. The error signal from the spectroscopy can then be used as feedback to frequency lock a laser which serves as an optical reference. This reference can then be either used directly or shifted to generate other needed optical frequencies.

A simple method to probe the atomic transitions of an atom is to use frequency modulation (FM) spectroscopy [58]. Near-resonant laser light is sent through an electro-optical modulator (EOM) to produce frequency sidebands on the carrier frequency. This modulated light is then passed through a glass cell filled with atomic vapor. If the laser frequency is centered on an atomic transition, some of the carrier will be absorbed (along with equal

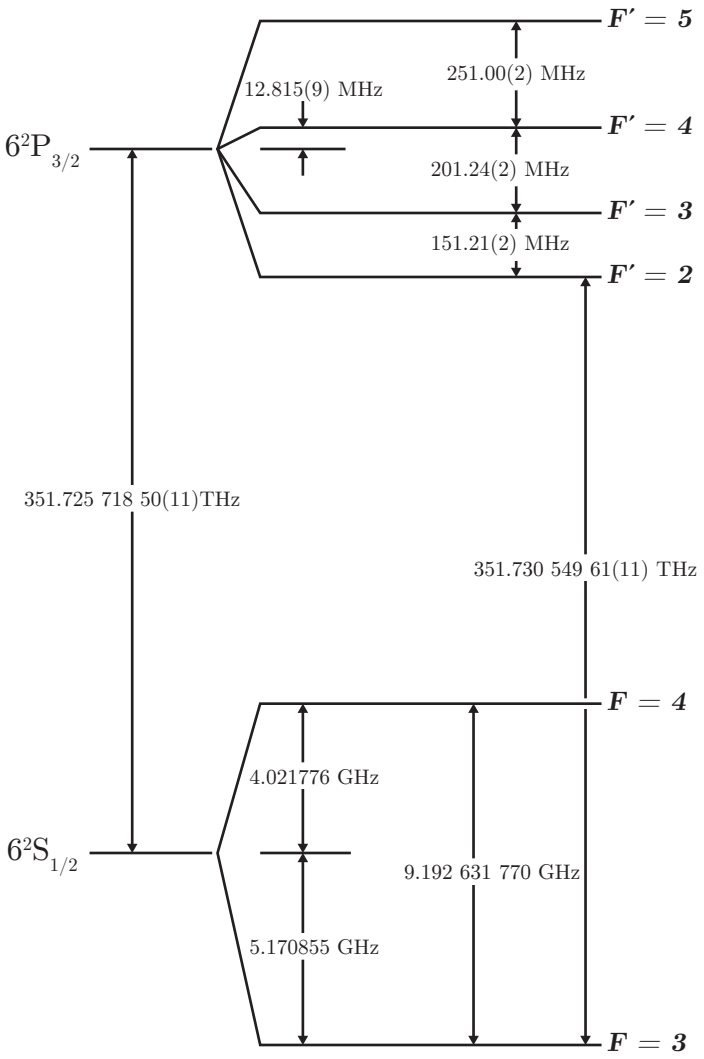

Figure 3.2: Hyperfine structure for the D_2 line of cesium. The hyperfine splitting of the $6^2S_{1/2}$ ground state currently defines the SI second and is therefore exact. The splittings between the $6^2P_{3/2}$ hyperfine states was measured by Tanner and Wienman [56] and the absolute frequency of the $6^2S_{1/2} \rightarrow 6^2P_{3/2}$ was measured by Udem et al. [57] using an optical frequency comb.

amounts of each sideband), which produces no net modulation on the transmitted beam. If the optical frequency is slightly off-resonance, then the sidebands will be absorbed by different amounts, which produces a beat on the transmitted beam. Since the sidebands have different relative phases, the beat signal will change phase depending on which sideband gets absorbed. By detecting and demodulating the transmitted light at the modulation frequency, an error signal is produced that can be used to stabilize the laser frequency. However, since the vapor is at a finite temperature, the hyperfine structure of the atoms can be unresolved due to Doppler broadening of the atomic transitions.

When laser light (the probe beam) is swept across the atom's hyperfine structure, a large Doppler broadened absorption dip is observed in the transmitted beam. To obtain a Doppler insensitive measurement of the hyperfine transitions, a saturation laser beam is passed through the vapor in the opposite direction. When both the saturation beam and the probe are resonant with the same Doppler class of atoms, then the atomic transition will be partially saturated producing a transmission bump on top of the absorption background [59]. These transmission bumps can then be probed by modulating the probe beam and using FM spectroscopy to produce a Doppler-free measurement of the atomic transitions. There are a couple of drawbacks to saturated FM spectroscopy that should be pointed out. First, the modulated probe still produces a Doppler broadened background on top of the Doppler-free signal which causes small offsets of the center frequencies in the error signal. In addition, the EOM can produce amplitude modulation on the probe beam in addition to the desired frequency modulation. Since the amplitude modulation has the same beat frequency as the FM spectroscopy signal, the demodulated signal will cause a DC offset error proportional to the amplitude modulation. For these reasons it is not optimal to use saturated FM spectroscopy for low frequency feedback to the laser, as drifts will cause absolute frequency errors in the lock.

A slightly different spectroscopy method that helps mitigate these problems is modulation transfer spectroscopy [60–62]. A probe laser is passed through the atomic vapor and detected while a modulated saturation beam is sent through from the other direction. When both beams are on Doppler resonance, there is a four-wave mixing process that occurs producing frequency sidebands on the transmitted probe. The probe is then detected and demodulated to obtain a Doppler-free error signal. Since the probe is not FM modulated in this configuration, the detected signal does not have the Doppler background or the amplitude modulation offset and thus produces a mostly drift-free error signal. The downside is that the four-wave mixing process produces a small signal and thus has relatively poor signal-to-noise compared to saturated FM spectroscopy. Therefore it is advantageous to combine the two spectroscopy methods to gain the benefits of both.

The optical setup for the reference laser and the spectroscopy is shown in Fig. 3.3. For the spectroscopy, about 600 μW of optical power is sent into AOM1 and split approximately evenly between the zeroth and minus first order. The minus first order is passed through a glass cell filled with room temperature ^{133}Cs vapor while the zeroth order is modulated by EOM1 and passed through the cell in the opposite direction. The EOM is modulated at 11 MHz using a crystal oscillator amplified by a resonant LC circuit using the intrinsic

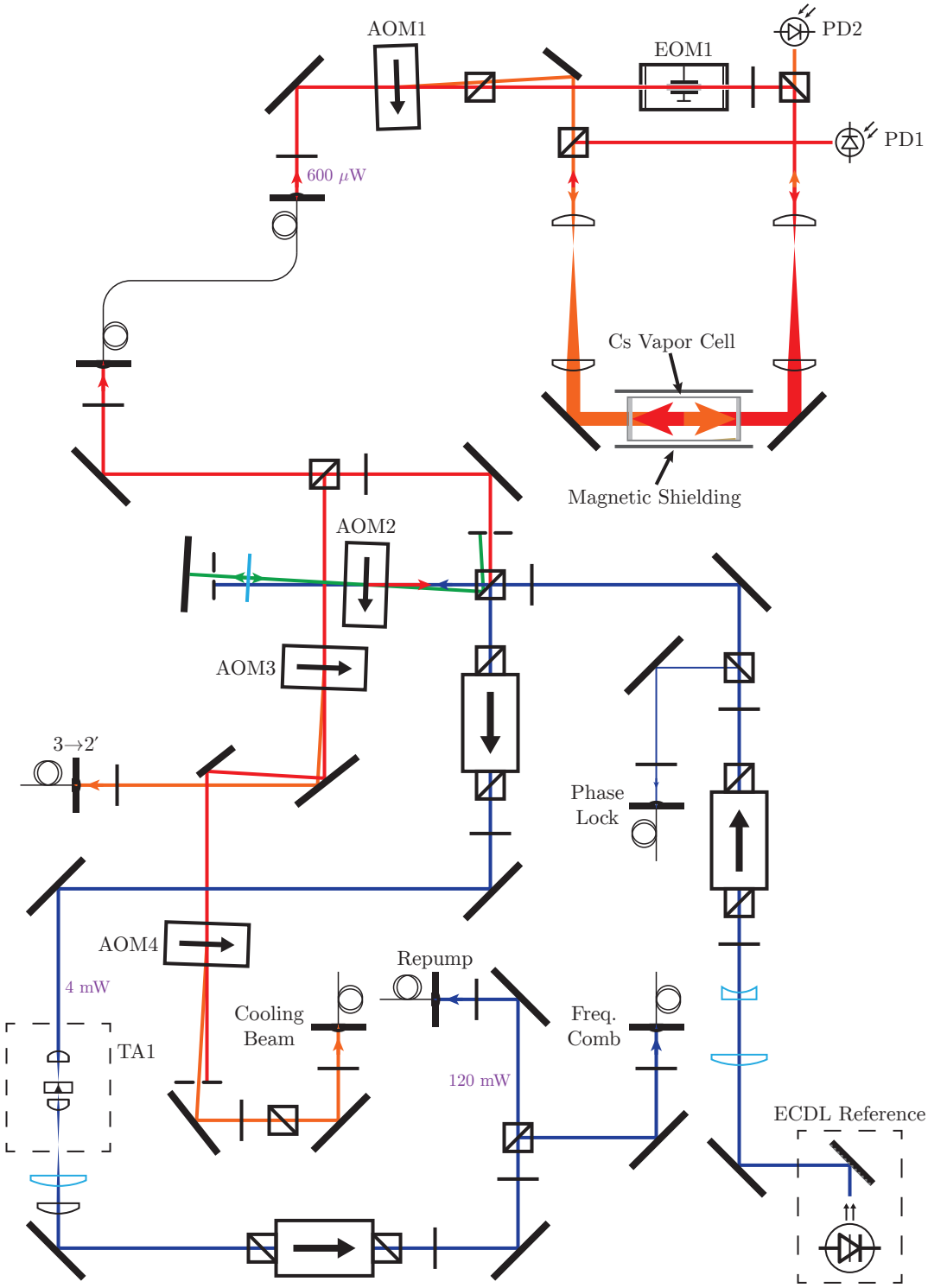

Figure 3.3: Optical setup for the reference laser and cesium spectroscopy.

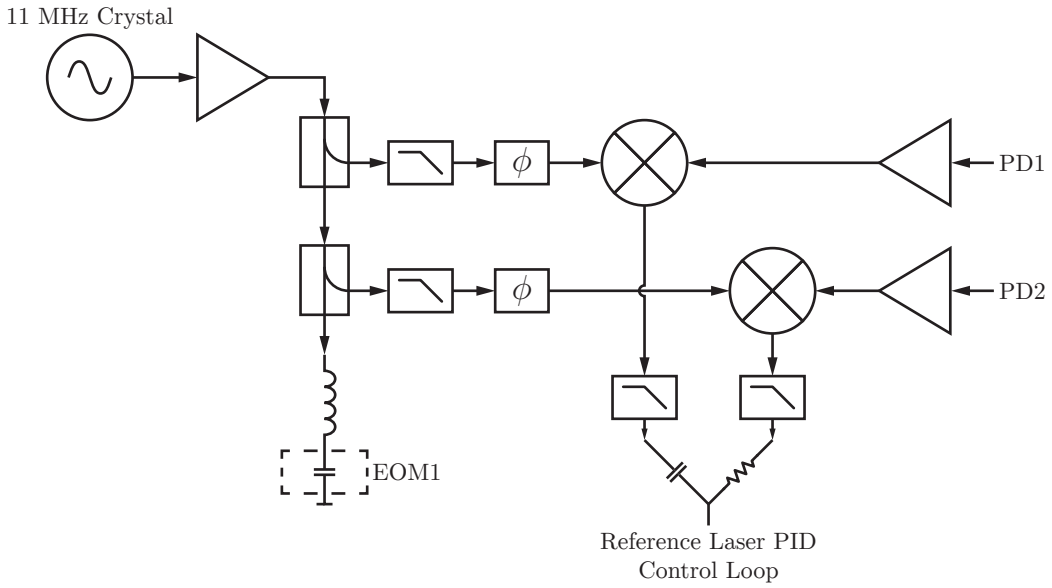

Figure 3.4: Electronics setup for producing the electro-optical modulation frequency and combined error signal from the spectroscopies.

capacitance of the EOM crystal and an external inductor. The saturated frequency modulation spectroscopy and modulation transfer spectroscopy signals are detected by photodiodes PD1 and PD2 respectively and demodulated using the circuit in Fig. 3.4. Variable phase shifters are applied to the demodulation frequencies so that both spectroscopies produce the same sign error signal, allowing the two to be combined. The FM spectroscopy error signal is high-pass filtered and added to the modulation transfer spectroscopy signal to produce a high signal-to-noise and lower drift lock point. The error signal is fed into a proportional-integral-derivative (PID) control loop and used to frequency stabilize a New Focus TLB-6917 external cavity diode laser (ECDL) which serves as the optical reference.

The spectroscopy is locked to the $F = 3 \rightarrow F' = 2$ transition of the D_2 line in ^{133}Cs as shown in Fig. 3.2. Since AOM1 frequency shifts the deflected laser light by -f_{AOM1}, the atoms that are Doppler resonant with both beams see a frequency that is the average of the two. Combined with the double-pass AOM2, the reference laser ends up locked to a frequency $f_{3,2'} + 2f_{\mathrm{AOM2}} + f_{\mathrm{AOM1}}$. Both f_{AOM1} and f_{AOM2} are chosen to be 141.0 MHz so that the reference laser is resonant with the $F = 3 \rightarrow F = 4'$ transition, which is useful for optical trapping. Without being locked, the free running reference laser has a linewidth of 160 kHz, as measured by an optical delay line beat [63]. Unfortunately, the linewidth increases to 180-240 kHz when the laser is locked to the spectroscopy, which is most likely caused by technical noise in the spectroscopy and lock electronics. The long-term stability of the lock is described in more detail in Section 6.1.1.

3.3 Optical Trapping

In order to create an atomic sample with the density and temperature needed for high sensitivity atom interferometry, the cesium atoms must first be trapped and cooled from room temperature. The basis for most optical trapping is an optical molasses [64–66], which consists of two counter-propagating laser fields that are both red-detuned from a cycling transition. When an atom moves in the field towards one of the beams, the frequency of that beam is Doppler shifted closer to resonance, which results in more photons being absorbed and scattered. This creates an effective force in the opposite direction of the atom's motion. When the optical molasses is applied in three dimensions, it can reduce an atom cloud's mean velocity and, therefore temperature, down to the Doppler temperature,

$$T_{\mathrm{D}} = \frac{\hbar\Gamma}{2k_{\mathrm{B}}},$$

limited by by the linewidth of the atomic transition Γ.

Since an optical molasses only provides a velocity-dependent force, there is no spatial confinement of the atoms. An atom will diffuse via a random walk by absorbing photons from all fields and randomly emitting them. To provide a position-dependent force, a quadrupole field is introduced to create a magneto-optical trap (MOT) [67]. The field provides a quantization axis for the atom's magnetic sublevels and shifts their energy by

$$\Delta E_{F,m_F} = \mu_B g_F m_F B_z,$$

where m_F is the magnetic sublevel quantum number, B_z is the strength of the magnetic field, and g_F is the hyperfine Landé g-factor[1] [68]. The gradient provided by the quadrupole field creates a spatially varying Zeeman energy splitting which flips sign through the center of the trap. Consider a transition between two states where g_F is positive for both the ground and excited state, such as the $F = 4 \rightarrow F' = 5$ transition on the D_2 line of ^{133}Cs. As an atom moves out from the center towards increasing magnetic field, $B_z > 0$, the σ^- transitions decrease in frequency. If the molasses light field coming from this direction is σ^- polarized and is red-detuned, this will result in more scattered photons, pushing the atom back towards the center. If the opposing molasses beam is σ^+ polarized,[2] then the atom will be confined at the magnetic zero where all Zeeman levels have the same energy. The density of trapped atoms at the center is ultimately limited by the reabsorption of scattered photons, which causes an outward radiation pressure on the trapped cloud. To limit this effect, one can use a dark-spot MOTs [69, 70] which reduces the amount of time atoms at the center spend in a resonant state by selectively depumping the atoms to a dark state.

While selection rules require the $F' = 5$ excited state to decay back to the $F = 4$ ground state, the finite Lorentzian linewidth of the excited states means there is a small probability

[1] The hyperfine Landé g-factor is equal to $g_F \simeq g_J \left[F(F+1) - I(I+1) + J(J+1)\right] / 2F(F+1)$ where g_J is the fine structure g-factor.

[2] In the other direction, the field is decreasing, $B_z < 0$, and the σ^+ transitions become more resonant.

that the $F' = 4$ state is excited instead. Once the $F' = 4$ state is excited, there is an approximately 50% chance that the atom decays to the dark $F = 3$ ground state where the cooling light is no longer resonant. The number of photons scattered per second by a particular transition is given by

$$R_{F,F'} = \left(\frac{\Gamma}{2}\right) \frac{s}{1 + 4(\omega_L - \omega_{F,F'})^2/\Gamma^2 + s},$$

where $\omega_L - \omega_{F,F'}$ is the detuning between the laser frequency and the atomic transition and $s = I/I_{\text{sat}}$ is the saturation parameter. For nominal parameters of $s \simeq 1$ and a detuning of $\omega_L - \omega_{4,5'} = -3\Gamma$, the relative excitation rate $R_{4,5'}/R_{4,4'}$ means that approximately 400 photons are scattered before the atom falls back to the dark state. To prevent atoms from accumulating in the dark ground state, a small amount of repump light is introduced on the $F = 3 \rightarrow F' = 4$ transition, which allows the atom to eventually decay back to the cooling transition.

3.3.1 2D MOT

In order to have a sufficiently high number of atoms in the chamber to quickly load a magneto-optical trap, the atoms must first be extracted from a reservoir placed in the vacuum chamber. Thermodynamic processes will cause a solid to evaporate until the background vapor pressure is in equilibrium with the condensed state. At room temperature, the equilibrium vapor pressure of solid cesium is approximately 10^{-6} torr [71]. While this is ideal for fast loading of a MOT, the high vapor pressure means that collisions with background gas would limit the coherence of atom interferometry. In order to retain the benefits of a fast MOT loading rate while having a much lower vacuum pressure, the main three-dimensional MOT is loaded by a two-dimensional MOT [72] instead of from background atoms.

The two-dimensional MOT cell is separated from the ultra-high vacuum main chamber by a differential pumping tube, as shown in Fig. 3.8, which creates a pressure differential by restricting the conductance of particles between the two regions. This allows the atoms to be loaded from a high background pressure vapor while still maintaining the low pressures needed in the experiment. In the ultra-low vacuum, molecular-flow regime, the conductance of a tube is given by

$$C = \frac{D^3}{6L}\sqrt{\frac{2\pi k_{\text{B}} T}{m}},$$

where D is the diameter and L is the length of the tube and m is the mass of the particle flowing through the tube. If the pressure of the 2D MOT cell is p_{cell}, then the pressure on the other side of the differential pumping tube will be

$$p = \frac{C(p_{\text{cell}} - p)}{S} \approx \frac{C p_{\text{cell}}}{S}$$

when pumped at a rate S [73]. The differential pumping tube used in the experimental setup has a diameter of 5 mm and a length of 14 cm. When considering the partial pressure of cesium in the cell, the pressure reduction should be approximately 1/1000 when the chamber is pumped at a rate of 55 l/s by the Varian ion pump. This is slightly lower than what is measured, but the vacuum chamber mostly likely has other contaminants that contribute to the final vacuum pressure.

In order to transport cesium atoms through the differential pumping tube, a 2D MOT is used to create a cooled atomic beam. Unlike a 3D MOT where all three dimensions are spatially confined, a 2D MOT only confines in two directions, allowing the trapped atoms to diffuse out the ends of the trap. The transversely cooled atoms will have a relatively low divergence angle upon exiting the trap, allowing the atom beam to pass through the differential pumping tube without a significant reduction in flux.

The reference laser frequency $f_{3,4'}$, described in Section 3.2, is used as the optical repump and as the basis for the cooling transition. The optical setup used to create the required 2D MOT frequencies are shown in Fig. 3.3 and Fig. 3.5. Approximately 4 mW of reference light is split and sent through a secondary optical isolator[3] and into a tapered amplifier (TA1), which amplifies the input to about 120 mW of $f_{3,4'}$ light. After coupling the majority of the light into a fiber (Fiber:Repump, where the Fiber:X notation corresponds to the fiber labeled X in the figures), the light is transported to another part of the table to serve as the MOT repump light and as the frequency reference for the cooling transition. The output of the fiber contains roughly 80 mW of laser light that is further split between the 3D MOT repump (minus first order of AOM5), the 2D MOT repump, and the fiber coupled electro-optical modulator (EOM2).

The cooling frequency should be slightly red of the $f_{4,5'}$ transition and therefore the $f_{3,4'}$ light needs to be shifted by a little more than the hyperfine splitting to have the correct frequency. To accomplish this, EOM2 is driven by 9.21 GHz to generate frequency sidebands on $f_{3,4'}$. The carrier and blue sideband are then filtered out by a passively temperature controlled etalon. The etalon is double passed to increase the filtering and to reduce the alignment sensitivity to tuning angle. Additionally the etalon is angled such that the reflections do not couple back into the fiber. The etalon has a thickness of 5 mm and a reflectivity of 85% and, therefore, has a linewidth of 1 GHz which is large enough that no active stabilization is required to keep the etalon resonant. The filtered light is further frequency shifted down twice by an acousto-optical modulator (AOM6) running at 130.4 MHz to a final frequency of $f_{4,5'} - 7.6$ MHz and coupled into a fiber.

The light out of the fiber is then sent into the rejection port of an optical isolator and coupled into a QLD-850-150S laser diode (LD1). If the free running laser diode has a wavelength close to that of the coupled light, then only a small amount of light is required to force the laser cavity to oscillate at the injected frequency in a process called injection locking [74]. This is a useful technique to make a laser run single mode without using a

[3]The isolator is needed to prevent the spontaneous emission of the tapered amplifier from disrupting the spectroscopy and laser lock.

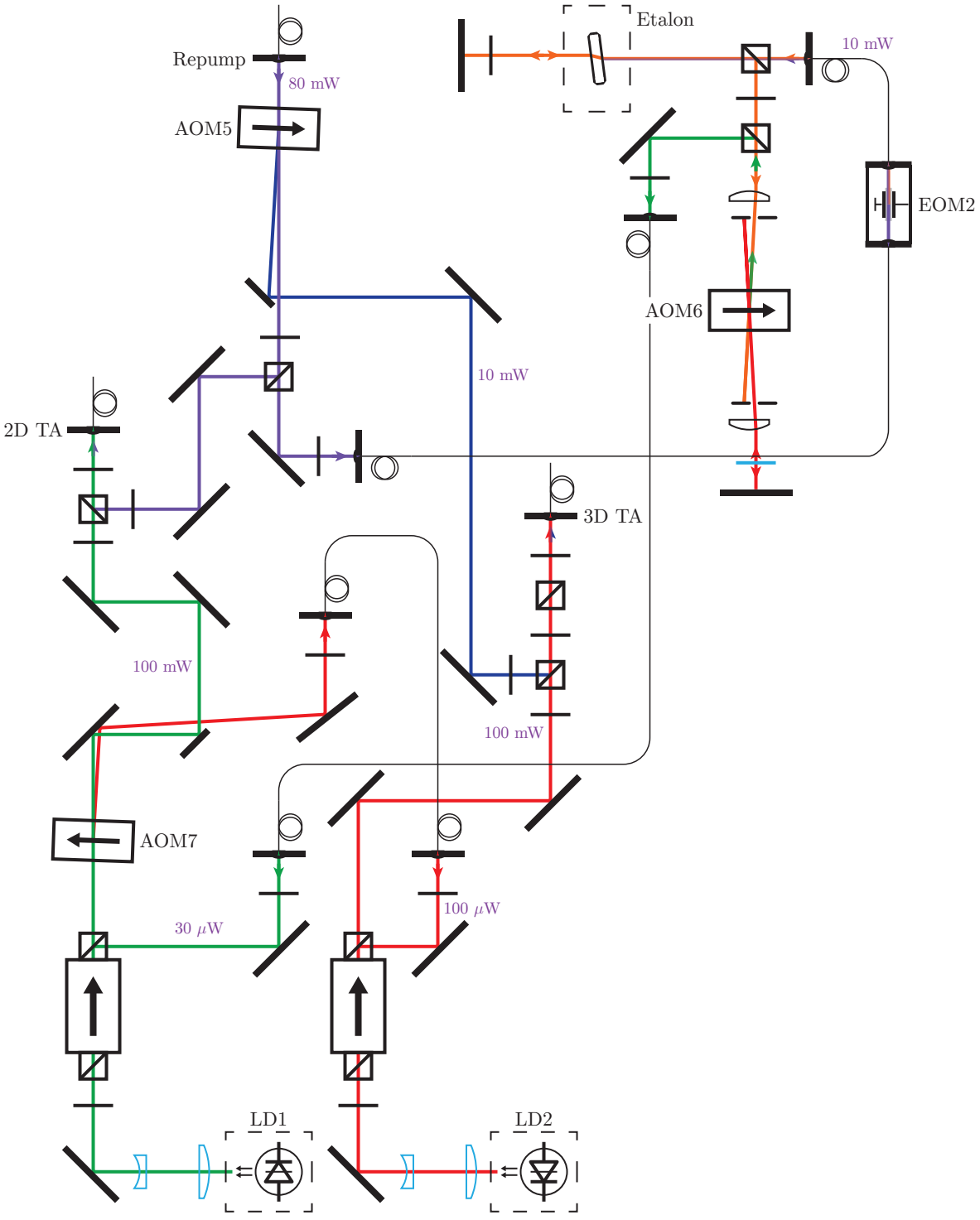

Figure 3.5: Optical setup for the magneto-optical trap frequency generation and laser injection locks.

more complex external cavity diode laser. The injection lock works optimally when the temperature is tuned such that the free running wavelength is within 1 nm of the injected wavelength. Additionally, adjustments to the diode current change the cavity length and allow the injected light to have a larger coupling efficiency. Approximately 30-50 μW of optical power is used to inject LD1 and the diode current wherein the laser is locked has a range of nearly 1 mA. By running the diode at the center of the current range, small fluctuations in air temperature and injection power will not perturb the lock, which makes the technique fairly robust as a passive lock.[4] Additionally, the injection frequency can be changed by a fairly large amount before the lock fails, which allows for frequency switching of the injected frequency.

A small amount of optical power from the output of LD1 is picked off by AOM7 to be used as another injection lock, while the majority of the power is coupled into Fiber:2D TA and sent to the setup in Fig 3.6. Overlapped on this fiber with the opposite polarization is a small amount of repump light from Fiber:Repump. Approximately 50 mW of combined cooling and repump light from the fiber output is split 50:50 and amplified by two EYP-TPA-0850-00500 tapered amplifiers (TA2 and TA3) running at 2.5 amps to a total power of 600-800 mW. The TA outputs are shaped with cylindrical lenses to an aspect ratio of 4:1 and enlarged to fill the glass cell. Dove prisms are used to rotate the orientation of the elliptical beams to match the rectangular cell and $\lambda/4$ waveplates make the beams circularly polarized. Although the ratio of cooling and repump light is around 10:1 at the input of the TA, the nonlinear amplification by the TA chip makes the final ratio difficult to estimate. Instead, the amount of repump in the 2D MOT is optimized by experimentally varying the amount of repump overlapped with the cooling light at the polarizing beam splitter cube with a $\lambda/2$ waveplate.

The field needed for the 2D MOT field is generated by two pairs of anti-Helmholtz coils placed around the cell's four rectangular windows. Each coil has 120 turns and is independently run at 1.6 amps. At the center of the cell, the four rectangular coils can be approximated by eight infinite wires, which gives a magnetic gradient of

$$\frac{\partial B_r}{\partial r} = \frac{\mu_0 n I a b}{\pi (a^2 + b^2)^2},$$

where n is the number of turns, I is the current, $2a$ is the coil pair separation and $2b$ is the diameter of the coil on the minor axis. The coils in the experiment have $a = 3.8$ cm and $b = 3.2$ cm which gives a field gradient of approximately 10 G/cm. In general, the 2D MOT is fairly unoptimized with a trap light detuning of -7.5 MHz and an intensity of around 3 mW/cm^2, but the parameter combination works well enough for our purposes.[5] One critical optimization is the alignment of the 2D MOT axis with the differential pumping

[4]Temperature stabilization/shielding and alignment are fairly critical for reliable operation. Alignment can be accomplished by sending the small amount of parasitic light that comes out of the rejection port of the isolator and coupling it back into the fiber. Coupling efficiencies of 50% are fairly typical.

[5]Curiously, previous configurations used only 0.8 amps in each coil which gives a field gradient that is more consistent with the observed optimal 3D MOT detuning and gradient.

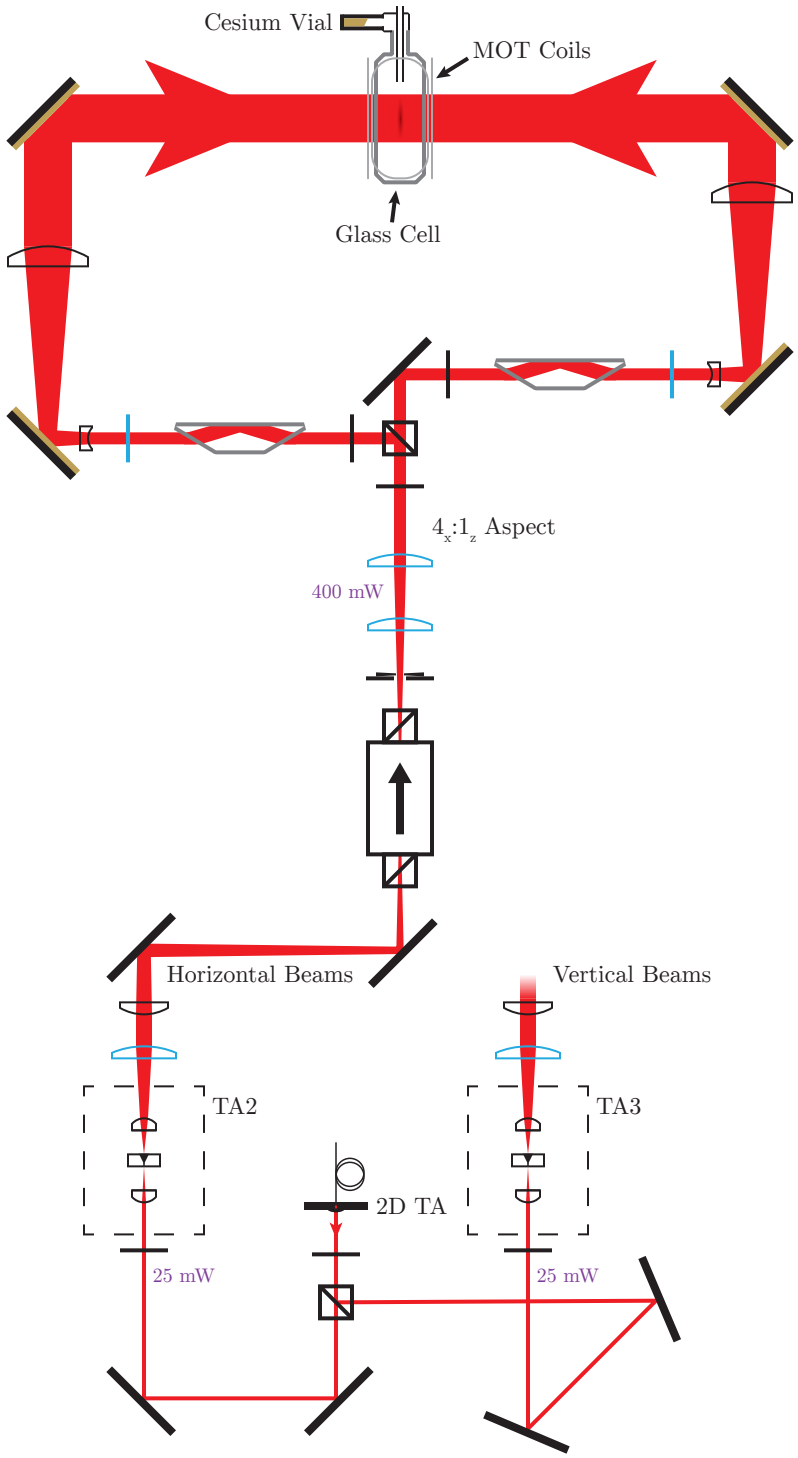

Figure 3.6: Optical setup for the two dimensional magneto-optical-trap.

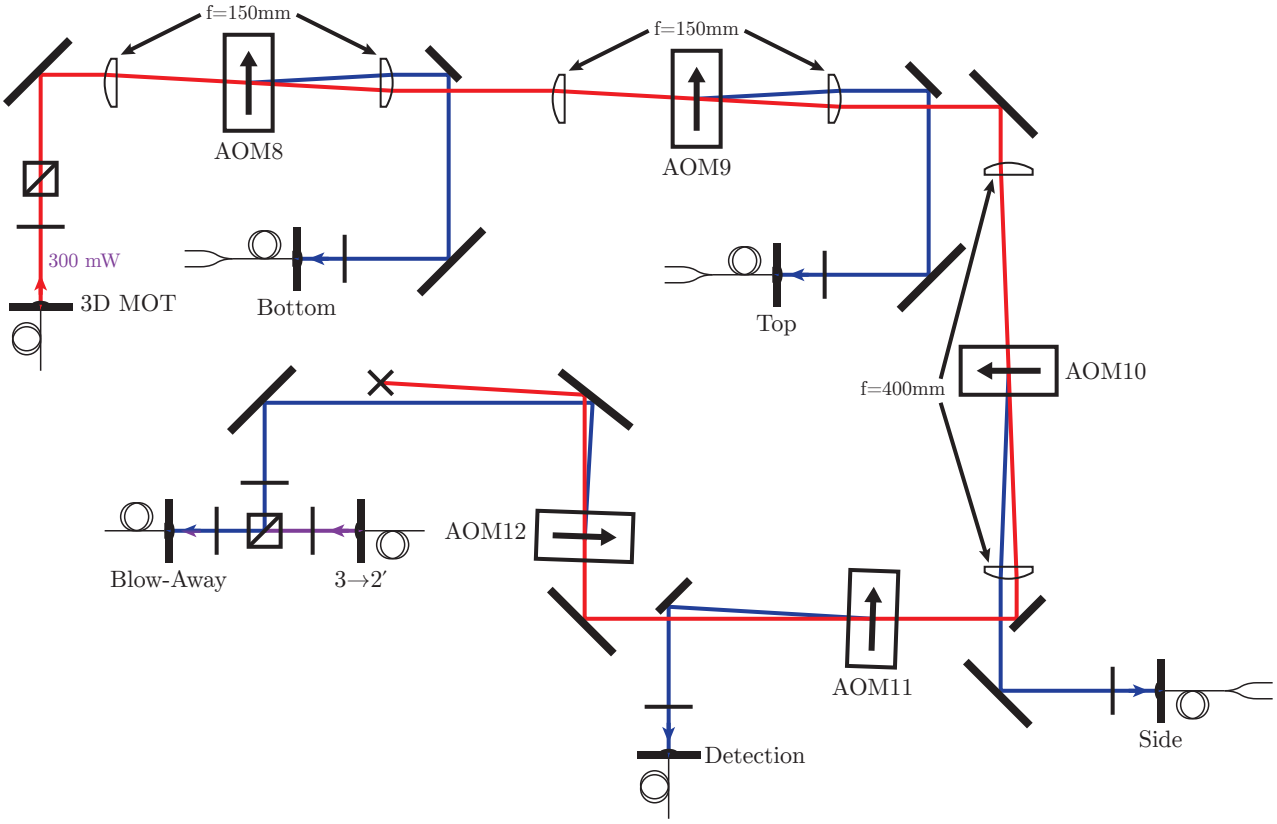

Figure 3.7: Optical setup for the three dimensional magneto-optical-trap and moving molasses launch.

tube which can be tuned by changing the power balance of the cooling beams and adjusting the difference in currents between the coils.

3.3.2 3D MOT

The two-dimensional MOT described above then allows for efficient collection of cesium atoms in the experiment's three-dimensional MOT while maintaining an ultra-high vacuum environment. The laser frequencies needed for the 3D MOT optics are similar to that of the 2D MOT and are generated by the optical layouts shown in Figures 3.5 and 3.7. The red-detuned trap light $f_{4,5'} - 7.6$ MHz from LD1 is frequency-shifted down by AOM7 running at 87.9 MHz and sent into a fiber to facilitate injection locking a second QLD-850-150S laser diode (LD2). Similar to LD1, approximately 100 μW of laser light is coupled into LD2 through the rejection port of the optical isolator giving the laser a current lock range of 2 mA. The double injection lock scheme (LD1 into LD2) has the benefit of further filtering of LD1's output frequency spectrum, which could still have small unfiltered components left over from the carrier and sidebands of EOM2.

The laser light from LD2 is overlapped on a polarizing beam splitter (PBS) cube with some repump light that was deflected by AOM5 running at 80 MHz. The two overlapped, oppositely polarized beams are then rotated and projected onto a second cube to give them the same polarization so they can be amplified by a Dilas TA-0850-2000 tapered amplifier (TA4) shown in Fig. 3.15. The input power to TA4, containing approximately 20 mW of trap light and 2 mW of repump light, is amplified to a total of 1.3 W when the TA is running at 3 amps. The tapered amplifier has two important protections which help extend the lifetime of the diode. First, the output of the TA is sent through an optical isolator to prevent parasitic reflections from coupling back into the amplifier. The input facet has a damage threshold of 50 mW and therefore even a small amount of light when amplified going backwards through the system could easily damage the front facet and destroy the chip. Additionally, since the TA chip dissipates a significant amount of its power in the optical field (25%), blocking the seed light could thermally damage the chip. To prevent this from happening, a small amount of light is picked off the TA input using a glass plate and sent to an interlock diode (PD3). When the diode detects a drop in optical power, the MOSFET supplying current to the TA chip is shut off to prevent excess heat from being generated.

The light from TA4 is coupled into a fiber for mode filtering which gives a total usable power of 600 mW. For normal MOT operation, the light is then directly coupled into a second fiber (Fiber:3D MOT) to be used for the six MOT beams. The fiber output containing 300 mW of combined power is then sent through three acousto-optical modulators in series (AOM8-10) which will provide power to the bottom, top, and side MOT beams. All three AOMs are driven at 80 MHz bringing the repump back onto resonance and the trap light to 15.5 MHz red-detuned from $f_{4,5'}$. The light from each AOM is coupled into a fiber splitter and delivered to the main vacuum chamber as six separate beams (as shown in Fig. 3.8), each containing 25 mW of power. The power balance of the splitters is not perfect and varies between 5-10%, but can be slightly compensated with adjustments to alignment and polarization of the MOT beams. Each of the six beams is expanded to a waist of 1.6 cm to give an intensity of roughly 5-6 saturation intensities.[6] A $\lambda/4$ waveplate before each telescope converts the linear polarization out of polarization-maintaining fibers to the circular polarization needed for the MOT.

The three-dimensional MOT quadrupole field is generated by two large, 60 turn coils in an anti-Helmholtz configuration. The coil itself is made out of 6.35 mm thick square hollow core copper wire, which allows water cooling to run through the length of the coils. The field gradient generated by an anti-Helmholtz pair is approximately given by

$$\frac{\partial B_z}{\partial z} \cong 3\mu_0 nI \frac{DR^2}{(D^2+R^2)^{\frac{5}{2}}}$$

along the coil axis, where $2D$ is the coil separation and R is the coil radius [75]. The

[6]For the cesium cycling transition of $F = 4, m_F = \pm 4 \rightarrow F' = 5, m_F = \pm 5$, I_{sat} is approximately 1.1 mW/cm^2.

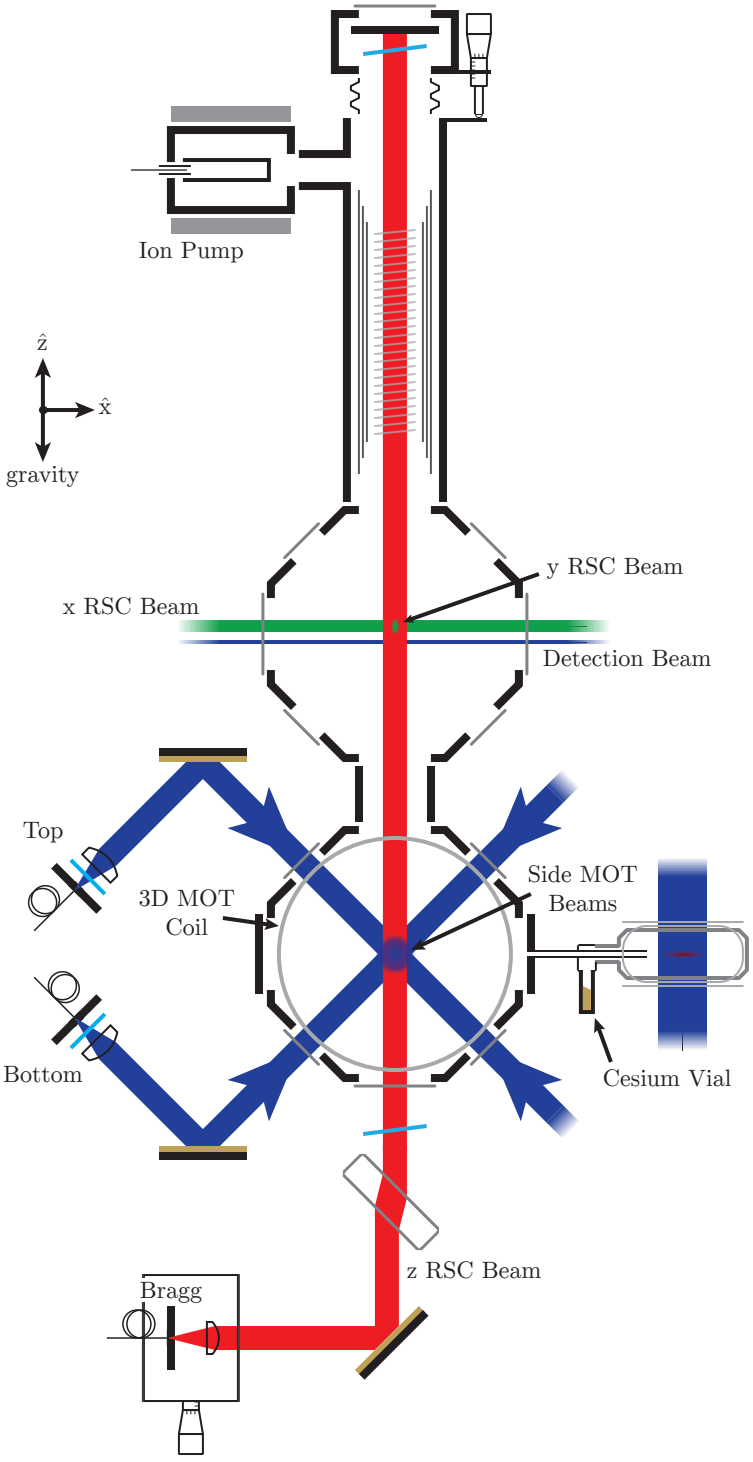

Figure 3.8: Optical setup relating to the vacuum chamber for the MOT beams, Raman sideband cooling beams, and detection beam.

field along the radial direction is simply half that of the axial direction. The coils in the experiment have a radius of 8.9 cm and a half separation of $D = 12$ cm, which when driven in series with 30 amps give a field gradient of 8.6 G/cm.

In a typical experimental run, the 3D MOT is loaded for 0.99 s, at which point the light for the 2D MOT (TA2-3) is shut off with two mechanical shutters. This allows the atoms in the 3D MOT to come into equilibrium without the introduction of new hot atoms from the atomic beam. It is estimated that the MOT loads between 10^9 and 10^{10} atoms; however the exact number was never calibrated.

3.3.3 Optical Molasses

Once the 3D MOT has been loaded with atoms for 1.00 s, the large magnetic field from the coils is shut off by turning off two 100 amp MOSFETs which act as switches for the MOT supply current. As the vacuum chamber is made primarily of steel, the large change in magnetic flux from shutting off the coils induces eddy currents in the chamber walls that last for many milliseconds. These eddy currents generate secondary magnetic fields and field gradients which would interfere with the cooling stages that come after the MOT. Therefore a molasses is kept on for 30 ms to prevent the atoms from escaping the trap region while the eddy current fields decay. This stage does not need to be optimized at all for temperature as the moving molasses launch that follows the will heat the atoms.

3.4 Atomic Fountain

In order to gain a longer force-free interaction period for interferometry measurements, the atoms are launched into the vacuum chamber as an atomic fountain. This increases the free-fall time by a factor of two (over a simple drop given the same chamber dimensions), at the cost of a higher experimental complexity. The easiest method to create an atomic fountain is with a moving molasses [76] which can be accomplished by slightly modifying the optical molasses setup in Section 3.3.3. Other methods of launching atoms such as with Raman sideband cooling [77] and optical lattices [78–80] have the benefit that they can simultaneously cool (or at very least not heat) the atom sample, but have diminished efficiency in our experiment since the lattices must be retro-reflected due to limited optical access. A retro-reflected lattice configuration which accelerates atoms from rest would also include a lattice traveling in the other direction, which would transport atoms in the wrong direction.

When an atom is cooled in a red-detuned one-dimensional optical molasses, the equilibrium point for the atom is when the scattering from the counter-propagating beams are balanced. If one of the molasses beams is increased in frequency while the other is decreased, then the atom will experience an effective force from the more resonant laser field as the atom begins to scatter more photons. As the atom increases in velocity, the two molasses

beams will be Doppler shifted, $f' = (1 + v_z/c)f_{\text{trap}}$, until the atom is at a velocity where the two molasses beams have the same apparent detuning in the frame of the atom.

For a cross configuration where the two upper molasses beams are pointing down at ± 45 degrees and the two lower beams are counter-propagating to the upper beams, then the vertical equilibrium velocity v_z is equal to

$$(1 - \frac{v_z}{\sqrt{2}c})(f_{\text{trap}} + \epsilon) = (1 + \frac{v_z}{\sqrt{2}c})(f_{\text{trap}} - \epsilon),$$

which simplifies to $v_z = \sqrt{2}c\epsilon/f$, where 2ϵ is the frequency difference between the upper and lower beams and c is the speed of light. The factor of $\sqrt{2}$ is due to the Doppler shift only applying to the velocity component along the 45 degrees beams. For a cesium trap frequency near the cycling transition frequency of $f_{4,5'}$, the moving molasses launch gives a launch velocity of approximately 1.2 m/s $\times$ (ϵ/MHz).

While an optical molasses has a theoretical cooling limit of the Doppler temperature, a subtle cooling mechanism called polarization gradient cooling [81–84] helps significantly decrease the final atom fountain temperature. For a one-dimensional optical molasses with counter-propagating beams along the z-axis and orthogonal $\sigma^+\sigma^-$ polarization, the electric fields interfere locally to create a linear polarization pointing in the x-y plane. In addition, the angle of this local polarization rotates along the z-axis linearly with the z-coordinate. If the external magnetic field is zero, then the polarization of the optical field defines a quantization axis for the atom's magnetic sublevels. As an atom travels along the z-axis in which the polarization rotates, the m_F quantum number is no longer a conserved quantity and therefore the magnetic sublevel populations will mix.

The energy of each magnetic sublevel in the absence of external fields is given by the ac-Stark shift caused by the molasses light fields. The energy shift to the ground state[7] magnetic sublevels caused by a red-detuned laser beam is given by

$$\Delta E_{m_F} = \sum_{m'_F} \frac{\hbar}{2} \left(\left[C^2_{m_F,m'_F} \frac{I}{I_{\text{sat}}} \frac{\Gamma^2}{2} + \Delta^2 \right]^{\frac{1}{2}} - \Delta \right),$$

where C_{m_F,m'_F} is the Clebsch-Gordan coefficient between ground and excited state and Δ is the single photon detuning [82, 85]. This creates a parabolic energy shift on the magnetic sublevels, with the $m_F = 0$ state having the lowest energy. As an atom is excited by the $\sigma^+\sigma^-$ polarized light, the atom will tend to decay into a lower $|m_F|$ state, reducing the atom's total energy. As the atom moves along the z-axis and the sublevels mix, the atom will gain potential energy since the populated low energy $|m_F|$ states mix into higher energy sublevels. The atom is then pumped by the field back into a lower energy sublevel removing energy from the system and, thus, cooling the atom.

Polarization gradient cooling only works if the rate at which the atom is pumped is much slower than the time it takes for the states to mix, otherwise the magnetic sublevels

[7]The shift to the excited state is equal to $\Delta E_{m'_F} = \sum_{m_F} \frac{\hbar}{2} \left(- \left[C^2_{m_F,m'_F} \frac{I}{I_{\text{sat}}} \frac{\Gamma^2}{2} + \Delta^2 \right]^{\frac{1}{2}} - \Delta \right)$.

adiabatically follow the polarization and energy is lost. Therefore the time it takes for an atom to travel a quarter optical wavelength,[8] $\tau_v = \lambda/4v$, should be much longer than the pump time

$$\tau_{\rm sc} = R_{\rm sc}^{-1} = \left[\left(\frac{\Gamma}{2}\right)\frac{s}{1+4(\Delta/\Gamma)^2+s}\right]^{-1},$$

which gives a bound on the one-dimensional temperature of

$$T_{\rm pgc} > \frac{m}{k_{\rm B}}\left(\frac{s\Gamma\lambda}{8(1+4(\Delta/\Gamma)^2+s)}\right)^2,$$

where λ is the wavelength of cooling light, m is the mass of the atom, and $s = I/I_{\rm sat}$ is the saturation parameter. Since the minimum temperature is inversely proportionally to the scattering rate $R_{\rm sc}$, polarization gradient cooling works better when lowering the intensity and increasing the detuning compared to a molasses.

Even though the polarization gradient cooling (PGC) mechanism applies in the moving optical molasses and in the magneto-optical trap [86], the optimal parameters for PGC are very different. The MOT is generally optimized for loading rate, while the moving molasses needs to change the trapped atom's velocity very quickly for an efficient launch since the beams have finite size. For this reason the PGC is generally applied as a second stage during the launch and not combined with the moving molasses.

3.4.1 Moving Molasses

After holding the trapped atoms in the optical molasses for 30 ms, the magnetic fields are sufficiently small to proceed with the moving molasses launch. It is important to minimize the stray fields in the molasses region since magnetic gradients will apply a force on the atom's magnetically sensitive sublevels which could interfere with the launch direction. In addition, the polarization gradient cooling applied immediately afterwards requires a zeroed magnetic field.

The moving molasses uses the same optics as for the stationary molasses, with the frequency of the top and bottom molasses beams shifted by the acousto-optic modulators in Fig. 3.7. The top molasses beams are frequency shifted $-\epsilon$ MHz by changing AOM8 from 80 MHz to 80 MHz $-\ \epsilon$, while the bottom beams are shifted by $+\epsilon$ MHz using AOM9. In order to shift the frequency of the AOMs using a single turnable source, a direct digital synthesizer (DDS) frequency generator is combined with a 80 MHz crystal source as shown in Fig. 3.9. Both the 80 MHz crystal and the launch shift frequency ϵ are split into quadrature components and mixed to create a pair of frequencies at 80 MHz $+\ \epsilon$ and 80 MHz $-\ \epsilon$. The two outputs are filtered with phase-locked voltage controlled oscillators and amplified before driving the acousto-optic modulators. The phase-lock loop allows a smooth transition between the 80 MHz frequency of the stationary molasses and the shifted frequency of the

[8] At higher velocities, the Doppler molasses cooling mechanism takes over.

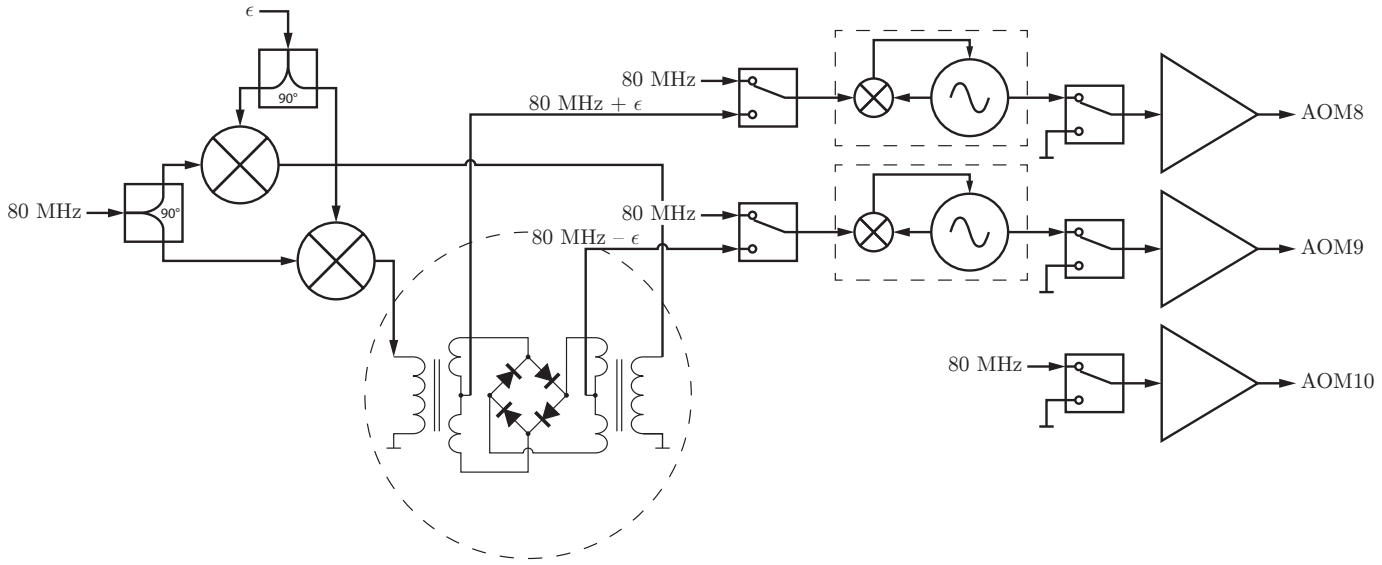

Figure 3.9: The electronics used to switch from the stationary optical molasses to the moving molasses launch. The dashed circle is a modified double balanced mixer with both IF port outputs and the dashed rectangles are phase-locked voltage controlled oscillators.

moving molasses. Additional tunable attenuators (not shown) before the amplifiers allow for adjustment of the AOM RF power to tune the deflection efficiency and balance the three beam pairs.

For the cross configuration used in the experiment, a typical shift of $\epsilon = 4$ MHz gives a moving molasses traveling at approximately 4.8 m/s vertically. This gives one second of free-fall time, 500 ms of which are inside the magnetically shielded interferometer region. One important factor to take into account when changing the frequency of an acousto-optic modulator is the change in deflection angle. The angle between the zeroth order and the plus/minus order is given by

$$\theta_a = \frac{\lambda f_a}{V_a},$$

where λ is the wavelength of the laser light, f_a is the AOM driving frequency, and V_a is the speed of sound in the AOM crystal [87]. Since the outputs of AOM8 and AOM9 are fiber coupled, a change in the drive frequency will cause the deflection angle to also change, reducing the fiber coupling efficiency. If the divergence of the Gaussian beam, $\theta \simeq \lambda/\pi w_0$, at the center of the AOM crystal is much larger than the change in deflection angle, then the two beams are indistinguishable and will have approximately the same coupling efficiency. Therefore the waist of the laser beam should be focused to

$$w_0 \ll \frac{V_a}{\pi\epsilon}$$

at the center of the AOM for optimal coupling. The modulators in the experiment use TeO_2 crystals[9] and therefore a 4 MHz frequency shift requires a waist of much less than 300 μm. A smaller waist also decreases the maximum deflection efficiency of the acousto-optic modulator, so a compromise must be made when designing the optics. Both AOM8 and AOM9 use a $f = 150$ mm telescope to focus the laser at center of the crystal, as shown in Fig. 3.7, which gives a waist of approximately 80 μm. The side MOT/molasses beams created by AOM10 do not need to change in frequency and therefore are created with a $f = 400$ mm telescope, which gives a waist closer to 200 μm.

The coupling efficiency for the shifted beams are still not perfect and differ by about 10% when optimized for one of the frequencies. To make the coupled power for both frequencies the same, the fiber coupling is optimized by switching between the two frequencies and aligning the fiber such that both frequencies have the same coupling loss.

3.4.2 Polarization Gradient Cooling

After 2 ms in the moving molasses, the laser intensity is reduced and the detuning is increased to cool the atoms with polarization gradient cooling. The detuning is increased from -15.5 MHz to -44.3 MHz by changing the frequency of AOM7 to 116.0 MHz. The change in deflection angle caused by the frequency switch is compensated by the double-pass AOM configuration [88]. Additionally, the injection lock of LD1 is mostly insensitive to small changes in optical power which facilitates switching between different laser detunings.

The intensity of the molasses beams is also reduced by a factor of 2-3 to further reduce the atom temperature. While one option to lower the intensity is to reduce the drive power to AOM8-10, this has the disadvantage that the three modulators are in series. Thus reducing the deflection efficiency on one increases the power deflected by those downstream. Instead, the current to TA4 is reduced to decrease the overall amplification of the molasses light. In order to protect the TA chip from current spikes during switching, a MOSFET is driven in parallel with the TA diode. During normal operation, the transistor is switched off allowing all the current to run through the diode. When the gate of the MOSFET is driven slightly open, current is drawn from the current source, thereby reducing the current available to the TA. The gate voltage of the MOSFET is controlled by a DDS arbitrary waveform generator which allows the intensity reduction to be programmed and ramped.

The polarization gradient cooling stage lasts for 1 ms, at which point the intensity is ramped off adiabatically in 500 μs by reducing the TA current to zero. This further cools the cloud by adiabatically releasing the atoms from the moving molasses lattice [89]. In the end, the final temperature of the atom sample is 1-2 μK as measured by time-of-flight, as described in Section 3.5.1.

It is fairly critical that the magnetic field be zeroed for the PGC cooling to work well; therefore, three orthogonal Helmholtz coil pairs are placed around the main chamber which are used to trim any residual magnetic fields. The bias coils need to be tuned often as the

[9] Speed of sound in TeO_2 is 4200 m/s.

stray magnetic fields in the lab can change as equipment is moved and nearby experiments modify their setup. Additionally, the ion pump which is used to maintain the UHV is placed as far away from the MOT region as possible since it contains large permanent magnets which generate magnetic fields/gradients in region surrounding the pump.

3.5 Detection

As the atoms are launched vertically through the vacuum chamber, they pass twice through a detection region that can be used to measure the interferometer outputs as well as characterize the atom cloud. Since the sample can expand considerably during the free-fall time, the final density can be quite low and therefore a sensitive detection scheme is needed to measure the atoms. As the atoms fall through the detection region, they are illuminated by a sheet of laser light perpendicular to the atom's trajectory as shown in Fig. 3.8. The light sheet is resonant with a cycling transition of the atoms, causing the atoms to scatter photons isotropically which are collected by a lens system and either imaged onto a camera or detected by a photodiode/photomultiplier tube.

Even though a camera has the advantage of spatial resolution, it ends up being less practical than a simpler photodiode setup. This is mainly due to the low cloud density which gives a poor per-pixel signal-to-noise. This can be overcome somewhat by binning the camera pixels, but still requires image quality optics which are expensive and difficult to make as large as simple collection optics. Additionally, the atom cloud is traveling quite fast through the detection region (approximately 4 m/s), which will blur the image vertically even for short exposure times. Complicating matters further, the different interferometer outputs are spatially separated by several centimeters, making it hard to image everything onto a single CCD. Therefore a simple photodiode setup is used in combination with fairly large condenser lenses as shown in Fig. 3.10.

A pair of large 100 mm diameter, $f = 100$ mm lenses collect the atomic fluorescence and focus the light onto a FDS100 silicon photodiode (PD4) which is amplified with a transimpedance amplifier [90]. Since the photodiode does not have the inherent spatial selectivity of a camera image, spatial filtering techniques are used to detect only the central atoms in the cloud (which will be important for systematics, see Section 5.4.2). A pinhole is placed at the focal plane of the condenser lens system using a 3-axis translation stage to limit the x-z components of the detected fluorescence. The transverse component is also filtered to a lesser extent since the focal point varies with z positions in the cloud and some of the diverging light is blocked. To increase the y-axis and z-axis selectivity, the 3.9 mm waist detection beam is truncated with a rectangular pinhole to approximately 4 mm $\times$ 600 μm (which also increases the intensity uniformity across the light sheet).

The detection light is resonant with the $F = 4 \rightarrow F' = 5$ cycling transition and is derived from the same light as the trapping light for the magneto-optical trap and molasses. To switch on the detection light, acousto-optical modulators AOM8-10 are switched off and AOM11 is turned on, diverting light to the detection fiber. Since intensity noise on the

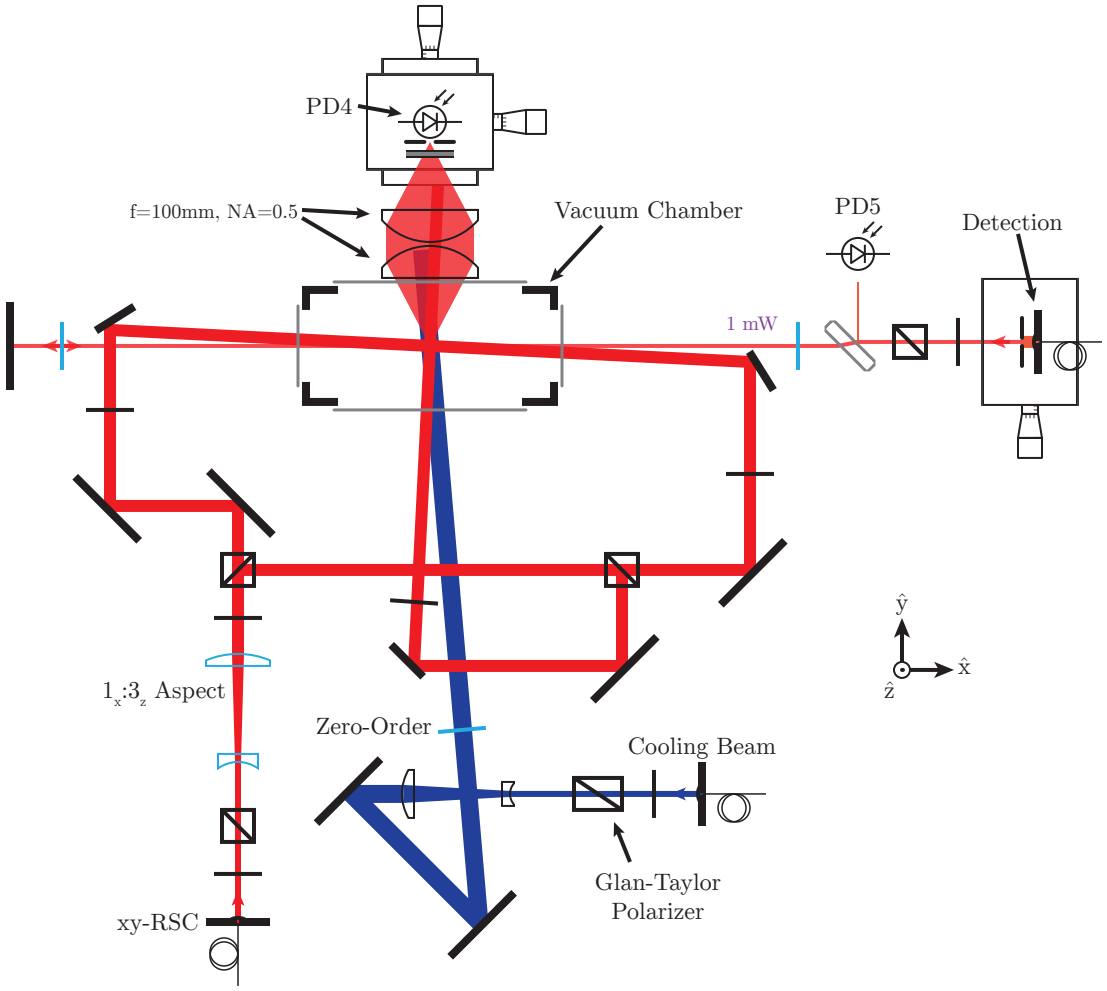

Figure 3.10: Optical setup for the atom detection and Raman sideband cooling.

detection beam will translate to noise in the fluorescence signal, the detection light out of the fiber is intensity stabilized by detecting a small fraction of the light (PD5) and feeding back to AOM11. The detection light is converted to circular polarization and retro-reflected with the opposite polarization. This creates a 1D molasses in the detection region which prevents the atom cloud from being pushed sideways during detection.[10] As with the MOT and optical molasses, repump light from AOM5 is mixed with the detection light to prevent atoms from being pumped to a dark state which would reduce the fluorescence signal. The entire detection region is then covered by a laser blackout material to reduce the background signal from the room lights and stray scattered laser beams. Additionally, the photodiode is covered by an optical long-pass filter which blocks most visible light.

Estimating the atom number: It is fairly straightforward to estimate the number of atoms

[10]If the detection beam is too strong, a vertical trap can be accidentally formed which reduces the z selectivity of the detection (and should be avoided).

in the detection region from the fluorescence signal by taking into account the geometry of the system and the gain of the detector. If the detection beam is on resonance, the atoms will scatter photons at a rate of

$$R_{\text{sc}} = \left(\frac{\Gamma}{2}\right)\frac{s}{1+s}$$

which simplifies to $\Gamma/2$ for the large saturation parameters typically used in the experiment. The photons scatter into a full 4π solid angle and are collected by the 50 mm radius, 100 mm focal length condenser lenses which gives a collection efficiency of

$$\Omega \cong \frac{\pi r^2}{4\pi f^2},$$

where $4\pi f^2$ is the surface area of a sphere with a radius equal to the lens focal length and πr^2 is the surface area of the lens. Taking into account the quantum efficiency η of the photodiode and the transmission coefficient T of the filter, the total current generated by the photodiode is

$$I_d = q\eta \cdot R_{\text{sc}} \cdot \Omega T,$$

where q is the elementary charge of an electron. The photocurrent from PD4 is amplified with a transimpedance amplifier with a 2 GΩ feedback resistor resulting in a voltage output per atom of $V_{\text{atom}} = I_d R_f$. Therefore for a signal size equal to V_{signal}, the number of detected atoms is approximately

$$N_{\text{atoms}} = V_{\text{signal}}\left[R_f(q\eta \cdot R_{\text{sc}} \cdot \Omega T)\right]^{-1}.$$

This gives an atom number of 5500 atoms/V with a photodiode efficiency of 0.55 amps/watt ($\eta = 0.8$ at 852 nm) and a long-pass filter transmission of 70%. The large feedback resistor on the amplifier also amplifies the dark current of the photodiode, causing a 200 mV offset that needs to be accounted for.[11] Additionally, to prevent saturation of the photodiode when measuring atomic fountain diagnostic signals (basically everything except the final velocity selected signal and interferometry), a neutral density filter is placed in front of the diode to reduce the incoming light by a factor of roughly 130.

3.5.1 Time-of-Flight

One useful characterization of the atomic sample that can be performed with this detection configuration is an estimation of the atom cloud temperature. After the atoms are released from the moving molasses, the cloud will begin to expand as the atoms ballistically fly away from each other due to their non-zero thermal velocity. Assuming the atoms are

[11] Without the neutral density filter, the background can be significantly larger than the 200 mV dark current offset due to scatter from the detection beam off the chamber and windows.

approximately thermalized during the cooling stages, then the atoms will have a velocity distribution (in a particular dimension) equal to a Maxwell-Boltzmann distribution

$$f(v) = \sqrt{\frac{m}{2\pi k_{\mathrm{B}} T}} e^{-mv^2/2k_{\mathrm{B}}T},$$

where k_B is the Boltzmann constant, T is the thermodynamic temperature of the ensemble,[12] and m is the mass of the particles. Given an initial atom density $\rho_0(z)$ along the vertical axis, the density $\rho(z,t)$ at some later time t can be calculated by considering the velocity distribution at each point in space.

In order for atoms to end up at position z at a time t, they must have originated from a position z' with a velocity $v = (z - z')/t$. The distribution of atoms $f(z, v, t)$ is then given by integrating the initial density over all possible starting positions, weighted by the velocity distribution, with the restriction that $vt = z - z'$:

$$f'(z, v, t) = \int_{-\infty}^{\infty} f(v)\rho_0(z')\delta(z - z' - vt)dz',$$

where $\delta(z)$ is the Dirac delta function. If the initial density is assumed to be Gaussian, $\rho_0(z) = N(2\pi\sigma_z^2)^{-\frac{1}{2}} \exp(z^2/2\sigma_z)$, then the integral simplifies to

$$f'(z, v, t) = \frac{N}{2\pi\sigma}\sqrt{\frac{m}{k_{\mathrm{B}}T}} \exp\left(\frac{-mv^2}{2k_{\mathrm{B}}T} - \frac{(z - vt)^2}{2\sigma^2}\right),$$

where N is a normalization factor. Integrating again over every possible velocity gives the atom number density

$$\begin{aligned}\rho(z, t) &= \int_{-\infty}^{\infty} f'(z, v, t)dv \\ &= \frac{N}{\sqrt{2\pi(\sigma^2 + k_{\mathrm{B}}Tt^2/m)}} \exp\left(-\frac{z^2}{2(\sigma^2 + k_{\mathrm{B}}Tt^2/m)}\right) \end{aligned} \tag{3.1}$$

as a function of the time t after releasing the atoms. With knowledge of the initial cloud size and the expansion time, (3.1) shows that the temperature can then be deduced via a measurement of the expanded cloud's Gaussian width: $\sigma^2 = \sigma_0^2 + k_{\mathrm{B}}Tt^2/m$. Since the initial cloud size is typically not well known, a time-of-flight measurement is performed at two separate times which allows us to solve for both the temperature and initial size.

As the atoms are launched vertically in a parabolic arc, one measurement is performed at a time t_1 when the atoms are traveling up and again at a time t_2 as the cloud falls back through the detection region. The two measurements are performed with separate

[12] Note that the temperature can be different in each dimension depending on how the cooling thermalizes the sample.

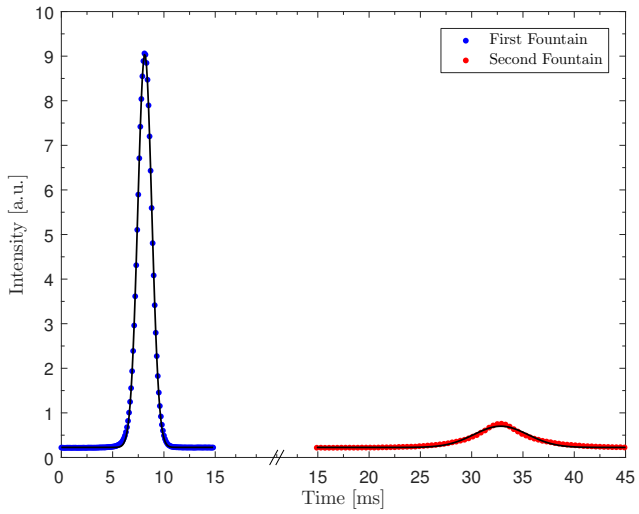

Figure 3.11: A sample time-of-flight signal. The blue dots show the florescence signal for the upwards moving cloud (first fountain), while the red dots show the downward moving fluorescence signal (second fountain). The time offsets for each signal are arbitrary and the black lines indicate Gaussian fits.

launches as each detection heats the atoms significantly. While there are more complicated time-of-flight temperature measurements that only use a single detection stage [91], multiple measurements are easier to measure and interpret. For simplicity, assume that the atom cloud does not expand as it traverses the detection beam, which is valid for traversal velocities v_d much greater than the expansion rate. Since the atom trajectory is parabolic, the atoms will have the same vertical traversal speed v_d during both detections and, thus, the measured temperature can be calculated as

$$T = \frac{m}{k_{\mathrm{B}}} \frac{v_d^2(\sigma_{t_2}^2 - \sigma_{t_1}^2)}{(t_2^2 - t_1^2)},$$

where σ_t is the temporal Gaussian width of the detected fluorescence signal.

An example time-of-flight measurement for a PGC cooled sample is shown in Fig. 3.11. The fluorescence of the upward moving cloud (shown in blue) has a fitted Gaussian width of $\sigma_{t_1} = 0.68$ ms and is measured $t_2 = 88.7$ ms after being released from the moving molasses. Similarly, if the falling cloud (shown in red) is fitted to a single Gaussian, then the fitted width is $\sigma_{t_2} = 2.63$ ms when measured at $t_2 = 892.3$ ms. The traversal velocity through the detection region is approximately 4 m/s, which would give a measured temperature estimate of 2 μK. However, a single Gaussian gives an extremely poor fit for the downward moving fountain signal as can be seen in Fig. 3.12 and it is possible that the cloud contains a mixture of two temperature distributions which can be fitted with a double Gaussian instead. The double Gaussian fit has widths equal to 1.44 ms and 4.12 ms giving estimated temperatures of 500 nK and 5.2 μK respectively, with approximately 30% of the atoms in the colder state.

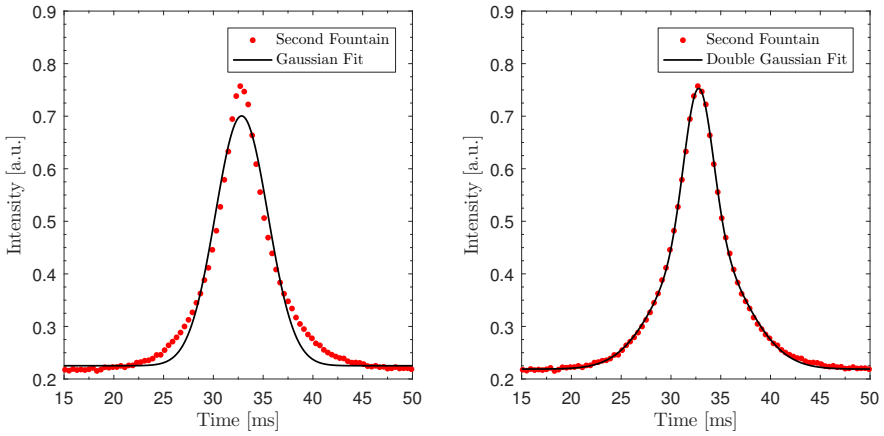

Figure 3.12: The downward moving fluorescence signal (second fountain) fitted to a single Gaussian (left) and a double Gaussian (right).

Atom Number Conservation: While it might be worrying that the two fountain signals in Fig. 3.11 clearly do not have the same integrated atom number, this is simply a consequence of the finite detection volume. The expanded cloud's 1σ radius is approximately 1 cm from the time-of-flight signals, which if the cloud is spherically symmetric, is much larger than the 4 mm wide detection beam (let alone the pinhole). By taking into account the relative signal sizes of the first and second fountain and the expansion of the cloud, an upper bound can be placed on the detection volume of $(6\text{ mm})^2 \times 600\ \mu\text{m}$, assuming the center of the cloud is detected.

3.6 Raman Sideband Cooling

Despite the microkelvin temperatures achieved by polarization gradient cooling, the atom cloud is far from an ideal source for atom interferometry. The populations of the various magnetic sublevels in the atoms are equally distributed which is problematic for systematics, requiring a state selection step (see Section 4.2) to select out atoms in the magnetically insensitive $m_F = 0$ state. For atom species with large nuclear spin (such as cesium), the ground states have a large number of possible magnetic sublevels due to the large total angular momentum $F = J + I$. Since the cesium atoms are in their $F = 4$ ground state after PGC, selecting only the $m_F = 0$ state would reduce the atom signal by a factor of 8/9. Additionally, microkelvin temperatures still cause the atom cloud to expand at a rate of nearly 1 cm/s, which results in loss of contrast and signal-to-noise as the atoms move transversely out of the interferometer beams. This velocity spread is also problematic for implementing Bragg diffraction (which requires sub-recoil velocity distributions), necessitating further signal loss with a velocity selection stage as described in Section 4.3.

In order to increase the signal-to-noise of the interferometer, the launched atoms are trapped in a moving optical lattice and cooled with Raman sideband cooling. While the

detailed theory of Raman sideband cooling [92] is beyond the scope of this thesis, some important details are described herein for cooling in a single dimension. If an atom is trapped in a far detuned one-dimensional optical lattice with a trapping potential equal to

$$U_{\text{lattice}} = -\frac{\hbar}{4}\frac{\Gamma^2}{\Delta}\frac{I}{I_{\text{sat}}}\sin^2(kz)$$

then the potential minimum can be approximated as having energy levels given by a harmonic oscillator with energy splittings

$$\begin{aligned}\Delta E_{\text{vib}} &= \hbar\omega_{\text{vib}} \\ &= \hbar\sqrt{\frac{\omega_r\Gamma^2}{\Delta}\frac{I}{I_{\text{sat}}}},\end{aligned}$$

where Δ is the nominal detuning from the D_2 hyperfine states, I/I_{sat} is the saturation parameter, k is the wave-vector of the optical lattice, and ω_r is the recoil frequency $\hbar k^2/2m$ of the trapped atom with mass m [93]. If an external magnetic field is applied to the atom, then each m_F state will have a different vibrational energy spectrum as shown in Fig. 3.13. If the Zeeman splitting $\Delta E_{\text{B}} = g\mu_{\text{B}}B$ is equal to the lattice vibrational energy splitting ΔE_{vib}, then atoms can be driven between adjacent m_F states by changing its vibrational quantum number ν through degenerate Raman transitions.

For compactness, the lattice beams themselves are used to drive the degenerate Raman transitions and therefore a careful choice of magnetic field direction and lattice polarization is necessary to ensure that the Raman coupling between $|m_F, \nu\rangle \, and \, |m_F - 1, \nu - 1\rangle$ is non-zero. For an optical lattice created by two counter-propagating beams whose linear polarizations subtends an angle α, the coupling matrix element is proportional to

$$\langle m_F, \nu| \, U_{\text{lattice}} \, |m_F - 1, \nu - 1\rangle \propto \sin\alpha \sin\beta,$$

where β is the angle the magnetic field makes to the wave-vector k [94]. Therefore in order to have degenerate Raman coupling, the polarization of the two fields that make up the optical lattice cannot be the same ($\alpha = 0$) or orthogonal ($\alpha = \pi/2$), as the former has zero coupling and the latter does not form a standing wave.

Cooling is performed by weakly pumping the atoms with σ^+ polarized light along the closed $|F = 3, m_F\rangle \rightarrow |F' = 2, m_F + 1\rangle$ transition. If the lattice is deep enough such that the atoms are tightly bound, then spontaneous decay will conserve the atom's vibrational quantum number and remove energy from the system. As shown in Fig. 3.13, an atom pumped from the $|m_F = 1, \nu\rangle$ state will preferentially decay to the $|m_F = 3, \nu - 2\rangle$ state, removing two quanta of energy.[13] Atoms that accumulate in the $|m_F = 3, \nu = 0\rangle$ state are

[13]The relative decay rates into other m_F state are given by the Clebsch-Gordan coefficients. Since the atom can at worst decay back to the same m_F with zero change in energy, cooling of all states will eventually take place.

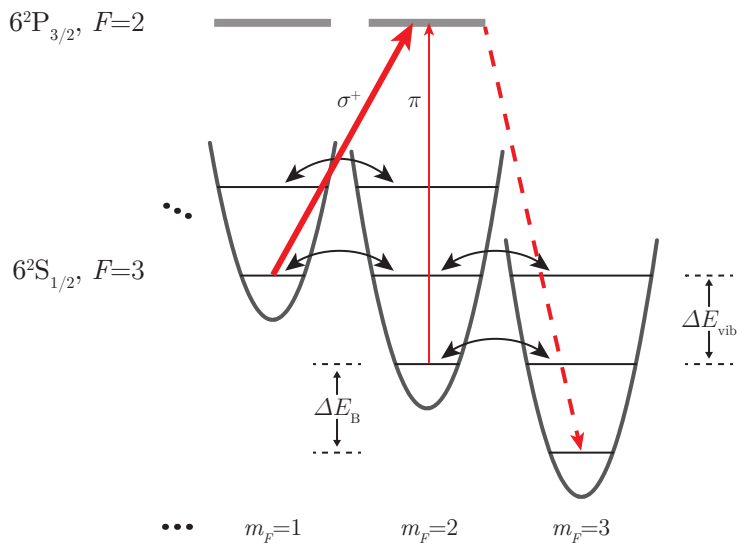

Figure 3.13: Energy diagram for the different states used in Raman sideband cooling. Each m_F state is shifted in energy by the Zeeman splitting ΔE_{B} and the vibrational levels of the lattice are split by ΔE_{vib}. Degenerate Raman transitions are represented by black arrows, while optical pumping (solid) and decay (dashed) are shown with red arrows.

dark since they cannot be optically pumped by $f_{3,2'}$ due to the lack of a $m_F = 4$ state in $F' = 2$, nor coupled by the Raman transitions since all other states have higher energy. To prevent $|m_F = 2, \nu = 0\rangle$ from also being dark, the pump beam is slightly misaligned from the magnetic field axis so that there is a small amount of π polarized light which can optically pump the state.

The atoms will continue to be cooled into lower lattice vibration until they reach equilibrium with the heating caused by any parasitic σ^- pump polarization and the far detuned single photon scattering of the lattice beam

$$R_{\mathrm{sc}} = \frac{\Gamma^3}{8\Delta^2}\frac{I}{I_{\mathrm{sat}}}.$$

In order to reduce single photon scatter, the lattice detuning Δ can be made arbitrary large. However, it is convenient to use a frequency of $f_{4,4'}$ for the lattice beams (which has a detuning of 8.8 GHz) as it also serves to pump atoms into $F = 3$, which is the hyperfine state required for cooling. Once the atoms are sufficiently cooled and optically pumped into the $|m_F = 3, \nu = 0\rangle$ state, the lattice is adiabatically turned off. This lowers the energy of the bound vibrational states which cools the trapped atoms further [89].

The optical lattice can be extended to three dimensions by adding two additional running waves along the other two axes [95], which allows for Raman sideband cooling (RSC) in all directions. Compared to previous 3D RSC experiments [77, 96], our setup is complicated slightly by the need to have the $\hat{z}$ RSC beam circularly polarized as it originates from the

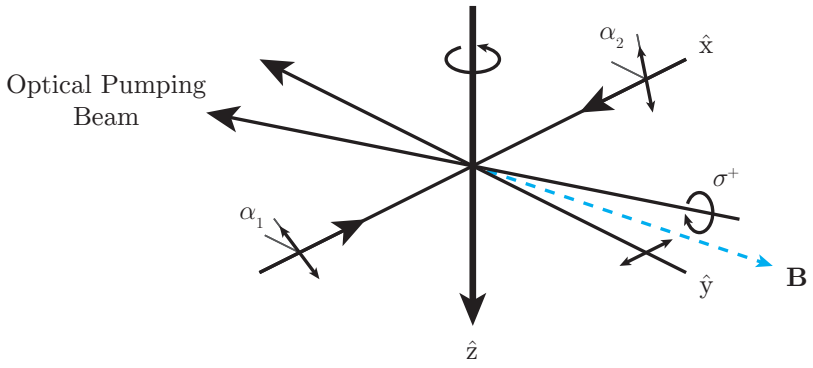

Figure 3.14: Diagram showing the relative polarizations and orientations of the Raman sideband cooling beams, optical pumping beam, and magnetic field.

same optics as Bragg diffraction (which requires circular polarization); see Figures 3.8 and 4.3. This means that unlike previous experiments, the lattice beams cannot be all linearly polarized with electric fields which all lie in the same plane. Instead, with the $\hat{z}$ lattice beam being circularly polarized in the x-y plane, the $\hat{y}$ beam is chosen to be linearly polarized along $\hat{x}$ and the two counter-propagating $\hat{x}$ beams are linearly polarized at a relative angle $\alpha_2 - \alpha_1$, as shown in Fig. 3.14.

The lattice beams in the experiment are derived from the same laser frequency as polarization gradient cooling. The x-y Raman sideband cooling lattice light is generated by AOM13 driven at 120.370 MHz as shown in Fig. 3.15, which shifts the laser frequency to $f_{4,4'}+6.3$ MHz. The z RSC light comes from AOM14 driven at 115.795 MHz which is coupled into Fiber:z-RSC and then again into the main Bragg fiber in Fig. 4.3. The $\hat{z}$ lattice light is red-detuned compared to the x-y lattice beams to compensate for the Doppler shift of the launched atoms and to create a lattice moving vertically at approximately 4 m/s. Since the $\hat{z}$ lattice optical path is retro-reflected in the chamber, there is necessarily a second parasitic lattice moving downwards against the atom trajectory. Assuming the launch speed is fast enough, the atoms will not be loaded into the second lattice and will instead interact with the time averaged light field which should not interfere too much with cooling.

The optical pumping light comes from a polarizing beam splitter pickoff before the spectroscopy fiber in Fig. 3.3, shifted down 65.0 MHz by AOM4 to $f_{3,2'} + 5.2$ MHz, and coupled into Fiber:Cooling Beam. The optical pumping frequency is purposefully chosen slightly off-resonance to allow for easier tuning of the pump rate without dealing with incredibly small optical intensities.

The atoms are loaded into the 3D lattice about 1 cm above the detection region and approximately 40 cm above the MOT location as shown in Fig. 3.8. To increase the time the atoms spend in the optical lattice as the atoms move upwards, the horizontal lattice beams are expanded vertically to a waist of 12 mm with an intensity equal to $\sim$75 mW/cm^2. The lattice beams are also sent into the vacuum chamber at about 5 degrees from normal incidence to prevent parasitic etalons from forming between the window surfaces. The $\hat{z}$

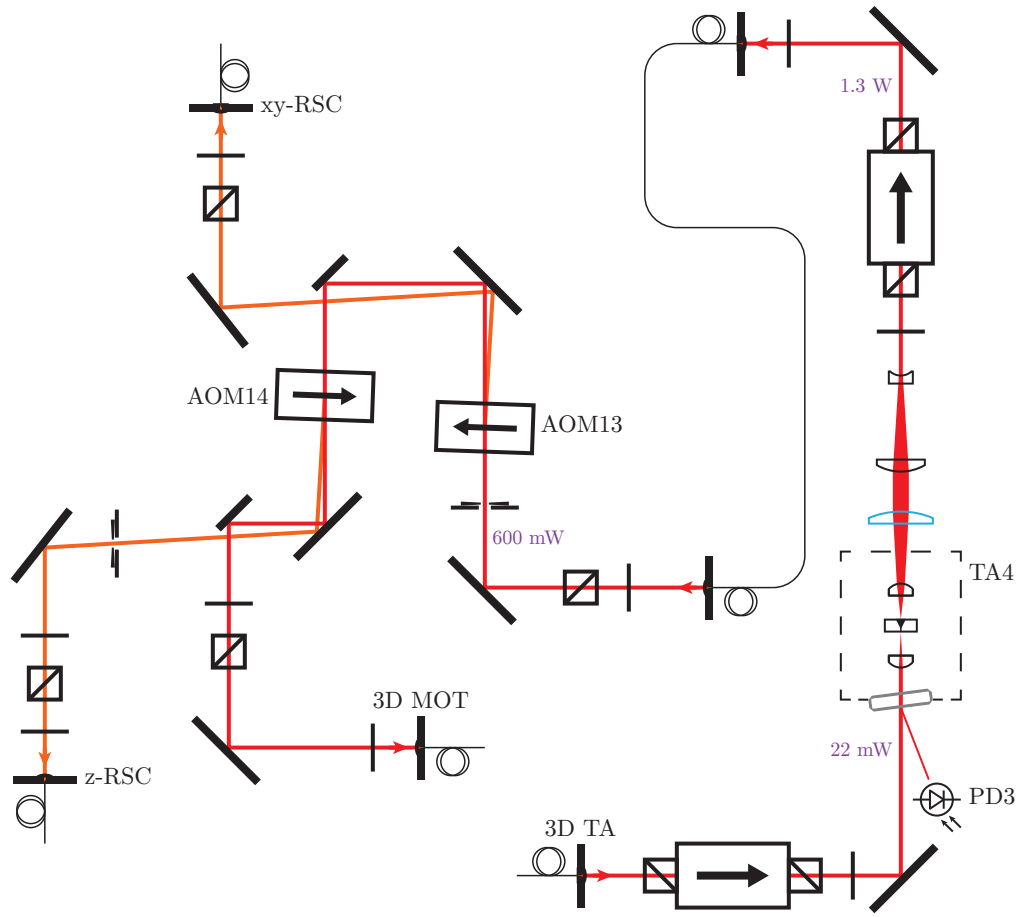

Figure 3.15: Optical setup for the Raman sideband cooling frequency shifting and main Tapered amplifier.

lattice beam has a waist of 6.2 mm with an intensity of ∼100 mW/cm^2 and is sent through the bottom of the chamber to be retro-reflected off the top mirror (since only the downwards going beam contributes to RSC). Lastly, the optical pumping beam's polarization is purified with a high extinction Glan-Taylor polarizer, expanded to a waist of 1 cm with an intensity of 100 μW/cm, and made circularly polarized with a high quality zero-order $\lambda/4$ waveplate. To adjust the magnetic field in the RSC region, three pairs of Helmholtz coils around the detection region are used to simultaneously zero the field and apply a small bias in the $\hat{y}$ direction for the optical pumping.

The timings for turning on the RSC lattice and the optical pumping beam, as well as the $\hat{z}$ lattice Doppler detuning, are critical to efficiently load the atoms into the optical lattice. With the repump light from AOM5 turned off, the optical lattice and optical pumping beam's are turned on at 1.1233 s (90.3 ms after the atoms are adiabatic released from the moving molasses). The atoms are then cooled for 2.8 ms, at which point the optical pumping beam is turned off and the lattice is adiabatically ramped off over 400 μs by decreasing the

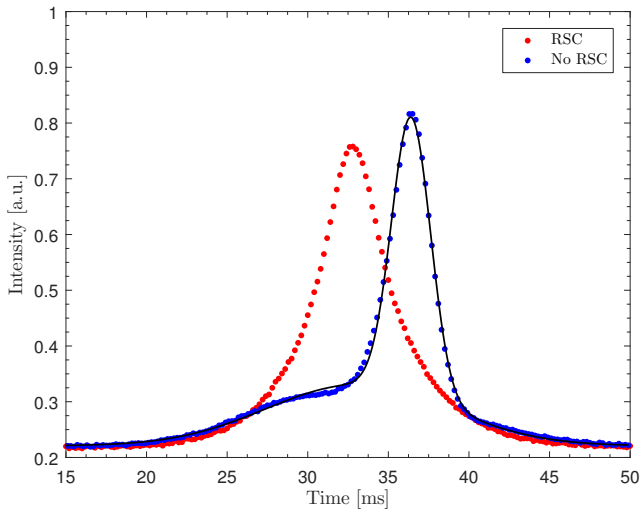

Figure 3.16: The time-of-flight signal of a Raman sideband cooled sample (blue) compared to a sample that has only been cooled by polarization gradient cooling (red). The black line is a fit to a double Gaussian function, which corresponds to an atom sample at 330 nK overlapped with a much hotter background cloud.

amplification of the tapered amplifier (by reducing the TA current).

As can be seen in Fig. 3.16, the cooled atoms (blue) arrive at the detector slightly later since they were unaffected by gravity while trapped in the constant velocity optical lattice. By fitting two Gaussians to the time-of-flight signal, we can estimate the temperature of the colder ensemble at 330 nK with a cooled fraction of 50%. For comparison, the recoil limited temperature for cesium is

$$T_r = \frac{\hbar^2 k^2}{2mk_{\mathrm{B}}} \approx 100 \text{ nK}.$$

It should be noted that since the Raman sideband cooling is performed above the detection region, it is not possible to do a two-point time-of-flight measurement. Instead, it is assumed that the entire vertical extent of the upward moving sample is cooled equally so that the same initial width can be used for the estimate. Some of the initial cloud width might be cut off in practice, which would imply a higher actual temperature.

3.6.1 Rapid Adiabatic Passage

Since the atoms are mostly in the $m_F = 3$ state after Raman sideband cooling, they must first be transferred to the $m_F = 0$ state before interferometry can be performed. While successive Raman or microwave transitions could be used to drive the atoms down into progressively lower m_F states, a more efficient technique is to use rapid adiabatic passage (RAP) [97] where a high power microwave source capable of driving hyperfine transition is slowly swept

down in frequency through the possible m_F transitions. When the Rabi frequency driving the hyperfine transitions is much faster than the microwave frequency ramp rate, then the atoms will be transferred to the final end state with a theoretical 100% efficiency.

If the atoms are to be transferred to the correct m_F state for interferometry, the magnetic quantization axis of $\hat{y}$ for RSC must first be rotated to align with the interferometer z-axis by switching the Helmholtz bias coils to apply a large bias field in the $\hat{z}$ direction. Since the drivers for the coils are somewhat slow, the magnetic field rotation is quasi-adiabatic and the atoms stay in the $m_F = 3$ state for the most part. A 10 watt traveling-wave tube amplifier is used to amplify a dielectic resonant oscillator (DRO) which is phase locked to +900 kHz above the cesium hyperfine frequency $f_{\rm hf} = 9.192631$ GHz. The amplifier is connected to a microwave horn which produces free space radiation that drive transitions in the cesium atoms. At 1.129 s, approximately 2 ms after the field is switched, the DRO frequency is swept down at a rate of 230.8 kHz/ms to a final frequency of $f_{\rm hf} - 121$ kHz over 5 ms. This transfers approximately 70% of the atoms into the $F = 4, m_F = 0$ state, which is probably limited by the random polarization of the microwave horn and imperfect initial $m_F = 3$ state occupation.

Chapter 4

Coherent Manipulation

4.1 Ti:Sapphire Lasers

Historically, the coherent manipulation of atom states and momentum in atom interferometry has been accomplished with two-photon Raman transitions between two ground states. While the frequency stability requirements for these kinds of experiments are strict, the power needs are fairly minimal with simple ECDL diode lasers supplying enough power for very high precision measurements [7]. If more laser power is required, tapered amplifiers have even been used to boost the reach of these laser systems [98].

The multi-photon nature of Bragg diffraction requires a different approach to the laser system as the optical intensities needed are significantly higher than for Raman, as discussed in Section 2.5. The power requirements are compounded by the need for larger detunings to minimize the single photon scattering (which can lead to the degradation of signal-to-noise). Some atomic species allow the luxury of using frequency doubled fiber lasers, some of which can output over 10 watts of optical power at 780 nm [99, 100] for experiments with rubidium. Unfortunately, high power fiber lasers at 1704 nm or 1788 nm (twice the D_1 and D_2 transition frequency in cesium) are still in the experimental stages [101], as is the doubling of such lasers [102]. Recently, high power tapered amplifiers with 3 watts of output power have become available at 852 nm, but these could potentially have deleterious effects on interferometry due to amplified spontaneous emission [103].

Instead, two solid state titanium-doped sapphire lasers are used to drive the Bragg beam splitters and the various required Raman pulses. A Coherent 899 Ti:Sapphire laser is pumped by a 10 watt Coherent Verdi V10 DPSS laser, outputting around 700 mW of single frequency laser light at 852 nm. A small amount of light is picked off at the output and sent to an external cavity to stabilize the laser wavelength as shown in Fig. 4.1. For precision interferometry, the laser frequency needs to be accurately referenced to an absolute optical frequency with a sufficiently large detuning from any atomic transition as to limit single photon scattering. Since our absolute frequency reference is tied to the spectroscopy, an offset lock is used to shift the frequency many gigahertz away from the D_2 line [104, 105]. A

small amount of light from the reference laser is coupled into a fiber (Fiber:Phase Lock) and combined on a partially reflecting mirror with some 899 light to create a beat note of the frequency difference. The combined light is coupled into a fiber (Fiber:Detector) which is connected to a Newport 1544 IR photodetector. The detected beat signal is mixed with an Agilent Microwave synthesizer, amplified, low pass filtered, and then sent to the main 899 locking circuit.

The locking circuit takes the beat signal and an external frequency source, divides them both by 32, and then compares the relative phases of the two signals with a digital phase detector. The error in the phase difference is used to feedback to the 899 laser and reference cavity, thus phase locking the laser to an absolute frequency reference (the spectroscopy). The frequency division step is critical as a 1:1 phase lock would be unstable due to the slow feedback mechanisms available for locking the 899 laser. The external frequency is supplied by a direct digital synthesizer (DDS) to give the flexibility of making small changes to the absolute laser frequency without changing the microwave synthesizer. The free running 899 laser has a linewidth of 150-200 kHz and a locked linewidth of 400 kHz, as measured by an optical delay line.

In order to amplify the 899 Ti:Sapphire light from hundreds of milliwatts to the several watts that are needed for the experiment, the light is injected into a stripped-down M Squared SolsTiS Ti:Sapphire laser. Since most of the loss in a Ti:Sapphire laser comes from the etalons needed to make the laser run single mode, removing these elements significantly increases the available output power. To force the laser to still lase at a single frequency, approximately 500 mW of 899 light is coupled into the laser to force stimulated emission at the injection wavelength. Unlike a tapered amplifier, the SolsTiS is still a laser cavity and thus must be locked to the injected light to get significant coupling into the cavity. Typical cavity locking schemes either involve modulating the cavity length, or generating frequency sidebands on the incoming laser frequency and measuring the transmission or reflection [106] to generate a locking error signal. These methods are unsuitable for this situation as they would create frequency sidebands on the laser output which would interfere with the experiment.

Instead, the cavity of the SolsTiS is stabilized using polarization spectroscopy [107] of the injected light reflecting off cavity's output coupler. In the original paper by Hänsch, a linear polarizer was placed inside a bow tie cavity at an angle θ relative to the linearly polarized input light. The uncoupled light reflecting off the cavity interferes with the circulating light to form a slightly elliptically polarized output. The magnitude and direction of the ellipticity is a function of the mismatch between the input laser frequency and the cavity length. Therefore by analyzing the polarization of the output light, an error signal is generated which can be used to lock the cavity. Instead of inserting a polarizer into the SolsTiS laser cavity, the input polarization is rotated by a small angle θ away from the polarization axis of the free running laser. The Brewster angle of the Ti:Sapphire crystal then provides a small amount of loss for the off-axis polarization component similar to the polarizer in the original paper. The SolsTiS output is then picked off and analyzed by sending it through a $\lambda/4$ waveplate at 45 degrees and into a Wollaston polarizer, which splits the polarization components onto a balanced photodetector (PD6). When the cavity is resonant with the

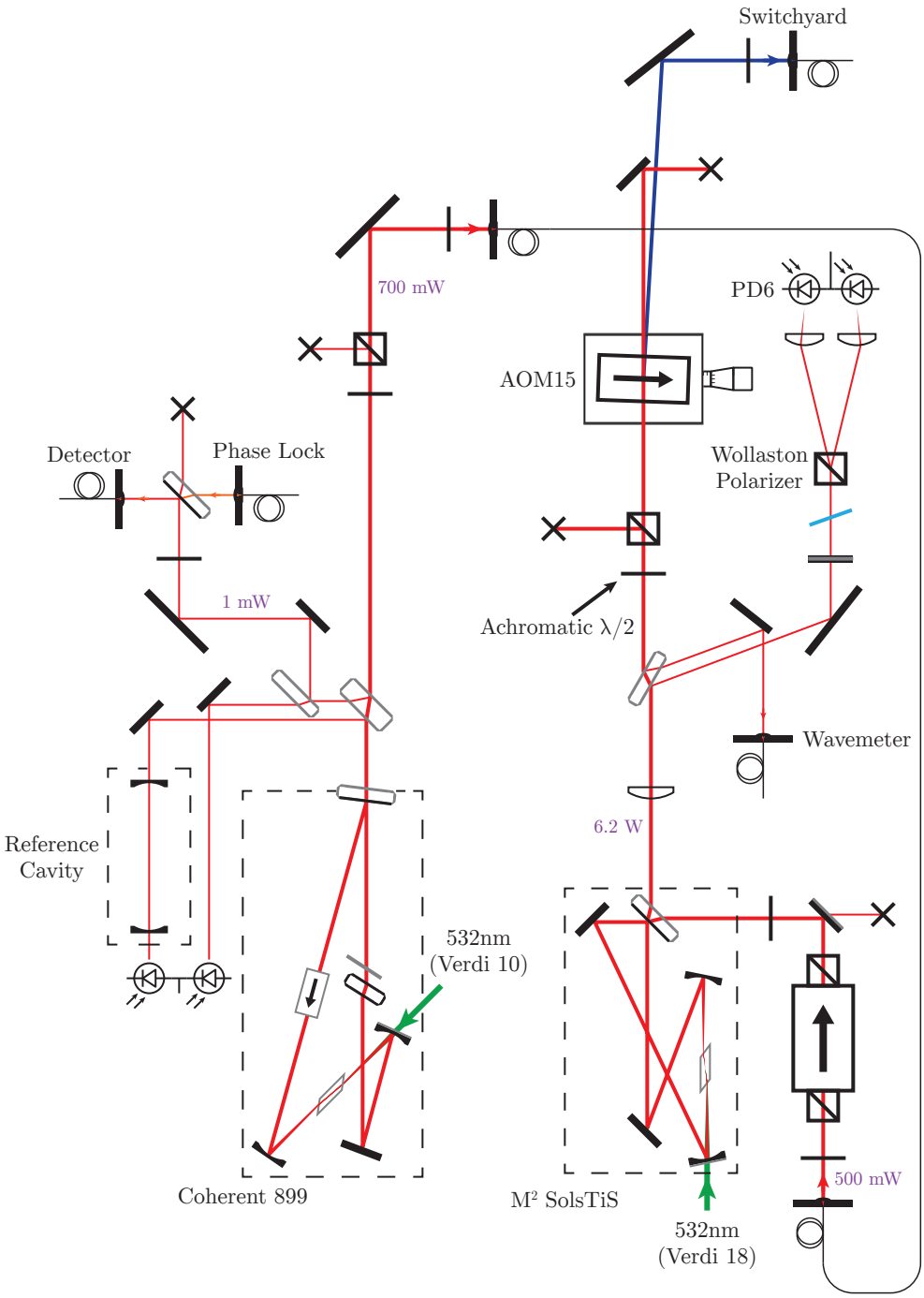

Figure 4.1: Optical setup for the Ti:Sapphire master laser (899) and master power amplifier (SolsTiS).

injected light, the polarizer splits the light equally and an error signal of zero is measured.[1] A nonzero error signal is created when the cavity is off resonant and the output becomes elliptical, causing an imbalance in the Wollaston polarizer outputs.

Applying this locking technique to titanium-sapphire laser cavities has been shown to produce output powers in excess of 6 watts with kilohertz linewidths [108]. Our SolsTiS is pumped with 18.5 watts from a Coherent Verdi V18 and, when injected with 500 mW of 852 nm light, can output a combined total of 6.2 watts (with a linewidth limited by our 899 master laser).

Safety Considerations: As can be seen in Fig. 4.1, there are a couple of elements that are required for clean and safe operation with our particular high power Ti:Sapphire. The stripped down SolsTiS does not have an optical diode and therefore does not have a preferred lasing direction when it is not injection locked. Additionally, because of the lack of frequency selective elements, the SolsTiS will naturally oscillate near 750 nm (the gain maximum for titanium-doped sapphire). To prevent watts of power from being sent back into the 899, a dichroic mirror that reflects wavelengths longer than 808 nm is used as a filter for the backwards lasing light. An optical isolator is also added to reduce any light not filtered by the mirror. The $\lambda/2$ waveplate that controls the power to the beam dump (for reducing the power during alignment) needs to be broadband so that it can rotate both 750 nm and 852 nm light in case the laser becomes unlocked. Lastly, there is a 852 nm bandpass filter in front of the polarization analyzing electronics so that the 750 nm light does not saturate the lock signal when the cavity is unlocked.

4.2 State Selection

With the titanium sapphire lasers locked to a far detuned laser frequency, we now have the means to coherently prepare the atom ensemble into a state that is suitable for atom interferometry.

After the launched atoms are cooled with Raman sideband cooling and transferred to the $|F = 4, m_F = 0\rangle$ state with rapid adiabatic passage, a small fraction of the atoms still remain in the $m_F \neq 0$ sublevels and in the $F = 3$ hyperfine state. In the presence of a weak external magnetic field, these states will shift in energy by

$$\Delta E_{\mathrm{B}} = g_F \mu_0 m_F B,$$

where the g_F is the Landé g-factor for the hyperfine state F, μ_0 is the Bohr magneton, and B is the external magnetic field. These energy shifts cause perturbations in the free evolution Hamiltonian from Section 2.5, manifesting as forces and additional phase shifts in the interferometer. If the magnetic field is constant, then these phase shifts cancel along the

[1] To compensate for parasitic ellipticity caused by dielectric mirrors and the pickoff, the $\lambda/4$ waveplate's angle relative to normal incidence is adjusted to change the retardation amount and make the error signal symmetric.

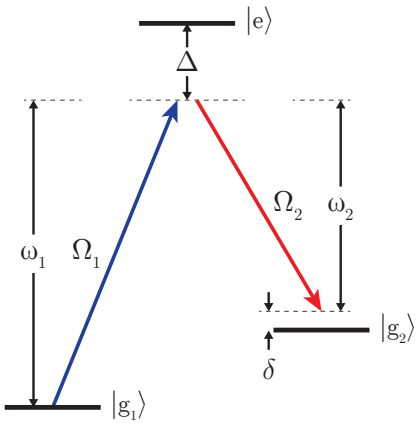

Figure 4.2: A three-level system with ground states $|g_1\rangle$ and $|g_2\rangle$ and excited state $|e\rangle$, driven by two electric fields of frequency $\{\omega_1, \omega_2\}$ with coupling strengths $\{\Omega_1, \Omega_2\}$. The detuning δ is the mismatch from two-photon resonance.

two trajectories and have zero net effect. However, in practice the magnetic field could have gradients or other local perturbations that would contribute to a net phase shift between the paths. Not only would these phase shifts cause systematics in the measurement, but they would also decrease the overall contrast of the interferometer. Therefore all atoms except those in the desired $m_F = 0$ state are removed from the cloud by a series of state selective manipulations. First, the atoms in the mostly unpopulated $F = 3$ state are resonantly accelerated so that they leave the interferometer region (see Section 4.2.1). Next, the atoms in the $|F = 4, m_F = 0\rangle$ state are coherently transferred to $|F = 3, m_F = 0\rangle$, followed by a second resonant pulse to remove any remaining $F = 4$ atoms resulting in a theoretically pure population in the $|F = 3, m_F = 0\rangle$ state.

In order to perform the population transfer without heating the atoms, the two $m_F = 0$ states are coupled using an optical Raman transition which is far detuned from the $6^2P_{3/2}$ manifold. If the different m_F states are sufficiently resolved (by applying a magnetic field), then the dynamics of the population transfer can be treated as a three-level system. Consider a system with two ground states $|g_1\rangle$ and $|g_2\rangle$ that are coupled to an excited state $|e\rangle$ by two co-propagating laser fields with frequencies $\{\omega_1, \omega_2\}$ [109], as illustrated in Fig. 4.2. If the Rabi frequencies $\{\Omega_1, \Omega_2\}$ and single photon detuning Δ of the fields are much larger than the Doppler shift resulting from atomic motion, then the momentum of the atom can be ignored and the Hamiltonian for the system can be written as

$$\hat{H} = -\hbar\omega_1 |g_1\rangle\langle g_1| - \hbar(\omega_2 + \delta)|g_2\rangle\langle g_2| + \hbar\Delta|e\rangle\langle e| - \frac{\hbar}{2}\left(\Omega_1 e^{-i\omega_1 t}|e\rangle\langle g_1| + \Omega_2 e^{-i\omega_2 t}|e\rangle\langle g_2| + h.c.\right),$$

where the rotating wave approximation has already been applied to the atom-field interaction

terms. The relevant dynamics of the system can be extracted by applying the unitary transformation $\hat{U} = e^{-i\omega_1 t|g_1\rangle\langle g_1| - i\omega_2 t|g_2\rangle\langle g_2|}$ to the eigenstates $|\Psi'\rangle = \hat{U}|\Psi\rangle$ and to the Hamiltonian which yields

$$\begin{aligned}\hat{H}' &= \hat{U}\hat{H}\hat{U}^\dagger - i\hbar\hat{U}\frac{\partial\hat{U}^\dagger}{\partial t} \\ &= -\hbar\delta\,|g_2\rangle\langle g_2| + \hbar\Delta\,|e\rangle\langle e| - \frac{\hbar}{2}\Big(\Omega_1\,|e\rangle\langle g_1| + \Omega_2\,|e\rangle\langle g_2| + h.c.\Big).\end{aligned}$$

The time evolution of the transformed eigenstates $|\Psi'\rangle = g_1(t)\,|g_1\rangle + g_2(t)\,|g_2\rangle + e(t)\,|e\rangle$ can then be determined by solving the Schrödinger equation $i\hbar\partial_t|\Psi'\rangle = \hat{H}'|\Psi'\rangle$. If the single photon detuning is large $|\Delta| \gg \{|\Omega_1|, |\Omega_2|, |\delta|\}$, then the excited state remains unpopulated and can be adiabatically eliminated by setting $\dot{e}(t)$ to zero and solving for $e(t)$. Substituting the solution into the equations for $\dot{g}_1$ and $\dot{g}_2$ eliminates the excited state and results in an effective two-level system:

$$\begin{aligned}i\hbar\dot{g}_1(t) &= -\frac{\hbar|\Omega_1|^2}{4\Delta}g_1(t) - \frac{\hbar\Omega_1\Omega_2^*}{4\Delta}g_2(t) \\ i\hbar\dot{g}_2(t) &= -\frac{\hbar\Omega_1^*\Omega_2}{4\Delta}g_1(t) - \hbar\left(\frac{|\Omega_2|^2}{4\Delta} - \delta\right)g_2(t).\end{aligned}$$

For a system initially in g_1 and driven with constant intensities, the coupled differential equations can be solved [110] for the time evolution of g_2 to give

$$|g_2|^2 = \frac{|\Omega_1|^2\,|\Omega_2|^2}{4\Delta^2\bar{\Omega}^2}\sin^2\left(\frac{\bar{\Omega}t}{2}\right), \tag{4.1}$$

where the effective Rabi frequency is

$$\bar{\Omega}^2 = \frac{\left(|\Omega_1|^2 + |\Omega_2|^2\right)^2}{(4\Delta)^2} + \frac{\delta\left(|\Omega_1|^2 - |\Omega_2|^2\right)}{2\Delta} + \delta^2.$$

Therefore a three-level system driven by a far detuned Raman pair undergoes Rabi oscillations with a frequency $\bar{\Omega}$. By varying the laser intensities and/or the interaction time t, the population in g_1 can be transferred to g_2 using a π-pulse such that the length of the pulse τ_π satisfies $\bar{\Omega}\tau_\pi = \pi$.

Since we are interested in only transferring atoms starting in $|g_1\rangle = |F = 4, m_F = 0\rangle$ to $|g_2\rangle = |F = 3, m_F = 0\rangle$, it is worth considering the effect of the laser fields on states other than $m_F = 0$. For the simplified case where the two Rabi frequencies are equal, $\Omega \equiv \Omega_1 = \Omega_2$, any off-resonant transitions will have a non-zero detuning δ and a suppressed (maximum) population transfer equal to

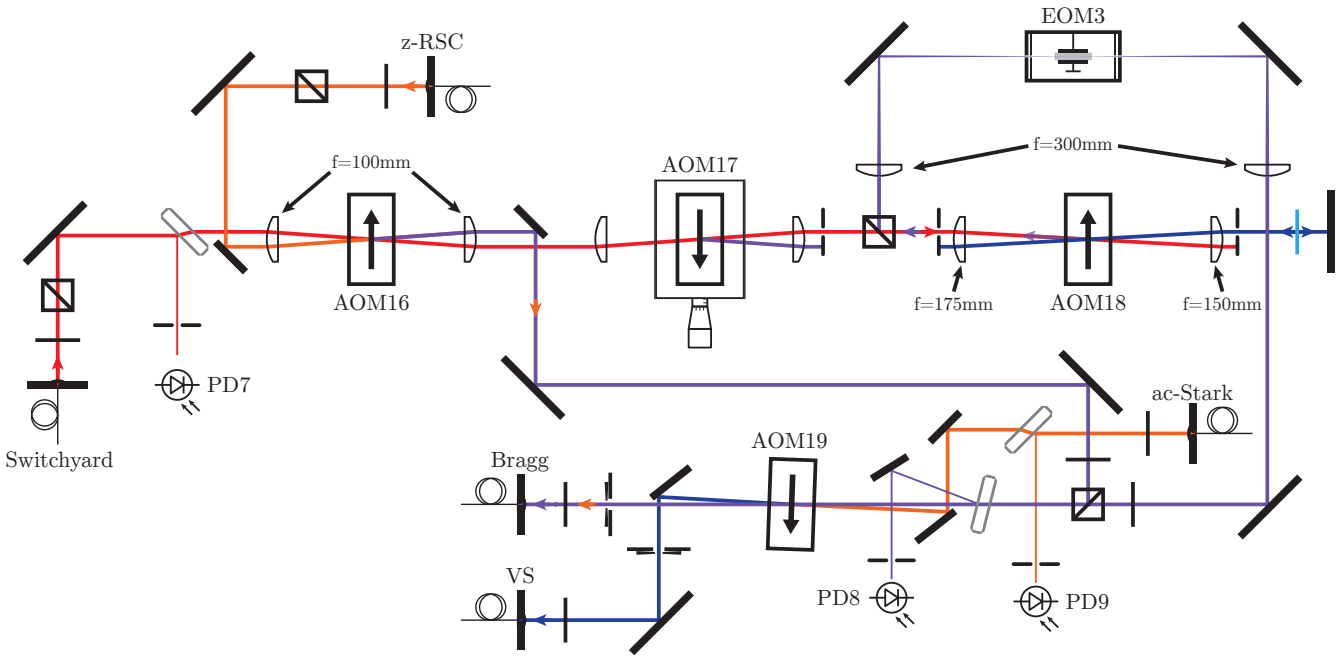

Figure 4.3: Optical setup for generating the frequencies for state selection, velocity selection, and Bragg diffraction.

$$|g_{F=3,m_F}|^2 = \frac{\Omega^4}{\Omega^4 + 4\delta^2\Delta^2},$$

given by the coefficient of (4.1). In order for the Raman pulse to transfer a negligible amount of $m_F \neq 0$ atoms, the detuning for those states must satisfy

$$|\delta| \gg \frac{|\Omega|^2}{2\,|\Delta|},$$

which can be accomplished by splitting the states with an external magnetic field such that

$$|B| \gg \frac{\hbar\,|\Omega|^2}{4 g_F \mu_0\,|\Delta|} \cong \frac{\hbar\pi}{2 g_F \mu_0 \tau_\pi},$$

where τ_π is the Raman pulse length used in the state selection to transfer the $m_F = 0$ atoms.

The magnetic field in our experiment is generated by a solenoid placed inside the vacuum chamber and aligned with the fountain axis as shown in Fig. 4.9. The solenoid consists of an aluminum tube with a 3.81 cm inner diameter that is wrapped with copper wire (0.867 mm diameter). The coil has a theoretical field of 14.5 mG/mA and a measured field of 13.7 mG/mA (which implies a fill factor of 94%) and is typically driven with 27.7 mA (producing a 380 mG field). The bias field is kept on for the duration of the experiment as it is needed to provide a quantization axis for velocity selection and Bragg diffraction as well.

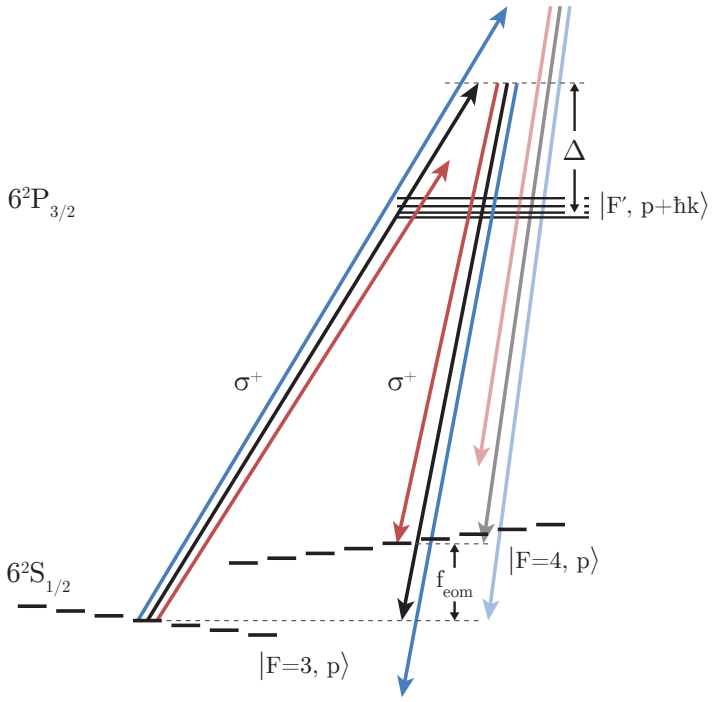

Figure 4.4: The carrier frequency (black) and sidebands (blue and red, respectively) used for the state selection Raman transition and the relevant atomic levels. The faded lines represent other possible frequency pairs with suppressed transition probability due to their increase detuning.

The state selection Raman frequencies are generated using the far detuned light from the SolsTiS laser and an electro-optic modulator (EOM3) shown in Fig. 4.3. The 899 laser (and therefore the SolsTiS laser) is typically locked to 15 GHz blue of the reference laser frequency $f_{3,4'}$. The injection locked light from the SolsTiS is switched on with AOM15 and coupled into a fiber to create a 70 μs square pulse that will drive the Raman transition. To generate the required Raman frequencies, the pulsed light is passed through EOM3 modulated at $f_{\text{eom}} = 9.192625$ GHz and coupled into a fiber (Fiber:Bragg). The light out of the fiber is collimated to a waist of 6.2 mm and converted to circular polarization with a $\lambda/4$ waveplate before being sent into the vacuum chamber along the $\hat{z}$ axis as shown in Fig. 4.9.

The relevant laser frequencies and atomic states that make up the state selection pulse are shown in Fig. 4.4. The dominant Raman transition is between the red sideband and the carrier of the modulated light, although there is a weaker transition using the blue sideband. Since the blue sideband has the opposite phase of the red sideband, these two transitions destructively interfere and reduce the overall Rabi frequency of the transition. Additionally, because of the retro-reflection mirror and waveplate inside the chamber, the σ^+ light that drives the atoms on the way up also interacts as σ^- polarization on the way down. Since the state selection pulse is Doppler insensitive, this σ^- light also drives Raman transitions with

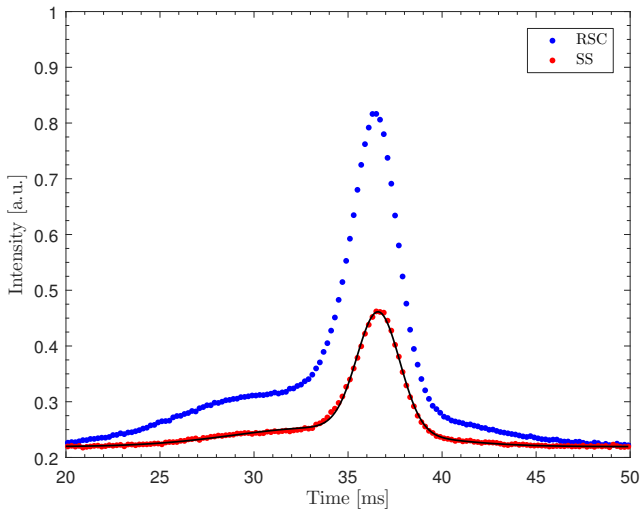

Figure 4.5: Time-of-flight signals for Raman sideband cooling (blue) and state selection (red) after the blow-away beams are applied. A double Gaussian fit to the state selection signal is shown in black.

approximately equal strength. The relative phase of the Rabi frequencies between the σ^+ and σ^- light varies as a function of height and will therefore oscillate between constructively and destructively interfering with a spatial period of 1.63 cm. For this reason it is important to check the location of the atoms during state selection to ensure they are located at a constructive maximum.

Detuning: The electro-optic modulator frequency of $f_{\text{eom}} = 9.192625$ GHz used in the experiment ends up being about -6 kHz different from the cesium hyperfine frequency. The reason is that the laser fields cause ac-Stark shifts in the ground state energy, modifying the resonance frequency. A detuning of $\delta = 0$ only results in maximum population transfer if the Rabi frequencies of the two fields are the same, which results in ac-Stark shifts that are equal for the two ground states. If the sideband produced by the EOM is not equal in strength to the carrier, then the optimal detuning occurs when $\delta \approx (|\Omega_2|^2 - |\Omega_1|^2)/4\Delta$ [109].

4.2.1 Blow-Away Beams

The resonant blow-away beams used before and after the state selection pulse to remove unwanted atoms are derived from the spectroscopy light and the MOT light as shown in Figures 3.3 and 3.7. For the 3-state blow-away, a small amount of reference light is picked off by a PBS cube before the spectroscopy and shifted by AOM3 driven at 66.8 MHz. The 4-state blow-away frequency is created by turning off the repump light and deflecting a small amount of MOT light with AOM12 driven at 95 MHz. Both frequencies are coupled together into Fiber:Blow-Away and sent to the main chamber as shown in Fig. 4.9.

The purpose of the blow-away beams is to scatter photons off atoms in a given hyperfine

state and accelerate them so they no longer overlap the remaining atoms during detection. The 3-state blow-away beam has a frequency of $f_{3,2'} + 3.7$ MHz (slightly blue-detuned from the $3 \rightarrow 2'$ cycling transition) to maximize the scattering rate when taking into account the Doppler shift from the accelerating atoms. The 4-state blow-away has more available power and therefore is just driven on resonance at $f_{4,5'}$.

The fiber carrying the blow-away beams is collimated to be diverging and the light is sent into the chamber slightly off-axis to reduce the amount of light reflecting off the retro-reflect mirror, which would otherwise push the atoms in the wrong direction (and create an optical molasses). The blow-away beams typically contain a couple milliwatts of power and are switched on for 2 ms to 6 ms. To prevent either blow-away beam from driving the atoms into dark states, the light is adjusted to an elliptical polarization with a $\lambda/4$ waveplate after the fiber.

A time-of-flight florescence signal of the state selected atoms after blow-away is shown in Fig. 4.5. The signal reduction compared to Raman sideband cooling comes from the residual $m_F \neq 0$ atoms being removed, as well as an inherent inefficiency in our Raman pulses most likely caused by the finite laser beam size and the spatial extent of the atoms. When performing state selection on simple atomic fountain without RSC, the state selection pulse reduces the signal by a factor of 15, lower than the factor of 9 expected from theory (if atoms are equally distributed into the nine m_F levels of $F = 4$).

4.3 Velocity Selection

As a final step to prepare the atomic sample for interferometry, the momentum width of the atoms in the vertical direction is reduced by a series of Doppler-sensitive Raman pulses. Since Bragg diffraction is very sensitive to the velocity of the atoms relative to the laser detunings, it is important to have a very narrow momentum distribution so the dynamics for all atoms in the sample are the same. The dependence of initial velocity on Bragg diffraction is described briefly in Section 2.5, but is also more explicitly shown in Fig. 4.6. For $n = 5$ Bragg diffraction, any atoms traveling faster than $|v_r|/10$ relative to the Bragg resonant velocities have significant population transfer into undesired states (as well as increased diffraction phase shifts).

Similarly, the plane-wave assumption in the derivation of the Bragg diffraction theory assumes that the atom is not localized and has infinite spatial extent. For thermalized atoms, the average wave-packet size can be approximated as the thermal de Broglie wavelength $\lambda_{\text{th}} = h/\sqrt{2\pi m k_{\text{B}} T}$. For a 300 nK sample of atoms this length is approximately 270 nm, which is smaller than the period of the Bragg potential $\lambda/2 = 426$ nm. In order for the plane-wave assumption to be somewhat valid, the atom should have a wave function that extends into multiple lattice sites so that the interaction can be treated as non-local. If an atom is velocity selected such that it has a momentum uncertainty σ_p, then the position uncertainty through the Heisenberg uncertainty principle can be considered as a type of coherence length

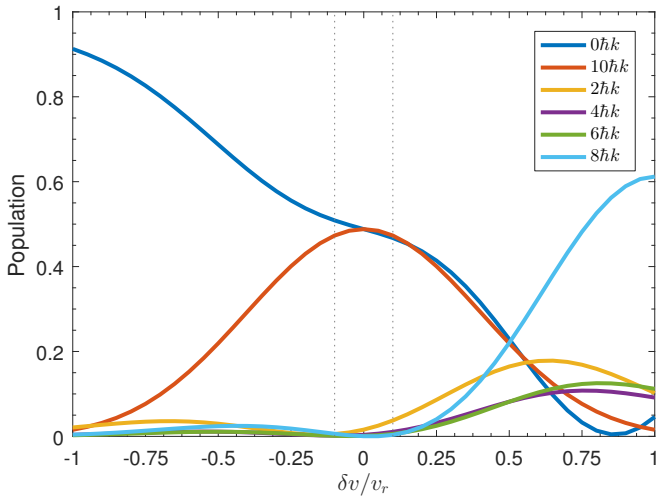

Figure 4.6: Population transfer of an atom in $|0\rangle$ to different momentum states for $n = 5$ Bragg diffraction as a function of the atom's velocity relative to resonance. Vertical dashed lines indicate the $\pm v_r/10$ velocities.

$\sigma_x = \hbar/2\sigma_p$. If the atom is selected to have a velocity uncertainty of $\sigma_p = mv_r/10$, then the corresponding position uncertainty $\sigma_x = 680$ nm is longer than a lattice period.

The Raman sideband cooling stage produces samples that are approximately 200-400 nK, which correspond to a 1σ velocity distribution of 1-1.5 v_r, where the recoil velocity $v_r = \hbar k/m$ is approximately 3.52 mm/s for cesium atoms and 852 nm photons. This velocity width is a factor of 10 larger than what is needed for clean Bragg diffraction and therefore an additional preparation step is required. One way this can be accomplished is by cooling the atoms further using sub-recoil techniques such as evaporative cooling [111, 112] or by manipulating the phase-space density using delta-kick cooling to reduce the effective temperature [113–115]. While these methods are quite powerful, they come at the cost of increased experimental complexity which would be hard to incorporate into our apparatus. Therefore the simplest option is to use a Doppler-sensitive Raman transition to transfer atoms with the correct velocity to a different hyperfine state so that the hot atoms can be removed with a blow-away pulse (similar to what was done with state selection).

In Doppler-insensitive Raman transitions, the state selectivity comes from the large detuning of the undesired states from the main transition relative to the Rabi frequency. If two counter-propagating lasers are used instead of two co-propagating lasers, then the momentum of the atoms becomes important as the Doppler shift for the two frequencies no longer cancel. If the Raman transition is on resonance with a particular velocity class of atoms, then any atoms with other velocities will have a larger detuning and therefore have a suppressed transition probability. Consider the Doppler-sensitive Raman transition shown in Fig. 4.7, where the two-photon detuning δ_{doppler} is now a function of the atom velocity. Similar to what was done in Section 4.2, the Hamiltonian for an atom interacting with counter-propagating electric fields can be solved by taking into account the momentum

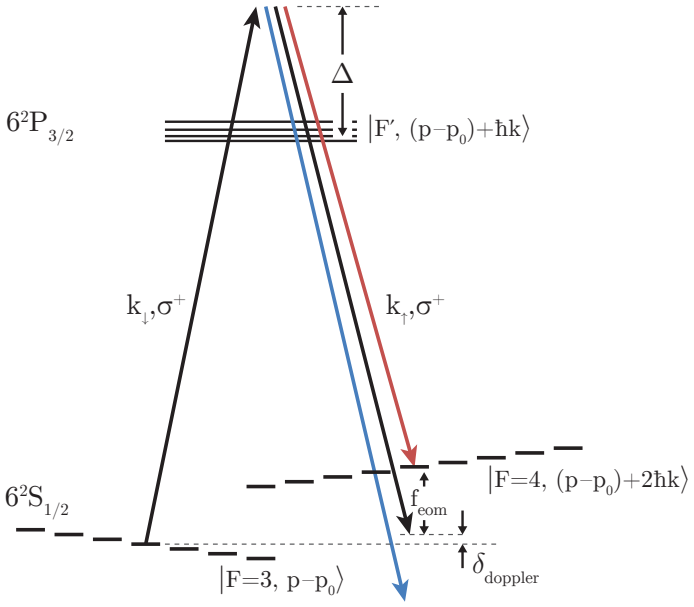

Figure 4.7: Frequency scheme for velocity selective Raman transitions between two ground states using a virtual excited states. The two wave-vectors $k_\downarrow$ and $k_\uparrow$ are counter-propagating.

transferred by the fields [116]. The resulting evolution of the initially unpopulated state $|g_2\rangle$,

$$|g_2|^2 = \frac{|\Omega_1|^2 |\Omega_2|^2}{4\Delta^2 \bar{\Omega}^2} \sin^2\left(\frac{\bar{\Omega} t}{2}\right)$$
$$\bar{\Omega}^2 = \frac{\left(|\Omega_1|^2 + |\Omega_2|^2\right)^2}{(4\Delta)^2} + \frac{\delta\left(|\Omega_1|^2 - |\Omega_2|^2\right)}{2\Delta} + \delta^2$$

is almost identical to the Doppler-insensitive Raman transition, except that detuning δ is a function of the atom's momentum

$$\delta \equiv \left(\frac{(p - \hbar k_\downarrow)^2}{2m\hbar} - \frac{(p + \hbar k_\uparrow)^2}{2m\hbar}\right) - \omega_{\rm hf} - (\omega_\downarrow - \omega_\uparrow),$$

where p is the momentum of the atom, $k = \omega/c$ is the wavenumber of the lasers, m is the mass of the atom, and $\omega_{\rm hf}$ is the hyperfine splitting. If the laser frequencies are chosen to be resonant with an arbitrary momentum p_0 such that $\delta = 0$, then any other atom with momentum p will have a detuning

$$\delta_{\rm doppler} = -\frac{p - p_0}{m}(k_\uparrow + k_\downarrow)$$
$$= -\frac{v - v_0}{c}(\omega_\uparrow + \omega_\downarrow),$$

which is just the Doppler shift of the two laser frequencies. This means that atoms that have a larger velocity difference are further off-resonance and will therefore tend to have a smaller transition amplitude.

A single Doppler-sensitive Raman transition will transfer the resonant atoms from the $F = 3$ state to $F = 4$ and kick the atoms with the momentum of two photons. A 3-state blow-away beam can then be used to remove the remaining $F = 3$ atoms from the cloud, resulting in an ensemble with a narrower velocity distribution. Since the Ti:Sapphire laser is locked to +15 GHz blue of $f_{3,2'}$, leaving the atoms in the $F = 4$ state would mean that there would be a 24 GHz single photon detuning for Bragg diffraction. As the SolsTiS laser cannot output the necessary laser power for such a detuning, the atoms are velocity selected with a second Raman pulse to transfer them back to $F = 3$ (followed by blowing away any remaining 4-state atoms).[2]

The effectiveness of using Raman transitions for velocity selection can be seen by considering a thermal cloud of atoms at 200 nK which has a 1-sigma velocity width of $\sigma_v = v_r$. For a double Raman pulse sequence centered on $p_0 = 0$, the resulting momentum distribution is then equal to

$$f(p) = \frac{1}{\sqrt{2\pi(mv_r)^2}} e^{-p^2/2(mv_r)^2} |g_2|^4.$$

To simplify the equation somewhat, we can assume the Rabi frequencies for the two beams are equal $\Omega \equiv \Omega_1 = \Omega_2$ and rescale $\{p, t, \Omega\}$ in terms of dimensionless parameters $\{u, \tau, a\}$ such that

$$f(u) = \frac{a^4}{\sqrt{2\pi}} e^{-u^2/2} \frac{\sin^4\left(\tau\sqrt{a^2+u^2}\right)}{(a^2+u^2)^2},$$

where $p = umv_r$, $t = \tau/\bar{k}v_r$, $\Omega^2 = 4a\Delta(\bar{k}v_r)$, and $\bar{k} = (k_\uparrow + k_\downarrow)/2$ is the average of the two laser wavenumbers.

A comparison between a single 800 μs ($\tau = 20.76$) velocity selection pulse and two consecutive 400 μs ($\tau = 10.38$) pulses is shown in Fig. 4.8, where the intensity of each pulse is optimized for $p = 0$ (which occurs when $a = \pi/2\tau$). While the double length velocity selection pulse results in a narrower distribution, it also produces a larger fraction of atoms with a velocity of $v_r/4$. On the other hand, the two-pulse velocity selection procedure produces a smoother distribution which can be approximated by a Gaussian with a 1-sigma standard deviation of

$$\sigma_v \approx \frac{v_r}{\sqrt{2}\tau} = \frac{1}{\sqrt{2}\bar{k}t}.$$

In a similar fashion to the state selection pulse, the velocity selection pulses are generated by the optics layout shown in Figures 4.1 and 4.3. The 400 μs square pulses used for the Raman pulses are created by switching on AOM15 at $t = 1.221$ s and $t = 1.231$ s, with a

[2]This has the added benefit of narrowing the velocity distribution further.

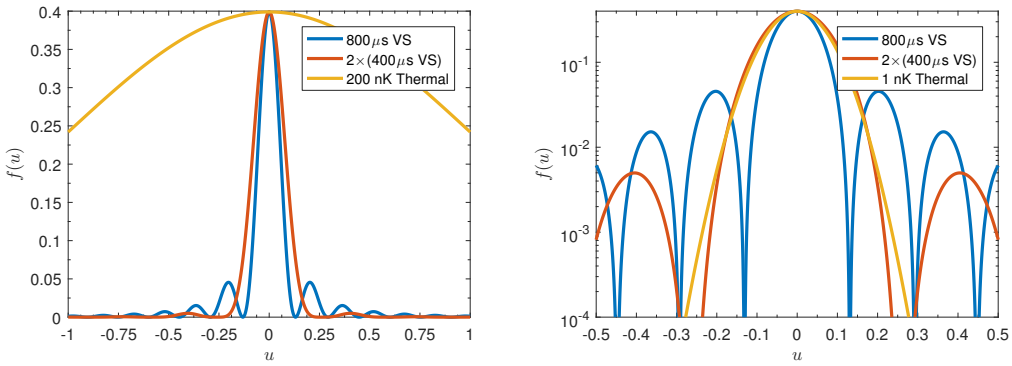

Figure 4.8: The velocity distributions of a 200 nK thermal sample after a 800 μs velocity selection pulse (blue) or two consecutive 400 μs pulses (red), in units of $u = v/v_r$. Left: The resulting distributions compared to that for 200 nK. Right: Log-scale comparison which also shows the similarities to a 1 nK thermal distribution approximation.

3-state blow-away at $t = 1.223$ s lasting 6 ms and a 4-state blow-away at $t = 1.233$ s for 2 ms. The light coupled into Fiber:Switchyard is split by AOM16 which is driven at 180 MHz and combined with the light that is double-passed by AOM18 and modulated by EOM3. The double pass is driven by a ramping DDS running between 80 and 90 MHz, which serves to compensate for the Doppler shift caused by gravity and is described in more detail in Section 4.3.1. The electro-optic modulator is driven at 9.188631 GHz, approximately 4 MHz lower than for state selection, to detune the velocity-insensitive Raman transition far from resonance so only the Doppler-sensitive transitions take place.

The EOM modulated light and the deflected light from AOM16 are combined on a PBS cube and either coupled into the main Bragg fiber or deflected by AOM19 and then sent to a secondary fiber (Fiber:VS) that has a smaller waist when collimated; see Fig. 4.9. Using the larger 6.2 mm Fiber:Bragg collimator for velocity selection tends to give a larger signal as the atom cloud has a reasonably large diameter. Alternatively, the Fiber:VS fiber port has a waist of 3.9 mm which allows for some transverse spatial selectivity which may be important for systematics, see Section 5.4.2. The two different paths for velocity selection are overlapped on an uncoated glass plate with 4% reflectivity and sent through a $\lambda/4$ waveplate and then into the chamber.

Since the two optical paths from AOM16 and EOM3 have opposite linear polarization going into the fiber, the waveplate converts those orthogonal polarizations in opposite circular polarizations in the vacuum chamber. For the Raman transition, the unmodulated light interacts with the atoms on the way up as σ^+. The EOM modulated frequencies which are traveling up as σ^- polarization get reflected off the top mirror and interact with the atoms traveling down as σ^+. A $\lambda/4$ waveplate at the top of the chamber ensures that the $\sigma^\pm$ polarizations going up convert to $\sigma^\mp$ on the way down. Due to the large Doppler shift of the moving atoms, the σ^- polarization pairing does not drive a transition as it is detuned by several megahertz.

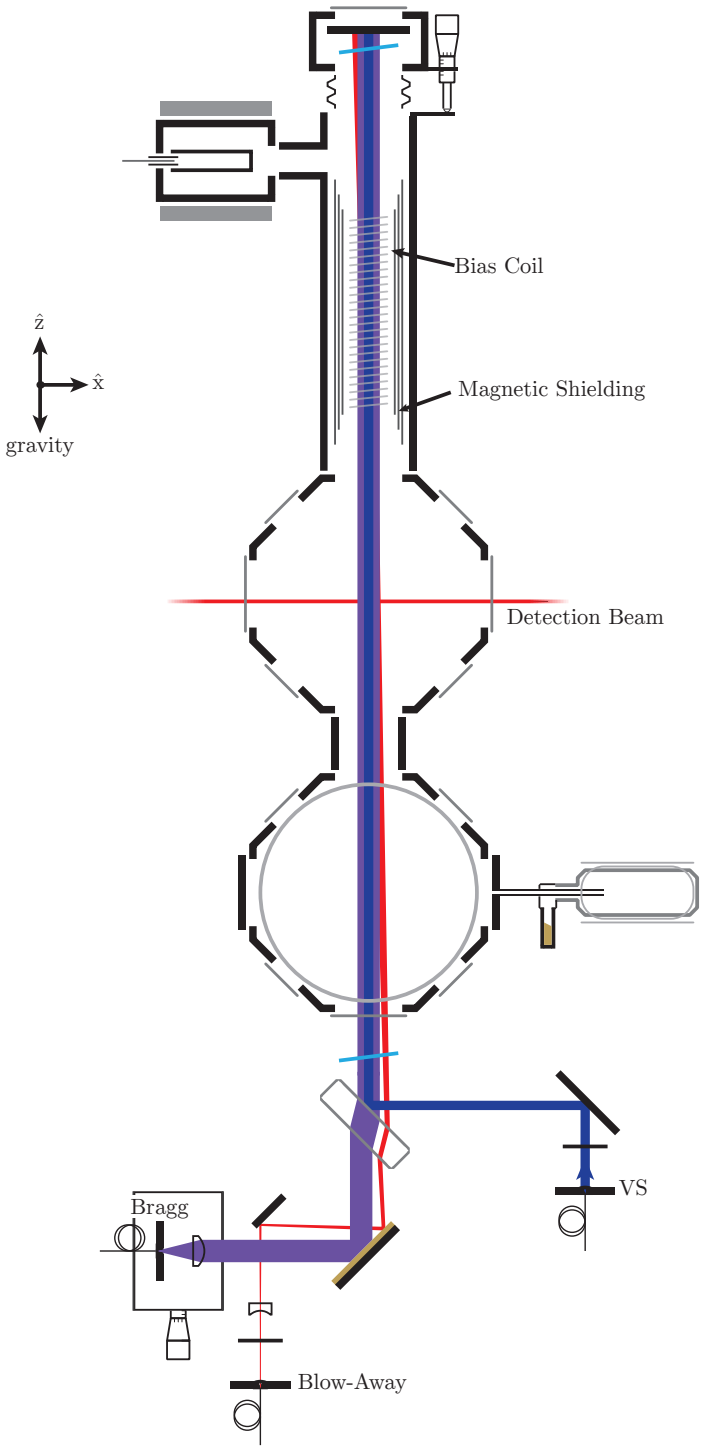

Figure 4.9: The optical setup of the state and velocity selection, Bragg beam splitters, and blow-away beams into the main vacuum chamber‘.

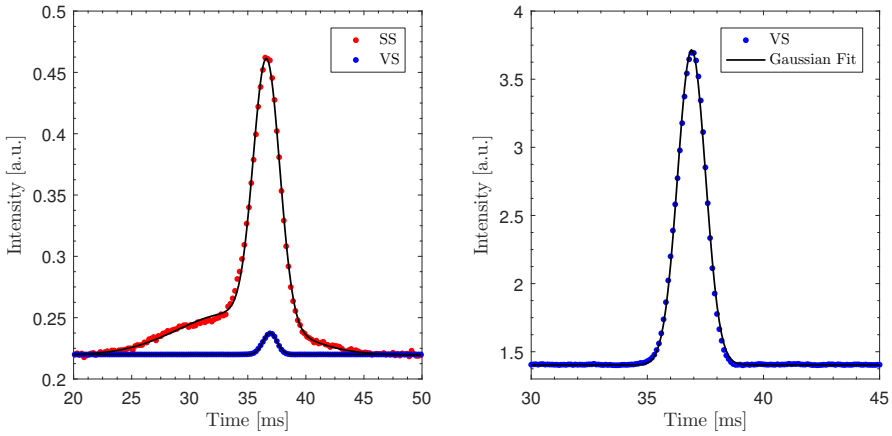

Figure 4.10: Time-of-flight signal of the velocity selected atom sample. Left: Comparison between the state selection (red) and velocity selection (blue) signals where the latter has been rescaled to take into account the neutral density filter used in the state selection. Right: Unscaled velocity selection signal with Gaussian fit (black) with no neutral density filter.

A sample time-of-flight signal of the atom cloud after two 400 μs velocity selections pulses and blow-away beams is shown in Fig. 4.10, as well as a comparison to the state selection signal. The velocity selection signal is fitted reasonable well to a Gaussian with a width of $\sigma = 0.6$ ms, as compared to the state selection signal which needs to be fit to a double Gaussian. It should be noted that the velocity selection width is smaller than that of the up-going fountain, which means that the Raman sideband cooling must be cutting off part of the cloud and the temperature estimates after RSC are probably too low.

In order to verify validity of the velocity selection calculations, the effective Raman frequency width of the transition was measured for different pulse lengths and compared to theory. For a given pulse length, the two-photon detuning and power for a single velocity selection (VS) pulse was optimized to give the largest detection signal. Then the effective frequency width was measured by sending in a second VS pulse and varying the two-photon detuning (while keeping the first VS pulse the same) to find the detuning that gave a full-width half-maximum (FWHM) signal. A comparison between theory and the measurements for 100-, 200-, 400-, and 800-μs pulses is shown in Fig. 4.11. The signal size is compared as a ratio to the 100-μs amplitude instead of as an absolute value to make the comparison to theory easier.

The theory contains no free parameters, with the assumption that the two Rabi frequencies are equal and that the initial velocity distribution[3] has a width of $\sigma_v = v_r$. Velocity selection distributions are calculated as a function of the second pulse detuning δ_2 and integrated over all velocities to get the total signal size $A(\tau, \delta_2)$ as a function of pulse width and detuning:

[3]The initial velocity width has little impact on the result as long as it is large.

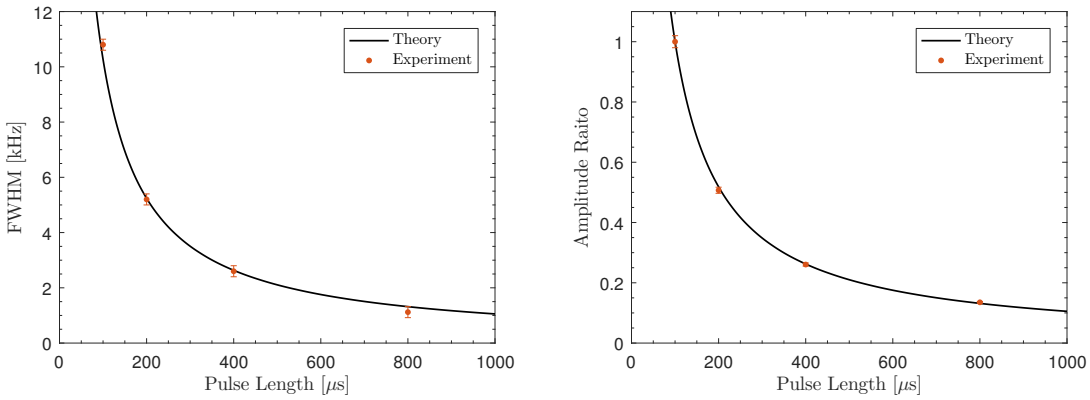

Figure 4.11: A comparison between the theory of velocity selection and experiments with different pulse lengths. Left: The effective frequency width of the velocity selection two-photon detuning (measured by the FWHM of the second of two VS pulses), as a function of pulse length. Right: The signal loss as a function of pulse length for two resonant velocity selections, normalized relative to the signal of the 100-μs velocity selection.

$$A(\tau, \delta_2) = \int \frac{1}{\sqrt{2\pi(mv_r)^2}} e^{-v^2/2v_r^2} \left|g_2(\tau, v)\right|^2 \left|g_2(\tau, v - \delta_2/2\bar{k})\right|^2 dv.$$

The full-width half-max $2\delta_\tau$ frequencies of the resulting amplitudes were then calculated numerically by solving $A(\tau, 0) = 2A(\tau, \delta_\tau)$ for δ_τ.

4.3.1 Gravity Ramp

Over the duration of the experiment, the velocity of the free-falling atoms is constantly changing due to the acceleration of gravity at a rate of $\Delta v = -gt$. Since the velocity selection and Bragg diffraction dynamics are velocity dependent, the laser beams need to be ramped to compensate for the changing Doppler shift.

Recall that the 899 Ti:Sapphire laser is offset locked to the reference laser frequency $f_{3,4'}$ by an amount $f_\mu + f_{\mathrm{PLL}}$, where f_μ is the microwave mixing frequency and f_{PLL} is the external frequency reference for the 899 phase lock. The two counter-propagating laser frequencies $\{f_{L_1}, f_{L_2}\}$ that interact with the atoms in the chamber are then

$$\begin{aligned} f_{L_1} &= f_{3,4'} + f_\mu + f_{\mathrm{PLL}} + f_{\mathrm{AOM15}} + f_{\mathrm{AOM16}} \\ f_{L_2} &= f_{3,4'} + f_\mu + f_{\mathrm{PLL}} + f_{\mathrm{AOM15}} + 2f_{\mathrm{AOM18}}. \end{aligned}$$

Consider what would happen if the frequencies for the phase lock and the double-pass AOM are chosen such that $f_{\mathrm{AOM18}} = -f_{\mathrm{PPL}} = f_0 + \Lambda_{\mathrm{d}} t$, where Λ_{d} is a frequency ramp rate and f_0 a frequency offset. Then in the freely falling reference frame of the atoms, the frequency difference between the lasers changes at a rate given by the difference in their Doppler shifts:

$$\begin{aligned}\frac{\partial(\Delta f)}{\partial t} &= \frac{\partial}{\partial t}\left[\left(1-\frac{gt}{c}\right)f_{L_1} - \left(1+\frac{gt}{c}\right)f_{L_2}\right] \\ &= -\frac{2g}{c}\left(f_{3,4'} + f_\mu + f_{\mathrm{AOM15}} + \frac{f_{\mathrm{AOM16}}}{2}\right) - 2\Lambda_\mathrm{d} \\ &= -22.9957\ \mathrm{MHz/s} - 2\Lambda_\mathrm{d}\end{aligned}$$

for typical values of $f_\mu = 15$ GHz, $f_{\mathrm{AOM15}} = 80$ MHz, $f_{\mathrm{AOM16}} = 180$ MHz, a cesium transition frequency of $f_{3,4'} = 351.730902$ THz, and a local gravitational acceleration of $g = 9.7995$ m/s taken from a measurement just outside of our lab in Berkeley, California. Therefore if we chose Λ_d to be equal to 11.4978 MHz/s, then the changing frequency shift due to gravity is canceled. In addition, because the phase lock frequency f_{PPL} is ramped in the opposite direction, the frequency sum (and therefore the effective wave-vector) is constant

$$f_{L_1} + f_{L_2} = 2\left(f_{3,4'} + f_\mu + f_{\mathrm{AOM15}} + \frac{f_{\mathrm{AOM16}}}{2}\right),$$

which is an important property for interferometers where the phase depends on the laser frequencies.

The ramp frequency $f_{\mathrm{ramp}} = f_0 + \Lambda_\mathrm{d} t$ is generated by an Analog Devices AD9958 DDS which is clocked to an external frequency synthesizer f_{clock}. To get the smoothest ramp possible, a very small frequency step and time step increment are used to create the frequency ramp, which presents a problem when trying to program arbitrary ramp rates. A DDS runs off an internal clock which is typically phased lock to some multiple of the external reference (usually 10 MHz). The synthesizer can only update the frequency ramp at integer multiples of the clock period and similarly the frequency step must also be an integer multiple of the clock frequency. For an internal clock of $f_{\mathrm{int}} = 20 \times f_{\mathrm{clock}}$, the time and frequency steps can be

$$\Delta t_{\mathrm{step}} = \frac{n}{f_{\mathrm{int}}}, \quad \Delta f_{\mathrm{step}} = \frac{m}{2^{32}} f_{\mathrm{int}}$$

for a 32-bit DDS, where $\{n, m\}$ are integers. For the AD9958, the minimum possible n is 4 and m is chosen to be 2 such that the ramp rate is

$$\frac{\Delta f_{\mathrm{step}}}{\Delta t_{\mathrm{step}}} = \Lambda_\mathrm{d} = \frac{(20 f_{\mathrm{clock}})^2}{2^{33}}.$$

In order to frequency ramp at a rate $\Lambda_\mathrm{d} = 11.4978$ MHz/s, the reference clock must therefore be $f_{\mathrm{clock}} = 15.7135$ MHz. Small changes to the gravity ramp rate can then be done by modifying the reference clock frequency without changing the DDS programing. The value of the offset frequency f_0 to the ramp rate is varied to optimize the velocity selection pulses and switched to a different value for Bragg diffraction. For velocity selection, the frequency

ramp has a frequency offset $f_0 = 93.6643$ MHz and the ramp is triggered starting at $t = 1.033$ s when the cloud is released from the moving molasses.

One important point that needs to be addressed is the ramping double-pass AOM18 since the deflection efficiency and fiber coupling will depend on the ramp frequency. The laser beam that goes through the AOM is focused into the crystal with an $f = 150$ mm lens, which helps minimize the efficiency change, but the result is far from perfect. To make sure that the power coupled into the fiber is constant regardless of the drive frequency, the RF power to the AOM is modified by an arbitrary waveform generator using a voltage controlled attenuator. The waveform is triggered at the same time as the ramp and is programmed such that the output voltage flattens the optical power of the double-pass AOM.

4.4 Bragg Diffraction

After preparing the atoms in the $|F = 3, m_F = 0\rangle$ state with a velocity spread of less than $v_r/10$, the sample is finally ready for interferometry using Bragg diffraction. Similar to velocity selection, two counter-propagating laser fields are used to drive a multi-photon Bragg transition between different momentum states of the atoms as described in Section 2.5.

For the first two Bragg pulses in the interferometer sequence, the frequency generation scheme is nearly identical to the velocity selection pulses with some small modifications. Since Bragg diffraction drives transitions directly between different momentum states without changing the atom's hyperfine state, the EOM which is used in state and velocity selection is disabled by switching off the microwave frequency to the amplifier and by turning off the amplifier voltage (to ensure there is no microwave leakage onto the Bragg beams). The two-photon resonance condition is also different for Bragg diffraction, so the ramp frequency $f_{\text{ramp}} = f_0 + \Lambda_{\text{d}} t$ that controls the double-pass AOM and the 899 phase lock is jumped to a second ramp with a different starting frequency f_0' using an RF switch. The frequency ramps for both the velocity selection and Bragg diffraction are generated on the same dual channel DDS and both ramps are triggered at the same time so that the detunings of the Bragg diffraction pulses are independent of the atom's free-fall velocity.

Just as before, the deflected light from AOM16 is coupled into Fiber:Bragg with one linear polarization and the zeroth order light that gets double passed by AOM18 is coupled into the fiber with the opposite polarization. The orthogonal polarizations of the two frequencies again allow the upwards moving σ^+ light to only interact with reflected σ^- polarized light (which gets converted to σ^+ by the retro-reflect mirror and waveplate). The $\sigma^+\sigma^+$ lattice that is created by the counter-propagating light fields produce the interaction potential that drives Bragg diffraction, assuming the frequency difference is resonant with the atoms. The conjugate $\sigma^-\sigma^-$ lattice which travels opposite the atoms is usually far enough Doppler detuned to be ignored. However, near the turn-around point of the atom's free-fall trajectory, the two moving lattices become degenerate and cause problems. This can be avoided exper-

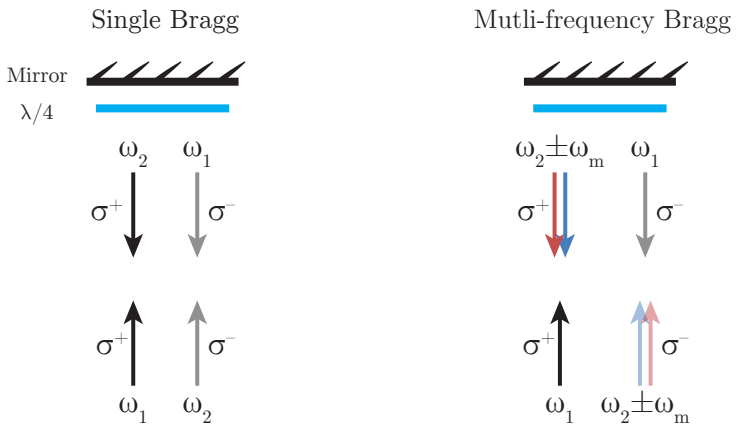

Figure 4.12: The polarization combinations that make up the Bragg diffraction interaction potentials for the first two Bragg pulses (single) and last two pulses (multi). The laser frequency ω_1 comes from AOM18, while ω_2 and $\omega_2 \pm \omega_m$ are generated by AOM16. The σ^- polarization lattices (faded arrows) do not contribute to Bragg diffraction as they are off-resonant by the Doppler shift.

imentally by making sure to never perform Bragg diffraction when any atom trajectory is near zero velocity in the lab frame.

For the last two Bragg pulses, the Ramsey-Bordé interferometer configuration requires that atoms with momentum $p = 2n\hbar k$ are diffracted up while the $p = 0$ atoms are diffracted down. If the two laser frequencies ω_1 and ω_2 are resonant with the transition between the $|0\rangle$ and $|n\rangle$ momentum states, then the laser frequencies that enable $|0\rangle \to |-n\rangle$ and $|n\rangle \to |2n\rangle$ are

$$\omega_1' = \omega_1, \qquad \omega_2' = \omega_2 \pm \omega_m = \omega_2 \pm 8n\omega_r,$$

where $\omega_r = \hbar(k_1 + k_2)^2/8m$. These two frequency pairs can be created by driving AOM16 with two frequencies instead of a single frequency. Since the laser beam is focused heavily into the AOM crystal with an $f = 150$ mm telescope and the frequency difference $(\omega_m/2\pi)$ is less than a megahertz, the two deflected frequencies are nearly overlapped and follow the same optical path into the fiber (allowing them to be coupled with approximately the same efficiency). More importantly, the overlap means that any path length fluctuations will be common mode to both frequency components and will not cause fluctuations in the phase of ω_m. This is critical as minimizing the phase noise of ω_m is necessary for a recoil frequency measurement using a conjugate Ramsey-Bordé configuration as was shown in Section 2.3. Previous experiments that did not use this dual-frequency AOM technique instead required that the beat frequency was locked to an external reference by feeding back to the laser phase [40].

Next, the frequency pair from AOM16 are again combined with the double-pass frequency, coupled into the fiber, and sent to the vacuum chamber. Whereas before only a single

frequency component from each direction contributed to the $\sigma^+\sigma^+$ lattice, now there are two frequencies with σ^+ polarization traveling downward which combine with the single upward traveling σ^+ frequency component to generate two moving lattices for the two Bragg resonances, as depicted in Fig. 4.12.

When driving the acoustic-optical modulator with two frequencies there is necessarily a beat in the deflected optical power due to interference of the two frequencies. Therefore the undeflected zeroth order of the AOM must also have an optical power beat due to conversation of energy. While the optical intensity beat on the frequency pair is unavoidable, the intensity beat on the counter-propagating laser which should have a single frequency is unnecessary and should be eliminated. To accomplish this, a complimentary acousto-optic modulator (AOM17) is driven with the same frequency difference but with a phase that is shifted by 90 degrees. When the RF to AOM16 is at a minimum and the transmitted power is maximized, AOM17 then deflects that excess power into a beam dump (and when the deflection of AOM16 is maximized the deflection of AOM17 is zero). The net effect is that if the deflection efficiency of AOM17 is chosen appropriately (by alignment and choice of RF attenuation), the optical power that is undeflected by AOM17 should be approximately constant.

If we assume that the first AOM has a deflection efficiency of α for a single frequency and 4α for two frequencies (where the factor of 4 comes from the beat), then the largest the undeflected power can be is $1-4\alpha$. If the double pass has an efficiency of β per pass, then the maximum Rabi frequency (and therefore minimum power needed) for Bragg diffraction occurs when

$$\begin{aligned} 0 = \frac{\partial}{\partial\alpha}\Omega_1\Omega_2 &\propto \frac{\partial}{\partial\alpha}\left[4\alpha\cdot(1-4\alpha)\beta^2\right] \\ &\propto 4(1-8\alpha)\beta^2 \end{aligned}$$

or $\alpha = 1/8$. Therefore the least power is required when AOM16 deflects one eighth the maximum power for a single frequency and at most half the power for dual-frequency operation. The efficiency of an AOM is given by

$$\eta \cong \sin^2\left(\frac{\pi}{\lambda}\gamma\sqrt{P_a}\right),$$

where λ is the wavelength of light, γ is a constant that depends on the device properties, and P_a is the power of the acoustic wave [87]. When driving the AOM with two frequencies with a frequency difference $2\omega_m$, the acoustic power has a beat and can be written as $P_a = P\sin^2\omega_m t$. The undeflected power through the multi-frequency AOM16 is then

$$\begin{aligned} (1-\eta_{16}) &= 1-\sin^2\left(\frac{\pi}{\lambda}\gamma\sqrt{P}\,|\sin\omega_m t|\right) \\ &= \cos^2\left(\frac{\pi}{4}\,|\sin\omega_m t|\right), \end{aligned}$$

where $\pi\sqrt{P}\gamma/\lambda = \pi/4$ for the optimized configuration that gives a peak-to-peak amplitude beat of 50% (or $4\alpha = 1/2$). If the compensating AOM17 is driven with the same frequency difference shifted by 90 degrees, then the undeflected power is

$$\begin{aligned}(1-\eta_{17}) &= (1-\eta_{16})\cos^2\left(\frac{\pi}{4}\left|\sin\left(\omega_m t+\pi/2\right)\right|\right)\\ &= \cos^2\left(\frac{\pi}{4}\left|\cos\omega_m t\right|\right)\cos^2\left(\frac{\pi}{4}\left|\sin\omega_m t\right|\right),\end{aligned}$$

which is unfortunately not exactly zero as one would hope (due to the AOM deflection non-linearity), thus resulting in a ripple that has a peak-to-peak amplitude of roughly 2%. While these small fluctuations do induce frequency sidebands on the laser, they should be small and off-resonant to the atoms in the interferometer. Some rudimentary systematic checks were performed by making the ripple larger with no measurable effect, but more careful analysis may be required.

The electronic setup that generates the frequencies for AOM16 and AOM17 are shown in Fig. 4.13. For single Bragg diffraction, the multi-frequency TTL is off and the 180 MHz crystal frequency is sent into the AOM amplifiers through the -10dB port of a directional coupler. For multi-frequency operation, the 180 MHz frequency is instead mixed with a frequency f_m which determines the frequency difference for the two Bragg beams. To get the 0 and 90 degree components to drive the AOM pair, an offset frequency $\delta = 4$ MHz is split by a 90 degree splitter and mixed with $\delta + f_m$ split by a zero degree splitter. After mixing and low pass filtering, the outputs of the two mixers are f_m and f_m shifted by 90 degrees. These frequencies are then used as inputs to a "compound mixer" as the IF frequency, while the LO is driven by the 180 MHz crystal to produce 180 MHz $\pm$ f_m at 0 and 90 degrees.

While a standard balanced mixer could serve this purpose, there is almost always a residual amount of LO frequency at the mixer RF output port which cannot be easily filtered due to the small IF frequency ($f_m < 1$ MHz). Instead, part of the 180 MHz is split off and decomposed to its quadrature components and combined back into the signal to cancel the LO frequency. By varying the current into the mixers, an effective attenuator is created which can be used to exactly tune the phase and amplitude needed to cancel both quadratures of carrier in the $f_m \times 180$ MHz mixer output.[4] The mixer output still has higher mixing harmonics, but those are less important to the interferometer as they are not resonant with anything, unlike the 180 MHz carrier (which gives the same frequency as the single-frequency Bragg diffraction).

Optimization: The various attenuators in Fig 4.13 are used to tune the RF power to the AOMs such that a) when AOM16 is running multi-frequency it has a deflected peak of 50%, b) AOM17 minimizes the resulting ripples of the undeflected beam, c) when AOM16 is running single frequency it deflects 12.5%, and finally d) when running single frequency, AOM17 should have the same undeflected power as when it is running multi-frequency. This

[4]The output of this type of mixer can have a LO carrier which is -80dB from the sidebands when tuned well.

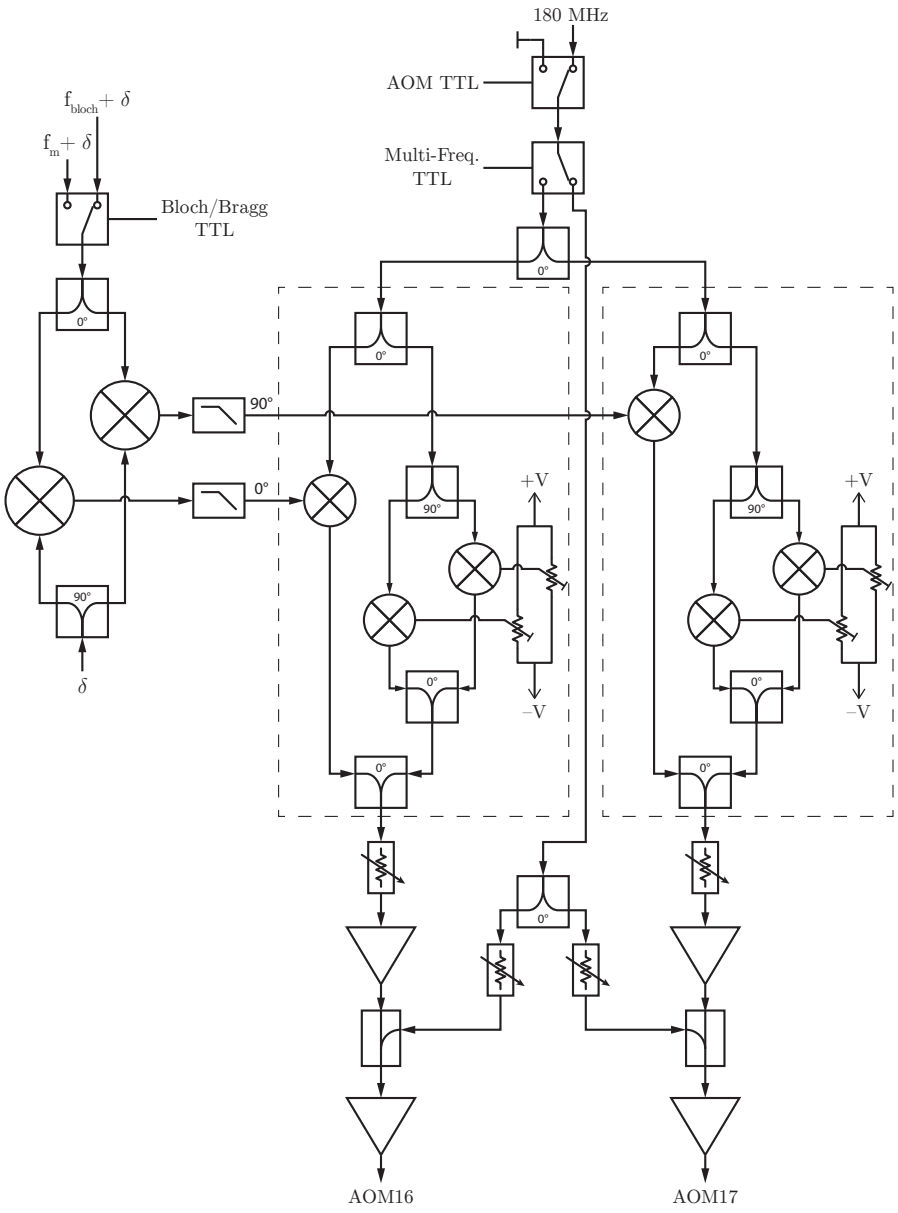

Figure 4.13: The electronics that generate the single and multi-frequency Bragg diffraction frequencies for AOM16 and AOM17. The left mixer pair produces the 0 and 90 degree components of f_m and f_{bloch}, while the dashed regions are compound mixers that trim the output LO frequency to zero.

ensures that all Bragg pulses will have the same power in each frequency component. In order to maximally cancel the ripples, the phase of the acoustic wave (at the point where it intersects the light) must be 90 degrees out of phase compared to AOM16. Since the speed of sound is much slower than the speed of light, this is easy to accomplish by translating the AOM sideways with a translation stage until the cancellation is optimal.

4.4.1 Intensity Feedback

As was discussed in Section 2.5, the pulse shape for Bragg diffractions is chosen to be a Gaussian function and not a square pulse as used in state and velocity selection. Since the laser pulses are created by turning on an acoustic-optical modulator, careful control over the RF power to the modulator will change the deflected power and enable arbitrarily shaped pulses. While the RF power could be set directly by an arbitrary waveform generator, a more flexible option is to use a feedback servo to lock the measured power to a reference signal. The servo then allows the pulse's shape and amplitude to be modified by simply changing the reference waveform. In addition, the feedback will allow the servo to cancel some of the intensity noise produced by the laser.

To decouple the SolsTiS laser optimization from the alignment of the Bragg frequency optics as much as possible, the pulse power is measured by a photodetector (PD7) after Fiber:Switchyard. While it would be better to measure the power at the vacuum chamber, this is impractical due to the intensity beats from the multiple frequencies in the beam. Instead, the photocurrent is detected by the feedback circuit shown in Fig. 4.14 and an error signal is created by comparing the detected power to a voltage reference. This error signal is integrated and used as feedback to control the RF power to the pulse shaping AOM15. To control the RF power, a mixer is driven on the LO port by the AOM frequency and a small current is injected into the IF port by the feedback box.[5] The current opens the diodes in the mixer and allows the LO to pass through with an RF power P_a proportional to the square of the injected current.

Unfortunately, this technique of using a mixer as an attenuator has the downside of creating nonlinearity in the feedback when considering the AOM deflection efficiency

$$\eta_a \cong \sin^2\left(\frac{\pi}{\lambda}\alpha\sqrt{P_a}\right).$$

When the mixer is driven with a current I_f from the feedback circuit causing a modulation of the RF power proportional to I_f^2, then the deflected optical power is approximately

$$\begin{aligned}\eta_a P_0 &\cong P_0 \sin^2\left(\frac{\pi}{\lambda}\alpha\sqrt{I_f^2}\right)\\ &\approx P_0\left(\frac{\pi}{\lambda}\alpha\right)^2 I_f^2\end{aligned}$$

[5] A mixer is preferable over other methods, such as voltage controlled attenuators, since the speed of a mixer can be much faster than the rest of the circuit.

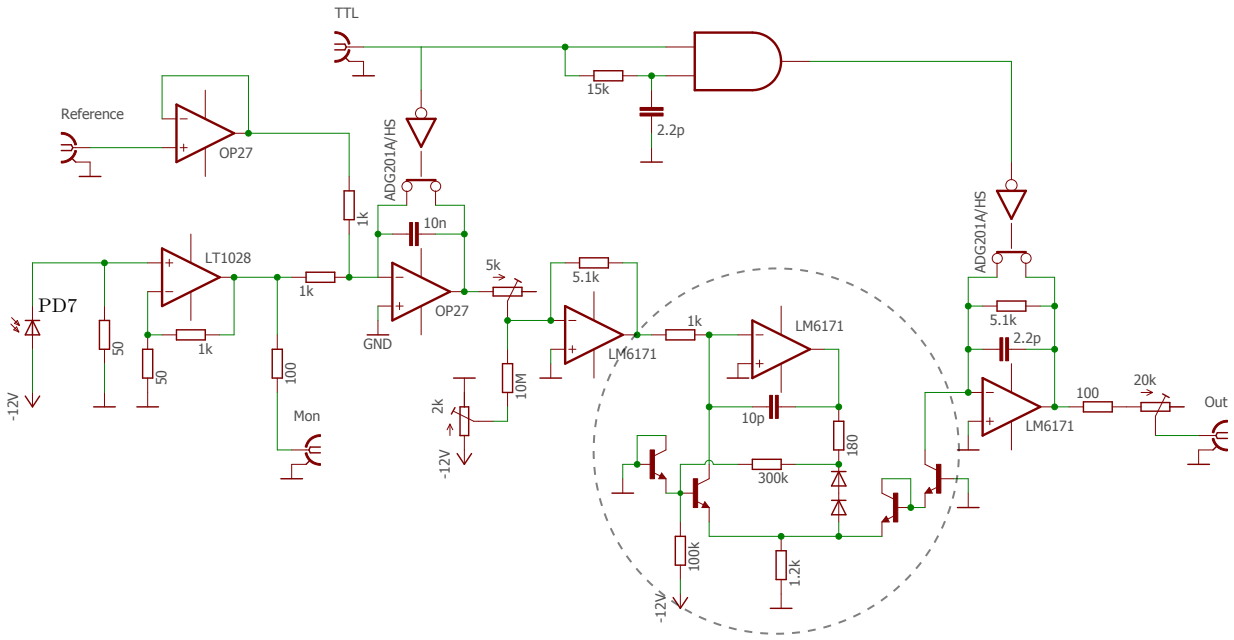

Figure 4.14: The intensity feedback circuit used to create the arbitrary pulse shapes. The photodiode signal is amplified and subtracted from a reference voltage to create the error signal. This is integrated and amplified before being sent to a square root circuit (dashed circle), followed by a transimpedance amplifier.

to leading order. Since the detected photocurrent I_d is linearly proportional to the optical power and, therefore, $I_d \propto I_f^2$, linear feedback theory does not apply as the size of the signal will change the feedback gain. To fix this nonlinearity, the circuit shown in Fig 4.14 contains a square-root element [117] which converts the circuit output to $\sqrt{I_f}$ instead of I_f. An alternate method to get around this inherent nonlinearity in intensity feedback circuits is to use a logarithmic photodetector and an exponential attenuator [118] (as opposed to a linear detector and a mixer).

Instead of using a more typical PI controller, the intensity feedback circuit uses a pure integrator which gives optimal performance when dealing with delay limited systems. Control theory states that a feedback loop is stable if the phase shift of the entire loop is less than 180 degrees when the gain is equal to one. Since the bandwidth of the AOM is much slower than all other elements due to the acoustic wave propagation speed, the delay of the AOM accounts for the only real bottleneck in the feedback design. As the phase shift caused by the acoustic wave delay increases linearly with feedback bandwidth without decreasing the gain (unlike an element like a low-pass filter), the only way to make the overall gain less than one before the phase shift reaches 180 degrees is with a $1/f$ frequency response (a pure integrator). To give the highest possible feedback bandwidth, the acoustic delay can be minimized by moving the AOM transducer closer to the laser beam. In our setup, AOM15 is placed on a translation stage and moved until the acoustic delay is about 500 ns. This delay

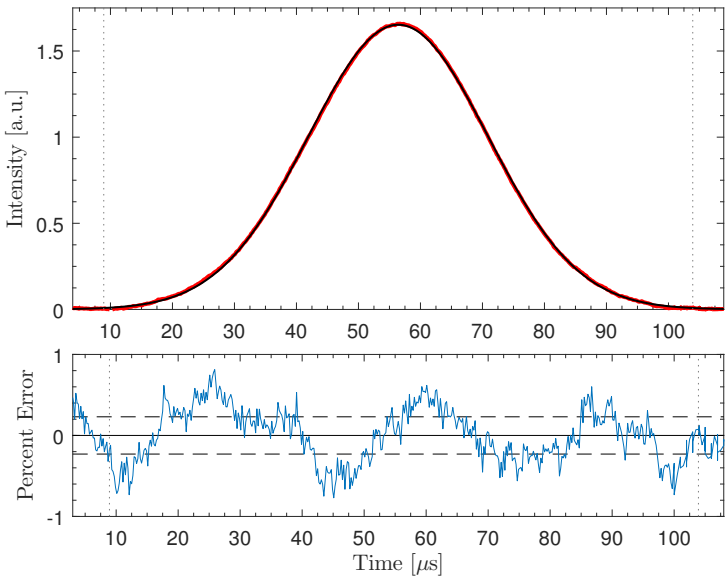

Figure 4.15: Oscilloscope trace of the intensity stabilized Gaussian pulse. Upper: Plot of the measured intensity (red) and a Gaussian best fit line (black). Lower: Deviation of the intensity stabilized intensity from a Gaussian, dashed lines represent the 1-sigma noise of the analog digitizer. The vertical dashed lines show the 95 μs reference pulse length window.

is limited by the size of the beam (i.e. a smaller beam waist would decrease the deflection efficiency) and minimizing the risk of damaging the transducer with the high intensity laser.

To prevent the integrator from accumulating error when the pulses are off (due to unavoidable circuit offsets and background on the photodiode), a voltage controlled switch is used to short the integrator capacitor, holding the output at zero. When a pulse needs to be generated, a TTL signal opens the switch enabling the integrator and a reference waveform is generated to be subtracted from the photodiode signal (producing the error signal). When the switch is opened, a small amount of charge is injected into the capacitor which propagates down the circuit resulting in a small intensity spike at the start of the pulse. To reduce this effect, a second shorted switch prevents the spike from exiting the last gain stage and is opened several hundred nanoseconds later once the charge injection of the integrator decays. Since the gain after the second switch is small, the resulting spike from the second switch is minimal.

For reliability of the experiment, all pulses including the square pulses for state and velocity selection are generated with the intensity feedback servo. An oscilloscope trace of an intensity stabilized Gaussian pulse is shown in Fig. 4.15, along with a plot of the deviation from a Gaussian fit function. When optimized appropriately, the deviation of the optical pulse from Gaussian is measured to be less than 2% peak-to-peak. The voltage waveform sent to the reference has a programmed length of 95 μs and the measured waveform has a fitted Gaussian width of $\sigma = 14.518(9)$ ms, giving an approximately cutoff value of $\tau = 3.272(2)\sigma$.

Optimization: The circuit requires a bit of fusing to optimize properly. The photodiode

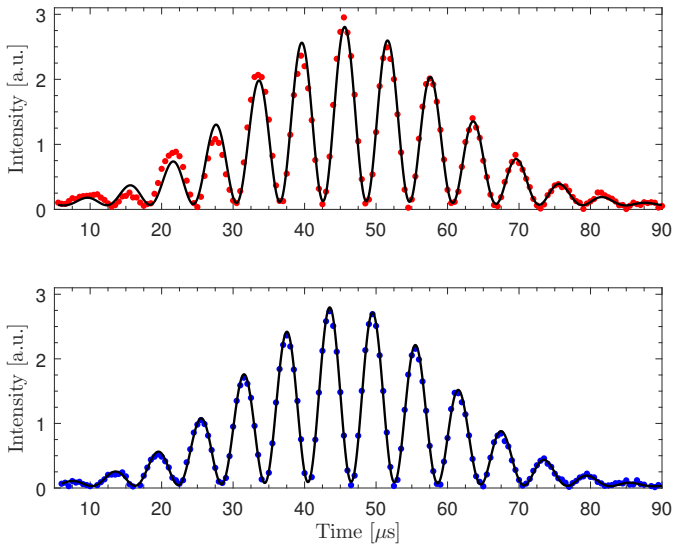

Figure 4.16: Oscilloscope traces of a Gaussian pulse being deflected by an AOM driven by two frequencies. Top: Switching on the AOM RF power 1 μs before the Gaussian pulse. Bottom: Switching on the RF power 1 ms before instead. Lines of best fit are shown in black.

current and the reference signal are trimmed so that the error signal is as close to zero as possible. The gain stage after the integrator has a small trim to force the signal before the square root circuit to be slightly positive (otherwise the circuit will lock up, taking many microseconds to recover). Since the speed of the circuit is limited by phase shifts, optimizing the number of op-amps and the type of op-amp might help in future designs. All op-amps except for the photodiode gain and integrator have a gain bandwidth product of over 100 MHz. Replacing the first two op-amps with faster ones would reduce the phase shift at the cost of worse DC offset performance (which could potentially be trimmed). The last transimpedance op-amp stage is actually unnecessary as the mixer requires a current input (which is what the output of the square root circuit produces) and not a voltage.

4.4.2 Pre-triggering

In order to minimize thermal lensing caused by the acousto-optical modulators as they are switched on and off, it is preferable to either keep the AOMs as close to a 0% duty cycle or a 100% duty cycle as possible; otherwise the alignment of the AOM will drift by an appreciable amount as the AOM is heating up and cooling off over second timescales. Keeping the duty cycle at one extreme or the other keeps the AOM crystal in thermal equilibrium as much as possible. Since AOM16 and AOM17 switch their acoustic power for the last two Bragg pulses, it is optimal to keep the AOMs nominally off to minimize thermal drift. Normally when switching an AOM on with a single frequency, the time required for the deflected optical power to settle is limited only by the frequency bandwidth of the AOM. However,

when driving an AOM with multiple frequencies, there is an inherent settle time that can be many hundreds of microseconds as seen in Fig. 4.16. If AOM16 is driven with RF starting 1 μs before the Gaussian pulse is sent through, there is significant distortion to the optical beat pattern. Also shown in the Fig. 4.16 is a best fit line of the form

$$A(\sin(\omega t + \phi)^2 + b)e^{(t-t_0)^2/2\sigma^2} + B$$

which helps visualize the distortion. While the exact mechanism for this behavior is a mystery, it can be eliminated by allowing the RF drive power to settle for 500 μs to 1 ms before the optical pulse is sent through.

4.4.3 Coriolis Compensation

During the interferometer sequence the atoms spend the majority of their time in free-fall without any external force interaction except through gravity. The inertial frame of the atom, however, must interact with the lab frame during the interferometer beam splitters which are rotating with the Earth at a rate Ω_e. Since the Bragg diffraction beam splitters transfer momentum to the atoms in the direction of the effective wave-vector $\vec{k}_{\text{eff}} = \vec{k}_1 + \vec{k}_2$, the atoms will be diffracted in a slightly different direction for each of the four interferometer pulses as the Earth rotates. Thus, the final position of the atoms from the two different interferometer paths will no longer perfectly overlap, causing systematic shifts and a loss of interference contrast at large pulse separation times [43, 119].

Assuming the lab is rotating about the $\hat{y}$-axis and the interferometer beams are vertical along $\hat{z}$, then the final displacement of the two trajectories for a Ramsey-Bordé interferometer sequence can be calculated as

$$\vec{\delta} = 4nv_r\Omega_e T(T + T')\cos(\theta)\hat{x},$$

where T and T' are the pulse separation times, n is the Bragg order, v_r is the recoil velocity, and θ is the geocentric latitude of the experiment in radians. If the atom wave-packets are approximated by

$$\Psi = \left(\frac{\det A}{\pi}\right)^{1/4} e^{-\vec{r}A\vec{r}^T/2},$$

where A is matrix with diagonal elements equal to the coherence lengths σ_i in each dimension, then the overlap integral between the displaced atom trajectories is

$$\begin{aligned}\int dr^3\Psi^*(\vec{r} + \vec{\delta})\Psi(\vec{r}) &= e^{-\vec{\delta}A\vec{\delta}^T/4} \\ &= e^{-\delta_x^2/4\sigma_x^2}.\end{aligned}$$

In a previous configuration of this experiment without Raman sideband cooling, the coherence lengths σ_i in the three spatial directions were measured to be $\sigma_x = \sigma_y \approx 100$ nm and

$\sigma_z = 800$ nm for a velocity selected ensemble with a transverse temperature of 2 μK. Our coherence length in the z-direction is similar to the previous experiment as the velocity selection procedure is the same. The transverse size can be estimated by the thermal de-Broglie wavelength $h/\sqrt{2\pi m k_{\rm B} T}$ for a 300 nK sample which gives a size of approximately 270 nm. For a typical interferometer sequence with $T = 160$ ms, $T' = 10$ ms, $n = 5$, and $\theta = 37.87$ degrees,[6] the displacement is 160 nm which would cause a contrast loss of 10%.

To prevent this loss of contrast and to eliminate possible displacement systematics, the retro-reflect mirror is rotated at a rate equal to the Earth's rotation rate (so that the downward traveling beam rotates at twice Earth's rate). This causes the effective wave-vector to rotate in the lab frame and therefore point in a constant direction in the atom's inertial frame. Even though the magnitude of the wave-vector no longer constant, the perturbation is small and is treated as a systematic in Section 6.1.2. The retro-reflect mirror is rotated by applying voltage ramps to piezoelectric actuators attached to each axis of the mirror. The optimal rotation rate is found by running the interferometer at a very long pulse separation time $T > 200$ ms and adjusting the rotation rate for maximum interferometer contrast, see [119].

4.5 Bloch Oscillations

In order to increase the sensitivity of the interferometer beyond what is realistically achievable with single Bragg diffraction pulses, the momentum splitting of the atoms can be increased through an adiabatic process which transfers successive momentum kicks of $2\hbar k$. When an atom is held in an optical lattice, the atom has a well defined quasi-momentum as determined by the band structure of the lattice. If the lattice is accelerated, then the atoms will undergo Bloch oscillations wherein the atoms oscillate between quantized momentum states that are spaced by $2\hbar k$ [120, 121]. If the lattice depth U_0 is comparable to the atom's recoil energy E_r and the atoms are accelerated at a rate

$$a \ll \frac{a_0}{16}\left(\frac{U_0}{E_r}\right)^2,$$

where the critical acceleration $a_0 = \hbar^2 k^3/m^2$, then the atom's quasi-momentum will adiabatically follow the velocity of the lattice in momentum steps of $2\hbar k$ [122]. Assuming the acceleration is stopped after N oscillation periods, where a single period is equal to

$$\tau_{\rm B} = \frac{2\hbar k}{ma},$$

then the final state of the atom will be a superposition of momentum states with an average value of $p = 2N\hbar k$ and density of state distribution given by the envelope of a Wannier function [123]. In the harmonic trap limit, the Wannier function has a Gaussian width

[6] Berkeley is at a geocentric latitude of 37.87 degrees.

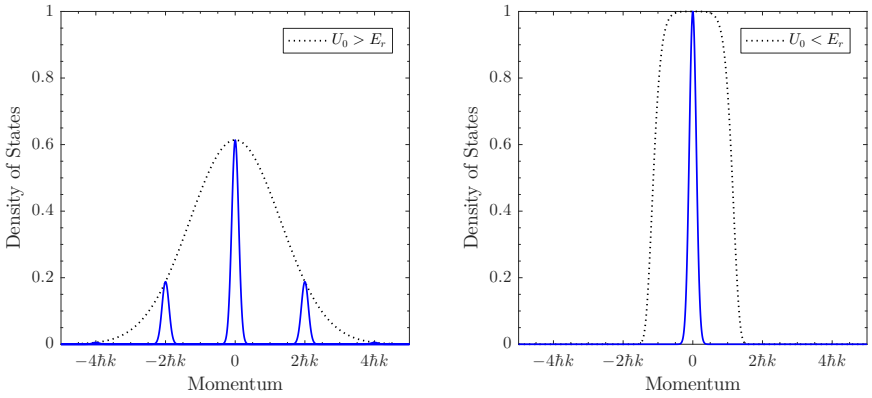

Figure 4.17: The density of states of an atom's quasi-momentum after undergoing Bloch oscillations, given by the envelope of a Wannier function (dashed). Left: The density of states has an approximate Gaussian distribution when the Bloch lattice is deeper than the recoil energy E_r. Right: As the lattice becomes shallower, the envelope turns into a square function, thus pushing the density of states to the center momentum.

proportional to $U_0^{1/4}$ while in the shallow potential limit it has a mostly square envelope extending to $\pm\hbar k$. If the atoms are adiabatically released from the lattice potential, then the Wannier function also adiabatically narrows down to the shallow potential limit, leaving the atoms in a pure state with momentum $p = 2N\hbar k$ [124] as shown in Fig. 4.17. If the lattice is switched off non-adiabatically or if the average quasi-momentum is not a multiple of $2\hbar k$, then the final atom state will be a superposition of momentum states (which is not ideal for interferometry).

There are two fundamental factors that limit the number of Bloch oscillations that can be applied to the atoms. If the atoms are accelerated too quickly, then the adiabatic condition is not satisfied and the probability that an atom is lost during each oscillation is equal to

$$P_{\text{loss}} = \exp\left[-\frac{a_0}{a}\frac{\pi}{64}\left(\frac{U_0}{E_r}\right)^2\right].$$

The probability that an atom does not finish all N oscillations is then $(P_{\text{loss}})^N$. On the other hand, if the lattice is accelerated too slowly, then the single photon scattering

$$R_{\text{sc}} = \frac{\Gamma^3}{8\Delta^2}\frac{I}{I_{\text{sat}}} \tag{4.2}$$

of the Δ detuned lattice will dominate and result in a loss of $P_{\text{sc}} = 1 - e^{-R_{\text{sc}}t}$. Therefore, a comprise must be made between time spent in the lattice and the acceleration rate. In practice, decoherence caused by ac-Stark shifts due to beam imperfections is a stronger limitation of Bloch oscillations for interferometry as discussed in Section 5.5.

While Bloch oscillations have been used in atom interferometers to accelerate both arms of the interferometer in opposite directions, thus increasing the momentum splitting from

$2n\hbar k$ to $2(n+2N)\hbar k$ [125], this configuration could potentially have many unknown systematic effects that would need to be studied with a more detailed theory (as was done for Bragg diffraction). Instead, it is much more common to use Bloch oscillations to accelerate both arms of an interferometer in the same direction [42]. While this does not change the momentum splitting, it does increase the sensitivity of a recoil measurement from n^2 to $n(n+N)$ by increasing the frequency difference $2\omega_m$ which is measured as a laser phase in the interferometer. Since both arms are accelerated in the same lattice, the systematic phase shifts should be common mode to both arms and cancel.

The optics used to create the optical lattice for Bloch oscillations are identical to that for multi-frequency Bragg diffraction. The only difference is that the frequency ω_m is replaced by a ramping frequency ω_{bloch} in the electronics shown in Fig. 4.13 and the pulse shape is modified. If the laser frequencies ω_1 and ω_2 are resonant with order n Bragg diffraction, then shifting the laser frequency from ω_2 to $\omega_2' = \omega_2 \pm 4n\omega_r$ will create lattices moving with the same velocity as the atoms in the $|0\rangle$ and $|n\rangle$ states. If the atoms are to be accelerated such that their momentum increases by $2N\hbar k$, then the laser detuning must be changed by

$$\delta = \frac{2N\hbar k}{m}\frac{(\omega_1+\omega_2)}{c} = 8N\omega_r$$

to account for the Doppler shift of the laser frequencies. To accelerate the atoms once they are loaded into the lattice, the laser frequency ω_2 is ramped from

$$\omega_2 \pm 4n\omega_r \quad \rightarrow \quad \omega_2 \pm 4(n+2N)\omega_r$$

which accelerates the atoms in the state $|0\rangle$ to $|-N\rangle$ and at the same time atoms in the state $|n\rangle$ to $|n+N\rangle$. If the ramp takes place over a time τ, then the ramp rate of $\Lambda_b = 8N\omega_r/\tau$ causes an acceleration of

$$a = \frac{2N\hbar k}{m\tau}.$$

In order to load the atoms into the optical lattice adiabatically, the laser pulse for the Bloch oscillations is ramped from zero intensity to the desired lattice depth over 100 μs while the multi-frequency AOMs are held constant at 180 MHz $\pm\, 4n\omega_r$. Once the atoms are loaded, the modulation frequency is ramped to $\omega_2 \pm 4(n+2N)\omega_r$ over 1 ms, driving AOM16 and AOM17 in the same manner as for multi-frequency Bragg diffraction. After the ramp is finished, the frequency is held constant again while the lattice intensity is ramped off over 100 μs to adiabatically release the atoms.

While the lattice depth for Bloch oscillations was never measured directly, it can at least be estimated by the ratio of the Bragg and Bloch intensity stabilized amplitudes. The effective Rabi frequency for Bragg diffraction of order n is given by the approximation (2.42)

$$\Omega_{\text{eff}}(t) \approx 8\omega_r \left(\frac{\bar{\Omega}(t)}{8\omega_r}\right)^n \frac{1}{(n-1)!^2},$$

where the Rabi frequency of the laser field $\bar{\Omega}(t) = \bar{\Omega}_0 e^{-t^2/2\sigma^2}$ is a Gaussian pulse. For a given pulse width $\sigma = \tau_{\text{bragg}}/\omega_r$, the Rabi frequency that results in a $\pi/2$ pulse must satisfy

$$\int_{-\infty}^{\infty} \Omega_{\text{eff}}(t)dt = 8\omega_r \left(\frac{\bar{\Omega}_0}{8\omega_r}\right)^n \frac{\sqrt{2\pi\sigma^2}}{(n-1)!^2\sqrt{n}} = \frac{\pi}{2}$$

$$\implies \bar{\Omega}_0 = 8\omega_r \left(\frac{\sqrt{\pi n}(n-1)!^2}{8\sqrt{2}\cdot\tau_{\text{bragg}}}\right)^{1/n}.$$

For a Bragg order of $n = 5$ and a typical pulse of $\tau = 0.188$, this gives a two-photon effective Rabi frequency equal to $\bar{\Omega}_0 = \Omega^2/2\Delta \approx 32\omega_r$. In our experiments the Bloch lattice amplitude is typically a factor of 5 smaller than for Bragg; this implies that the Bloch oscillations have a lattice potential of approximately $U_{\text{bloch}} = \hbar\bar{\Omega}_{\text{bloch}} \approx 6\hbar\omega_r$. Therefore when transferring $N = 25$ Bloch oscillations in 1 ms, the expected atom loss is nearly 40% (dominated entirely by tunneling losses), which is similar to what is observed in the experiment.

Chapter 5

Experiment

5.1 Interferometer

To assemble the components from the previous two chapters into a working interferometer, all that is required is a timing system and data acquisition. The coarse experimental timings are run using two programmable National Instrument cards (PCI-6534 and PCI-DIO-32HS) which are used to create TTL signals for atom preparation and to initiate the interferometer sequence.

The atom preparation sequence controlled by the National Instrument cards begins with the loading of the 3D MOT for 1.000 s, followed by the moving molasses launch at 1.033 s. After the Raman sideband cooling and rapid adiabatic passage, the atoms are state selected and velocity selected to their final momentum width and atomic state. The interferometer sequence is initiated at 1.239 s when the NI card triggers the first of several delay generators and a final trigger starts the fluorescence detection and data acquisition at 1.880 s (which lasts for roughly 100 ms). Everything is then reset and the experiment is triggered again to perform the next measurement, with a total cycle time of 2.1 seconds.

Recall that the phase of the interferometer is directly proportional to the pulse separation time and therefore the individual beam splitter pulse timings need to be accurate. Since the NI card only has a timing resolution of 1 μs, a set of SRS DG535 digital delay generators are used to control the individual beam splitter pulses (which have a timing jitter of only 100 ps). For a Ramsey-Bordé interferometer configuration (Fig. 5.2), the first SRS generator (SRS1) is used to trigger a second generator (SRS2) twice, creating two pairs of pulses (corresponding to the first two and last two pulses). The primary TTL trigger from the NI card starts SRS1 which is programmed to delay for a wait time t_0 before triggering two pulses at $t = t_0$ and $t = t_0 + T + T'$. These two pulses in turn trigger SRS2 which creates two pairs of pulses separated by a time T, for a total of four pulses at $t = \{t_0, t_0 + T\}$ and $t = \{t_0 + T + T', t_0 + 2T + T'\}$. By having a single delay generator control the timing of both T separations, any drifts or offsets in the timing will be symmetric, which reduces the potential for systematics effects.

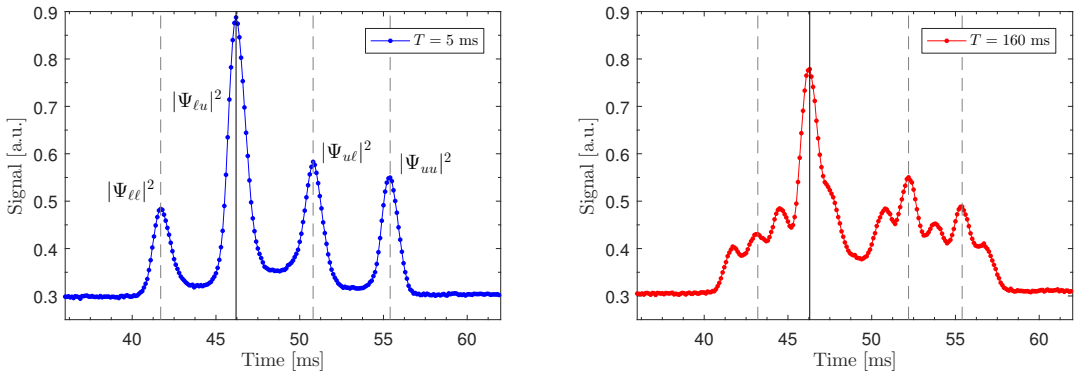

Figure 5.1: Time-of-flight interferometer signals for $n = 5$, $T' = 10$ ms, and $T = 5$ ms (left) and $T = 160$ ms (right). The solid line indicates the $0\hbar k$ momentum trajectory which includes the $|\Psi_{\ell u}|^2$ output and dashed lines indicate the position of the $|\Psi_{\ell\ell}|^2$, $|\Psi_{u\ell}|^2$, and $|\Psi_{uu}|^2$ outputs. For $T = 160$ ms, the extra trajectories that do not interfere are more resolved. Detection occurs 505 ms after the last Bragg pulse for $T = 5$ ms and after 350 ms for $T = 160$ ms.

Each of the four TTL signals from SRS2 then trigger a third SRS, which is used to create the timings for switching AOM15-17, starting the intensity stabilization and triggering the Gaussian waveform. The Gaussian waveform is stored on an Agilent 3320A arbitrary waveform generator and provides the reference signal for the intensity stabilization described in Section 4.4.1. (The Agilent 3320A has a trigger jitter of approximately 1 ns and could potentially be a source of interferometer noise in the future.) To switch the frequency of AOM16 and AOM17 for the last two pulses, the falling edge of the second pulse from SRS2 is used as a trigger (after a roughly 2 ms delay). This ensures that the frequency switch occurs during T' and allows for sufficient settling time before the next Bragg pulse.

After the Ramsey-Bordé sequence is performed on the atoms, the different interferometer trajectories are allowed to separate before being detected on a photodetector by fluorescence imaging. The photocurrent is amplified with a transimpedance amplifier and filtered with a 10-kHz low-pass filter before being digitized with a National Instruments NI4474 card, which has a sample rate of 102.4 kS/s and a resolution of 24 bits. The detected time-of-flight signals, shown in Fig. 5.1, are then analyzed by subtracting off the background and measuring the populations in the four output ports. Because the different trajectories can potentially be overlapped, only a narrow section of each peak is measured and is typically chosen to be ± 1 ms.

Since a Ramsey-Bordé interferometer consists of four $\pi/2$ pulses, there are 16 output trajectories (with interference between four pairs) to create a total of potentially 12 spatially separated interferometer outputs, as shown in Fig. 5.2. If the pulse separation time is small, then the 12 trajectories will have a separation smaller than the cloud radius and thus all trajectories with the same momentum will overlap to form a total of four detection peaks (as shown in Fig 5.1). If the pulse separation time is long enough, then the paths have

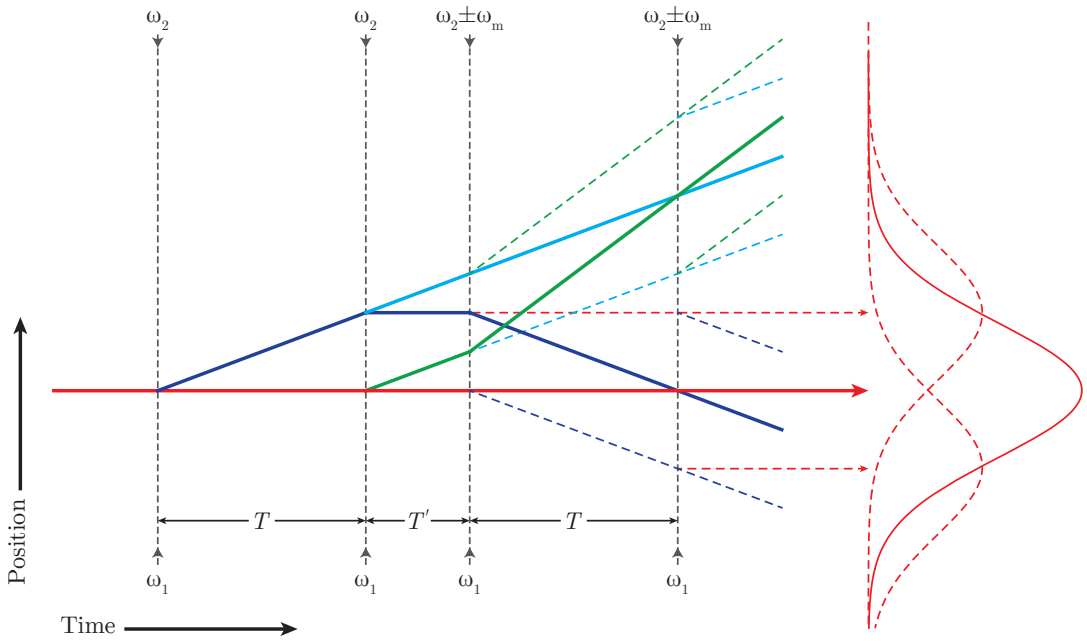

Figure 5.2: A space-time diagram of all 12 Ramsey-Bordé outputs, including those that do not interfere. Each of the four possible Bragg orders will have three corresponding atom trajectories, all of which may overlap depending on the length of the pulse separation time T and the width of the cloud (shown in red, with dashed lines indicating non-interfering atom clouds).

time to separate out, revealing more of the interferometer trajectories in the time-of-flight fluorescence. On the other hand, the spatial separation of the individual momentum classes $\{-2n\hbar k, 0\hbar k, 2n\hbar k, 4n\hbar k\}$ is proportional to the time between the last beam splitter and the detection, which can be upwards of several hundreds of milliseconds. However, this creates a small problem for very long Ts, as the available separation time gets smaller and thus the momentum peaks become less resolved.

The extra overlapped trajectories are not a concern, however, as the normalization procedure $x = (|\Psi_{\ell u}|^2 - |\Psi_{\ell\ell}|^2)/(|\Psi_{\ell u}|^2 + |\Psi_{\ell\ell}|^2)$ and $y = (|\Psi_{uu}|^2 - |\Psi_{u\ell}|^2)/(|\Psi_{uu}|^2 + |\Psi_{u\ell}|^2)$ removes the influence of background atoms on the extracted phase. The background atoms do reduce the effective contrast of the interference, however, which impacts the signal-to-noise of the interferometer. For $T \ll \sigma_{\text{atom}}/2nv_r$ (where σ_{atom} is the atom cloud width and $v_r = 3.5$ mm/s is the recoil velocity), the contrast is limited to a maximum of 50% and gives a baseline for coherence measurements.

After each experimental run, the normalized interference measurements $\{x, y\}$ are recorded along with a raw trace of the detection signal. These points are used to build up an ellipse like the one shown in Fig. 5.3. Individually, the interference signals (x and y) produce seemingly random noise, but when the two are combined a very clear ellipse is formed. The ellipse continues to build up as more trials are recorded and after 20-30 points the data is

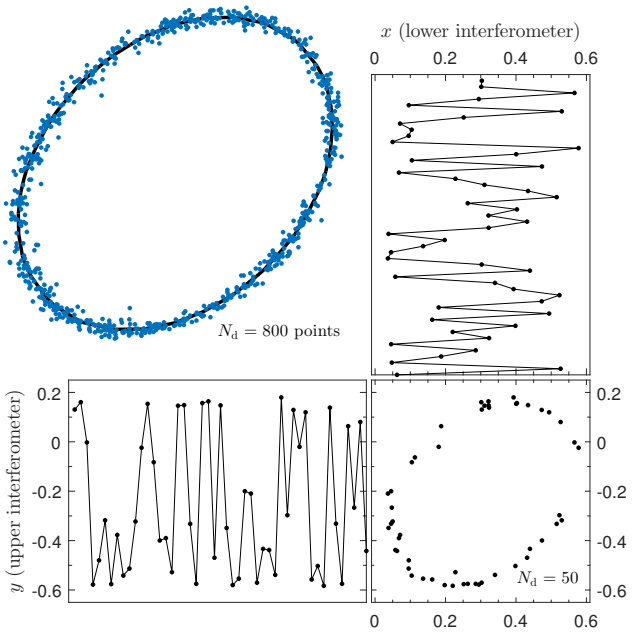

Figure 5.3: A set of 50 measured data points from the lower interferometer (x) and upper interferometer (y) for $n = 5$, $T = 160$ ms, and $T' = 10$ ms. When viewed independently they seem to measure random phases, but when plotted together form an ellipse. An ellipse with 800 points is shown in blue to show how the vibrations evenly spread out the phase.

fitted and the measured phase is recorded. The interferometer contrast for the lower and upper interferometers can then be inferred by the fitted x and y amplitudes of the ellipse. This method of determining the interference contrast is much more rigorous than looking at the maximum and minimum variation in signal since the fitting method will tend not to overestimate the contrast when noise is present.

5.1.1 Alignment

The high sensitivity of Bragg diffraction to intensity and detuning requires great care when aligning and optimizing the beam splitters to the atomic fountain. An external camera is used to measure the position of the fountain in the x-y plane as the atom cloud travels up through the detection region and on the way back down. The fountain alignment is iterated until both detected signals occur at the same position; this procedure aligns the fountain with gravity. Next, the Bragg beam is aligned vertically by centering the beam on the input view-port and looking for a small transmission signal through the top retro-reflect (dielectric) mirror with a camera. The retro-reflect mirror is glued to the inside of a view-port, which is connected to a flexible bellows that can be tilted with two large micrometer screws. The mirror is adjusted such that the Bragg beam is reflected back into the launching fiber which ensures optimal counter-propagating alignment. A photodiode (PD8 in Fig. 4.3) picks off

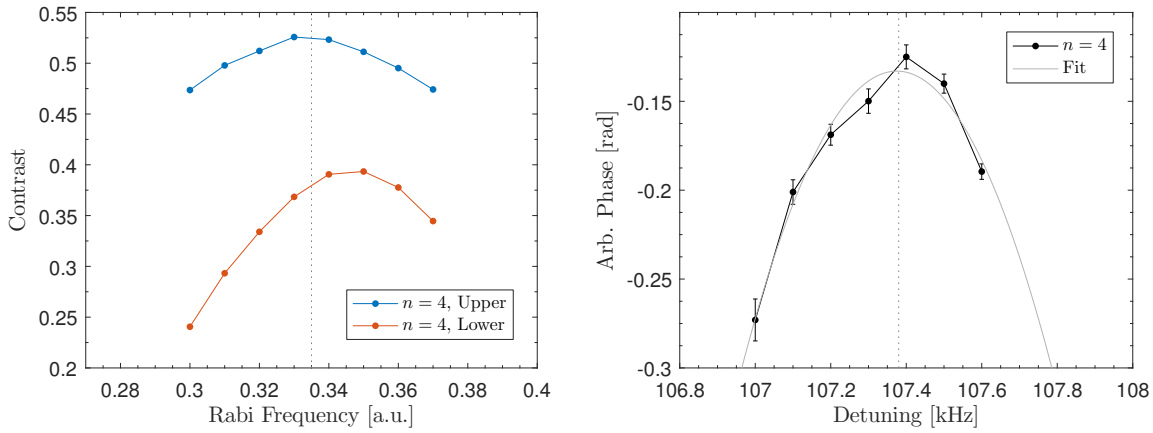

Figure 5.4: Tuning curves for $n = 4$ Bragg diffraction. The interference contrast as a function of intensity control voltage (left) and the phase as a function of detuning (right). The dashed lines indicate the optimal parameters. ($T = 160$ ms, $\Delta = 15$ GHz blue single photon detuning)

some of the back-coupled light and is used to help optimize the retro-mirror and monitor the alignment.

While running the fountain with single Bragg diffraction pulses, the intensity and detuning are roughly adjusted until the desired Bragg transition is visible. The intensity is then lowered slightly and the Bragg beam aligned more carefully to optimize the diffraction efficiency (taking care to readjust the retro-reflect mirror to keep the back-coupling). To ensure that the Bragg beam axis is centered with the fountain axis, this single Bragg diffraction alignment procedure is performed at various fountain heights (thus different times for a fixed launch velocity) and iterated to maximize all signals. Once the Bragg beam is centered with the atom launch axis, a final adjustment of intensity and detuning can then be performed.

The full interferometer sequence is then run with all four Bragg pulses using an estimate for the modulation frequency, $\omega_m = 8n\omega_r$, for the last two pulses. The contrast of the resulting ellipses is then measured for different intensities (set by the amplitude of the intensity stabilization Gaussian waveform) until a maximum is found, as seen in Fig 5.4, which corresponds to the "$\pi/2$" intensity. The term $\pi/2$ is used somewhat loosely in this case since the finite spatial size of the cloud means that not all of the atoms see the same intensity and, therefore, the optimal contrast has some atoms under-rotated between the two Bragg orders while others are over-rotated. This is further emphasized by looking at the contrast vs. intensity for the upper and lower interferometers, which have maxima at different intensities. Since the lower interferometer path contains the majority of the initial atom cloud (which is quite large), more intensity is needed to rotate the atoms further out in the cloud's radius. Typically the maximum contrast of the upper interferometer is used for alignment since the atoms that participate in the upper interferometer have more ideal characteristics (velocity, spatial distribution) and match a theoretical $\pi/2$ pulse more closely.

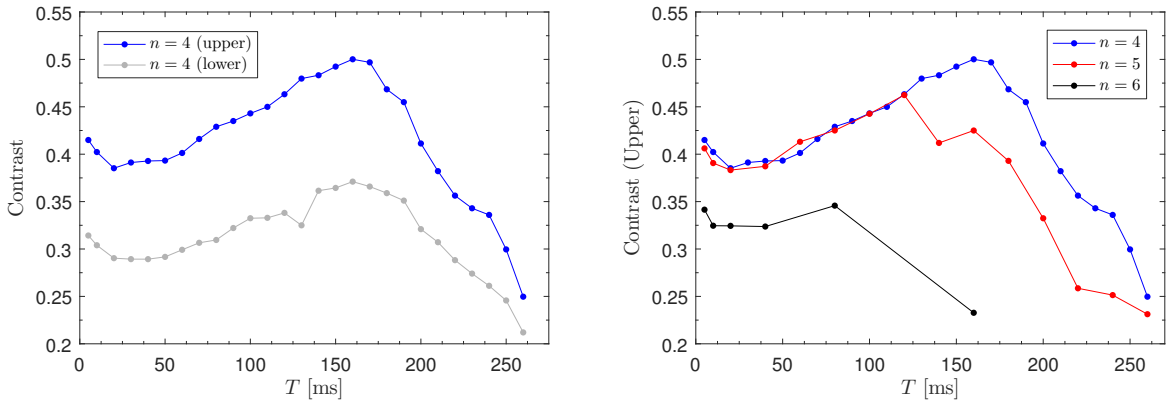

Figure 5.5: Plot of the Ramsey-Bordé interferometer contrast as a function of the pulse separation time T with $T' = 10$ ms. Left: The difference in contrast between the upper and lower interferometer with $n = 4$. Right: The upper interferometer contrast for different Bragg orders n.

The detuning is optimized by measuring the phase of the interferometer ellipse as a function of the AOM18 double-pass start frequency and finding the extrema as discussed in Section 2.5.2.

The contrast of our Ramsey-Bordé interferometer at different pulse separation times T is shown in Fig 5.5. As a general rule of thumb, the contrast for the lower interferometer is always less than the upper interferometer due to the background of the initial atom cloud. Also observed is the characteristic increase in contrast for pulse separation times around 160 ms, where the interfering atoms spatially separate from the background atoms. This increase in contrast at longer T is convolved with a linear contrast decay (most evident at short T) which is most likely caused by differential ac-Stark shifts, which will be elaborated on in Section 5.5. Similarly, as the Bragg order is increased, the contrast decays at a faster rate which limits the ability to increase the sensitivity of the interferometer by increasing the momentum transfer.

5.1.2 With Bloch Oscillations

Applying common-mode Bloch oscillations to the sequence is relatively straightforward once the simultaneous conjugate interferometer is working. The Bloch oscillations are applied in the middle of the T' free evolution approximately 5 ms after the second beam splitter pulse. The falling edge of the second pulse from SRS2 is sent through a 5 ms delay box and is used to trigger another SRS delay generator which is used to control the timings for the Bloch intensity stabilization and frequency switching (similar to the Bragg pulses). The intensity stabilization waveform is generated by a second Agilent 3320A which creates the linear 100 μs ramp on, followed by a variable constant intensity section, and ending with a 100 μs ramp off. To start the lattice acceleration, the frequency ramp f_{bloch} from an Analog

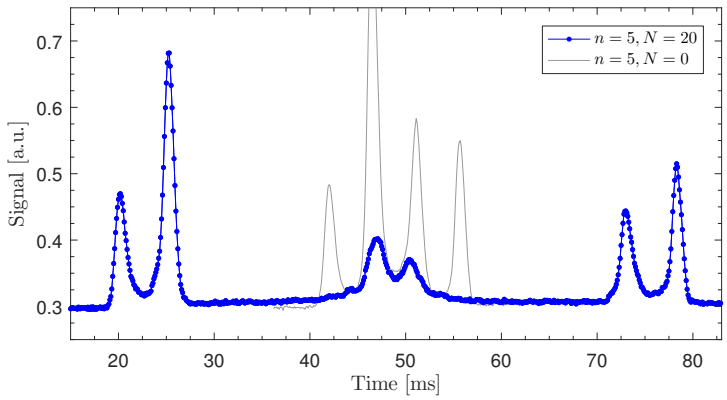

Figure 5.6: Time-of-flight signal for an interferometer with common mode Bloch oscillations (blue) using $n = 5$, $N = 20$, and $T = 5$ ms. The center two peaks are not part of the interferometer and are instead leftover atoms that did not follow the Bloch lattice. Also plotted is an interferometer without Bloch oscillations (gray) for comparison to show the difference in momentum separation between the upper and lower interferometers.

Devices AD9959 DDS is triggered 100 μs after the Agilent waveform (coinciding with the start of the constant intensity part of the waveform). The length of the Bloch intensity waveform is adjusted to match the frequency ramp rate for a given Bloch order such that the ramp ends right before the lattice depth is lowered for adiabatic release.

The rest of the interferometer then follows the same sequence as before, except that the modulation frequency $\omega_m = 8n\omega_r$ is changed to $8(n + N)\omega_r$ to account for the momentum added by the Bloch oscillations. Since the timings of the Bloch oscillations pulses are only relevant for systematic effects, the duration of the Bloch oscillations is approximated as zero and the pulse separations before and after Bloch are labeled T_1' and T_2', respectively, such that $T' \approx T_1' + T_2'$.

A typical time-of-flight signal for a conjugate Ramsey-Bordé with $n = 5$, $N = 20$, and $T = 5$ ms is shown in Fig. 5.6. The lower interferometer (leftmost peaks) and upper interferometer (rightmost peaks) are now highly separated due to the extra momentum received by the Bloch oscillations. As the lattice accelerates, some of the hotter atoms fall out of the lattice and are left behind in the center of the time-of-flight signal. These atoms do not participate in the interferometer and are therefore not measured for the ellipses. Additionally, since these hotter atoms would normally contribute to the background, the contrast of the lower interferometer can be much larger when Bloch oscillations are used, as shown in Fig. 5.7. Unfortunately, the introduction of Bloch oscillations also significantly enhances the T dependent contrast decay; the reason is that the atoms spend much more time in the laser field during Bloch oscillations ($t_{\text{bloch}} = 1$ ms) than during a Bragg beam splitter ($\sigma_{\text{bragg}} = 14.5$ μs) even though the intensity differs by a factor of 5 between the two.

The ac-Stark dephasing mechanism is also the reason that Bloch oscillations do not work very well with a red-detuned optical lattice. Atoms in a red-detuned lattice are trapped at

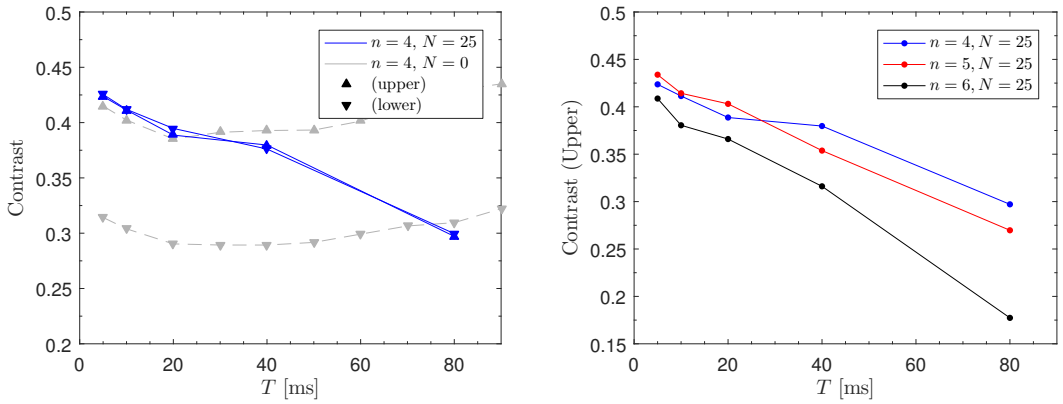

Figure 5.7: Plot of the Ramsey-Bordé interferometer contrast as a function of the pulse separation time T with $T_1' = 5$ ms and $T_2' = 5$ ms. Left: The difference in contrast between $N = 0$ and $N = 25$ for a Bragg order of $n = 4$. Both upper and lower interferometer contrasts for both configures are plotted, showing the improvement in lower contrast with Bloch oscillations. Right: The upper interferometer contrast for different Bragg orders n with $N = 25$. ($\Delta = 15$ GHz blue)

the intensity maxima and therefore see a much stronger oscillating electric field than with a blue-detuned lattice (which traps at intensity minima). Since the lattice depth and ac-Stark shifts are proportional, increasing the single photon detuning does not suppress the effect and, therefore, blue lattices are used almost exclusively with Bloch oscillations. In addition, the dephasing puts a limit on how deep (and therefore how efficient) the Bloch lattice can be made because an increase in signal size is countered by a decrease in contrast. Typically a compromise is made between signal size and contrast to optimize the overall signal-to-noise ratio.

5.1.3 Measurement

Since the fundamental purpose of our Ramsey-Bordé interferometer is to measure the recoil frequency $\omega_r = \hbar k^2/2m$, a priori knowledge of $\hbar/m$ should not be used as the basis for setting the modulation frequency $\omega_m = 8(n + N)\omega_r$. Instead, a bootstrapping method is employed wherein measurements of the recoil frequency are made at progressively longer pulse separation times to systematically find the correct value.

First, a crude measurement value of $\hbar/m$ is used in combination with the laser wavelength to calculate a guess for the center modulation frequency $\omega_m = 2\pi f_0$. Two sets of data are generated by running the interferometer sequence with a very short T while alternating between the $\pm\pi/4$ modulation frequencies ($f_m \pm 1/8nT$) for each experimental run to create two ellipses as discussed in Section 2.4.2. Once 20-30 points are recorded for each of the $\pm$ modulations, the ellipses are fit and the phase difference is used to apply a correction to the center modulation frequency f_m. This is repeated until the ellipses are approximately ± 90

degrees from zero phase, at which point the accuracy of the center modulation frequency is given by a final measurement of the phase difference.

Since the interferometer phase is π periodic (not 2π due to the ellipse fitting), the initial guess for the modulation frequency must be accurate to

$$\frac{\delta\omega_m}{\omega_m} < \frac{\pi}{16n(n+N)\omega_r T_0},$$

where T_0 is the shortest possible pulse separation time T. For a simple interferometer with $T_0 = 2$ ms, $n = 4$, and $N = 0$, then the modulation frequency need only be known to 0.1 parts per thousand for the measurement to give the correct center frequency. The center frequency measurement at T_0 is then used as the modulation frequency for a larger pulse separation time $T_1 > T_0$ allowing for a more sensitive measurement. This is repeated until the modulation frequency is accurate enough to run the most sensitive interferometer configuration.

Ideally, the recoil frequency would then be measured by fitting ellipses at $\pm\pi/4$ until the desired accuracy of $\omega_r = \omega_m/8(n+N)T$ is achieved. However, as was shown in Section 2.5.3, the Bragg dynamics create a large diffraction phase systematic that must be dealt with.

5.2 Diffraction Phase

Recall that the total differential phase between the upper and lower interferometers in a dual conjugate Ramsey-Bordé is

$$\Delta\Phi = 16n(n+N)\omega_r T - 2n\omega_m T + \phi_0, , \tag{5.1}$$

where the extra phase ϕ_0 is the diffraction phase caused by using Bragg diffraction for the beam splitters. When determining the recoil frequency ω_r using the bootstrapping method outlined in the previous section, one will find that the modulation frequency that gives zero phase is a function of the pulse separation time T,

$$\omega_m = 8(n+N)\omega_r + \frac{\phi_0}{2nT}. \tag{5.2}$$

Since values of the diffraction phase can be as large as several hundred milliradians, the measured value of the recoil frequency,

$$\omega_r = \frac{\omega_m}{8(n+N)} - \frac{\phi_0}{16n(n+N)T},$$

can be off by as much as 100 ppb for $n = 5$, $N = 16$, and $T = 80$ ms. Since it is not feasible to calculate ϕ_0 to a part-per-thousand accuracy using the theory for Bragg diffraction, a different method must be employed to deal with the systematic shift.

A plot of the measured modulation frequency $f_m(T)$ as a function of the pulse separation time is shown in Fig. 5.8 for $n = 5$ Bragg diffraction with and without $N = 16$ Bloch

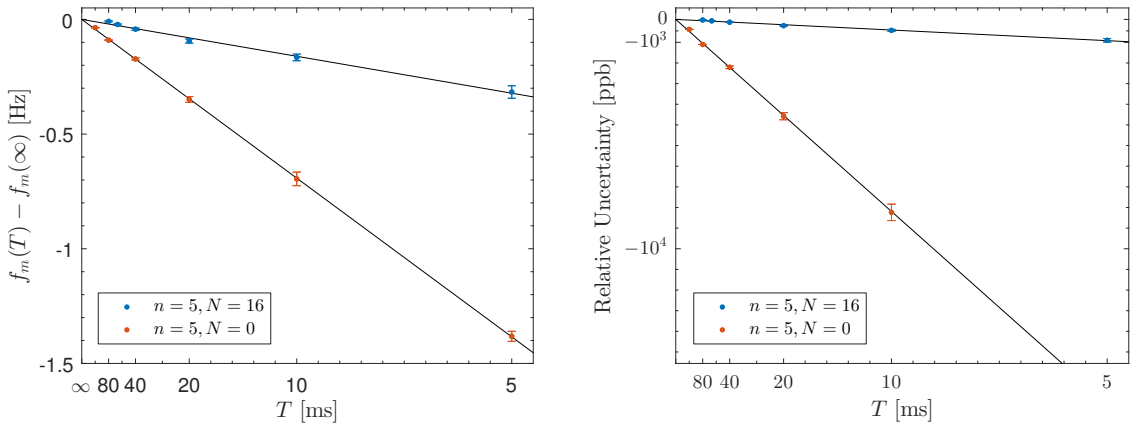

Figure 5.8: Plots of the measured modulation frequency f_m as a function of the pulse separation time T, with a 1/T scale to emphasize the asymptotic behavior and linear best fit lines (black). Left: The difference between the measured frequency $f_m(T)$ and the extrapolated frequency $f_m(\infty)$, for $n = 5$ with $N = 0$ and $N = 16$. Right: The relative uncertainty in the recoil frequency $f_r = f_m(T)/8(n + N)$ due to the diffraction phase.

oscillations. When the pulse separation time is plotted on a $1/T$ scale, the asymptotic nature of the measurement becomes apparent. As the pulse separation time approaches infinity, the modulation frequency (and therefore the measured recoil frequency f_r) approaches the "correct" value. When Bloch oscillations are added, not only does the fractional uncertainty decrease due to the increase in total phase, but the value of the diffraction phase ϕ_0 also tends to get smaller [44]. The reason is that the increased velocity difference between the upper and lower interferometer causes the non-resonant Bragg pair to be further Doppler detuned and thus contribute less to the dynamics of the beam splitter. This increased symmetry cancels some of the diffraction phase (primarily the contributions from the last beam splitter), as was shown in Section 2.5.2.

The diffraction phase can be measured by fitting the modulation frequency vs. 1/T data to a straight line. For convenience, the diffraction phase is sometimes referenced as a frequency slope $\partial f_m/\partial(1/T) = \bar{\phi}_0 = \phi_0/(4\pi n)$ in units of Hz·s. For a measurement with only two pulse separation times T_1 and T_2 with corresponding measured modulation frequencies f_1 and f_2, the recoil frequency and diffraction phase can be solved as

$$8(n + N)f_r = \frac{f_2T_2 - f_1T_1}{T_2 - T_1}, \text{ and} \qquad \bar{\phi}_0 = T_1T_2\left(\frac{f_2 - f_1}{T_1 - T_2}\right). \tag{5.3}$$

By making alternating measurements between long and short Ts, both the recoil frequency and the diffraction phase can be solved simultaneously.

This method of extracting the recoil frequency depends heavily on the diffraction phase ϕ_0 being a constant; therefore, great care must be taken to ensure all parameters are the same for different pulse separation times. The two factors that are the most likely to change during the interferometer sequence are the transverse atom positions due to a misaligned launch

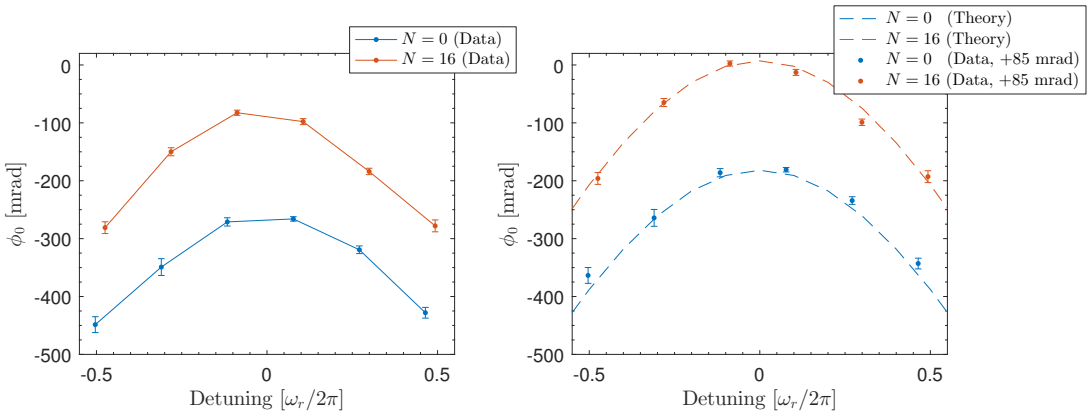

Figure 5.9: Left: The measured diffraction phase as a function of detuning (in units of recoil frequency) for $n = 5$ Bragg diffraction and $N = 0$ or $N = 16$ Bloch oscillations (pulse length of 95 μs, Gaussian width of 14.52 μs). Right: The same data shifted up by 85 mrad to compare to a theoretical curve using the parameters $\Omega_0 = 31.23\omega_r$, $\sigma = 0.188\omega_r^{-1}$, and $\tau = 3.272\sigma$.

direction and the deflected power from the ramping double-pass AOM18. These will both change the laser intensity at the atoms during the interferometer sequence. Luckily, as was shown in Section 2.5.2, the diffraction phase depends most strongly on the intensity of the Bragg beam for the second and third beam splitter. Since the Ramsey-Bordé interferometer is symmetric about the middle two pulses (which are separated by T'), the second and third beam splitters can always be made to occur at the same absolute time by delaying the first pulse. Aligning the interferometers this way means that the double-pass efficiency and the atom position will be the same for every interferometer time T, even if the transverse velocity is not exactly zero (or if the double pass has a time dependent deflection efficiency). Since the diffraction phase of the first beam splitter cancels and the sensitivity to the last beam splitter is suppressed when using Bloch oscillations, the intensities for first and last beam splitters need not be perfect.

The equations describing Bragg diffraction from Section 2.5 only have two free parameters: the detuning 2δ between the counter-propagating Bragg beams and the effective Rabi frequency $\bar{\Omega}(t)$ which is proportional to intensity. To experimentally explore the diffraction phase dependence on these two parameters, a recoil measurement is made with different detunings and intensities at a variety of pulse separation times. To measure the phase that results from the detuning δ, the frequency offset of the double-pass AOM18 is stepped across the Bragg resonance. At each detuning step, two modulation frequency measurements are made at $T_{\text{short}} = 5$ ms and $T_{\text{long}} = 80$ or 160 ms (with and without Bloch osculations, respectively). The diffraction phase was then calculated and the results are plotted in Fig. 5.9. As the detuning increases, so does the size of the diffraction phase as predicted by theory. Just as before, the addition of Bloch oscillations suppresses the diffraction phase for all values of the detuning, but not as much as was predicted by the theory. While the curvature of the

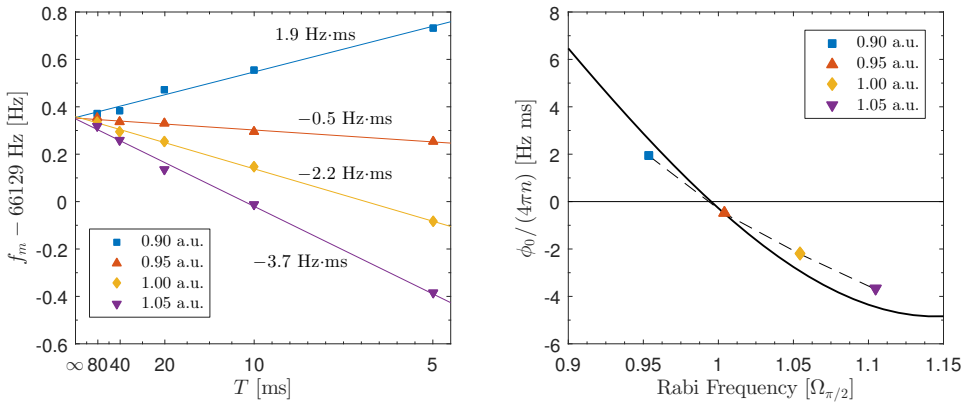

Figure 5.10: Left: The measured modulation frequency as a function of the pulse separation for a variety of intensities for $n = 4$ and $N = 0$ (pulse length of 95 μs, Gaussian width of 14.52 μs). An intensity of 1.00 a.u. corresponds to the maximum contrast for the upper interferometer. Inscribed on each fit is the measured diffraction phase in units of Hz·ms. Right: The diffraction phase at each intensity overlaid with a theory curve (black) using the parameters $\Omega_0 = 31.23\omega_r$, $\sigma = 0.188\omega_r^{-1}$, and $\tau = 3.272\sigma$. The 0.95 a.u. intensity point is arbitrarily chosen to coincide with the theory line to show the comparison.

diffraction phase is predicted rather well, the overall offset differs by roughly 85 mrad. As the theory was calculated for a single resonant atom velocity with close to ideal parameters, it is not too surprising that the theory disagrees due to the velocity and position distributions of the atoms in the experiment. To account for the non-ideal nature of the interferometer, the Bragg differential equations can be solved for a variety of parameters and the diffraction phase of the ensemble can be calculated in a Monte Carlo simulation, which will be discussed in Section 5.4.

To check the intensity dependence of the diffraction phase, several $1/T$ measurements were made at 5% intensity intervals for $n = 4$ and the results are plotted in Fig. 5.10. Since the absolute laser intensity is not well calibrated, the intensity that gives the maximum contrast is labeled as 1.00 arbitrary units (a.u.) and all other intensity settings were referenced to this value. The data shows that the diffraction phase increases as the intensity decreases with a zero crossing occurring at an intensity of 0.94 arbitrary units. This zero crossing in the diffraction phase is also present in the theory, but with a different intensity. The Rabi frequency that gives a $\pi/2$ pulse ($\Omega_{\pi/2}$) and, thus, optimal contrast, has nearly zero diffraction phase in the theory, while the 1.00 a.u. experimental measurement has a significant negative phase. This shift in the "optimal" intensity between theory and experiment is explained by the ensemble behavior of the atom cloud and is observed in the Monte Carlo simulation of the diffraction. Such a zero crossing also exists for $n = 5$, but occurs at a far lower intensity in a parameter region where the interferometer does not work well.

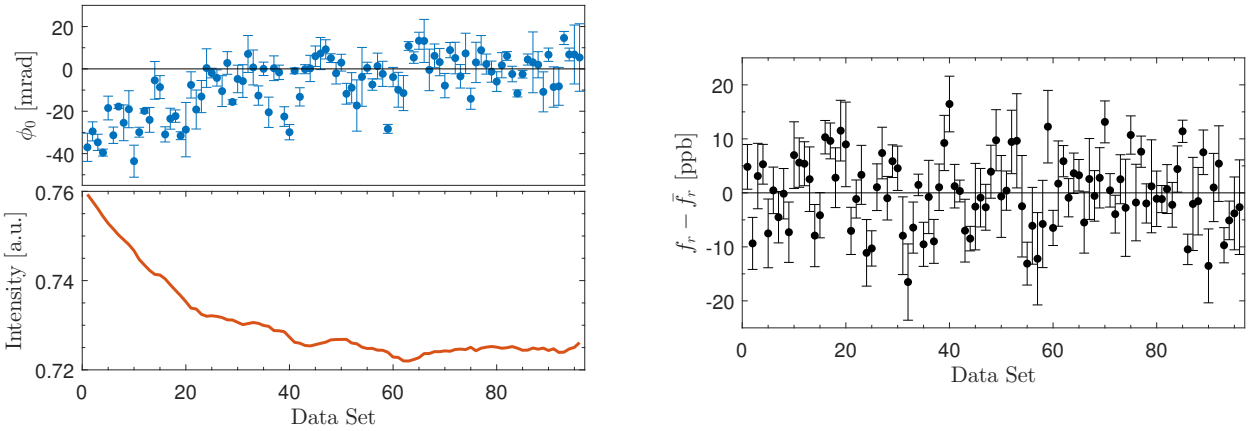

Figure 5.11: A dataset taken over a period of 25.3 hours with $T = \{5, 80\}$ ms, $n = 4$, and $N = 25$ using feedback to null the diffraction phase. Top: The measured diffraction phase as it is being zeroed by the changing intensity. Bottom: The control voltage/intensity of the Bragg beams as it is being updated by the feedback servo. Right: The relative recoil frequency f_r measured for each dataset. (Each dataset contains the average of 5 measurements, where each measurement is calculated from two $T = 5$ ms and four $T = 80$ ms ellipses (including the $\pm\pi/4$ modulations), with 30 points per ellipse.)

5.2.1 Zeroing the Phase

While one could imagine adjusting the Bragg parameters such that the diffraction phase is zero in order to perform the recoil measurement, the sensitivity to drifts in alignment would be far too large for this to work effectively. However, since the intensity of the Bragg beams is a relatively simple parameter to control (by means of the intensity feedback servo), it is straightforward to zero the diffraction phase by active feedback to the intensity.

To perform the recoil measurement with diffraction phase feedback, the interferometer is run by taking sets of ellipses at long and short pulse separation times. Once a complete measurement of at least four ellipses is taken ($\pm\pi/4$ for both T_{short} and T_{long}), the diffraction phase is calculated with (5.3) and used as an error signal for a digital proportional-integral servo which controls the voltage of the Bragg waveform. An example of a measurement using intensity feedback is shown in Fig. 5.11 using $n = 4$ Bragg diffraction and $N = 25$ Bloch oscillations. The pulse separation time is alternated between $T_{\text{short}} = 5$ ms and $T_{\text{long}} = 80$ ms, with twice as many ellipses taken at T_{long} due to the lower signal-to-noise. Also plotted in the figure are the corresponding recoil measurements (relative to the mean frequency), which show no dependence on the diffraction phase due to the extrapolation. The combined set of data ends up having a statistical 1-sigma relative uncertainty of 0.58 ppb in the recoil frequency.

While zeroing the diffraction phase with intensity feedback may not end up being particularly useful for our measurement of $\hbar/m$ due to the noisy measurements, it may be useful in the future for two particular scenarios. First, if the signal-to-noise is excellent at short

T, but relatively poor at long T, then an occasional measurement at T_{short} could be enough to measure the drift in diffraction phase, while the majority of the integration time can be spent at the more sensitive T_{long}. Second, for real time measurements, zeroing the diffraction phase with periodic calibrations could enable faster rep rates, without requiring measurements at multiple Ts (as long as the errors caused by drifts in diffraction phase are within the tolerance of the measurement).

5.3 Gravity Gradient

One of the next largest systematic after the diffraction phase that needs to be accounted for is the effects caused by the gravity gradient of Earth. While the simultaneous conjugate Ramsey-Bordé interferometer cancels the effects of a constant acceleration, the experiment is sensitive enough that higher-order corrections need to be considered. The Lagrangian and time-dependent trajectories for a particle in Earth's field that were calculated in Section 2.3 already include corrections from the gravity gradient γ, but the interferometer phase discussed so far has neglected those higher order terms. The differential Ramsey-Bordé phase including the gradient is

$$\begin{aligned}\Delta\Phi =& 16n(n+N)\omega_r T - 2n\omega_m T \\ &+ \frac{4}{3}n\omega_r\gamma T\left[n\left(2T^2+3T(T_1'+T_2')+3(T_1'+T_2')^2\right)+N\left(2T^2+6TT_2'+6T_2'^2\right)\right],\end{aligned}$$

where the last term is the contribution from the gradient. The times T_1' and T_2' are the durations between the second pulse and the Bloch oscillations and between the Bloch and third pulse, respectively. Since the correction is small, the errors caused by not taking into account the Bloch acceleration time are negligible. The fractional error in the recoil frequency ω_r is then

$$\begin{aligned}\frac{\delta\omega_r}{\omega_r} &= \frac{\gamma}{12(n+N)}\left[n\left(2T^2+3T(T_1'+T_2')+3(T_1'+T_2')^2\right)+N\left(2T^2+6TT_2'+6T_2'^2\right)\right] \\ &\approx \gamma\cdot 1.2\times 10^{-3}\ \text{s}^2\end{aligned}$$

for typical parameters of $n = 5$, $N = 25$, $T = 80$ ms, and $T_1' = T_2' = 5$ ms. The value of the gravity gradient above Earth's surface is approximately 3×10^{-6} s^{-2} and, therefore, the gravity gradient correction is 4 ppb for the stated interferometer parameters. Since the fractional correction depends on T^2, larger pulse separation times require significantly larger correction. For example, the same interferometer parameters with $N = 0$ and $T = 160$ ms increases the needed correction to 14 ppb.

To ensure that the gravity gradient does not dominate the systematics for a 0.5 ppb recoil measurement, it is then necessary to know the value of γ to a few percent accuracy. Due to the fact that the experiment is located partially underground in the basement of a building, it is not appropriate to use the typical value of the gradient above Earth's surface.

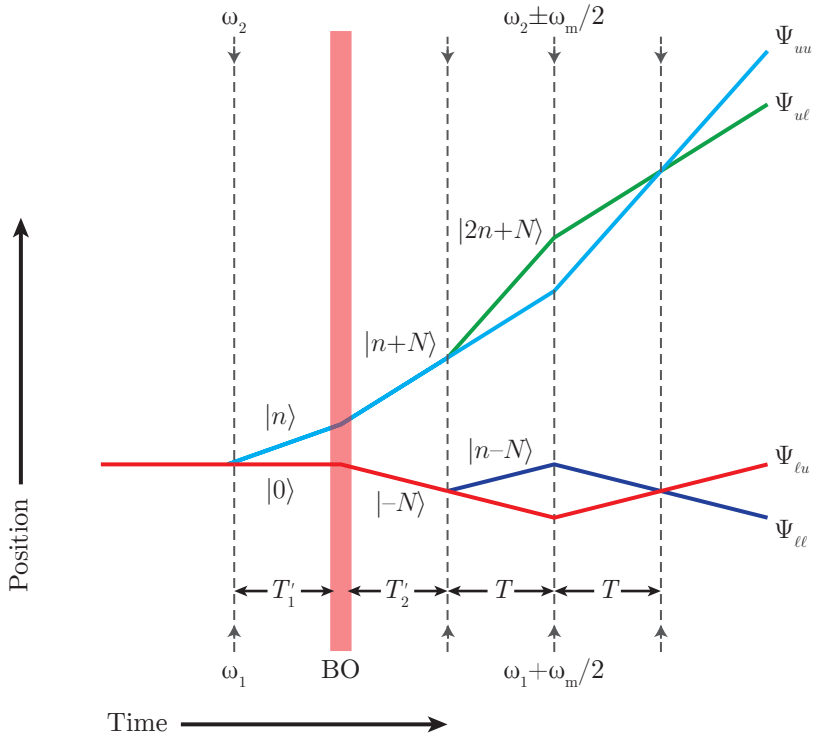

Figure 5.12: A space-time diagram for a gravity gradiometer geometry. The vertical dashed lines indicate Bragg beam splitters, while the shaded red line is the Bloch oscillations. The last three Bragg pulses are run with multiple frequencies to address both Mach-Zehnder interferometers.

Instead the value must be measured experimentally, which can be done using a gradiometer consisting of two vertically separated Mach-Zehnder interferometers as shown in Fig. 5.12. The Mach-Zehnder geometry provides a measurement of the gravitational acceleration of the atoms [7] and, thus, two such measurements with knowledge of the separation gives the gradient.

Converting the existing Ramsey-Bordé geometry into a gravity gradiometer [126] is relatively straightforward. The atom cloud is first split by a Bragg beam splitter and then the atoms trajectories are accelerated apart using Bloch oscillations as shown in Fig. 5.12. The Bloch oscillations are performed in exactly the same manner as in the Ramsey-Bordé with the $|0\rangle$ momentum atoms accelerated down and the $|n\rangle$ atoms accelerated up. After the atom clouds have had time to spatially separate, simultaneous Mach-Zehnder interferometers are performed on the two cloud trajectories. Since the two interferometers are performed at the same time, the common mode acceleration g and any phase shifts due to vibrations are canceled, thus leaving just the differential gravity gradient signal γ. The differential phase of the configuration shown in Fig. 5.12 can be calculated as

$$\Delta\Phi_\gamma = 2n\omega_r\gamma T^2\big[2N(T+T_2') + n(T+T_1'+T_2')\big], \tag{5.4}$$

where T_1' is the time between the first beam splitter and the Bloch oscillations, T_2' is the time after the Bloch oscillations until the first Mach-Zehnder beam splitter, and T is the pulse separation time of the Mach-Zehnder.

To ensure that the sign of the two gravimeters are aligned such that vibrations and g cancel, both interferometers need to be kicked up by the beam splitters for the three Mach-Zehnder pulses. This is accomplished by shifting the double-pass AOM18 frequency up by $\omega_m/2 = 4(n+N)\omega_r$ and modulating the multi-frequency AOMs (AOM16 and AOM17) by $\omega_m/2$ instead of ω_m.[1] All four Bragg beam splitters are chosen to be $\pi/2$ pulses for simplicity, instead of using a π pulse for the middle Mach-Zehnder pulse. The four outputs are analyzed exactly the same as before by creating ellipses from the normalized outputs of the upper and lower interferometer.

Since the gravity gradient is quite small, so will be the measured phase even for fairly modest interferometer parameters. To ensure the ellipse is operated away from zero degrees (where the ellipse looks like a line), a phase modulation is applied in a similar manner to the Ramsey-Bordé interferometer. By ramping the multi-frequency modulation $\omega_m' = \omega_m/2$, a laser phase is imprinted on the atoms that has the opposite sign for the two interferometers. If the frequency is ramped as

$$\omega_m'(t) = \frac{\omega_m}{2} + \Lambda_{\text{ramp}}t$$

during the Mach-Zehnder interferometer, then the resulting phase is

$$\Delta\Phi = 2n\omega_r T^2\gamma\big[2N(T+T_2') + n(T+T_1'+T_2')\big] + 2n\Lambda_{\text{ramp}}T^2.$$

The ramp rate Λ can then be adjusted to give a modulation angle ϕ_m by choosing $\Lambda = \phi_m/2nT^2$. The gradient is then measured by fitting ellipses at $\pm\phi_m$ to give the center phase. For historical reasons, the modulation angle of the ellipses was chosen to be $\pi/6$ instead of $\pi/4$. Some measured ellipses from the gradiometer data are shown in Fig. 5.13 for the interferometer parameters of $n = 5$, $N = 20$, $T_1' = 5$ ms, $T_2' = 45$ ms. As the pulse separation is increased, the phase from the gradient can be observed in the ellipse angle as an asymmetry between the plus and minus ramp modulations.

Since the data was taken before much consideration was given to the ellipse modulation angle, the ellipses taken at large T were fit using Bayesian estimation [47] instead of least squares to reduce the potential of systematics due to fitting errors. The measured gravity gradient phase as a function of pulse separation time T is plotted in Fig. 5.14. The data is fit to the functional form of (5.4), which results in measured gravity gradient equal to

$$\gamma = 2.17(3) \times 10^{-6}\ \text{s}^{-2}$$

[1] In order to run this particular geometry, Bloch oscillations must be present; otherwise, the two beam splitters will necessarily interact with each other as one would be driving $|n\rangle \to |2n\rangle$ while the other $|n\rangle \to |0\rangle$.

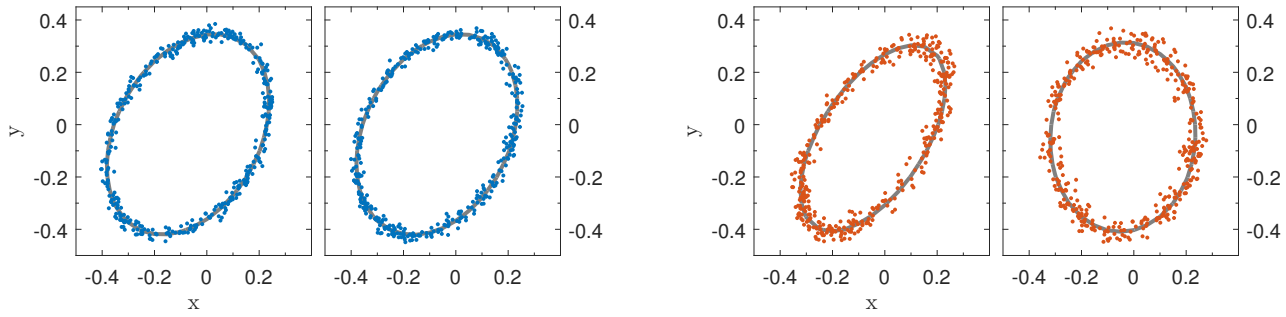

Figure 5.13: Measured gradiometer ellipses for $T = 40$ ms (blue) and $T = 160$ ms (red) with interferometer parameters $n = 5$, $N = 20$, $T_1' = 5$ ms, $T_2' = 45$ ms. The left and right variation of each T corresponds to the $\pm\pi/6$ ramp modulation.

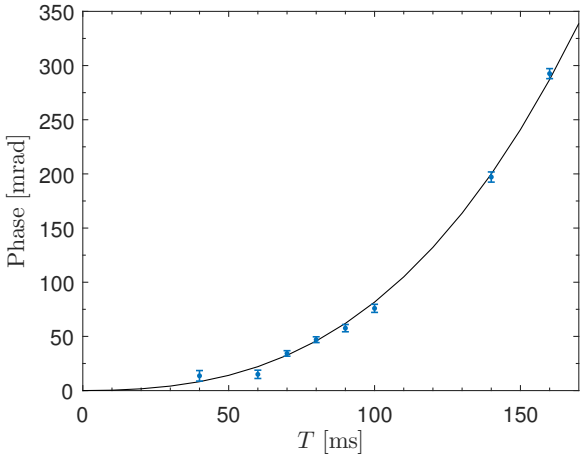

Figure 5.14: The measured phases of the gradiometer at different Mach-Zehnder pulse separation times T. A best fit line to the functional form of Eq. (5.4) is shown in black.

in the region of the experiment. This value of the gravity gradient can then be used to correct the measured frequencies in the Ramsey-Bordé experiment before the extrapolation is performed to remove the gradient systematic. It is not too surprising that the measured value differs significantly from the value near Earth's surface (3.07×10^{-6} s^{-2}). As one goes below Earth's surface the gradient from the Earth changes sign and magnitude, therefore being in a basement one would expect a value part way between the two theoretical values.

Diffraction Phase: Due to the very symmetric nature of the double Mach-Zehnder configuration, the diffraction phase from the Bragg beam splitters cancels exactly. Measurements of the ellipses at very short pulse separation times T, in fact, result in zero measured phase within the statistical uncertainty of a few milliradians.

5.3.1 Systematic Correction

The phase of a Ramsey-Bordé interferometer including gravity gradients is

$$\begin{aligned}\Delta\Phi =& 16n(n+N)\omega_r T - 2n\omega_m T \\ &+ \frac{4}{3}n\omega_r\gamma T\left[n\left(2T^2+3T(T_1'+T_2')+3(T_1'+T_2')^2\right)+N\left(2T^2+6TT_2'+6{T_2'}^2\right)\right]\end{aligned}$$

and, therefore, the fractional correction to the recoil frequency is

$$\frac{\delta\omega_r}{\omega_r} = \frac{\gamma}{12(n+N)}\left[n\left(2T^2+3T(T_1'+T_2')+3(T_1'+T_2')^2\right)+N\left(2T^2+6TT_2'+6{T_2'}^2\right)\right].$$

For typical parameters of $n = 5$, $N = 25$, $T = 80$ ms, $T_1' = T_2' = 5$ ms, and a gravity gradient of $2.17(3) \times 10^{-6}$ s^{-2}, the fractional shift in the recoil frequency is 2.78(4) ppb.

5.4 Monte Carlo Simulations

While the Bragg diffraction theory discussed in Section 2.5 describes the qualitative behavior of the observed diffraction phase, it fails to account for the motion of the atoms and the position and velocity distributions of the atomic ensemble. The finite velocity spread along the axis of Bragg diffraction will cause atoms to have different effective Bragg detunings, while the transverse spatial distribution will cause atoms to sample different intensities (for a finite sized laser waist). The transverse velocity spread will also contribute as the atoms will sample different intensities at each of the four beam splitters.[2]

This transverse motion can also introduce an intensity dependence on the measured diffraction phase when varying the intensity of the first and last beam splitters, despite the cancellation observed for a single atom (Section 2.5.2). To elaborate, consider the scenario diagrammed in Fig. 5.15 where two different atoms interact with the four beam splitter pulses. If the atoms have different transverse velocities and the Bragg beams are Gaussian with a finite waist, then the two atoms will pick up different diffraction phases from the middle two beam splitters (the first and last still do not contribute diffraction phase). These two trajectories will be spatially overlapped during detection (assuming the transverse velocity is small) and the measured phase will be some type of average of the two interferences. If the intensity of the first (or last) beam splitter is changed, then the interference contrast of the two atom paths will also change. Since the contrast is not linear with the intensity, the ensemble will now have a different average interference pattern and thus a different effective diffraction phase.

[2]Keep in mind that for each individual atom, all arms of the interferometer will still see the same intensity for a single beam splitter (as the transverse motion is common to all interferometer paths), but each beam splitter can have a different intensity for a particular atom in the ensemble.

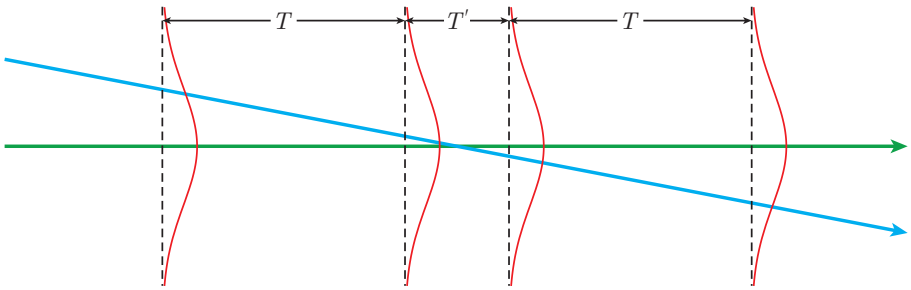

Figure 5.15: A diagram of two possible atom trajectories through the four Bragg beam splitters, one going through the center (green) of the laser beam and one having a transverse velocity (blue). The dashed black lines represent the time of the beam splitters, while the red Gaussian shows the spatial intensity distribution of the laser. The interferometer trajectories caused by the beam splitters on the two different atoms are not shown, but are always along the direction of the beam splitter and not along the direction of the initial atom velocity.

As the interference pattern caused by N_a atoms with different diffraction phases is non-trivial, especially when taking into account the ellipse fitting, a Monte Carlo approach is taken to simulate the measurement. Solving the differential equations (2.41) for a single Ramsey-Bordé interferometer can take more than a second even on a rather powerful computer; thus, it would be impractical to solve the equations for $N_a = 10^6$ atoms each with a random position and velocity (especially if multiple parameters are to be varied). Instead, all relevant matrix elements $\langle a| \hat{H}_{n,N} |b\rangle$ and $\langle a| \hat{H}_n |b\rangle$ are precomputed for a 2D grid of intensities Ω_0 and velocity offsets Δv (the velocity difference from resonance). The matrix elements are then interpolated in the complex plane to give the intermediate values; doing so speeds up the calculation by many orders of magnitude with only a small loss of precision.

The Monte Carlo simulation is performed as follows: For each of the N_a atoms to be simulated, a random position is generated, which is weighted by a Gaussian probability distribution with a width σ_{xyz} given by the atom cloud's initial size (as calculated from the temperature time-of-flight measurements). An x and y velocity is also generated from a Maxwell-Boltzmann distribution ($\sigma_{v_{xy}}$) based on the Raman-sideband cooling temperature of the atoms. The z velocity is sampled from a Gaussian approximation of the momentum spread (σ_{v_z}) resulting from the velocity selection in Section 4.3. Other parameters such as an overall transverse velocity and position offset can be added to each atom to simulate an imperfect launch, if desired. To increase the integration rate of the computation, a parameter for the detection radius r_{det} is used to immediately throw out any atoms that would not end up in the detection region after the full time-of-flight. (To keep the statistical resolution of the simulation, new atoms are generated until one is created that does end up in the detection region.)

Once an atom is initialized (given its initialized position and velocity and assuming the initialized atom was released at a time coinciding with the end of the Raman-sideband cooling), the position of the atom is then calculated at the state selection pulse, at each

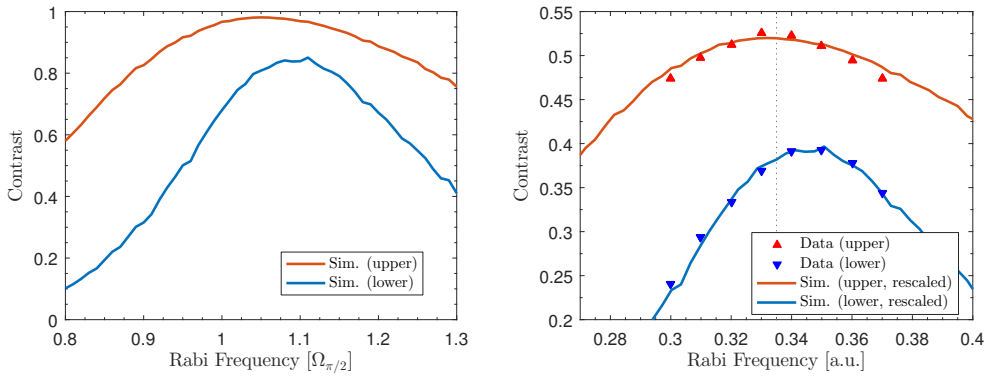

Figure 5.16: A Monte Carlo simulation for an $n = 4$, $N = 0$ interferometer with $T = 160$ ms. Left: The simulated contrasts for the upper (red) and lower (blue) interferometers as a function of the Rabi frequency in units of the $\pi/2$ Rabi-frequency, $\Omega_{\pi/2}$. Right: A comparison to the measured contrast for a $n = 4$ interferometer with the Rabi frequencies rescaled to match the data and the contrasts scaled by 53% for the upper simulation and 46% for the lower simulation to show the similarity of the intensity dependence.

of the two velocity selection pulses, and at all four Bragg diffraction pulses. The state selection and velocity selection positions will determine three amplitude coefficients. Each coefficient is determined by the Rabi oscillation transition amplitude given by the laser intensity at the atom's position (for a beam waist of w_0). At the position of each Bragg pulse, the complex matrix element for each interferometer path is computed given the intensity at the location of the atom and the atom's z velocity. The total probability amplitude coefficient c_{ijk} is then computed for each of the 8 possible paths as given in Section 2.5.2, including the additional amplitude coefficients from the state and velocity selection. The total interferometer amplitudes are then calculated as

$$|\Psi_{uu}|^2 = \sum_{j=1}^{N_a} \left| c^j_{uuu} + c^j_{u\ell u} e^{-i(\phi_c+\phi_m)} \right|^2, \qquad |\Psi_{u\ell}|^2 = \sum_{j=1}^{N_a} \left| c^j_{uu\ell} + c^j_{u\ell\ell} e^{-i(\phi_c+\phi_m)} \right|^2,$$

$$|\Psi_{\ell\ell}|^2 = \sum_{j=1}^{N_a} \left| c^j_{\ell u\ell} e^{i(\phi_c+\phi_m)} + c^j_{u\ell\ell} \right|^2, \qquad |\Psi_{\ell u}|^2 = \sum_{j=1}^{N_a} \left| c^j_{\ell uu} e^{i(\phi_c+\phi_m)} + c^j_{u\ell u} \right|^2,$$

where c^j is a probability amplitude coefficient for the jth atom, ϕ_c is the common mode phase (the differential phase is assumed to be zero), and the modulation phase ϕ_m is used to shift the phase away from zero. These interferometer amplitudes are calculated for values of ϕ_c between 0 and 2π and $\phi_m = \pm\pi/4$ to generate ellipses, which are then fit to obtain the simulated diffraction phase. The amplitude of the ellipse also gives a measure of the maximum theoretical contrast.

The results of one such simulation for $n = 4$, $N = 0$, and $T = 160$ ms are plotted in Fig. 5.16, with atom parameters listed in Table 5.1, taken from experimental measurements. The

Table 5.1: Parameters used in the Monte Carlo simulations, unless otherwise noted.

Parameter	Symbol	Value
Bragg diffraction order	n	5
Bloch oscillation order	N	25
Pulse width	σ	$0.188\omega_r^{-1}$
Gaussian cutoff	τ	3.272σ
Intensity	Ω_0	$1.05\Omega_{\pi/2}$
Vertical velocity spread	σ_{v_z}	$0.07v_r$
Transverse velocity spread	$\sigma_{v_{xy}}$	$1.5v_r$
Position spread	σ_{xyz}	2.2 mm
Initial position offset	x_0	0
Initial x-velocity	v_{x_0}	0
Initial z-velocity	v_{z_0}	0
Pulse separation time	T	80 ms
Center separation time	T'	10 ms
Detection radius	r_{det}	2 mm
Laser waist	w_0	6.2 mm
Number of simulations	N_a	10^6
Bins used for statistics	N_{bin}	10

plot shows the simulated contrast as a function of the Rabi frequency – where it becomes apparent that more than the theoretical $\pi/2$ pulse intensity is required for maximum contrast. Additionally, the lower and upper interferometer have different optimal intensities, which is consistent with the fact that the lower interferometer has the majority of the hotter atoms. Also plotted is a comparison to the data from Fig. 5.4, where the Rabi frequency of the simulation has been scaled to match the data. The contrast vs. intensity simulations agree fairly well, assuming the simulated upper interferometer contrasts are scaled by 53% and the lower contrasts are scaled by this and another 88% (for a total of 46%). The overall scaling of 53% is most likely due to a combination of background atoms and other decoherence sources which are not accounted for in the simulation. The extra contrast loss in the lower interferometer is probably due to the sample being less ideal than the simulated parameters.

To check the sensitivity of the diffraction phase to the individual pulse intensities, the Monte Carlo simulation was run with $n = 5$ and $N = 0$ or $N = 25$ to compare with the results from Fig. 2.19 for a single atom interferometer. The same atom parameters described in Table 5.1 are used, with $T = 160$ ms for $N = 0$ and $T = 80$ ms for $N = 25$. The intensity Ω_0 used for the Bragg pulses was chosen to be 5% higher than the $\pi/2$ pulse intensity $\Omega_{\pi/2}$ in order to operate at the maximum observed contrast. The third and last pulse intensities were then varied proportional to $1.05\Omega_{\pi/2}$, with results plotted in Fig. 5.17. The immunity to the last pulse intensity is no longer present, but the variation is still suppressed when compared to the third pulse intensity. Also plotted is the diffraction phase as a function of

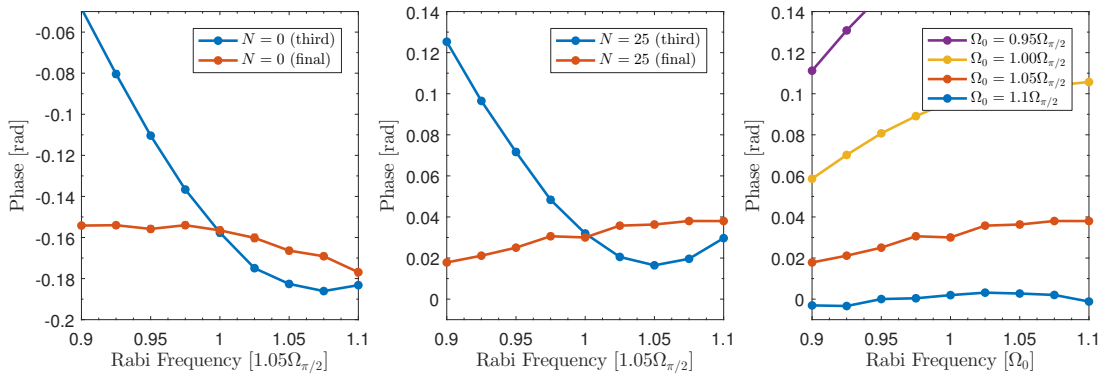

Figure 5.17: Monte Carlo simulated diffraction phases for an $n = 5$ interferometer as a function of the third and last pulse intensities. Left: The diffraction phase for $N = 0$ and $T = 160$ ms using an overall intensity of $\Omega_0 = 1.05\Omega_{\pi/2}$ for all pulses except the one being varied, either the third (blue) or last (red). Center: The same simulation but with $N = 25$. Right: A comparison of diffraction phase vs. last pulse intensity for several overall intensities Ω_0 for $N = 25$.

the last pulse intensity for several overall intensities Ω_0. At a Rabi frequency of $\Omega_0 = 1.1\Omega_{\pi/2}$, the diffraction phase sensitivity to the last pulse diminishes, which might end up being a promising operating point to reduce systematics.

5.4.1 Parasitic Interferometers

Since Bragg diffraction has the potential to populate momentum states other than the desired orders, it is possible to create parasitic interferometers that can cause shifts in the measurements [79]. Due to the momentum selectivity of the Bloch oscillations, the most likely parasitic interferometers are Ramsey-Bordé like, where the momentum of the atom matches the lattice velocity ($|0\rangle$ or $|n\rangle$) during T', as shown in Fig. 5.18. The phase accumulated along these parasitic Ramsey-Bordé trajectories can be calculated as

$$\phi_p = \pm 8n_p(n_p + N)\omega_r T \pm n_p\omega_m T + \phi_c(n_p),$$

where the plus and minus corresponds to the lower and upper parasitic interferometers, respectively, n_p is the Bragg order, and $\phi_c(n_p)$ is the common mode phase due to vibrations. The modulation frequency ω_m is unchanged, which means that when the phase of the main Ramsey-Bordé interferometer is canceled with $\omega_m \approx 8(n + N)\omega_r$, then the parasitic phase reduces to

$$\begin{aligned}\phi_p &= 8n_p(n_p + N)\omega_r T - 8n_p(n + N)\omega_r T + \phi_c(n_p)\\ \phi_p &= 8n_p(n_p - n)\omega_r T + \phi_c(n_p).\end{aligned}$$

Since the effective Rabi frequency decreases as the Bragg order increases, the parasitic interferometers that are most likely to occur are those with $n_p = 1$. This corresponds to a

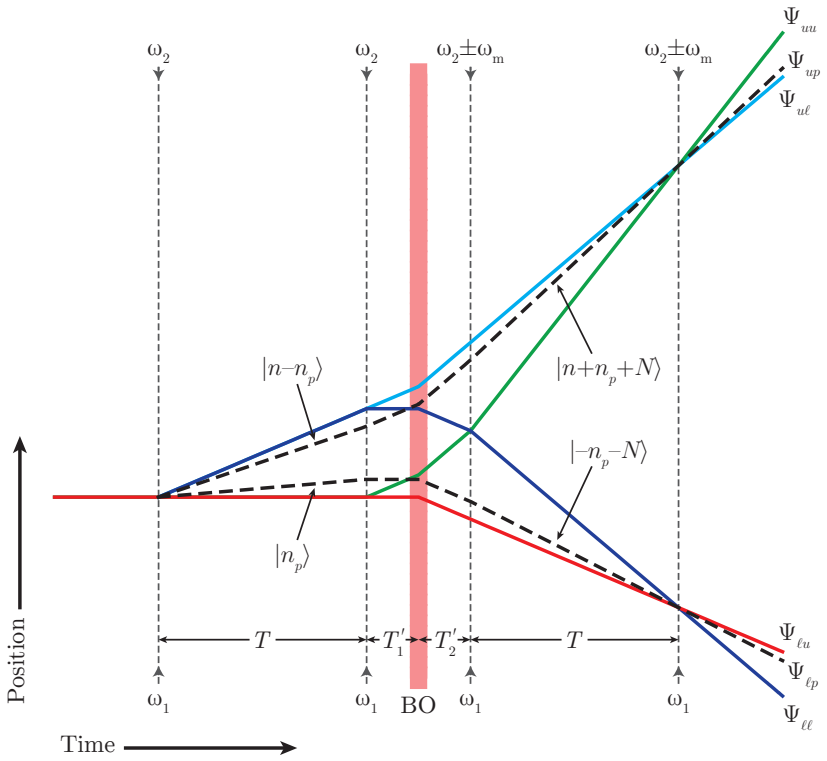

Figure 5.18: A space-time diagram for a Ramsey-Bordé interferometer with Bloch oscillations, showing a few possible parasitic interferometer trajectories (dashed) in addition to the desired paths (solid).

Ramsey-Bordé interferometer where the atom gets kicked by $2\hbar k$ from rest and the conjugate interferometer where the atom gets kicked by $2(n - n_p)\hbar k$ at the first beam splitter (followed by kicks of only $2\hbar k$). The conjugate interferometer will most likely have a smaller amplitude since the first transition from $|0\rangle \rightarrow |n - n_p\rangle$ is suppressed, but it is included here for symmetry.

To investigate the influence of these parasitic interferometers on the recoil measurement, the Monte Carlo simulation was modified to include these unwanted interferometer paths. The resulting amplitudes of the four interferometer outputs including the parasitic trajectories are then

$$
\begin{aligned}
|\Psi_{uu}|^2 &= \left|c_{uuu} + c_{u\ell u}e^{-i(n\phi_c+\phi_m)} + c_{upu}e^{i(\phi_r-n_p\phi_c)}\right|^2, \\
|\Psi_{u\ell}|^2 &= \left|c_{uu\ell} + c_{u\ell\ell}e^{-i(n\phi_c+\phi_m)} + c_{up\ell}e^{i(\phi_r-n_p\phi_c)}\right|^2, \\
|\Psi_{\ell u}|^2 &= \left|c_{\ell uu}e^{i(n\phi_c+\phi_m)} + c_{u\ell u} + c_{\ell pu}e^{i(\phi_r+n_p\phi_c)}\right|^2, \\
|\Psi_{\ell\ell}|^2 &= \left|c_{\ell u\ell}e^{i(n\phi_c+\phi_m)} + c_{u\ell\ell} + c_{\ell p\ell}e^{i(\phi_r+in_p\phi_c)}\right|^2,
\end{aligned}
$$

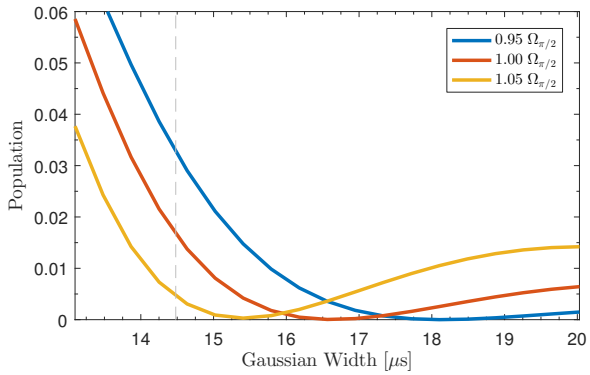

Figure 5.19: Population transfer to the first diffracted order vs. Gaussian pulse width σ for $n = 5$ and Gaussian cutoffs of $\tau = 3.272\sigma$. The intensity $\Omega_{\pi/2}$ is recalculated at each Gaussian width to give an optimal $\pi/2$ pulse. The blue and yellow curves show the population transfer for $\pm 5\%$ the $\pi/2$ intensity. The dashed line indicates the usual experimental value of $\sigma = 0.188\omega_r^{-1} = 14.48\mu$s.

where $\phi_r = n_p(n_p - n)\omega_r T + n_p\phi_m/n$ and the probability amplitudes c_{ipk} for the $i = [\ell, u]$ interferometer and the $k = [\ell, u]$ output port are given by the matrix elements:

$$
\begin{aligned}
c_{upu} &= \langle 2n+N|\,\hat{H}_{n,N}\,|n+n_p+N\rangle\,\langle n+n_p+N|\,\hat{H}_{n,N}\,|n+N\rangle\,\langle n|\,,\hat{H}_n\,|n-np\rangle\,\langle n-n_p|\,\hat{H}_n\,|0\rangle\,,\\
c_{up\ell} &= \langle n+N|\,\hat{H}_{n,N}\,|n+n_p+N\rangle^2\,\langle n|\,\hat{H}_n\,|n-np\rangle\,\langle n-n_p|\,\hat{H}_n\,|0\rangle\,,\\
c_{\ell pu} &= \langle -N|\,\hat{H}_{n,N}\,|-n_p-N\rangle^2\,\langle n_p|\,\hat{H}_n\,|0\rangle^2\,,\\
c_{\ell p\ell} &= \langle -n-N|\,\hat{H}_{n,N}\,|-n_p-N\rangle\,\langle -n_p-N|\,\hat{H}_{n,N}\,|-N\rangle\,\langle n_p|\,\hat{H}_n\,|0\rangle^2\,.
\end{aligned}
$$

Since the common mode phase ϕ_c is different for the parasitic trajectory due to the number of photons transferred from the laser field, the vibrations are rescaled to $n\phi_c$ and $n_p\phi_c$ for the two interferometer orders. It is no longer valid to assume that the vibrations will cause an evenly distributed set of points around the ellipse and therefore, the distribution of phase will have an effect on the interferometer pattern due to the n vs. n_p scaling. The vibration phase distribution was estimated based on seismometer data taken from a neighboring experiment in the lab. For a pulse separation time of $T = 20$ ms, the distribution of ϕ_c is estimated to be Gaussian with a standard deviation of $\sigma_\phi = 1.2$.

The atom population that gets transferred to the undesired order $n_p = 1$ is a strong function of the Bragg pulse width σ as shown in Fig. 5.19. For typical experimental parameters of $\sigma = 0.188\omega_r^{-1} = 14.5$ μs, the population transferred to the first order by the Bragg beam splitter can be as much as a few percent. There does exist a local minimum at a slightly longer pulse length, but it is dependent on the intensity used. As a compromise, a value of $\sigma = 0.216\omega_r^{-1} = 16.6$ μs is simulated as a comparison to the typical $\sigma = 0.188\omega_r^{-1}$ value.

Some results of the Monte Carlo simulation with parasitic interferometers are shown in Fig. 5.20 for $n = 5$ and $N = 0$ for pulse separation times near $T = 20$ ms (in steps of 2 μs). Simulations for both the typical $\sigma = 0.188\omega_r^{-1}$ and the optimized $\sigma = 0.216\omega_r^{-1}$ (with the

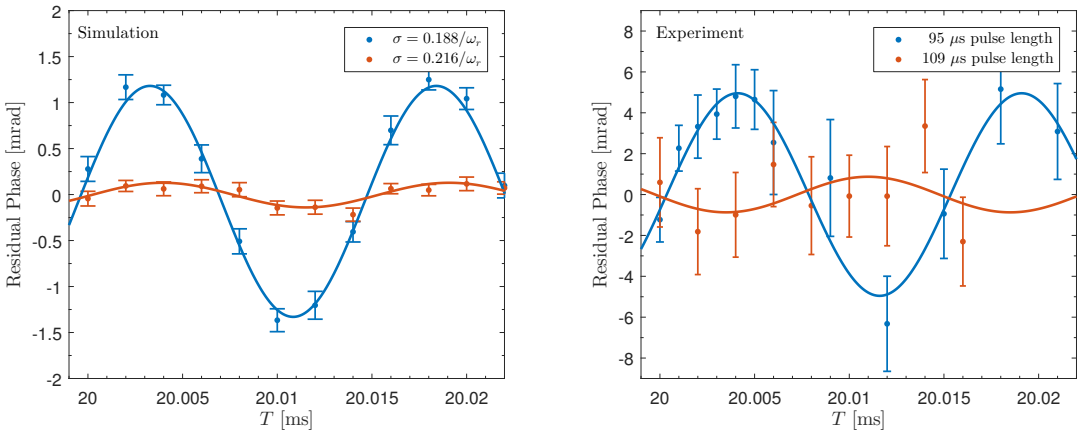

Figure 5.20: Left: The residual diffraction phase obtained by Monte Carlo simulation when parasitic interferometers are included for $n = 5$, $N = 0$, $n_p = 1$, and T varied between 20 and 20.02 ms. Right: The experimentally measured residual diffraction phase for 95 μs and 109 μs Gaussian pulse lengths, which correspond to $\sigma = 0.188\omega_r^{-1}$ and $\sigma = 0.216\omega_r^{-1}$ pulse widths, respectively. Also plotted are sinusoidal best fits (with all parameters free, except for the 109 μs experimental data where the period is fixed).

same pulse cutoffs of $\tau = 3.272\sigma$) are plotted for comparison. The Monte Carlo parameters are the same as before, except that an intensity of $\Omega_0 = \Omega_{\pi/2}$ is used. The simulations show a fringe with a period of $8n_p(n - n_p)\omega_r = 2\pi \cdot 66$ kHz, which is suppressed by almost an order of magnitude for the optimized pulse length. In general, if the common mode phase distribution is made to be smaller than $\sigma_\phi = 1.2$ radians, then the oscillations get stronger (and suppressed for a distribution larger than 1.2 radians). Additionally, decreasing the Rabi frequency has the effect of increasing the oscillation amplitude, as one would expect from the calculations in Fig. 5.19.

Also plotted in Fig. 5.20 is experimental data for a Ramsey-Bordé interferometer when using a 95 μs ($\sigma = 0.188\omega_r^{-1}$) Bragg pulses and the optimized 109 μs ($\sigma = 0.216\omega_r^{-1}$) pulse length. To observe any potential parasitic interferometers, ellipses were measured at $T_{\text{short}} = 5$ ms and $T_{\text{long}} = 80$ ms in addition to values near 20 ms. The diffraction phase was then extracted by fitting the measured frequencies to a $1/T$ curve, and then the resulting phase fit residuals are plotted. The observed oscillation for the $\sigma = 0.188\omega_r^{-1}$ pulse data has the same frequency as predicted from theory (66 kHz), which confirms that the observed parasitic interferometer has order $n_p = 1$. The peak-to-peak amplitude of the fitted oscillation for the $\sigma = 0.216\omega_r^{-1}$ data is zero within experimental error (2.4 ± 2 rad) and is consistent with the reduction seen in the simulation. While the fitted amplitude of the oscillation in the 95 μs pulse length data does not agree entirely with the simulation, the fact that the oscillation is larger is not surprising since any misalignments are likely to increase the size of the parasitic interferometers.

5.4.2 Time Dependent Diffraction Phase

One possible source of systematic error that has yet to be discussed is a diffraction $\phi(T)$ that is a function of the pulse separation. Since the only real way to eliminate the diffraction phase systematic is to extrapolate the measured frequency ω_m as T approaches infinity (as was discussed in Section 5.2), a linear T dependence in ϕ will result in a systematic shift in the inferred value of ω_r. Consider a zero phase measurement from Eq. (5.1), where $\phi_0 \to \phi(T)$ is instead written as a power series in T such that

$$2n\omega_m T = 16n(n+N)\omega_r T + \left[\phi_0 + \frac{\partial\phi}{\partial T}T + \mathcal{O}(T^2)\right], \tag{5.5}$$

where ϕ_0 is the usual constant diffraction phase. If higher order powers in T are ignored, then (5.5) can be rewritten as

$$\begin{aligned}\frac{\omega_m}{8(n+N)} &= \omega_r + \frac{1}{16n(n+N)T}\left(\phi_0 + \frac{\partial\phi_0}{\partial T}T\right) \\ &= \left[\omega_r + \frac{1}{16n(n+N)}\left(\frac{\partial\phi}{\partial T}\right)\right] + \frac{\phi_0}{16n(n+N)}\frac{1}{T},\end{aligned}$$

where the linear dependent part of the diffraction phase is grouped with the recoil phase for clarity. If the pulse separation time is extrapolated to infinity, then there will be a systematic error in ω_r of

$$\delta\omega_r = \frac{1}{16n(n+N)}\left(\frac{\partial\phi}{\partial T}\right),$$

which cannot be determined with a Ramsey-Bordé measurement as it is indistinguishable from the recoil signal. The only two options to deal with this type of systematic are to either perform the experiment at different parameters (n, N, etc.) and assume the linear dependence of the diffraction phase is not constant or instead estimate the size of the effect with theoretical calculations. Since the Monte Carlo simulation already deals with the time dependent dynamics of the atoms, one can use it to estimate the size of $\phi_1 \equiv \partial\phi/\partial T$ for a given set of parameters.

Some examples of systematic searches using Monte Carlo simulation are shown in Fig. 5.21 for $n = 5$, $N = 25$, $\sigma = 0.216\omega_r^{-1}$ and the usual parameters listed in Table 5.1 (unless otherwise noted). A value of ϕ_1 was determined by calculating the phase at $T = \{5, 10, 20, 40, 60, 80\}$ ms and using a linear $1/T$ fit. The intensity dependent systematic shows a minimum shift in the region of $1.05\Omega_{\pi/2} \pm 5\%$ with errors below 0.2 ppb in ω_r. Large variations are seen if the detection region is factor of 2 larger, with systematic errors approaching 1 ppb. Therefore it is very important to detect only the central-most atoms through heavy spatial filtering of the signal. By spatially filtering the sample during velocity selection using a smaller beam waist (Fiber:VS in Fig. 4.9) rather than using the Bragg beam fiber-port, the sensitivity to intensity can be reduced slightly. Therefore, this might be a viable strategy to reduce position dependent systematic phase shifts.

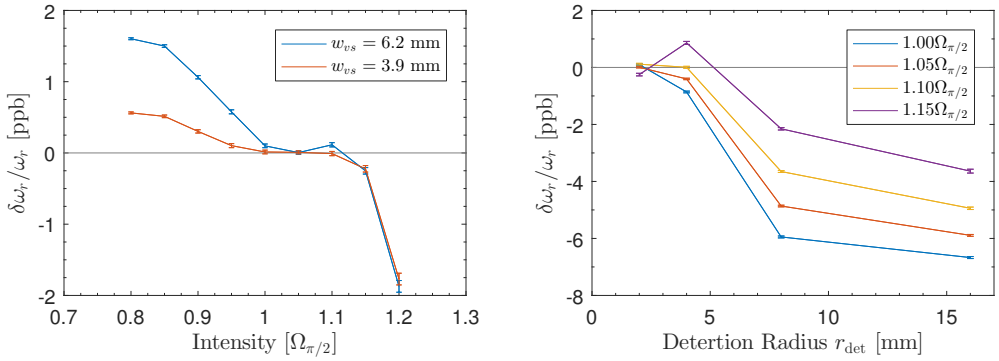

Figure 5.21: Monte Carlo simulated shifts in the measured recoil frequency ω_r due to a linear diffraction phase term ($\partial\phi/\partial T$) as a function of experimental parameters, with $\sigma = 0.216\omega_r^{-1}$ and the usual parameters listed in Table 5.1. Left: The systematic shift in ω_r as a function of the overall intensity in units of $\Omega_{\pi/2}$, for different velocity selection beam waists. Right: The shift as a function of detection radius for different overall intensities, for the normal velocity selection waist of 6.2 mm.

5.5 Compensation

One factor preventing the use of more Bloch oscillations is the large contrast decay at longer pulse separation time, limiting the number of Bloch oscillations to around $N = 25$. To investigate the cause of the decoherence, interferometer data was taken with varying Bloch lattice depths U_0 and Bloch ramp times t_{bloch}. Fig. 5.22 shows the measured interferometer contrasts and the observed Bloch transfer efficiencies for $n = 4$, $N = 50$, $T = 80$ at 15 GHz blue-detuned, where the efficiency was measured as the fraction of atoms transferred to the $|-N\rangle$ state from $|0\rangle$. Universally, a deeper lattice or a longer ramp rate decreases the contrast while simultaneously increasing the transfer efficiency. While this might seem consistent with decoherence due to single photon scattering

$$\begin{aligned} P_{\mathrm{loss}} &= 1 - \exp\left(-\frac{\Gamma^3}{8\Delta^2}\frac{I}{I_{\mathrm{sat}}}t\right) \\ &= 1 - \exp\left(-\frac{\Gamma U_0}{2\hbar\Delta}t\right) \end{aligned}$$

from (4.2), the theoretical rate is much too low. In Section 4.5 it was determined that a single Bloch lattice had a depth of approximately $6\hbar\omega_r$. The single photon scattering intensity then is a factor of 3 larger to account for the two other simultaneous lattices. With parameters of $\Gamma = 2\pi \cdot 5.2$ MHz, $\Delta = 2\pi \cdot 15$ GHz, $U_0/\hbar \approx 20\omega_r$, and a Bloch time of 1.5 ms, the single photon scattering rate should only be 6%. Additionally, this would not explain why the contrast decreases for increased pulse separation time T, which should be independent of the single photon scattering.

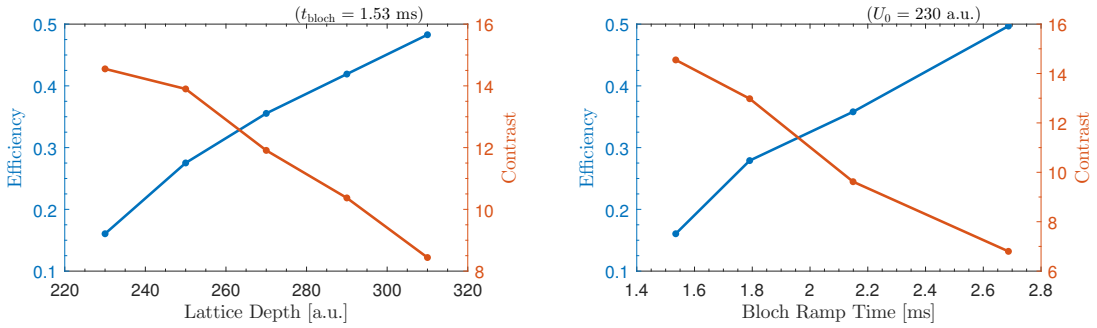

Figure 5.22: A plot of the measured transfer efficiencies of the Bloch oscillations (blue) as a function of lattice depth (left) and Bloch ramp time (right) for $n = 4$, $N = 50$, $T = 80$ ms and Δ= 15 GHz. Plotted in red are the measured contrasts of the upper interferometer of the Ramsey-Bordé interferometer for the same parameters.

Instead, a differential ac-Stark shift mechanism dominates the contrast loss as proposed and experimentally solved by Kovachy et. al. [55]. It is normally assumed that during the interferometer, each part of the atom superposition experiences the same optical intensity along each interferometer path since any transverse motion is common mode between the atom superposition states. However, if the Gaussian beam intensity is not translationally invariant due to divergence, diffraction or scatter, then the ac-Stark shift will be different between the paths causing a phase shift in the interferometer. When the differential ac-Stark shift is common to all atoms in the ensemble, then the ac-Stark shift will cause a systematic shift in the measured phase. On the other hand, if each atom in the ensemble sees a different ac-Stark shift, then the effective contrast will decrease due to the averaging of many interference patterns.

Consider a scenario where the Gaussian beam is diffracted by a circular aperture (lens, window, fiber-port etc.) or from dust on an optical component. The intensity distribution across the beam will change as a function of distance with larger variations occurring at longer distances. As the pulse separation time increases in a Ramsey-Bordé interferometer, so does the spatial separation and thus the intensity variation, decreasing the measured contrast of the ensemble. With an effective intensity of $20\omega_r$ for all of the Bloch lattices, a 1 ms Bloch pulse causes $20\omega_r \cdot 10^{-3}$s ≈ 260 radians of common mode phase due to ac-Stark shifts. If the intensity variation across the atom cloud is only 1%, then the phase difference between different parts of the cloud will nearly exceed π and no interference will be observed.

To compensate for this decoherence effect, a second laser frequency is added to the Bloch beam during the Bloch oscillation pulse. Since the second beam travels along the exact same path into the chamber, it will also (to first order) get diffracted and scattered in the same way. If the second laser has the opposite single photon detuning, then the ac-Stark shift caused by the second beam will have the opposite sign. Therefore, by selecting the intensity appropriately, the two ac-Stark shifts can cancel and the contrast will be restored.

In order to generate the compensation light, a free running external cavity diode laser is

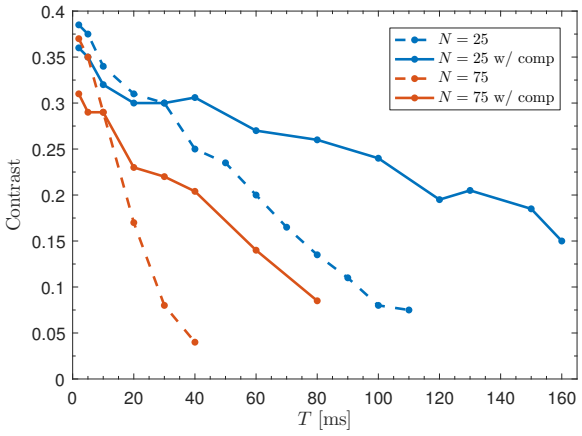

Figure 5.23: The measured upper interferometer contrast of a Ramsey-Bordé interferometer with $n = 5$, $N = 25$ (blue) and $N = 75$ (red) showing the improved contrast resulting from the ac-Stark compensation beam.

amplified by a tapered amplifier, coupled into a fiber (Fiber:ac-Stark), and mixed with the Bloch beam as shown in Fig. 4.3. To overlap the beams, AOM19 is run at 50% efficiency and the compensation beam is sent into the other AOM input port. Since 50% of the Bloch power is now lost, the intensity of the Bloch beam is increased by a factor of 2 to compensate. The intensity of the compensation beam is controlled by measuring the intensity at PD9 and feeding back to the TA current.

The results of using ac-Stark shift compensation are shown in Fig. 5.23 where the upper interferometer contrast was measured at different pulse separation times with and without compensation for $n = 5$, $N = 25$ and $N = 75$. The compensation beam improves the contrast significantly at long T, especially for $N = 75$. The small loss of contrast at short T is most likely due to additional single photon scatter from the compensation beam. Further improvements to this method might enable the use of higher order Bloch oscillations at longer T for improved sensitivity in the future.

5.6 Recoil Measurement

The ultimate goal of this experimental apparatus is a measurement of the recoil frequency $\omega_r = \hbar k^2/2m_{\mathrm{Cs}}$ in order to determine $\hbar/m_{\mathrm{Cs}}$ for cesium to better than 0.5 ppb uncertainty. To that end, this chapter concludes with data from an attempt at a final measurement and the reason why more work needs to be done.

After completing a fresh alignment of the fountain and Bragg beams, a series of recoil measurements with $n = 5$, $N = 25$, and a Gaussian pulse length of 95 μs ($\sigma = 0.188\omega_r^{-1}$) was taken between November 15 and November 31, 2015. To check for possible T dependent diffraction phases, modulation frequency measurements were made at pulse separation times of $T = \{5, 10, 20, 40, 60, 80\}$ ms. For each T, 30 ellipse points were taken for both plus

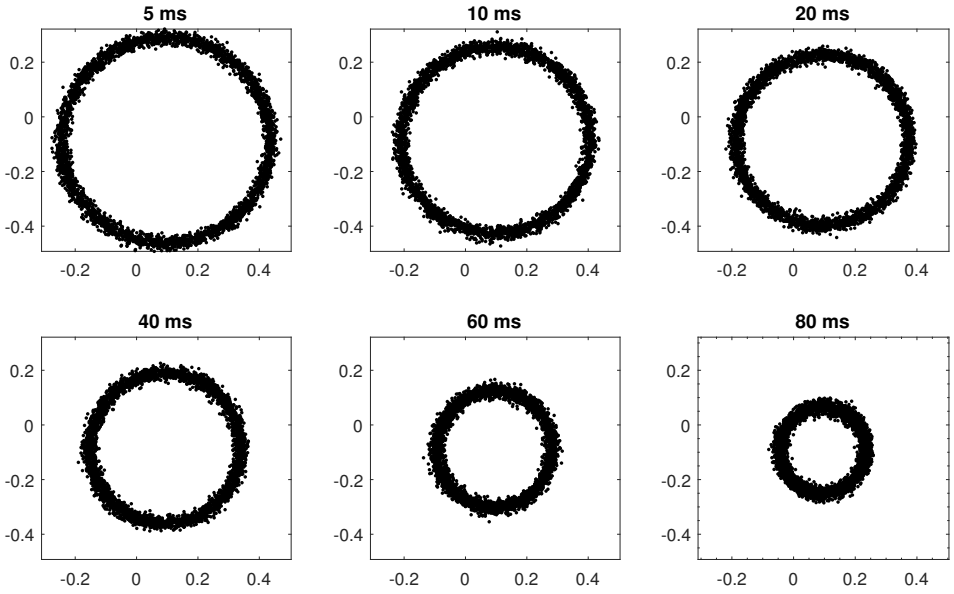

Figure 5.24: All of the $+\pi/4$ modulated ellipse data taken on November 23rd, 2015 for an interferometer with $n = 5$ and $n = 25$.

and minus modulation frequencies, at which point the ellipses were fit and the next T was measured in the same way. After all 6 pulse separation times were completed, the set of measured modulation frequencies were fit to a $1/T$ line and extrapolated (as was done in Section 5.2) to obtain a measurement of the recoil frequency. These fits took into account all currently known systematics including gravity gradients, laser frequency, beam alignment, etc. (which are described in Chapter 6). This was then repeated continuously until the experiment failed, at which point it was fixed, realigned, and a new measurement cycle was started over. By repeatably measuring the set of Ts, drifts in the diffraction phase slower than the repetition rate ($60 \times 6 \times 2.1$ seconds = 12.6 minutes) are canceled.

Some of the measured ellipses from the November 23rd dataset are shown in Fig. 5.24 for each pulse separation time used. The plotted dataset consists of just the $+\pi/4$ modulated ellipses and shows only 21600 out of the 202260 total ellipse points taken over the month. Every few days, the measured recoil frequencies were binned and a statistical error bar was calculated. The result of all 6 measurement sets are shown in Fig. 5.25, along with a weighted average of the entire set. The weighted average has a statistical error bar of 0.6 ppb in ω_r and thus in $\hbar/m_{Cs}$.

When calculating the $1/T$ fits to the $\omega_m(T)$ data, the residuals were also calculated; the average of all residuals are shown in Fig. 5.25. It is very clear that some pulse separation times deviate significantly from the fit line, which indicates that those Ts have a slightly different diffraction phase than the baseline (fit value). This "anomalous" residual phase poses a serious problem for a recoil measurement and was the main motivation for the Monte Carlo simulation and the work done to reduce the parasitic interferometers. Despite

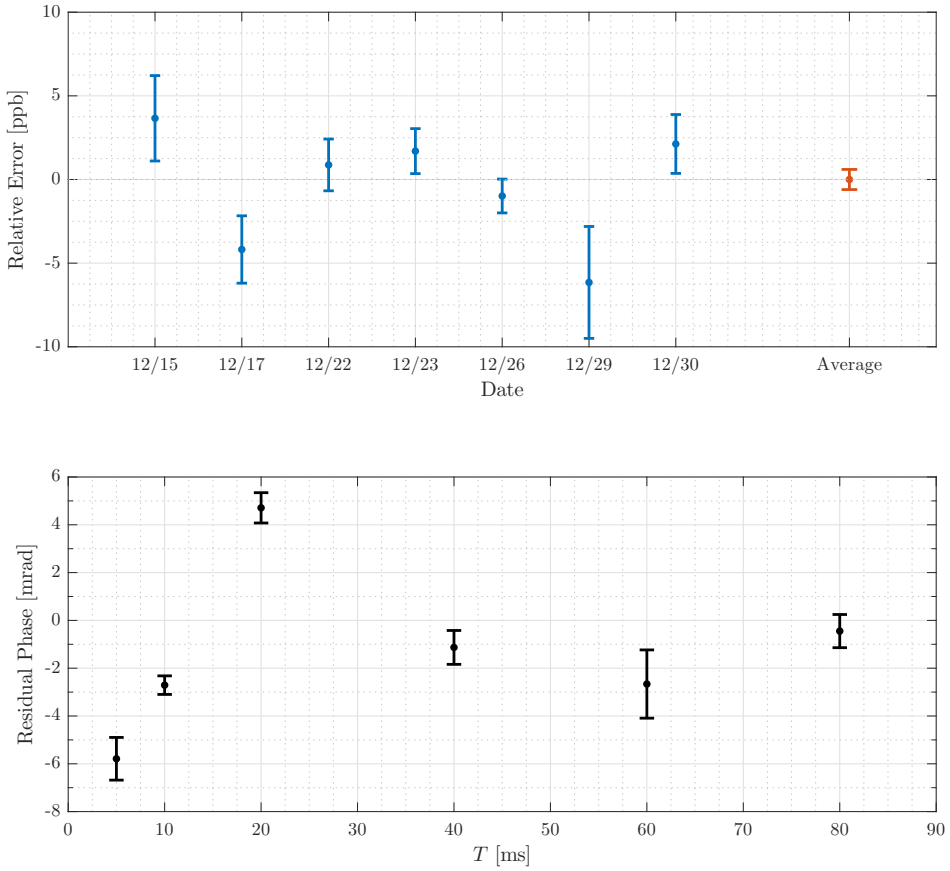

Figure 5.25: Recoil measurement data taken over the month of November (2015) for an interferometer with $n = 5$ and $N = 25$. Top: The relative error in ω_r for the six measurement sets and a final weighted average with an uncertainty of 0.6 ppb. Bottom: The residual diffraction phase (as measured from the fitted constant diffraction phase) for each pulse separation time used. Several points statistically deviate from zero, which indicates a diffraction phase that is not constant for all T.

the work done since this measurement was taken, including the ultimate change in the pulse length to 109 μs (which was not used in this data), this anomalous diffraction phase is still present. There are some hints that this anomaly is related to fountain and Bragg alignment, but the results are still preliminary. For this reason, the value of the averaged measurement in Fig. 5.25 will not be listed in this thesis so that the final measurement can remain blind.

Chapter 6

Systematics

6.1 Wave-vector Systematics

When obtaining a measurement of $\hbar/m$ from the recoil frequency $\omega_r = \hbar k_{\text{eff}}^2/8m$, one needs to be very careful about the treatment of the effective wave-vector $\vec{k}_{\text{eff}} = \vec{k}_1 + \vec{k}_2$. The exact momentum transferred to the atoms during a beam splitter is influenced by four factors: laser frequency, beam alignment, the Gouy phase, and the wavefront curvature.

6.1.1 Laser Frequency

The conversion between ω_r and h/m requires a very precise measurement of the laser frequencies which determines k_{eff}. For a laser frequency uncertainty of $\delta\omega_L = c\delta k_{\text{eff}}/2$, the resulting uncertainty in $\hbar/m$ is

$$\frac{\delta(\hbar/m)}{\hbar/m} = 4\frac{\delta\omega_L}{\omega_L}.$$

Therefore, a fractional uncertainty of 0.1 ppb in $\hbar/m$ requires the laser's frequency to be accurate to 10 kHz for 852 nm light. Since all function generators are referenced to a rubidium frequency standard (which is calibrated by the GPS 10-MHz signal), the frequency shifting from AOMs and the offset lock are known to much better than 1 Hz accuracy. This only leaves the uncertainty of the spectroscopy which determines the reference laser frequency.

In theory, the spectroscopy should be stabilized exactly to the $3 \rightarrow 2'$ D_2 transition in cesium which has a frequency of 351.73054961(11) THz (from Fig. 3.2). However, there are inevitably systematic shifts and drifts despite the resilience of the modulation transfer spectroscopy. To measure the exact frequency of the reference laser, a small amount of light is coupled into a fiber after TA1 (see Fig. 3.3) and sent to a Menlo Systems Titanium:Sapphire frequency comb. The frequency comb generates thousands of laser frequencies that are all equally spaced by the laser repetition rate of $f_{\text{rep}} = 200$ MHz with a known frequency offset f_{offset} from zero [127]. By overlapping the reference laser with one of the comb teeth and

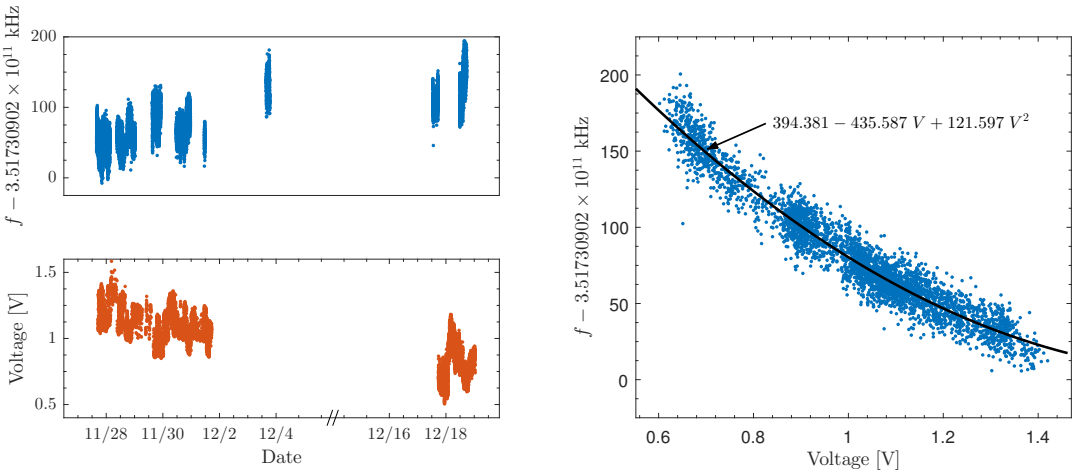

Figure 6.1: The measured reference laser frequency and correlation with the spectroscopy photodiode voltage. Top: The reference laser frequency as measured by the comb, with gaps occurring when the frequency comb was non-functional. Bottom: The spectroscopy photodiode voltage as a function of time. As the voltage decreases, the measured frequency increases. Right: The correlation between the voltage and the frequency as measured by the comb. The correlation is approximately quadratic, with a best fit shown in black.

detecting the resulting beat frequency, a measurement of the laser frequency difference Δf between the comb tooth and the reference can be made. With knowledge of the absolute comb tooth number from a rough laser frequency measurement (from a wave-meter), the absolute frequency of the reference can then be calculated as

$$f_{\text{ref}} = f_{\text{offset}} + n f_{\text{rep}} + \Delta f,$$

where n is the comb tooth number. Since both f_{offset} and f_{rep} are also referenced to the rubidium frequency standard, they are known to approximately 0.01 ppb. The reference laser can then be measured to roughly 3.5 kHz with the frequency comb.

A plot of the measured reference frequency over the course of a month is shown in Fig. 6.1, which shows a drift in the spectroscopy locked frequency of 100 kHz. The drift is correlated with the total photodiode signal voltage (not the demodulated signal) and, thus, drifts in the absolute power of the spectroscopy seem to be causing a drift in the reference laser frequency. Since the long term stability of the spectroscopy is determined by modulation transfer spectroscopy, this drift is most likely caused by the EOM1 modulated light being parasitically reflected off the vapor cell and detected by PD2. The parasitic modulated light will be demodulated and cause a DC offset in the lock that changes with laser power.

Without improving the alignment, this drift can be calibrated out by recording the photodiode signal and correcting the recoil data in post processing using the calibration curve shown in Fig. 6.1. To determine the effectiveness of this approach, the extrapolated frequency is compared to the comb measured frequency and the difference is plotted in Fig.

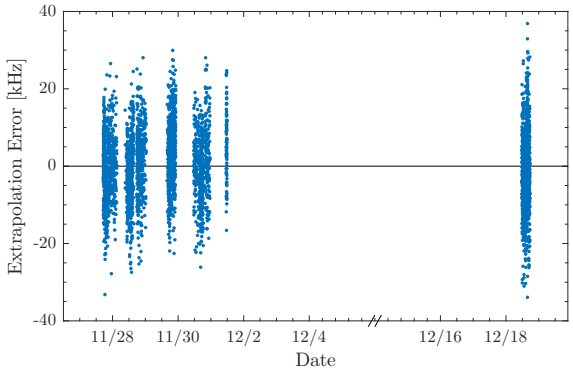

Figure 6.2: The residual frequency difference between the frequency as measured by the comb and the extrapolated value using the calibration curve in Fig. 6.1. The spread has a 1-sigma standard deviation of 10 kHz.

6.2. The frequency residual has a mean of 0 kHz ±10 kHz, which is good enough for a 0.03 ppb measurement of the laser frequency.

Ideally, the frequency of the laser would be measured directly during the experimental run to provide a more accurate measurement of the frequency for post correction. However, the comb has proven to be somewhat unreliable and thus this calibration method can serve to bridge the gaps when the comb fails.

6.1.2 Beam Alignment

The magnitude and direction of the momentum kick during the beam splitter are dependent on the relative direction of the two wave-vectors $\vec{k}_1$ and $\vec{k}_2$ (which are ideally perfectly counter-propagating). When taking into account the direction of these wave-vectors, the recoil frequency can be written as

$$\begin{aligned}\omega_r &= \frac{\hbar}{8m}k_{\text{eff}}^2 \\ &= \frac{\hbar}{8m}(\vec{k}_1 + \vec{k}_2)\cdot(\vec{k}_1 + \vec{k}_2) \\ &= \frac{\hbar}{8m}(k_1^2 + k_2^2 + 2|k_1||k_2|\cos\theta),\end{aligned}$$

where θ is the angle between the two wave-vectors. Since the frequency difference between the lasers is small compared to the absolute laser frequency, we can approximate $k_1 \approx k_2 \equiv k$ so that

$$\begin{aligned}k_{\text{eff}}^2 &\approx 2k^2(1+\cos\theta) \\ &\approx 4k^2 - k^2\theta^2 + \mathcal{O}(\theta^4)\end{aligned}$$

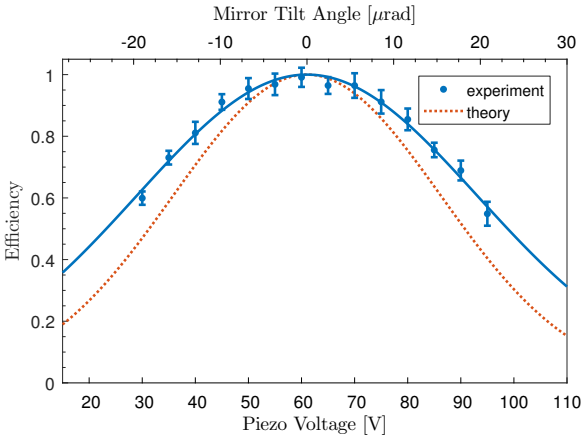

Figure 6.3: The measured back-coupling efficiency of the retro-reflect mirror (blue) as a function of the mirror tilt piezo voltage. The measured data is also plotted against the theoretical mirror angle assuming the piezo actuates on a lever arm of 185 mm and has a displacement of 0.166 μm/V. The coupling efficiency data is normalized to be equal to one at the maximum. The theoretical coupling efficiency (red) is plotted as a function of the theoretical mirror angle for comparison.

for a small relative θ. The error in k_{eff}^2 from the ideal value of $k_{\text{eff}} = (\omega_1 + \omega_2)/c$ based on the measured laser frequencies is then

$$\begin{aligned} \delta k_{\text{eff}}^2 &= -k^2\theta^2 \\ \implies \frac{\delta k_{\text{eff}}^2}{k_{\text{eff}}^2} &\approx -\frac{\theta^2}{4} \end{aligned}$$

and therefore the error in $\hbar/m$ due to the relative angle between the beam splitter lasers is

$$\frac{\delta(\hbar/m)}{\hbar/m} = -\frac{\theta^2}{4}. \tag{6.1}$$

The experiment is set up such that the two wave-vectors k_1 and k_2 originate from same fiber with opposite polarization. To create the counter-propagating lattice, the lasers are retro-reflected off a mirror at the top of the chamber. The relative angle θ between the two wave-vectors is then twice the angle the mirror makes with the up-going wave-vector, $2\theta_{\text{m}} = \theta$. To determine the angle the mirror makes with the laser, the light is back-coupled into the launching fiber and monitored on PD8 in Fig. 4.3. When the fiber coupling is maximized, the retro-reflected light must be perfectly counter-propagating and therefore the angle is zero. As the mirror is tilted away from zero degrees, the coupling efficiency will decrease. By measuring the coupling efficiency during the experimental run, the relative angle can be determined which allows for post correction of the data to reduce the beam alignment systematic.

The retro-reflect mirror angle is adjustable by two large micrometers and two piezoelectric actuators to control the x and y tilt. To calibrate the mirror tilt against the coupling efficiency, the retro-reflect coupling was measured as a function of the applied piezo voltage and fitted to a Gaussian function as shown in Fig. 6.3. The angle of the mirror was estimated based on the lever arm of the piezo to the rotation axis (185 mm) and the theoretical piezo displacement of 17 ± 2 μm/150 volts. To compare this measurement with the theoretical back-coupling efficiency, assume that the launched laser is a plane wave with a Gaussian electric field amplitude of

$$E_1 = |E| e^{-(x^2+y^2)/w_0^2}$$

and the retro-reflected laser is approximated by the wave tilted by an angle $2\theta_{\mathrm{m}}$ about the y-axis such that

$$E_2 \approx |E| e^{-(x^2+y^2)/w_0^2} e^{-i2kx\theta_{\mathrm{m}}},$$

where $\phi = 2kx\theta_{\mathrm{m}}$ is a spatially dependent phase term along x-axis resulting from the tilted plane wave. The coupling efficiency η is then defined as the overlap integral of the two electric fields

$$\begin{aligned}\eta &= \frac{1}{E^2}\left|\iint E_1 E_2^* \, dx\, dy\right|^2 \\ &= \exp\left[\frac{-4\pi^2 w_0^2 \theta_{\mathrm{m}}^2}{\lambda^2}\right].\end{aligned}$$

The theoretical coupling efficiency is also plotted in Fig. 6.3 using the estimated angle of the mirror from the piezo voltage. The two agree reasonably well with $\lambda = 852$ nm and $w_0 = 6.2$ mm, although it seems that the mirror angle might be somewhat overestimated.[1] The two would match if the mirror angle was 25% smaller than the estimate based on the piezo displacement. The larger of the two estimates is used as an upper bound and the angle as a function of coupling efficiency can be fitted from the data to be

$$|\theta_m| = \sqrt{\ln \eta} \cdot 25.2 \ \mu\mathrm{rad}.$$

Some sample retro-reflect data is plotted in Fig. 6.4 showing the measured retro-reflect efficiency as a function of time. Also plotted is the corresponding error in $\hbar/m$ from (6.1) using the inferred angle based on the coupling data. The error has a mean of 0.22 ppb and can have a maximum deviation of 0.6 ppb; therefore, post correction on the data is required. The post correction is limited by the standard deviation of the back-coupling efficiency over the timescale required to take a single measurement (two ellipses), which gives an error of 0.03 ppb.

Coriolis Compensation: The Coriolis compensation from Section 4.4.3 requires that the mirror be rotated to compensate for Earth's rotation. For an interferometer with a pulse

[1] An actual tilt measurement with a calibrated tilt sensor might be required.

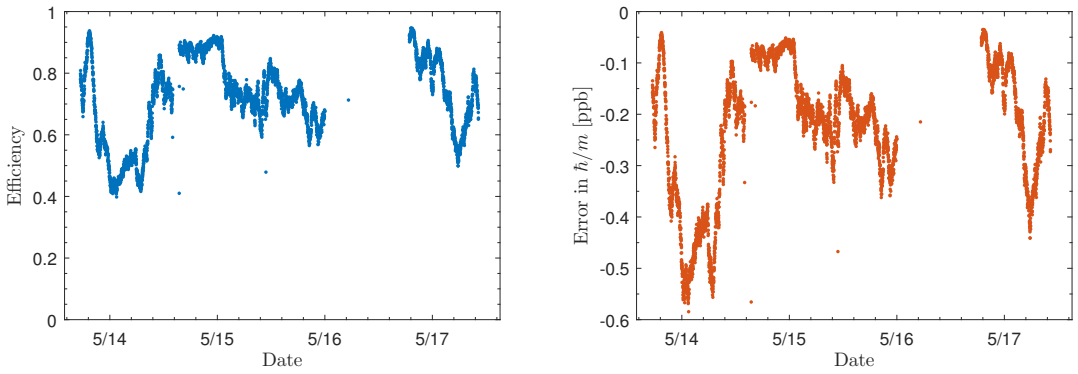

Figure 6.4: Left: A plot of the retro-reflect coupling as a function of time, normalized to the maximum signal size. Each point is the average coupling over a period of one minute. Right: The corresponding errors in $\hbar/m$ due to the inferred mirror angle based on the data in Fig. 6.3.

separation time of $T = 160$ ms and $T' = 10$ ms, the mirror will rotate by only 3.8 μrad. This corresponds to an error of 0.01 ppb in $\hbar/m$ and can be ignored.

6.1.3 Gouy Phase

The last corrections to consider come from the Gaussian beam nature of the beam splitters. If we take the surface of the retro-reflect mirror to be at $z = 0$, then the electric field describing the beam splitter laser traveling in the $+\hat{z}$ direction can be written as

$$E_1(z,r) = |E(z,r)|\, e^{i\left[k(z-z_0)-\omega t+\frac{kr^2}{2R(z-z_0)}-\zeta(z-z_0)\right]},$$

where w_0 is the Gaussian waist, z_0 is the location of the waist, and $k = k_1 \approx k_2$ is the laser's wave-vector. The last two terms in the exponential are a curvature phase term $kr^2/2R(z-z_0)$ and a Gouy phase term $\zeta(z-z_0)$, where $R(z) = z(1+z_R^2/z^2)$ and $\zeta(z) = \tan^{-1}(z/z_R)$. The Rayleigh range $z_R = \pi w_0^2/\lambda$ is the distance over which the Gaussian beam is approximately collimated.

After the laser beam reflects off the retro-reflect mirror, the downward traveling electric field can be written as

$$E_2(z,r) = |E(z,r)|\, e^{i\left[-k(z+z_0)-\omega t-\frac{kr^2}{2R(z+z_0)}+\zeta(z+z_0)\right]},$$

where the signs of some terms have changed to indicate the change in beam direction. The incoming and reflected beams are diagrammed in Fig. 6.5, as are the effective locations of the waists.

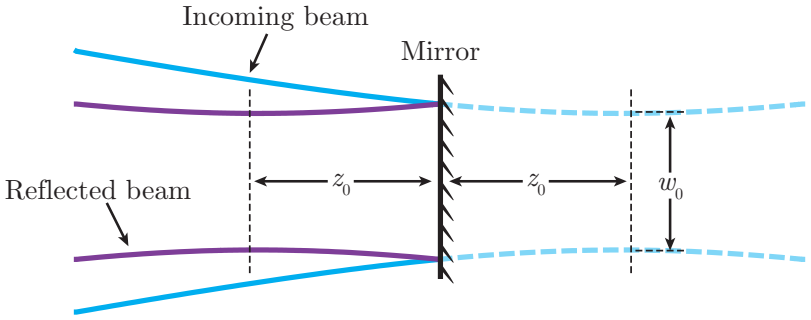

Figure 6.5: A diagram of the Gaussian beam reflecting off the mirror in the chamber. The incoming beam (blue) has a virtual waist at $z = z_0$ and the reflecting beam (purple) has a real waist at $z = -z_0$.

The wave-vector that interacts with the atoms can be thought of as the gradient of the laser phase with respect to z and, therefore, the total effective wave-vector k_{eff} is

$$\begin{aligned} k_{\text{eff}} =& \frac{\partial}{\partial z}\left[k\left(z-z_0\right)-\omega t+\frac{k\rho^2}{2R\left(z-z_0\right)}-\zeta\left(z-z_0\right)\right] \\ &-\frac{\partial}{\partial z}\left[-k\left(z+z_0\right)-\omega t-\frac{k\rho^2}{2R\left(z+z_0\right)}+\zeta\left(z+z_0\right)\right]. \end{aligned}$$

Since we care about the behavior of the effective wave-vector near the mirror, k_{eff} is expanded with $z/z_R << 1$ and to first order in z_0/z_R, which yields

$$k_{\text{eff}} \approx 2k - \frac{2}{z_R} + 2\frac{z_0^2}{z_R^3} + \frac{kr^2}{z_R^2} + \mathcal{O}(z_0^2/z_R^2).$$

In the plane wave limit where w_0 and z_R are large, the effective wave-vector reduces to $k_{\text{eff}} = 2k$ as expected. The first two corrections are from the Gouy phase which modify the wave-vector in the vicinity of the waist and the last correction is the wavefront curvature and is only relevant when the atoms interact with the laser away from the beam center. The fractional change in k_{eff} can be expressed as

$$\frac{\delta k_{\text{eff}}}{k_{\text{eff}}} = -\frac{\lambda^2}{2\pi^2 w_0^2}\left(1 - \frac{z_0^2}{z_R^2} - \frac{r^2}{w_0^2}\right). \tag{6.2}$$

Ignoring the r^2 dependence for now, we can see that the correction depends on the waist w_0 of the laser and the position of the waist z_0 relative to the mirror at $z = 0$. (Ideally the waist would be very close to the mirror, $z_0/z_R \ll 1$, but this may not always be the case if the beam is slightly defocused due to collimation errors.)

To characterize the Bragg laser beam, knife edge measurements were taken along the x and y axes of the beam before it goes into the chamber and as it exits the chamber after the retro-reflect. The results of the measurements are shown in Fig. 6.6, with each set of data fitted to an error function to obtain the waist. The x and y waist measurements differ

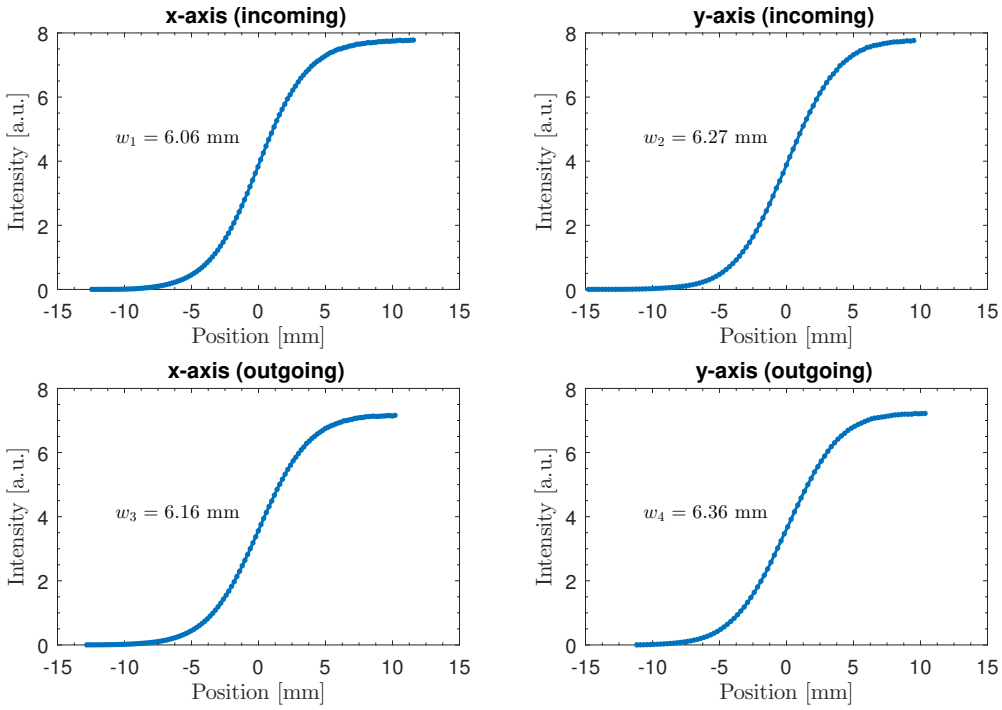

Figure 6.6: Knife edge measurements of the Bragg beam along each axis as it goes into the vacuum chamber (incoming) and as it exits the vacuum chamber after being retro-reflected (outgoing). Each measurement is fit to an error function (integrated Gaussian) to determine the waist at the location of measurement. Both the incoming and outgoing measurement were done approximately 2.5 meters from the retro-reflect mirror.

by about 1.5% and the waist expands by approximately 1.5% between the two measurement positions. (The distance from the first measurement position to the retro-reflect mirror and back is about $2z_m = 5$ meters.) The waist of a Gaussian beam changes with distance according to

$$w(z) = w_0\sqrt{1 + \frac{z^2}{z_R^2}}.$$

Therefore, the waist parameter w_0 and the waist position z_0 can be determined by solving the set of equations:

$$w(-z_m - z_0) = (w_1 + w_2)/2, \qquad w(z_m - z_0) = (w_3 + w_4)/2,$$

for w_0 and z_0, which gives $w_0 = 5.70(7)$ mm and $z_0 = -52(5)$ meters. These values result in a correction to the effective wave-vector (6.2) equal to $\delta k_{\text{eff}}/k_{\text{eff}} = -0.90(3)$ ppb and thus a correction to $\hbar/m$ of $-1.80(6)$ ppb.

Table 6.1: Monte Carlo simulations of the wavefront curvature phase for $n = 5$, $N = 25$, $T = 80$ ms, and $\sigma = 0.216\omega_r^{-1}$. The detection radius r_{det} and displacement of Gaussian beam from the atoms Δx is varied to get a sense for the upper bound of the phase. At each set of parameters r_{det} and Δx, the intensity is optimized (in units of $\Omega_{\pi/2}$) for maximum contrast.

$r_{\text{det}}[mm]$	Δx [mm]	Intensity [$\Omega_{\pi/2}$]	Contrast	Phase [mrad]
2	0	1.05	96%	0.15
2	2	1.10	90%	0.25
2	4	1.25	78%	0.60
4	0	1.05	90%	0.20
4	2	1.10	83%	0.29
4	4	1.30	74%	0.66

6.1.4 Wavefront Curvature

The last term in Eq. (6.2) depends on the radial location of the atoms relative to the beam center. To estimate the size of this effect, the Monte Carlo simulation from Section 5.4 was used to determine the average wavefront curvature phase of the ensemble. Since the atoms can potentially have a different radial position for each beam splitter, we must first have some way of quantifying the effect of the wavefront curvature term.

If the Ramsey-Bordé interferometer phase is calculated with a small perturbation δk to the effective wavenumber at each beam splitter pulse, then the resulting phase shift is equal to

$$\delta\Phi = \frac{8n\omega_r}{k_{\text{eff}}}\Big(n\left[T(\delta k_2 + \delta k_3 + 2\delta k_4) + (T_1' + T_2')(\delta k_4 - \delta k_3)\right] + 2N\left[T_2'(\delta k_4 - \delta k_3) + T(\delta k_4 + \delta k_B)\right]\Big), \tag{6.3}$$

where δk_B is the wave-vector perturbation during the Bloch oscillations and δk_i is the correction for the ith Bragg beam splitter (and noting that the first beam splitter has no contribution). During the Monte Carlo simulation, the radial position r_i is recorded for all beam splitters and used to calculate the wavefront curvature correction to the effective wave-vector

$$\delta k_i = -\frac{\lambda^2}{2\pi^2 w_0^4} r_i^2.$$

The wave-vector perturbation is then used to calculate the phase shift (6.3) for each atom and the Monte Carlo takes the weighted average of the phase, taking into account the relative interference contrasts. Since the wavefront curvature is quadratic in r, the simulation is performed with different values of the detection radius r_{det} and different Gaussian beam

displacements Δx (from the center of the atoms), with results presented in Table 6.1. Even for very extreme parameters ($r_{\rm det} = 4$ mm, $\Delta x = 4$ mm), the wavefront curvature systematic shifts ω_r by less than 0.25 ppb. For more typical parameters with $r_{\rm det} = 2$ mm and $\Delta x = 0$ mm, the wavefront curvature systematic is less than 0.1 ppb.

6.2 Sagnac Effect

The Ramsey-Bordé interferometer configuration ideally has zero enclosed spatial area if the atom launch direction and the Bragg beams are aligned with gravity such that all motion takes place in the vertical dimension. If there is a misalignment such that the two interferometer paths enclose a spatial area A and the entire interferometer is rotating at a rate Ω relative to the inertial frame of the atoms, then there will be an extra phase shift applied to the atoms equal to

$$\Phi_\Omega = \frac{4\pi m}{\hbar}\vec{A}\cdot\vec{\Omega}$$

due to the Sagnac effect [128]. The magnitude of this phase is proportional to the dot product $\vec{A}\cdot\vec{\Omega}$, where the direction of $\vec{\Omega}$ is the axis of rotation and the direction of $\vec{A}$ is normal to the enclosed area. This effect can be quite large and is often used in gyroscopes to measure rotational effects [5], but presents itself as a possible systematic effect in our experiment. The enclosed areas of the upper and lower interferometers should mostly cancel in the case of a simultaneous conjugate Ramsey-Bordé, but any residual difference needs to be calculated for possible systematic shifts.

The piecewise trajectory in the x-z plane of all four paths (upper/lower path for the upper/lower interferometer) are easily calculated parametrically as a function of time t using the equations of motion and the relevant momentum kicks of the beam splitters. The resulting trajectories $\{x_{ij}(t), z_{ij}(t)\}$ can then be used to calculate the enclosed area of an interferometer by computing

$$A_i = \int x_{iu}(t)\frac{d}{dt}z_{iu}(t)dt - \int x_{i\ell}(t)\frac{d}{dt}z_{i\ell}(t)dt,$$

where A_i is the area of the $i = [u, \ell]$ interferometer and $\{x_{ij}(t), z_{ij}(t)\}$ are the parametric coordinates for the $j = [u, \ell]$ path for each interferometer i. Each integral computes the area under the parametric curve; the difference is the total area of the interferometer. Any difference in area between the upper and lower interferometer, $A_u - A_\ell$, then contributes to a Sagnac phase. For completeness, atom trajectories were calculated with the atoms having an initial velocity v_0 and a launch angle of ϕ relative to vertical. The beam splitter laser is treated as being at an initial angle θ (with respect to gravity) and rotating in the atom's inertial frame at an angular rate ω. The laser rotation rate is zero if there is perfect Coriolis compensation and $\omega = \Omega_e$ (i.e. the rotation rate of the Earth) if there is no compensation.

The full calculation is much too long to show here, but for the simplified case of when $\theta = 0$ and $T_1' = T_2' = 0$, the difference in area between the upper and lower interferometers can be written as

$$A_u - A_\ell = -n(n+N)v_r^2 T^2 \left[\frac{4}{3}(12+\gamma T^2) - (12+5\gamma T^2)\cos\omega T\right]\sin\omega T,$$

which is a result of any residual rotation ω of the Earth that is not canceled with the Coriolis compensation. In general, the initial atom velocity v_0 and the launch angle ϕ do not contribute to the area difference and the angle of the Bragg beam θ only contributes at a level below 0.01 ppb. For typical interferometer parameters of $n = 5$, $N = 25$, $T = 80$ ms, $T_1' = T_2' = 5$ ms, and $\gamma = 2.2 \times 10^{-6}$ s^{-2}, the resulting differential Sagnac phase is below 0.25 ppb in ω_r when $\omega = \Omega_e$. The Earth's rotation is easily canceled to below 10% using the techniques outlined in [119] and, therefore, the systematic should be negligible.

6.3 Zeeman Effect

Even though the atoms are in the $m_F = 0$ state (which is mostly insensitive to magnetic fields), there is still a small energy shift due to the quadratic Zeeman shift. If the arms of the interferometers travel through different magnetic field regions, then there will be a systematic phase shift proportional to energy differences caused by the fields.

For intermediate strength magnetic fields, the Breit-Rabi formula [129, 130] can be used to calculate the energy shift of the $6^2S_{1/2}$ hyperfine levels as

$$\Delta E_{F=I\pm1/2} = -\frac{\Delta E_{\rm hfs}}{2(2I+1)} + g_I\mu_B m_F B \pm \frac{\Delta E_{\rm hfs}}{2}\left(1 + \frac{4m_F x}{2I+1} + x^2\right)^{1/2},$$

where the factor $x = (g_J - g_I)\mu_B B/\Delta E_{\rm hfs}$, μ_B is the Bohr magneton, $g_J = 2.002540$ is the fine-structure Landé g-factor, and $g_I = -0.000398$ is the nuclear g-factor [131]. For the special case of the magnetically insensitive $m_F = 0$ state, the leading order B-field term in the Breit-Rabi formula is

$$\Delta E_{F=I\pm1/2} = \pm\frac{(g_I - g_J)^2\mu_B^2}{4\Delta E_{\rm hfs}}B^2(z), \tag{6.4}$$

where $g_J \approx 2$ for the $6^2S_{1/2}$ state and the nuclear g-factor can be neglected ($g_I \approx 0$).

The magnetic field in the interferometer region can be modeled as having a constant magnetic field B_0 due to the bias-coil, in addition to a magnetic gradient B' and curvature B'' which are caused by external fields and bias-field imperfections [132]:

$$B(z) \approx B_0 + B'z + B''z^2 + \mathcal{O}(z^3).$$

For atoms in the $F = 3$ ground state, the Lagrangian of the system can then be modified by adding a contribution L_B due to the magnetic field energy (6.4),

$$\begin{aligned} L_B(z, \dot{z}) &= \frac{g_J^2 \mu_B^2}{4\Delta E_{\text{hfs}}} B^2(z) \\ &= \hbar\beta \left[B_0^2 + 2B_0 B' z + \left(B'^2 + 2B_0 B'' \right) z^2 \right] + \mathcal{O}(z^3), \end{aligned} \tag{6.5}$$

where $\beta = 2\pi \cdot 213.1$ Hz/G^2 for cesium. The B_0^2 term is common mode to all arms of the interferometer and can be ignored. For the other terms, it is useful to compare (6.5) to the Lagrangian due to gravity (2.24). One can see that terms scaling with z look similar to a linear gravitational potential and terms that scale with z^2 look like gravity gradients. Therefore, the phase shift caused by magnetic fields are identical in form to (2.25) with

$$\begin{aligned} g &\to \frac{2\hbar\beta}{m} B_0 B' \\ \gamma &\to \frac{2\hbar\beta}{m} (B'^2 + 2B_0 B''). \end{aligned}$$

Since acceleration terms cancel in the simultaneous conjugate Ramsey-Bordé interferometer, we can also ignore the $B_0 B'$ magnetic field terms. The terms that act like gravity gradients do not cancel, however, but can be explored in two different ways. First, any measurement of the gravity gradient, such as in Section 5.3, also measures the curvature of the magnetic field. By applying gravity gradient corrections from the gradiometer measurements, we have also already dealt with these magnetic gradients. However, the $B_0 B''$ term can be studied independently by varying the bias field strength B_0 and looking for a shift in the measured recoil frequency.[2]

To test the sensitivity of the experiment to bias field current, one measurement of the recoil frequency was taken at normal operating parameters with a bias current of 27.7 mA (0.38 G) between Nov. 27th and Nov. 30th in 2014. Then a second measurement was performed with 271.4 mA (3.7 G) on Dec. 2nd, 2014, where the field was increased by a factor of ten approximately 5 ms after velocity selection (which was done so that all atom preparation stages use the nominal field strength). Both measurements used alternating pulse separation times of 2 ms and 80 ms, with $n = 5$, $N = 20$. The difference between the two measurements was 1.5(1.4) ppb in ω_r, which corresponds to a possible systematic shift of 0.15(14) ppb for the normal operating conditions with a current of 27.7 mA.[3]

[2]The B'^2 term is insensitive to varying the bias field unless the bias coil itself has a magnetic gradient component.

[3]The exact dates these experiments were performed are explicitly listed above, since the external field which contributes to B'' could possibly change as our lab or neighboring labs modify their experiments. For this reason it is recommended to either monitor the external field for changes or to perform this type of magnetic field sensitivity experiment close to the date of the final measurement.

6.4 Density Shifts

Typically the atom source of an interferometer is treated as non-interacting when calculating the interferometer phase and equations of motion. However, there is a small self-energy associated with the cloud that scales with the density which contributes to the phase along a particular interferometer path. Since the energy is proportional to density, this shift will cancel if the beam splitters diffract the atoms with exactly 50% probability, as each arm will have an equal population. More realistically, the beam splitters efficiency is not perfect, resulting in a population imbalance in the interferometer arms. Additionally, shot-noise will always cause an atom number imbalance proportional to $\sqrt{N}$, where N is the number of atoms.

The atom-atom interaction energy can be estimated based on the Gross-Pitaevskii equation [110], with a self-interaction Hamiltonian equal to

$$H_\rho = 4\pi\hbar^2 a_s/m|\Psi(\vec{r})|^2,$$

where a_s is the s-wave scattering cross section, m is the mass of the atom, and $|\Psi(\vec{r})|^2 \approx \rho$ is the number density of the atom ensemble. While the Gross-Pitaevskii equation only applies to ensembles at very low temperatures where collisions can be treated as pure s-wave scattering, corrections due to d-wave scattering at higher temperatures can be neglected for our purposes. For example, at 7 μK it was found that including d-wave collisions changes the theoretical energy shift by only 5% [133].

The energy shift in our atom cloud due to the density shifts can then be approximated as $E_\rho = \rho 4\pi\hbar^2 a_s/m$, where $a_s = 280(10)a_0$ for cesium [134] and a_0 is the Bohr radius. The density of the atom cloud can be estimated based on the detection efficiency from Section 3.5, which approximates the signal as 5500 atoms/volt with a detection volume of less than (6 mm)$^2\times$ 600 μm. For typical interferometer signals of 1 volt, this corresponds to an atom number density during detection of approximately 2.5×10^5 atoms/cm^3. Since the clouds expand for roughly 500 ms before being detected, the density during the interferometer sequence is closer to $\rho = 10^6$ atoms/cm^3. If we assume a huge beam splitter imbalance such that the two atom clouds have a splitting ratio of 3:1, then the differential density shift will cause a net interferometer phase of

$$\begin{aligned}\delta\Phi_\rho &= \frac{\Delta E_\rho}{\hbar}(2T + T') \\ &= \left(\frac{3\rho}{4} - \frac{\rho}{4}\right)\frac{4\pi\hbar a_s}{m}(2T + T').\end{aligned}$$

For typical parameters of $T = 80$ ms and $T' = 10$ ms, this gives a phase of 8 μrad corresponding to a negligible 0.003 ppb shift in ω_r. This phase is more of a concern for interferometers that use Bose-Einstein condensates as a source, where the density shifts can be significant [112].

6.5 Differential ac-Stark Shifts

During Bloch oscillations, the atoms are shifted in energy by an amount

$$\delta E_{ac} = \frac{\hbar\Omega^2}{4\Delta}$$

due to the ac-Stark effect, where Ω is the Rabi frequency and Δ is the single photon detuning. This energy shift applies for each component of the Bloch lattice beam for a total of 6 possible beams (where the frequencies $\{\omega_1, \omega_\pm\}$ travel up and the same 3 frequencies after retro-reflect travel down). Since the Bloch lattice is blue-detuned, the atoms sit at a potential minimum and do not experience an ac-Stark shift from the accelerating lattice to first order. Instead, they only see a time averaged energy shift from the other 4 off-resonant beams. To calculate the energy shifts on the arms of the interferometer, first we need to know the intensity at the location of the atoms.

The intensity of the laser beam as a function of height for the up-going beams is given by

$$I_\uparrow(z) = I_0 \frac{w_0}{w(z - z_0)},$$

where $w(z) = w_0\sqrt{1 + z^2/z_R^2}$. The parameters w_0 and z_0 are the waist and waist position, respectively, found in Section 6.1.3 with $z = 0$ being defined at the mirror surface. Similarly, the intensity of the downward moving laser is given by

$$I_\downarrow(z) = I_0 \frac{w_0}{w(z + z_0)}.$$

For the atoms being accelerated upwards, the frequencies that contribute to the Bloch lattice consist of ω_1 traveling upwards and ω_- traveling downwards. Therefore, the frequency components that contribute to the ac-Stark shift are $\omega_\pm$ traveling upwards and ω_1, ω_+ traveling downwards. The differential ac-Stark shift for the atoms accelerated upwards is then

$$\delta E_u(z) = \frac{\hbar}{4\Delta}\left[(\Omega_+^2 + \Omega_-^2)\frac{w_0}{w(z - z_0)} + (\Omega_1^2 + \Omega_+^2)\frac{w_0}{w(z + z_0)}\right].$$

Similarly, for the atoms accelerated downward:

$$\delta E_\ell(z) = \frac{\hbar}{4\Delta}\left[(\Omega_+^2 + \Omega_-^2)\frac{w_0}{w(z - z_0)} + (\Omega_1^2 + \Omega_-^2)\frac{w_0}{w(z + z_0)}\right],$$

where the only difference is that the Rabi frequency of the ω_+ frequency is replaced with ω_- for the downward accelerated atoms since they get loaded into the ω_+ frequency lattice.

Since the atoms are separated by a distance $\Delta z = 2nv_rT$ during the Bloch pulse, the differential ac-Stark shift between the arms of each interferometers is

$$\Delta E_u = \delta E_u(z + 2nv_rT) - \delta E_u(z),$$

$$\Delta E_\ell = \delta E_\ell(z + 2nv_rT) - \delta E_\ell(z)$$

and thus the total differential ac-Stark shift for the full conjugate interferometer is

$$\Delta E_u - \Delta E_\ell \approx \frac{\hbar}{\Delta} \frac{z_R \left(\sqrt{z_R^2 + z_0^2} - \sqrt{z_R^2 + (2nv_rT + z_0)^2} \right)}{\sqrt{z_R^2 + z_0^2}\sqrt{z_R^2 + (2nv_rT + z_0)^2}} (\Omega_-^2 - \Omega_+^2)$$

for $z/z_R \ll 1$ (near the mirror surface). The systematic phase shift in the interferometer due to the differential ac-Stark shift is then

$$\delta\Phi_{ac} = \frac{1}{\hbar}(\Delta E_u - \Delta E_\ell) t_{\text{bloch}},$$

where t_{bloch} is the length of the Bloch pulse. If the intensities of the two modulated frequency sidebands $\Omega_\pm$ are equal, then all phase shifts cancel and there is no systematic. However, let us assume that the power balance is off by 10% and that each lattice beam has a Rabi frequency of around $\Omega^2/4\Delta \approx 3\omega_r$ (from Section 4.5) such that $(\Omega_-^2 - \Omega_+^2)/\Delta \approx \omega_r$. Then for the interferometer parameters of $n = 5$, $T = 80$ ms, $t_{\text{bloch}} = 1$ ms, and beam parameters $\{z_0 = -52 \text{ m}, w_0 = 5.8 \text{ mm}\}$, the phase shift comes out to

$$\begin{aligned} \delta\Phi_{ac} &= \left(-7.5 \times 10^{-6}\right) \frac{(\Omega_-^2 - \Omega_+^2)}{\Delta} t_{\text{bloch}} \\ &\approx \left(-7.5 \times 10^{-6}\right) \omega_r t_{\text{bloch}} \\ &\approx 100 \ \mu\text{rad} \end{aligned}$$

or less than 0.04 ppb in ω_r. Since the two frequencies $\omega_\pm$ are generated from the same AOM, the power balance is probably much better than 10% and the systematic is negligible.

6.6 Index of Refection

The laser phase derived in Section 2.2 is proportional to the phase accumulated while traveling in the vacuum chamber and thus is sensitive to the refraction index of the medium in which the laser propagates. Since the inside of the chamber is an ultra-high vacuum environment, the only significant contribution to the index of refraction comes from the dispersion due to the background cesium atoms.

The refractive index in an atomic vapor is related to the complex absorption coefficient α by the relation

$$\begin{aligned} n - 1 &= \frac{\text{Im}(\alpha)}{k} \\ &= \frac{\sigma_0 \rho}{k} \left(\frac{2}{\Gamma}\right) \frac{\Delta}{1 + s + 4\Delta^2/\Gamma^2}, \end{aligned}$$

where σ_0 is the resonant scattering cross section, ρ is the atom number density, Γ is the natural linewidth, Δ is the single photon detuning, and s is the saturation parameter I/I_{sat} [135]. In the limit of a far detuned laser, $\Delta/\Gamma \gg 1$, the index of refraction simplifies to

$$n - 1 = \frac{\rho\sigma_0}{4k}\frac{\Gamma}{\Delta}.$$

As an upper bound, we can assume that the cesium partial pressure is equal to the vacuum pressure of 10^{-9} torr and thus has a background density of 10^7 atoms/cm^3 at 300 K. For a laser detuning of $\Delta = 15$ GHz and a resonant cross section for the cesium D_2 line of $\sigma_0 \approx 2.5 \times 10^{-9}$ cm^2, the index of refraction shift is at most $n - 1 = \delta k/k = 0.03$ ppb. The background cesium density is realistically much lower since the background fluorescence is smaller than the atom cloud signal (which was estimated to have a density of 2.5×10^5 atoms/cm^3 in Section 6.4). Therefore the index of refraction shift in the wave-vector is negligible and can be ignored.

6.7 Modulation Frequency Wavenumber

During the third and fourth beam splitters of a simultaneous conjugate Ramsey-Bordé interferometer, the effective wave-vector for the upper and lower interferometers differ by $\pm\omega_m/c$ due to the extra modulation frequency added to the laser to drive both Bragg orders. This perturbation in the wave-vector causes a systematic phase shift $\delta\Phi_{\omega_m}$ of

$$\delta\Phi_{\omega_m} = \frac{\omega_m}{c}\left(-ngT(3T + 2T') + 2n^2 v_r T\right),$$

where g is the gravitational acceleration and v_r is the recoil velocity. The fractional shift in ω_r is

$$\begin{aligned}\frac{\delta\omega_r}{\omega_r} &= \frac{\omega_m}{16(n+N)\omega_r c}\left(-g(3T + 2T') + 2nv_r\right) \\ &\approx \frac{1}{2c}\left(-g(3T + 2T') + 2nv_r\right)\end{aligned}$$

for $\omega_m \approx 8(n + N)\omega_r$. The term proportional to v_r is negligible and contributes less than 0.0006 ppb, but the gravity term is quite large. For typical parameters of $T = 80$ ms and $T' = 10$ ms, the correction is -4.25 ppb. Since the value of $g = \vec{g} \cdot \vec{k}/|k|$ is the projection of gravity onto the wave-vector, the Bragg beam should be within 70 mrad of vertical for less than a 0.01 ppb uncertainty in the correction.

6.8 Carrier-Envelope Phase

The system of equations used to calculate the transition matrix elements $\langle b|\, \hat{H}_{n,N}\, |a\rangle$ for the multi-frequency optical Bloch equation in Section 2.5.2 was derived as

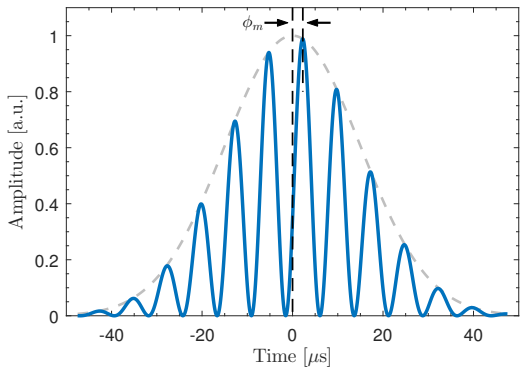

Figure 6.7: The intensity profile of a multi-frequency Gaussian pulse as a function of time. The dashed curve shows the intensity stabilized Gaussian envelope and ϕ_m is the carrier envelope phase offset.

$$i\dot{g}_n = 4\cos(\omega_m t)\bar{\Omega}(t)\left[g_{n+1}e^{i2\delta t}e^{-i4(2n+1)\omega_r t} + g_{n-1}e^{-i2\delta t}e^{i4(2n-1)\omega_r t}\right],$$

where ω_m is the modulation frequency. However, this makes the assumption that the modulation frequency phase is always zero relative to the peak of the Gaussian intensity envelope, $\bar{\Omega}(t)$. In general, this carrier envelope phase ϕ_m is non-zero and therefore the system of equations (2.46) should be generalized to

$$i\dot{g}_n = 4\cos(\omega_m t + \phi_m)\bar{\Omega}\left[g_{n+1}e^{i2\delta t}e^{-i4(2n+1)\omega_r t} + g_{n-1}e^{-i2\delta t}e^{i4(2n-1)\omega_r t}\right],$$

where the envelope function $\cos(\omega_m t)\bar{\Omega}(t)$ has been replaced with $\cos(\omega_m t + \phi_m)\bar{\Omega}(t)$ as diagrammed in Fig. 6.7. The carrier envelope phase slightly modifies the effective Rabi frequency seen by the atoms and can therefore change the diffraction phase. When running the Ramsey-Bordé interferometer sequence with a pulse separation time of T, the relative carrier envelope phase between the third and fourth pulse is

$$\Delta\phi_m = \left(\omega_m \pm \frac{\pi}{4nT}\right)T \mod 2\pi,$$

where the $\pm\pi/4nT$ comes from the modulation phase used to shift the ellipses away from zero phase.

The theoretical diffraction phase of the Ramsey-Bordé interferometer is shown in Fig. 6.8 as a function of the carrier envelope phase of the third pulse.[4] With $n = 5$ Bragg diffraction and no Bloch oscillations, the diffraction phase can vary by several milliradians, dependent on the relative carrier envelope phase $\Delta\phi_m$. When Bloch oscillations are used, the total diffraction phase variation decreases to a few hundred μrad. As the modulation frequency

[4]In order to extract the diffraction phase from the calculation, one must first subtract out the phase $\phi_L = 2n\omega_m T = 2n\Delta\phi_m$ caused by the modulation frequency imprinting the laser phase on the atoms directly (as discussed in Section 2.2).

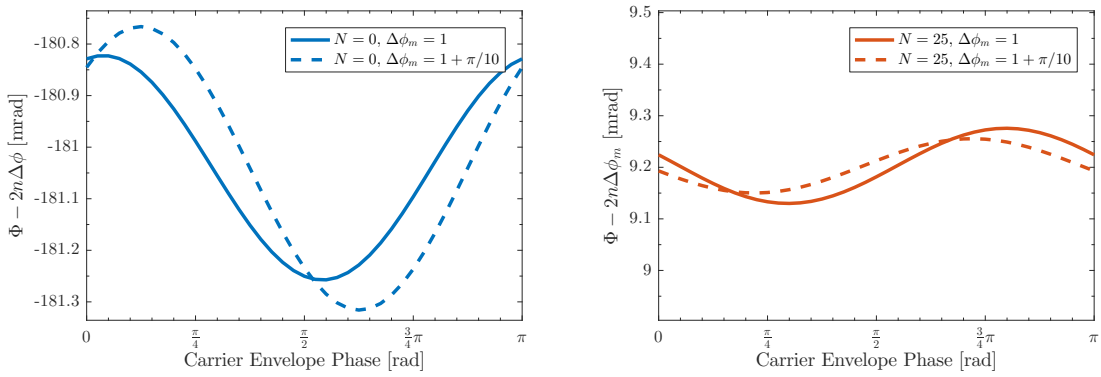

Figure 6.8: The simulated diffraction phase as a function of the third pulse carrier envelope phase for $n = 5$, $N = 0$ (left) and $N = 25$ (right). The diffraction phase is obtained by subtracting the induced laser phase $2n\Delta\phi_m$ from the simulated interferometer phase Φ. The relative carrier envelope phase $\Delta\phi_m$ is plotted for two different values to show the variation when modulating ω_m by $\pm\pi/4nT$, which corresponds to a phase of $\pm\pi/20$ for $n = 5$. The relative carrier envelope phase of $\Delta\phi_m = 1$ is arbitrary for this simulation and will change with the pulse separation time T.

increases, the oscillations inside of the Gaussian envelope are more uniform and the variation of the effective Rabi frequency gets smaller (thus reducing the diffraction phase variation).

This carrier envelope induced diffraction phase can be taken care of in one of two ways. Firstly, if the third pulse phase is left to vary randomly from shot to shot, then the diffraction phase will average out and produce no net systematic shift (and is the method used in the experiment). This has the downside of introducing phase noise on the ellipses, but this effect is small compared to the phase noise in our ellipses from other sources. Secondly, for future generations of the experiment, it might be beneficial to stabilize the carrier envelope phase, alternating between $\phi_m = 0$ and $\phi_m = \pi/2$ as two separate ellipses. In this way the average diffraction phase is obtained without increasing the phase noise.

6.9 Finite Pulse Length

When deriving the interferometer phase, it was assumed that the beam splitter pulses have zero length such that the pulse separation time T is well-defined. In the actual experiment, the beam splitter pulses take about 95 μs from start to finish with a Gaussian envelope that has no well defined start and stop. Therefore it is possible that the relevant timescale for the free evolution phase of the atom is slightly shorter than T by an amount τ such that the interferometer phase is actually

$$\Phi = 16n(n+N)\omega_r(T-\tau) - 2n\omega_m T + \phi_0,$$

where ϕ_0 is the usual diffraction phase. Since τ is independent of the pulse separation time, that phase can be rewritten as

$$\Phi = 16n(n+N)\omega_r T - 2n\omega_m T + (\phi_0 + 16n(n+N)\omega_r \tau).$$

Therefore, any finite pulse length effects will look just like a diffraction phase and are taken care of by extrapolating T to infinity.

Chapter 7

Future Prospects

While a determination for the value of $\hbar/m_{\mathrm{Cs}}$ for cesium was not finalized over the course of this thesis, great improvements have been made in both the interferometer sensitivity and understanding sources of systematic error. Increasing the Ramsey-Bordé momentum transfer to $n = 5$ Bragg diffraction with $N = 25$ Bloch oscillations has increased the total phase of the interferometer to nearly 2.5 million radians at a pulse separation time of $T = 80$ ms. The largest (known) systematic corrections are characterized with an uncertainty below 0.1 ppb and great improvements have been made in our understanding of the Bragg induced diffraction phase. A table of the current experimental systematics is shown in Fig. 7.1, which are by far dominated by the unknown anomaly discussed in Section 5.6. The future of our recoil measurement will hinge on understanding this additional systematic and suppressing its contribution to the error budget.

There are several promising ways to move forward in the experiment beyond what is presented in this thesis. Improving the ac-Stark shift compensation described in Section 5.5 will enable even higher-order Bloch oscillations to increase the total interferometer phase and reduce the fractional contribution of the anomalous diffraction phase. Increasing the Bloch oscillations to $N = 100$ could potentially suppress the anomaly systematic to a relative uncertainty of 0.5 ppb in $\hbar/m_{\mathrm{Cs}}$, thus enabling a competitive measurement of α. There is also some preliminary evidence suggesting that better alignment of the atomic fountain and Bragg beam reduces the size of the anomalous phase; therefore, with better characterization of the system, the systematic might be eliminated entirely.

Beyond improvements to the current system, there are other possible avenues to pursue for future measurements by increasing the total momentum splitting (and not just the common mode momentum) and cleaning up the Bragg beams. After compensating for the ac-Stark shift dephasing, the momentum splitting is mostly limited by the intensity requirements of Bragg diffraction. Splittings larger than $n = 6$ for our beam waist will require a new high-power laser system and/or a different splitting method such as differential Bloch oscillations [125] to accelerate both interferometer arms in different directions. The power requirements and ac-Stark compensation can also be improved by using a cavity to resonantly enhance the beam splitter electric field [136]. The cavity increases the power while

Table 7.1: Systematic corrections and errors in the determination of $\hbar/m_{\mathrm{Cs}}$ for $n = 5$ Bragg diffraction, $N = 25$ Bloch oscillations, and $T = 80$ ms.

Systematic	Correction (ppb)	Uncertainty (ppb)
Gravity Gradient	-2.78	0.04
Laser Frequency		0.04
Gouy Phase	1.80	0.06
Beam Alignment	0.22†	0.03
Modulation Wave-vector	4.25	0.01
Wavefront Curvature		0.1
Sagnac Effect		< 0.02
Zeeman Effect	-0.15	0.14
Density Shift		< 0.003
Differential ac-Stark Shift		< 0.04
Index of Refraction		< 0.03
Linear Diffraction Phase		< 0.1
Statistical		0.6
Total		0.64
Diffraction Phase Anomaly††		< 2.5

† The beam alignment correction is an average for the data listed in Section 6.1.2 and varies for each data set.

†† The diffraction phase anomaly from Section 5.6 is a most 6 mrad and would, by far, dominate the error budget, if included.

also cleaning up the laser mode to reduce differential ac-Stark effects and scatter.

However, the most significant improvement that can be made to the experiment that would enable a competitive fine structure constant measurement is reducing the interferometer noise. If the system was shot-noise limited, then a single interferometer ellipse would be enough to measure $\hbar/m$ to the desired accuracy, thus allowing for much more rapid systematic checks. As it stands now, a 24 hour data set is needed to measure the diffraction phase anomaly which limits our ability to check for potential solutions. Unfortunately, the cause of the noise is somewhat of a mystery as the cause does not seem to be tied to the detection or to the atom number.

Bibliography

[1] A. A. Michelson and E. W. Morley, "On the Relative Motion of the Earth and the Luminiferous Ether," *American Journal of Science*, vol. 34, pp. 333–345, 1887.

[2] R. Santagata, A. Beghi, J. Belfi, N. Beverini, D. Cuccato, A. D. Virgilio, A. Ortolan, A. Porzio, and S. Solimeno, "Optimization of the geometrical stability in square ring laser gyroscopes," *Classical and Quantum Gravity*, vol. 32, no. 5, p. 055013, 2015.

[3] T. R. Schibli, I. Hartl, D. C. Yost, M. J. Martin, A. Marcinkevičius, M. E. Fermann, and J. Ye, "Optical frequency comb with submillihertz linewidth and more than 10W average power," *Nature Photonics*, vol. 2, pp. 355–359, May 2008.

[4] R. Geiger, V. Ménoret, G. Stern, N. Zahzam, P. Cheinet, B. Battelier, A. Villing, F. Moron, M. Lours, Y. Bidel, A. Bresson, A. Landragin, and P. Bouyer, "Detecting inertial effects with airborne matter-wave interferometry," *Nature Communications*, vol. 2, p. 474, Sep 2011. Article.

[5] T. L. Gustavson, P. Bouyer, and M. A. Kasevich, "Precision rotation measurements with an atom interferometer gyroscope," *Phys. Rev. Lett.*, vol. 78, pp. 2046–2049, Mar 1997.

[6] T. Müller, M. Gilowski, M. Zaiser, P. Berg, C. Schubert, T. Wendrich, W. Ertmer, and E. M. Rasel, "A compact dual atom interferometer gyroscope based on laser-cooled rubidium," *The European Physical Journal D*, vol. 53, no. 3, pp. 273–281, 2009.

[7] A. Peters, K. Y. Chung, and S. Chu, "High-precision gravity measurements using atom interferometry," *Metrologia*, vol. 38, no. 1, p. 25, 2001.

[8] M. J. Snadden, J. M. McGuirk, P. Bouyer, K. G. Haritos, and M. A. Kasevich, "Measurement of the earth's gravity gradient with an atom interferometer-based gravity gradiometer," *Phys. Rev. Lett.*, vol. 81, pp. 971–974, Aug 1998.

[9] G. Rosi, F. Sorrentino, L. Cacciapuoti, M. Prevedelli, and G. M. Tino, "Precision measurement of the newtonian gravitational constant using cold atoms," *Nature*, vol. 510, pp. 518–521, Jun 2014. Letter.

[10] H. Muller, A. Peters, and S. Chu, "A precision measurement of the gravitational redshift by the interference of matter waves," *Nature*, vol. 463, pp. 926–929, Feb 2010.

[11] P. Hamilton, M. Jaffe, P. Haslinger, Q. Simmons, H. Müller, and J. Khoury, "Atom-interferometry constraints on dark energy," *Science*, vol. 349, no. 6250, pp. 849–851, 2015.

[12] S.-Y. Lan, P.-C. Kuan, B. Estey, D. English, J. M. Brown, M. A. Hohensee, and H. Müller, "A clock directly linking time to a particle's mass," *Science*, vol. 339, no. 6119, pp. 554–557, 2013.

[13] A. Arvanitaki, S. Dimopoulos, A. A. Geraci, J. Hogan, and M. Kasevich, "How to test atom and neutron neutrality with atom interferometry," *Phys. Rev. Lett.*, vol. 100, p. 120407, Mar 2008.

[14] M. A. Hohensee, B. Estey, P. Hamilton, A. Zeilinger, and H. Müller, "Force-free gravitational redshift: Proposed gravitational aharonov-bohm experiment," *Phys. Rev. Lett.*, vol. 108, p. 230404, Jun 2012.

[15] R. Bouchendira, P. Cladé, S. Guellati-Khélifa, F. Nez, and F. Biraben, "New determination of the fine structure constant and test of the quantum electrodynamics," *Phys. Rev. Lett.*, vol. 106, p. 080801, Feb 2011.

[16] F. G. Mariam, W. Beer, P. R. Bolton, P. O. Egan, C. J. Gardner, V. W. Hughes, D. C. Lu, P. A. Souder, H. Orth, J. Vetter, U. Moser, and G. z. Putlitz, "Higher precision measurement of the hfs interval of muonium and of the muon magnetic moment," *Phys. Rev. Lett.*, vol. 49, pp. 993–996, Oct 1982.

[17] E. Krüger, W. Nistler, and W. Weirauch, "Determination of the fine-structure constant by a precise measurement of h/m_n : the final result," *Metrologia*, vol. 35, no. 3, p. 203, 1998.

[18] E. R. Williams, G. R. Jones, S. Ye, R. Liu, H. Sasaki, P. T. Olsen, W. D. Phillips, and H. P. Layer, "A low field determination of the proton gyromagnetic ratio in water," *IEEE Transactions on Instrumentation and Measurement*, vol. 38, pp. 233–237, Apr 1989.

[19] A. M. Jeffery, R. E. Elmquist, L. H. Lee, J. Q. Shields, and R. F. Dziuba, "Nist comparison of the quantized hall resistance and the realization of the si ohm through the calculable capacitor," *IEEE Transactions on Instrumentation and Measurement*, vol. 46, pp. 264–268, Apr 1997.

[20] A. Wicht, J. M. Hensley, E. Sarajlic, and S. Chu, "A preliminary measurement of the fine structure constant based on atom interferometry," *Physica Scripta*, vol. 2002, no. T102, p. 82, 2002.

[21] R. S. Van Dyck, P. B. Schwinberg, and H. G. Dehmelt, "New high-precision comparison of electron and positron g factors," *Phys. Rev. Lett.*, vol. 59, pp. 26–29, Jul 1987.

[22] D. Hanneke, S. Fogwell, and G. Gabrielse, "New measurement of the electron magnetic moment and the fine structure constant," *Phys. Rev. Lett.*, vol. 100, p. 120801, Mar 2008.

[23] T. Beier, H. Häffner, N. Hermanspahn, S. G. Karshenboim, H.-J. Kluge, W. Quint, S. Stahl, J. Verdú, and G. Werth, "New determination of the electron's mass," *Phys. Rev. Lett.*, vol. 88, p. 011603, Dec 2001.

[24] S. Sturm, F. Kohler, J. Zatorski, A. Wagner, Z. Harman, G. Werth, W. Quint, C. H. Keitel, and K. Blaum, "High-precision measurement of the atomic mass of the electron," *Nature*, vol. 506, pp. 467–470, Feb 2014. Letter.

[25] S. Rainville, M. P. Bradley, J. V. Porto, J. K. Thompson, and D. E. Pritchard, "Precise measurements of the masses of cs, rb and na–a new route to the fine structure constant," *Hyperfine Interactions*, vol. 132, no. 1-4, pp. 177–187, 2001.

[26] B. J. Mount, M. Redshaw, and E. G. Myers, "Atomic masses of ^{6}Li,^{23} Na,^{39,41} K,^{85,87} Rb, and ^{133}Cs," *Phys. Rev. A*, vol. 82, p. 042513, Oct 2010.

[27] P. J. Mohr, B. N. Taylor, and D. B. Newell, "Codata recommended values of the fundamental physical constants: 2006*," *Rev. Mod. Phys.*, vol. 80, pp. 633–730, Jun 2008.

[28] T. Aoyama, M. Hayakawa, T. Kinoshita, and M. Nio, "Tenth-order qed contribution to the electron $g-2$ and an improved value of the fine structure constant," *Phys. Rev. Lett.*, vol. 109, p. 111807, Sep 2012.

[29] C. Schwob, L. Jozefowski, B. de Beauvoir, L. Hilico, F. Nez, L. Julien, F. Biraben, O. Acef, J.-J. Zondy, and A. Clairon, "Optical frequency measurement of the $2S-12D$ transitions in hydrogen and deuterium: Rydberg constant and lamb shift determinations," *Phys. Rev. Lett.*, vol. 82, pp. 4960–4963, Jun 1999.

[30] M. Davier, A. Hoecker, B. Malaescu, and Z. Zhang, "Reevaluation of the hadronic contributions to the muon g2 and to $\alpha(m_Z^2)$," *The European Physical Journal C*, vol. 71, no. 1, pp. 1–13, 2011.

[31] F. Terranova and G. M. Tino, "Testing the a_μ anomaly in the electron sector through a precise measurement of h/m," *Phys. Rev. A*, vol. 89, p. 052118, May 2014.

[32] M. Kasevich and S. Chu, "Atomic interferometry using stimulated raman transitions," *Phys. Rev. Lett.*, vol. 67, pp. 181–184, Jul 1991.

[33] H. Müller, S.-w. Chiow, Q. Long, S. Herrmann, and S. Chu, "Atom interferometry with up to 24-photon-momentum-transfer beam splitters," *Phys. Rev. Lett.*, vol. 100, p. 180405, May 2008.

[34] A. Zee, *Quantum Field Theory in a Nutshell*. Princeton University Press, 2010.

[35] P. Storey and C. Cohen-Tannoudji, "The feynman path integral approach to atomic interferometry. a tutorial," *Journal de Physique II*, vol. 4, no. 11, pp. 1999–2027, 1994.

[36] J. J. Sakurai, *Modern Quantum Mechanics*. Addison-Wesley, 1994.

[37] S. Dimopoulos, P. W. Graham, J. M. Hogan, and M. A. Kasevich, "General relativistic effects in atom interferometry," *Phys. Rev. D*, vol. 78, p. 042003, Aug 2008.

[38] D. M. S. Johnson, *Long Baseline Atom Interferometry*. PhD thesis, Stanford University, 2011.

[39] S. Haroche and J. M. Raimond, *Exploring the Quantum: Atoms, Cavities, and Photons*. Oxford: Oxford Univ. Press, 2006.

[40] S.-w. Chiow, S. Herrmann, S. Chu, and H. Müller, "Noise-immune conjugate large-area atom interferometers," *Phys. Rev. Lett.*, vol. 103, p. 050402, Jul 2009.

[41] J. M. Hensley, A. Peters, and S. Chu, "Active low frequency vertical vibration isolation," *Review of Scientific Instruments*, vol. 70, no. 6, pp. 2735–2741, 1999.

[42] M. Cadoret, E. de Mirandes, P. Cladé, S. Guellati-Khélifa, C. Schwob, F. m. c. Nez, L. Julien, and F. m. c. Biraben, "Combination of bloch oscillations with a ramsey-bordé interferometer: New determination of the fine structure constant," *Phys. Rev. Lett.*, vol. 101, p. 230801, Dec 2008.

[43] P.-C. Kuan, *Compton clock and recoil frequency measurements using a large momentum transfer atom interferometer*. PhD thesis, University of California at Berkeley, 2013.

[44] B. Estey, C. Yu, H. Müller, P.-C. Kuan, and S.-Y. Lan, "High-resolution atom interferometers with suppressed diffraction phases," *Phys. Rev. Lett.*, vol. 115, p. 083002, Aug 2015.

[45] W. Gander, G. H. Golub, and R. Strebel, "Least-squares fitting of circles and ellipses," *BIT Numerical Mathematics*, vol. 34, no. 4, pp. 558–578, 1994.

[46] D. K. Prasad, M. K. Leung, and C. Quek, "Ellifit: An unconstrained, non-iterative, least squares based geometric ellipse fitting method," *Pattern Recognition*, vol. 46, no. 5, pp. 1449 – 1465, 2013.

[47] J. K. Stockton, X. Wu, and M. A. Kasevich, "Bayesian estimation of differential interferometer phase," *Phys. Rev. A*, vol. 76, p. 033613, Sep 2007.

[48] S.-w. Chiow, J. Williams, and N. Yu, "Noise reduction in differential phase extraction of dual atom interferometers using an active servo loop," *Phys. Rev. A*, vol. 93, p. 013602, Jan 2016.

[49] A. Fitzgibbon, M. Pilu, and R. B. Fisher, "Direct least square fitting of ellipses," *IEEE Transactions on Pattern Analysis and Machine Intelligence*, vol. 21, pp. 476–480, May 1999.

[50] W. M. Itano, J. C. Bergquist, J. J. Bollinger, J. M. Gilligan, D. J. Heinzen, F. L. Moore, M. G. Raizen, and D. J. Wineland, "Quantum projection noise: Population fluctuations in two-level systems," *Phys. Rev. A*, vol. 47, pp. 3554–3570, May 1993.

[51] F. Sorrentino, Q. Bodart, L. Cacciapuoti, Y.-H. Lien, M. Prevedelli, G. Rosi, L. Salvi, and G. M. Tino, "Sensitivity limits of a raman atom interferometer as a gravity gradiometer," *Phys. Rev. A*, vol. 89, p. 023607, Feb 2014.

[52] E. Wright and P. Meystre, "Theory of an atomic interferometer in the raman-nath regime," *Optics Communications*, vol. 75, no. 5, pp. 388 – 396, 1990.

[53] H. Müller, S.-w. Chiow, and S. Chu, "Atom-wave diffraction between the raman-nath and the bragg regime: Effective rabi frequency, losses, and phase shifts," *Phys. Rev. A*, vol. 77, p. 023609, Feb 2008.

[54] T. Kovachy, S.-w. Chiow, and M. A. Kasevich, "Adiabatic-rapid-passage multiphoton bragg atom optics," *Phys. Rev. A*, vol. 86, p. 011606, Jul 2012.

[55] T. Kovachy, P. Asenbaum, C. Overstreet, C. A. Donnelly, S. M. Dickerson, A. Sugarbaker, J. M. Hogan, and M. A. Kasevich, "Quantum superposition at the half-metre scale," *Nature*, vol. 528, pp. 530–533, Dec 2015. Letter.

[56] C. E. Tanner and C. Wieman, "Precision measurement of the hyperfine structure of the ^{133}Cs $6P_{3/2}$ state," *Phys. Rev. A*, vol. 38, pp. 1616–1617, Aug 1988.

[57] T. Udem, J. Reichert, T. W. Hänsch, and M. Kourogi, "Absolute optical frequency measurement of the cesium D_2 line," *Phys. Rev. A*, vol. 62, p. 031801, Aug 2000.

[58] G. C. Bjorklund, "Frequency-modulation spectroscopy: a new method for measuring weak absorptions and dispersions," *Opt. Lett.*, vol. 5, pp. 15–17, Jan 1980.

[59] W. Demtröder, *Laser Spectroscopy: Vol. 2: Experimental Techniques*. Laser Spectroscopy, Springer Berlin Heidelberg, 2008.

[60] G. Camy, C. Bord, and M. Ducloy, "Heterodyne saturation spectroscopy through frequency modulation of the saturating beam," *Optics Communications*, vol. 41, no. 5, pp. 325 – 330, 1982.

[61] R. K. Raj, D. Bloch, J. J. Snyder, G. Camy, and M. Ducloy, "High-frequency optically heterodyned saturation spectroscopy via resonant degenerate four-wave mixing," *Phys. Rev. Lett.*, vol. 44, pp. 1251–1254, May 1980.

[62] J. H. Shirley, "Modulation transfer processes in optical heterodyne saturation spectroscopy," *Opt. Lett.*, vol. 7, pp. 537–539, Nov 1982.

[63] T. Okoshi, K. Kikuchi, and A. Nakayama, "Novel method for high resolution measurement of laser output spectrum," *Electronics Letters*, vol. 16, pp. 630–631, July 1980.

[64] P. D. Lett, W. D. Phillips, S. L. Rolston, C. E. Tanner, R. N. Watts, and C. I. Westbrook, "Optical molasses," *J. Opt. Soc. Am. B*, vol. 6, pp. 2084–2107, Nov 1989.

[65] T. Hänsch and A. Schawlow, "Cooling of gases by laser radiation," *Optics Communications*, vol. 13, no. 1, pp. 68 – 69, 1975.

[66] E. L. Raab, M. Prentiss, A. Cable, S. Chu, and D. E. Pritchard, "Trapping of neutral sodium atoms with radiation pressure," *Phys. Rev. Lett.*, vol. 59, pp. 2631–2634, Dec 1987.

[67] C. G. Townsend, N. H. Edwards, C. J. Cooper, K. P. Zetie, C. J. Foot, A. M. Steane, P. Szriftgiser, H. Perrin, and J. Dalibard, "Phase-space density in the magneto-optical trap," *Phys. Rev. A*, vol. 52, pp. 1423–1440, Aug 1995.

[68] D. A. Steck, "Cesium D Line Data," available online at http://steck.us/alkalidata (revision 2.1.4, 23 December 2010).

[69] C. G. Townsend, N. H. Edwards, K. P. Zetie, C. J. Cooper, J. Rink, and C. J. Foot, "High-density trapping of cesium atoms in a dark magneto-optical trap," *Phys. Rev. A*, vol. 53, pp. 1702–1714, Mar 1996.

[70] J. Kim and D. Cho, "Dark-spot magneto-optical trap of cesium atoms," *Journal of the Korean Physical Society*, vol. 39, pp. 864–868, 11 2001.

[71] C. B. Alcock, V. P. Itkin, and M. K. Horrigan, "Vapour Pressure Equations for the Metallic Elements: 298-2500K," *Canadian Metallurgical Quarterly*, vol. 23, no. 3, pp. 309–313, 1984.

[72] J. Schoser, A. Batär, R. Löw, V. Schweikhard, A. Grabowski, Y. B. Ovchinnikov, and T. Pfau, "Intense source of cold rb atoms from a pure two-dimensional magneto-optical trap," *Phys. Rev. A*, vol. 66, p. 023410, Aug 2002.

[73] A. Chambers, *Modern Vacuum Physics*. Masters series in physics and astronomy, Taylor & Francis, 2004.

[74] B. Saxberg, B. Plotkin-Swing, and S. Gupta, "Active stabilization of a diode laser injection lock," *Review of Scientific Instruments*, vol. 87, no. 6, 2016.

[75] T. Bergeman, G. Erez, and H. J. Metcalf, "Magnetostatic trapping fields for neutral atoms," *Phys. Rev. A*, vol. 35, pp. 1535–1546, Feb 1987.

[76] S.-i. Ohshima, T. Kurosu, T. Ikegami, and Y. Nakadan, "Cesium atomic fountain with two-dimensional moving molasses," *Japanese Journal of Applied Physics*, vol. 34, no. 9A, p. L1170, 1995.

[77] K. Chung, *Applications of atom interferometry using an improved laser cooling method*. PhD thesis, Stanford University, 2001.

[78] J. Hecker-Denschlag, J. E. Simsarian, H. Hffner, C. McKenzie, A. Browaeys, D. Cho, K. Helmerson, S. L. Rolston, and W. D. Phillips, "A bose-einstein condensate in an optical lattice," *Journal of Physics B: Atomic, Molecular and Optical Physics*, vol. 35, no. 14, p. 3095, 2002.

[79] P. A. Altin, M. T. Johnsson, V. Negnevitsky, G. R. Dennis, R. P. Anderson, J. E. Debs, S. S. Szigeti, K. S. Hardman, S. Bennetts, G. D. McDonald, L. D. Turner, J. D. Close, and N. P. Robins, "Precision atomic gravimeter based on bragg diffraction," *New Journal of Physics*, vol. 15, no. 2, p. 023009, 2013.

[80] S. M. Dickerson, J. M. Hogan, A. Sugarbaker, D. M. S. Johnson, and M. A. Kasevich, "Multiaxis inertial sensing with long-time point source atom interferometry," *Phys. Rev. Lett.*, vol. 111, p. 083001, Aug 2013.

[81] J. Dalibard and C. Cohen-Tannoudji, "Laser cooling below the doppler limit by polarization gradients: simple theoretical models," *J. Opt. Soc. Am. B*, vol. 6, pp. 2023–2045, Nov 1989.

[82] P. J. Ungar, D. S. Weiss, E. Riis, and S. Chu, "Optical molasses and multilevel atoms: theory," *J. Opt. Soc. Am. B*, vol. 6, pp. 2058–2071, Nov 1989.

[83] D. S. Weiss, E. Riis, Y. Shevy, P. J. Ungar, and S. Chu, "Optical molasses and multilevel atoms: experiment," *J. Opt. Soc. Am. B*, vol. 6, pp. 2072–2083, Nov 1989.

[84] C. Salomon, J. Dalibard, W. D. Phillips, A. Clairon, and S. Guellati, "Laser cooling of cesium atoms below 3 k," *EPL (Europhysics Letters)*, vol. 12, no. 8, p. 683, 1990.

[85] D. G. Enzer, W. M. Klipstein, and R. L. Tjoelker, "Light shift measurements in a cesium fountain without the use of mechanical shutters," in *Proceedings of the 2005 IEEE International Frequency Control Symposium and Exposition, 2005.*, pp. 6 pp.–, Aug 2005.

[86] M. Drewsen, P. Laurent, A. Nadir, G. Santarelli, A. Clairon, Y. Castin, D. Grison, and C. Salomon, "Investigation of sub-doppler cooling effects in a cesium magneto-optical trap," *Applied Physics B*, vol. 59, no. 3, pp. 283–298, 1994.

[87] J. E. H. Young and S.-K. Yao, "Design considerations for acousto-optic devices," *Proceedings of the IEEE*, vol. 69, pp. 54–64, Jan 1981.

[88] E. A. Donley, T. P. Heavner, F. Levi, M. O. Tataw, and S. R. Jefferts, "Double-pass acousto-optic modulator system," *Review of Scientific Instruments*, vol. 76, no. 6, p. 063112, 2005.

[89] A. Kastberg, W. D. Phillips, S. L. Rolston, R. J. C. Spreeuw, and P. S. Jessen, "Adiabatic cooling of cesium to 700 nk in an optical lattice," *Phys. Rev. Lett.*, vol. 74, pp. 1542–1545, Feb 1995.

[90] P. C. D. Hobbs, *Building Electro-Optical Systems: Making It All Work*. Wiley Publishing, 2nd ed., 2009.

[91] T. M. Brzozowski, M. Maczynska, M. Zawada, J. Zachorowski, and W. Gawlik, "Time-of-flight measurement of the temperature of cold atoms for short trap-probe beam distances," *Journal of Optics B: Quantum and Semiclassical Optics*, vol. 4, no. 1, p. 62, 2002.

[92] A. J. Kerman, *Raman sideband cooling and cold atomic collisions in optical lattices*. PhD thesis, Stanford University, 2002.

[93] M. Greiner, *Ultracold quantum gases in three-dimensional optical lattice potentials*. PhD thesis, Ludwig-Maximilians-Universität München, April 2003.

[94] V. Vuletić, C. Chin, A. J. Kerman, and S. Chu, "Degenerate raman sideband cooling of trapped cesium atoms at very high atomic densities," *Physical Review Letters*, vol. 81, no. 26, p. 5768, 1998.

[95] A. Rauschenbeutel, H. Schadwinkel, V. Gomer, and D. Meschede, "Standing light fields for cold atoms with intrinsically stable and variable time phases," *Optics Communications*, vol. 148, no. 13, pp. 45 – 48, 1998.

[96] P. Treutlein, K. Y. Chung, and S. Chu, "High-brightness atom source for atomic fountains," *Phys. Rev. A*, vol. 63, p. 051401, Apr 2001.

[97] V. Malinovsky and J. Krause, "General theory of population transfer by adiabatic rapid passage with intense, chirped laser pulses," *The European Physical Journal D - Atomic, Molecular, Optical and Plasma Physics*, vol. 14, no. 2, pp. 147–155, 2001.

[98] S. Merlet, L. Volodimer, M. Lours, and F. Pereira Dos Santos, "A simple laser system for atom interferometry," *Applied Physics B*, vol. 117, no. 2, pp. 749–754, 2014.

[99] S. S. Sané, S. Bennetts, J. E. Debs, C. C. N. Kuhn, G. D. McDonald, P. A. Altin, J. D. Close, and N. P. Robins, "11 w narrow linewidth laser source at 780nm for laser cooling and manipulation of rubidium," *Opt. Express*, vol. 20, pp. 8915–8919, Apr 2012.

[100] S. wey Chiow, T. Kovachy, J. M. Hogan, and M. A. Kasevich, "Generation of 43 w of quasi-continuous 780 nm laser light via high-efficiency, single-pass frequency doubling in periodically poled lithium niobate crystals," *Opt. Lett.*, vol. 37, pp. 3861–3863, Sep 2012.

[101] J. M. O. Daniel, N. Simakov, M. Tokurakawa, M. Ibsen, and W. A. Clarkson, "Ultrashort wavelength operation of a thulium fibre laser in the 1660-1750 nm wavelength band," *Opt. Express*, vol. 23, pp. 18269–18276, Jul 2015.

[102] G. Frith, T. McComb, B. Samson, W. Torruellas, M. Dennis, A. Carter, V. Khitrov, and K. Tankala, "Frequency doubling of tm-doped fiber lasers for efficient 950nm generation," in *Advanced Solid-State Photonics*, p. WB5, Optical Society of America, 2009.

[103] M. Andia, Étienne Wodey, F. Biraben, P. Cladé, and S. Guellati-Khélifa, "Bloch oscillations in an optical lattice generated by a laser source based on a fiber amplifier: decoherence effects due to amplified spontaneous emission," *J. Opt. Soc. Am. B*, vol. 32, pp. 1038–1042, Jun 2015.

[104] S. Schilt, R. Matthey, D. Kauffmann-Werner, C. Affolderbach, G. Mileti, and L. Thévenaz, "Laser offset-frequency locking up to 20 ghz using a low-frequency electrical filter technique," *Appl. Opt.*, vol. 47, pp. 4336–4344, Aug 2008.

[105] J. J. Maki, N. Campbell, C. Grande, R. Knorpp, and D. McIntyre, "Stabilized diode-laser system with grating feedback anf frequency-offset locking," *Optics Communications*, vol. 102, no. 3, pp. 251 – 256, 1993.

[106] R. W. P. Drever, J. L. Hall, F. V. Kowalski, J. Hough, G. M. Ford, A. J. Munley, and H. Ward, "Laser phase and frequency stabilization using an optical resonator," *Applied Physics B*, vol. 31, no. 2, pp. 97–105, 1983.

[107] T. Hänsch and B. Couillaud, "Laser frequency stabilization by polarization spectroscopy of a reflecting reference cavity," *Optics Communications*, vol. 35, no. 3, pp. 441 – 444, 1980.

[108] S.-w. Chiow, S. Herrmann, H. Müller, and S. Chu, "6w, 1khz linewidth, tunable continuous-wave near-infrared laser," *Opt. Express*, vol. 17, pp. 5246–5250, Mar 2009.

[109] R. Han, H. K. Ng, and B.-G. Englert, "Raman transitions without adiabatic elimination: a simple and accurate treatment," *Journal of Modern Optics*, vol. 60, no. 4, pp. 255–265, 2013.

[110] H. J. Metcalf and P. van der Straten, *Laser Cooling and Trapping*. New York: Springer-Verlag, 1999.

[111] Y. Torii, Y. Suzuki, M. Kozuma, T. Sugiura, T. Kuga, L. Deng, and E. W. Hagley, "Mach-zehnder bragg interferometer for a bose-einstein condensate," *Phys. Rev. A*, vol. 61, p. 041602, Feb 2000.

[112] J. E. Debs, P. A. Altin, T. H. Barter, D. Döring, G. R. Dennis, G. McDonald, R. P. Anderson, J. D. Close, and N. P. Robins, "Cold-atom gravimetry with a bose-einstein condensate," *Phys. Rev. A*, vol. 84, p. 033610, Sep 2011.

[113] H. Ammann and N. Christensen, "Delta kick cooling: A new method for cooling atoms," *Phys. Rev. Lett.*, vol. 78, pp. 2088–2091, Mar 1997.

[114] H. Müntinga, H. Ahlers, M. Krutzik, A. Wenzlawski, S. Arnold, D. Becker, K. Bongs, H. Dittus, H. Duncker, N. Gaaloul, C. Gherasim, E. Giese, C. Grzeschik, T. W. Hänsch, O. Hellmig, W. Herr, S. Herrmann, E. Kajari, S. Kleinert, C. Lämmerzahl, W. Lewoczko-Adamczyk, J. Malcolm, N. Meyer, R. Nolte, A. Peters, M. Popp, J. Reichel, A. Roura, J. Rudolph, M. Schiemangk, M. Schneider, S. T. Seidel, K. Sengstock, V. Tamma, T. Valenzuela, A. Vogel, R. Walser, T. Wendrich, P. Windpassinger, W. Zeller, T. van Zoest, W. Ertmer, W. P. Schleich, and E. M. Rasel, "Interferometry with bose-einstein condensates in microgravity," *Phys. Rev. Lett.*, vol. 110, p. 093602, Feb 2013.

[115] T. Kovachy, J. M. Hogan, A. Sugarbaker, S. M. Dickerson, C. A. Donnelly, C. Overstreet, and M. A. Kasevich, "Matter wave lensing to picokelvin temperatures," *Phys. Rev. Lett.*, vol. 114, p. 143004, Apr 2015.

[116] K. Moler, D. S. Weiss, M. Kasevich, and S. Chu, "Theoretical analysis of velocity-selective raman transitions," *Phys. Rev. A*, vol. 45, pp. 342–348, Jan 1992.

[117] "Super matched bipolar transistor pair sets new standards for drift and noise (rev. b)," National Semiconductor Application Note 222, May 2013.

[118] A. W.-C. Peng, *Quantum Gas Microscope With Optical Lattice*. PhD thesis, Harvard University, 2010.

[119] S.-Y. Lan, P.-C. Kuan, B. Estey, P. Haslinger, and H. Müller, "Influence of the coriolis force in atom interferometry," *Phys. Rev. Lett.*, vol. 108, p. 090402, Feb 2012.

[120] M. Ben Dahan, E. Peik, J. Reichel, Y. Castin, and C. Salomon, "Bloch oscillations of atoms in an optical potential," *Phys. Rev. Lett.*, vol. 76, pp. 4508–4511, Jun 1996.

[121] E. Peik, M. Ben Dahan, I. Bouchoule, Y. Castin, and C. Salomon, "Bloch oscillations of atoms, adiabatic rapid passage, and monokinetic atomic beams," *Phys. Rev. A*, vol. 55, pp. 2989–3001, Apr 1997.

[122] P. Cladé, E. de Mirandes, M. Cadoret, S. Guellati-Khélifa, C. Schwob, F. m. c. Nez, L. Julien, and F. m. c. Biraben, "Precise measurement of $hm_{\rm rb}$ using bloch oscillations in a vertical optical lattice: Determination of the fine-structure constant," *Phys. Rev. A*, vol. 74, p. 052109, Nov 2006.

[123] G. H. Wannier, "The structure of electronic excitation levels in insulating crystals," *Phys. Rev.*, vol. 52, pp. 191–197, Aug 1937.

[124] P. Cladé, "Bloch oscillations in atom interferometry," *Rivista del Nuovo Cimento*, vol. 38, pp. 173–207, Apr 2015.

[125] H. Müller, S.-w. Chiow, S. Herrmann, and S. Chu, "Atom interferometers with scalable enclosed area," *Phys. Rev. Lett.*, vol. 102, p. 240403, Jun 2009.

[126] A. Bertoldi, G. Lamporesi, L. Cacciapuoti, M. de Angelis, M. Fattori, T. Petelski, A. Peters, M. Prevedelli, J. Stuhler, and G. M. Tino, "Atom interferometry gravity-gradiometer for the determination of the newtonian gravitational constant g," *The European Physical Journal D - Atomic, Molecular, Optical and Plasma Physics*, vol. 40, no. 2, pp. 271–279, 2006.

[127] M. Niering, R. Holzwarth, J. Reichert, P. Pokasov, T. Udem, M. Weitz, T. W. Hänsch, P. Lemonde, G. Santarelli, M. Abgrall, P. Laurent, C. Salomon, and A. Clairon, "Measurement of the hydrogen $1S$- $2S$ transition frequency by phase coherent comparison with a microwave cesium fountain clock," *Phys. Rev. Lett.*, vol. 84, pp. 5496–5499, Jun 2000.

[128] F. Riehle, T. Kisters, A. Witte, J. Helmcke, and C. J. Bordé, "Optical ramsey spectroscopy in a rotating frame: Sagnac effect in a matter-wave interferometer," *Phys. Rev. Lett.*, vol. 67, pp. 177–180, Jul 1991.

[129] G. Breit and I. I. Rabi, "Measurement of nuclear spin," *Phys. Rev.*, vol. 38, pp. 2082–2083, Dec 1931.

[130] P. Kusch, S. Millman, and I. I. Rabi, "The Radiofrequency Spectra of Atoms Hyperfine Structure and Zeeman Effect in the Ground State of Li^6, Li^7, K^{39} and K^{41}," *Phys. Rev.*, vol. 57, pp. 765–780, May 1940.

[131] E. Arimondo, M. Inguscio, and P. Violino, "Experimental determinations of the hyperfine structure in the alkali atoms," *Rev. Mod. Phys.*, vol. 49, pp. 31–75, Jan 1977.

[132] G. D'Amico, F. Borselli, L. Cacciapuoti, M. Prevedelli, G. Rosi, F. Sorrentino, and G. M. Tino, "Bragg interferometer for gravity gradient measurements," *Phys. Rev. A*, vol. 93, p. 063628, Jun 2016.

[133] P. J. Leo, P. S. Julienne, F. H. Mies, and C. J. Williams, "Collisional frequency shifts in ^{133}Cs fountain clocks," *Phys. Rev. Lett.*, vol. 86, pp. 3743–3746, Apr 2001.

[134] C. Chin, V. Vuletić, A. J. Kerman, and S. Chu, "High resolution feshbach spectroscopy of cesium," *Phys. Rev. Lett.*, vol. 85, pp. 2717–2720, Sep 2000.

[135] P. Meystre and M. Sargent, *Elements of quantum optics*. Springer Berlin Heidelberg, 2007.

[136] P. Hamilton, M. Jaffe, J. M. Brown, L. Maisenbacher, B. Estey, and H. Müller, "Atom interferometry in an optical cavity," *Phys. Rev. Lett.*, vol. 114, p. 100405, Mar 2015.

Appendix A

Phase Calculation

The Mathematica code used to calculated the various interferometer phases and corrections is listed here. The global variable **state** is used to store all of the interferometer trajectories, and the functions **pulse()** and **evolve()** are used for the beam-splitter pulses and free evolution respectfully. Once the entire interferometer is completed, the **interfere()** function is called to interfere the spatially overlapped momentum states. The phase difference for each output is then calculated using the function **phase()**.

Note: The global variable [state] is used to hold the interferometer trajectories. Call the PrepareState[] function to re-initialize the vector before each interferometer calculation.

Definitions

Reserved variables

```
Clear[g, γ, m, z0, v0, ħ, keff];
Clear[Δk, k1, k2, k3, k4, kB];
gravity = True;
gradient = True;
xOffset = True;
vOffset = True;
useIntegratedL = True;
```

Replacement list for any pertibations that cause the interferometer to not close

```
zero = {γ → 0, Δk → 0, k1 → 0, k2 → 0, k3 → 0, k4 → 0, kB → 0, δt → 0};
```

Equations of motion and Largangian needed for free evolution phase calculation

```
X[x_, v_, t_, g_, γ_] := (x + v * t - g * t^2 / 2) + γ * t^2 * (x / 2 + v * t / 6 - g * t^2 / 24);
V[x_, v_, t_, g_, γ_] := (v - g * t) + γ * t * (x + v * t / 2 - g * t^2 / 6);
If[useIntegratedL,
  iL[x_, v_, t_, g_, γ_] :=
   g^2 m t^3 / 3 - g m t^2 v + m t v^2 / 2 - g m t x + (2 g^2 m t^5 - 10 g m t^4 v +
       10 m t^3 v^2 - 20 g m t^3 x + 30 m t^2 v x + 15 m t x^2) γ / 30,
  L[x_, v_, t_, g_, γ_] := m / 2 * V[x, v, t, g, γ]^2 - m * g * X[x, v, t, g, γ] +
    m * γ / 2 * X[x, v, t, g, γ]^2
 ];
```

Initial State {position, velocity, complex amplitude, diffraction order}

```
state = {{z0, v0, 1, 0}};

PrepareState[n_: 0] := Module[{x, v},
   If[xOffset, x = z0, x = 0];
   If[vOffset, v = v0, v = 0];
   state = {{x, v, 1, n}}
  ];
```

Evolve states by a time T

```
Evolve[T_] := Module[{x, v, ϕ, i, z, ϕnew, new},
  new = {};

  For[i = 1, i <= Length[state], i++,
   ϕ = state[[i, 3]];

   (* Only calculate evolution if the amplitude is non-zero *)
   If[! SameQ[ϕ, 0],
    z = state[[i]];
    x = state[[i, 1]];
    v = state[[i, 2]];
    z[[1]] = Simplify[X[x, v, T, If[gravity, g, 0], If[gradient, γ, 0]]];
    z[[2]] = Simplify[V[x, v, T, If[gravity, g, 0], If[gradient, γ, 0]]];
    If[useIntegratedL,
     ϕnew = iL[x, v, T, If[gravity, g, 0], If[gradient, γ, 0]] / ħ,
     ϕnew =
       Integrate[L[x, v, t, If[gravity, g, 0], If[gradient, γ, 0]], {t, 0, T}] / ħ;
    ];
    z[[3]] = ϕ * Exp[I * ϕnew];
    AppendTo[new, z];
   ];

  ];

  state = new
 ]
```

Perform a θ beam splitter between orders n1 and n2 on the state vector, with an optional δk pertibation

```
Pulse[θ_, n1_, n2_, δk_: 0] := Module[{x, v, ϕ, n0, i, new},
  new = state;

  (* Loop through each element in the
   state and check if the beam splitter applies to it *)
  For[i = 1, i ≤ Length[state], i++,
   {x, v, ϕ, n0} = state[[i]];

   (* Is the order of the state
    element equal to one side of the beam splitter *)
   If[TrueQ[n0 == n1],
    (* split state by θ *)
    AppendTo[new, {x, v, ϕ * Cos[θ / 2], n0}];
    new[[i, 2]] = v + (n2 - n1) / 2 * (keff + δk) * ħ / m;
    new[[i, 3]] = I * Sin[θ / 2] * ϕ * Exp[I * (n2 - n1) / 2 * ((keff + δk) * x)];
    new[[i, 4]] = n2;,
    (* Is the order of the state
     element equal to the other side of the beam splitter *)
    If[TrueQ[n0 == n2],
     (* split state by θ *)
     AppendTo[new, {x, v, ϕ * Cos[θ / 2], n0}];
     new[[i, 2]] = v - (n2 - n1) / 2 * (keff + δk) * ħ / m;
     new[[i, 3]] = I * Sin[θ / 2] * ϕ * Exp[-I * (n2 - n1) / 2 * ((keff + δk) * x)];
     new[[i, 4]] = n1;
    ]
   ]
  ];
  state = new
 ]
```

Interfere any overlapping states

```
Interfere[] := Module[{x, δx, v, ϕ, ϕ2, n0, i, j, k, assumptions, in, new, ϕδx},
  in = state;
  new = state;

  (* Loop through each element in the
   state and check if the beam splitter applies to it *)
  For[i = 1, i ≤ Length[in], i++,
   {x, v, ϕ, n0} = in[[i]];

   (* Check if the state interferes
    with another state (same position and order) *)
   k = 0;
   For[j = 1, j ≤ Length[in], j++,
    If[TrueQ[Simplify[(in[[j, 1]] == x) /. zero]] && (in[[j, 4]] == n0) /. n → 1,
     If[i ≠ j, k = j]
    ]
   ];

   If[k > 0,
    (* Two states are interfering, new state is combination of the two *)
    ϕ2 = in[[k, 3]];
    δx = (x - in[[k, 1]]);
    ϕδx = δx (in[[k, 2]] + v) / 2 * m / ℏ; (* separation phase *)
    new[[i, 3]] = ϕ + Exp[I * ϕδx] * ϕ2;
    in = Delete[in, k];
    new = Delete[new, k];
   ];
  ];
  state = new
 ]
```

Calculate the real amplitude of a wavefunction (slow)

```
SlowAmplitude[] := Module[{i, a, new, s},
   s = state;
   new = {};
   For[i = 1, i ≤ Length[s], i++,
    a = s[[i, 3]];
    AppendTo[new, FullSimplify[ComplexExpand[a * a-]]];
   ];
   new
  ];
```

Find the location of the exponentials for faster phase and amplitude caclulations

```
FindExp[a_] := Module[{result, i},
   result = {};
   If[Length[a] > 0,
    For[i = 1, i ≤ Length[a], i++,
      If[Length[a[[i]]] > 1,
        result = FindExp[a[[i]]];
        If[Length[result] > 0, result = Join[{i}, result]];
        ,
        If[a[[i]] == E, result = {i + 1}; Return[result];];
       ];
     ];
    ,
    If[a == E, result = {1}, result = {};];
   ];
   result
  ];
```

Calculate the phase of output states only (sign of phase not well defined)

```
Phase[] := Module[{i, a, new, ϕ1, ϕ2, pos, s},
    s = state;
    new = {};
    For[i = 1, i ≤ Length[s], i++,
     a = Expand[s[[i, 3]]];
     If[Length[a] > 1,
      If[TrueQ[a[[0]] == Plus],
       pos = FindExp[a[[1]]];
       ϕ1 = Extract[a[[1]], pos] / I;
       If[ϕ1 == {}, ϕ1 = 0];
       pos = FindExp[a[[2]]];
       ϕ2 = Extract[a[[2]], pos] / I;
       If[ϕ2 == {}, ϕ2 = 0];
       ,
       ϕ1 = 0;
       ϕ2 = 0;
      ];
      If[gradient,
       AppendTo[new, {Simplify[Normal[Series[ϕ1 - ϕ2, {γ, 0, 2}]]], s[[i, 4]]}]
       ,
       AppendTo[new, {Simplify[ϕ1 - ϕ2], s[[i, 4]]}]
      ]
      ,
      AppendTo[new, {0, s[[i, 4]]}];
     ];
    ];
    new
   ];
```

Calculate the real amplitude of a wavefunction

```
Amplitude[] := Module[{i, a, new, ϕ1, ϕ2, pos, s, A1, A2, δϕ},
    s = state;
    new = {};
    For[i = 1, i ≤ Length[s], i++,
     a = Expand[s[[i, 3]]];
     If[Length[a] > 1,
      Print[i];
      If[TrueQ[a[[0]] == Plus],
       pos = FindExp[a[[1]]];
       ϕ1 = Extract[a[[1]], pos] / I;
       If[TrueQ[ϕ1 == {}],
        ϕ1 = 0; A1 = a[[1]];,
        If[Length[pos] > 1,
           A1 = a[[1, 1 ;; pos[[1]] - 1]] * a[[1, pos[[1]] + 1 ;; -1]], A1 = 1];
       ];
       pos = FindExp[a[[2]]];
```

```
    ϕ2 = Extract[a[[2]], pos] / I;
    If[TrueQ[ϕ2 == {}],
     ϕ2 = 0; A2 = a[[2]];,
     If[Length[pos] > 1,
       A2 = a[[2, 1 ;; pos[[1]] - 1]] * a[[2, pos[[1]] + 1 ;; -1]], A2 = 1];
    ];
    ,
    pos = FindExp[a];
    ϕ1 = Extract[a, pos] / I;
    If[TrueQ[ϕ1 == {}],
     ϕ1 = 0; A1 = a;,
     If[Length[pos] > 1,
       A1 = a[[1 ;; pos[[1]] - 1]] * a[[pos[[1]] + 1 ;; -1]], A1 = 1];
    ];
    ϕ2 = 0;
    A2 = 0;
   ];
   If[gradient,
    δϕ = Simplify[Normal[Series[ϕ1 - ϕ2, {γ, 0, 2}]]];
    ,
    δϕ = Simplify[ϕ1 - ϕ2];
   ];
   If[FreeQ[A1 * A2, _Complex],
    AppendTo[new,
     {Simplify[ComplexExpand[A1 * A1- + A2 * A2- + 2 * A1 * A2- Cos[δϕ]]], s[[i, 4]]}],
    AppendTo[new, {Simplify[ComplexExpand[A1 * A1- + A2 * A2- + 2 * A1 * A2- Sin[δϕ]]],
      s[[i, 4]]}]
   ];
   ,
   AppendTo[new, {a, s[[i, 4]]}];
  ];
 ];
 new
];
```

Example Caclulations

Ramsey-Borde Interferometer with Bloch Oscillations

```
gravity = True;
gradient = True;
xOffset = False;
vOffset = False;
PrepareState[];

Pulse[π / 2, 0, 2 * n];
Evolve[T];

Pulse[π / 2, 0, 2 * n];
Evolve[Tp1];

(* Bloch Oscillation Momentum Transfer *)
Pulse[π, 0, -2 * NN];
Pulse[π, 2 * n, 2 * n + 2 * NN];
Evolve[Tp2];

Pulse[π / 2, -2 * NN, -2 * n - 2 * NN, Δk];
Pulse[π / 2, 2 * n + 2 * NN, 4 * n + 2 * NN, -Δk];
Evolve[T];

Pulse[π / 2, -2 * NN, -2 * n - 2 * NN, Δk];
Pulse[π / 2, 2 * n + 2 * NN, 4 * n + 2 * NN, -Δk];

Interfere[];
ϕdB = Phase[];
ϕdB = Simplify[Normal[Series[ϕdB, {γ, 0, 1}]]];

Expand[Simplify[ϕdB[[2, 1]] + ϕdB[[1, 1]]]] /. Δk * γ → 0 /. Δk^2 → 0
```

$$3\,g\,n\,T^2\,\Delta k + 2\,g\,n\,T\,Tp1\,\Delta k + 2\,g\,n\,T\,Tp2\,\Delta k + \frac{2\,keff^2\,n^2\,T\,\hbar}{m} +$$
$$\frac{2\,keff^2\,n\,NN\,T\,\hbar}{m} + \frac{keff^2\,n^2\,T^3\,\gamma\,\hbar}{3\,m} + \frac{keff^2\,n\,NN\,T^3\,\gamma\,\hbar}{3\,m} + \frac{keff^2\,n^2\,T^2\,Tp1\,\gamma\,\hbar}{2\,m} +$$
$$\frac{keff^2\,n^2\,T\,Tp1^2\,\gamma\,\hbar}{2\,m} + \frac{keff^2\,n^2\,T^2\,Tp2\,\gamma\,\hbar}{2\,m} + \frac{keff^2\,n\,NN\,T^2\,Tp2\,\gamma\,\hbar}{m} +$$
$$\frac{keff^2\,n^2\,T\,Tp1\,Tp2\,\gamma\,\hbar}{m} + \frac{keff^2\,n^2\,T\,Tp2^2\,\gamma\,\hbar}{2\,m} + \frac{keff^2\,n\,NN\,T\,Tp2^2\,\gamma\,\hbar}{m} - \frac{keff\,n^2\,T\,\Delta k\,\hbar}{m}$$

Gravity Gradiometer

```
gravity = True;
gradient = True;
xOffset = True;
vOffset = True;
PrepareState[];

(* Initial splitting *)
Pulse[π / 2, 0, 2 * n];
Evolve[Tp1];
(* Bloch Oscillation Momentum Transfer *)
Pulse[π, 2 * n, 2 * n + 2 * NN];
Pulse[π, 0, -2 * NN];
Evolve[Tp2];

(* MZ for top and bottom trajectories *)
Pulse[π / 2, 2 * n + 2 * NN, 4 * n + 2 * NN, -Δk];
Pulse[π / 2, -2 * NN, 2 * n - 2 * NN, Δk];
Evolve[T];
Pulse[π / 2, 2 * n + 2 * NN, 4 * n + 2 * NN, -Δk];
Pulse[π / 2, -2 * NN, 2 * n - 2 * NN, Δk];
Evolve[T];
Pulse[π / 2, 2 * n + 2 * NN, 4 * n + 2 * NN, -Δk];
Pulse[π / 2, -2 * NN, 2 * n - 2 * NN, Δk];

Interfere[];
ϕdmz = Phase[];
ϕdmz = Simplify[Normal[Series[ϕdmz, {γ, 0, 1}]]];

Expand[Simplify[ϕdmz[[2, 1]] - ϕdmz[[1, 1]]]] /. Δk * γ → 0 /. Δk^2 → 0
```

$$2\,g\,n\,T^2\,\Delta k + \frac{keff^2\,n^2\,T^3\,\gamma\,\hbar}{m} + \frac{2\,keff^2\,n\,NN\,T^3\,\gamma\,\hbar}{m} + \frac{keff^2\,n^2\,T^2\,tp\,\gamma\,\hbar}{m} + \frac{keff^2\,n^2\,T^2\,tp2\,\gamma\,\hbar}{m} + \frac{2\,keff^2\,n\,NN\,T^2\,tp2\,\gamma\,\hbar}{m}$$